Investigation of In-Situ Parameter Control in Novel Semiconductor Optical Amplifiers

A thesis submitted in Partial Fulfilment of the Requirements
for the Degree of Doctor of Philosophy
(Electronic Engineering)

By
Kevin Carney
B.A. Physics

School of Electronic Engineering
Faculty of Engineering and Computing
Dublin City University

Research Supervisor
Dr. Pascal Landais

May 2012

DECLARATION

I hereby certify that this material, which I now submit for assessment on the programme of study leading to the award of Doctor of Philosophy is entirely my own work, that I have exercised reasonable care to ensure that the work is original, and does not to the best of my knowledge breach any law of copyright, and has not been taken from the work of others save and to the extent that such work has been cited and acknowledged within the text of my work.

Signed: _______________________

ID No.: _______________________

Date: _________________________

ACKNOWLEDGEMENTS

This thesis is the result of four years of work, and could not have been accomplished without the help of many people, for which I am forever grateful.

My supervisor, Dr. Pascal Landais, who brought me onto this project and has been a constant source of help and guidance.

Thanks also to Dr. Robert Manning and Dr. Prince Anadarajah for agreeing to examine my thesis and defence, and for the helpful comments.

Dr. Ramon Maldonado-Basilio and Dr. Sylwester Latkowski, who were on hand to answer any questions I had while I was getting my bearings in the world of research. I'll certainly miss the nights out and the football games!

All of the guys in the lab, who have made my time here so memorable, in no particular order: Kai, Rob, Karl, Colm, Prince, Daniele, Elif, Frank, Josue, Severine, Krzysztof, Eamon, Tam, Rui, Haymen, Liam, Regan, Doug, Antonio, Arsalan.

Special thanks to David Grimes and Roisin O'Regan for proof reading and general suggestions.

Dr. Louise Bradley in Trinity, for the helpful discussions and suggestions. All the Trinity guys: Ronan, Joe, Ciaran, Ed, Diarmuid and John. Special thanks to Rob Lennox, who knows more than most about what went into this work.

My heartfelt thanks go to my family, my parents and my two brothers, who have supported me unconditionally throughout.

Finally, I could not have gone through these last four years without the help, support, and comfort of my girlfriend, Roisin. She has been there for every step along the way, particularly in the last few months, and this is for her.

TABLE OF CONTENTS

TABLE OF FIGURES

ABSTRACT

Investigation of In-Situ Parameter Control in Novel Semiconductor Optical Amplifiers

Kevin Carney

B.A. Physics

Fibre optic networks form the backbone of modern communications systems. As demand for ever increasing bandwidth continues to grow, technologies that enable the expansion of optical networks will be the key to future development. The semiconductor optical amplifier (SOA) is a technology that may be crucial in future optical networks, as a low cost in-line amplifier or as a functional element. As fibre networks extend closer to the end user, economical ways of improving the reach of these networks are important. SOAs are small, relatively inexpensive and can be readily integrated in photonic circuits. Problems persist with the development of SOAs, however, in the form of a relatively high noise figure and low saturation output power, which limits their use in many circumstances. The aim of this thesis is to outline a concept for control of these parameters such that the SOA can achieve the performance required. The concept relies on the control of the carrier density distribution in the SOA. The basic characteristics of the SOA and how they are affected by changes in the carrier density are studied. The performance of the SOA in linear and high power transmission of CW and pulsed signals is determined. Finally, the wavelength conversion characteristics of the SOA are outlined. The role of the carrier density control in shaping all of these characteristics will be explained.

INTRODUCTION

In the last two decades, the field of optical communications has seen tremendous growth. It has both driven and been driven by the expansion of the internet as a means of communication and lately also by the ever increasing demand for high definition television, online gaming, and video streaming applications. A communications revolution was initiated by the invention and wide-scale deployment of optical fibres as a means of data transmission. The use of optical fibres for long range communications was shown to have numerous advantages over the traditional copper cable network. The attenuation of optical signals in standard single mode fibres is ~ 0.2 dB/km in the 1.5 μm transmission window, far below that of electrical signals in copper wire. Optical fibres do not suffer from electromagnetic interference. The main advantage they possess over copper cable is their enormous transmission bandwidth, meaning that fibre can transmit orders of magnitude more information than a comparable copper cable. Thus it has been installed in trans-oceanic links and backbone networks throughout the world. This level of expansion was made possible due to the invention of optical amplifiers such as Erbium doped fibre amplifiers (EDFA). Whereas before this, attenuation in long fibre links would have to be compensated by expensive and bulky electrical repeaters, optical amplifiers allowed the amplification of the signal without electrical conversion, massively increasing efficiency. They also made possible the use of wavelength multiplexing transmission schemes due to their wide amplification bandwidth.

Current speeds for single channels in optical networks are 10 Gb/s or 40 Gb/s, with the introduction of up to 100 Gb/s speeds underway. However, the fundamental speed limit on processing electronics means that an optical solution to signal processing needs must be found. In addition to this, as fibre networks are expanded closer to the end user, cheaper and more flexible amplification solutions will be needed to allow range extension of optical networks. Semiconductor optical amplifiers (SOA) are ideally placed in both scenarios, as they are compact, relatively cheap, and are a versatile technology. They have an advantage over other optical amplifiers in that they incorporate signal processing capabilities due to non-linear effects in the semiconductor medium. With regards to in-line amplification, the lower cost and ease of deployment of SOAs makes them attractive for range extension of passive optical networks in particular. Problems exist with this application however, due to both the noise penalty imposed by the SOA at low optical power and the effects of gain saturation at high optical powers. What is needed is a flexible solution that can adapt to network demands.

This thesis presents designs for SOAs that aim to introduce this flexibility, both in terms of reduced noise and saturation effects. This is accomplished through control of the SOA carrier density. One design utilizes gain clamping using a laser cavity embedded laterally within part of the device, whereas the second design provides for the injection of current through multiple electrical contacts, allowing for flexible control of the carrier density. The thesis will be outlined as follows.

Chapter 1 reviews historical development of semiconductor optical amplifiers and details the various technological advancements that have accompanied their development. The physics and functionality of SOAs are outlined, and the processes contributing to optical gain and carrier recombination in semiconductors is outlined. Finally, the various parameters of interest in an SOA are detailed.

Chapter 2 explores further the concept of noise figure and saturation power in SOAs, and details the limitations imposed on signal amplification by these characteristics. The various methods that have been proposed to alleviate these problems are detailed. Finally, the proposed concept for controlling the noise figure and saturation power is described.

Chapter 3 gives the results of an experimental and simulated characterisation of the steady state characteristics of the SOAs under test. A simulation based on the travelling wave model of an SOA is used to illustrate the concept introduced in Chapter 2, and then the results of the experimental characterisation are compared with the simulated results.

Chapter 4 examines the effect of the carrier density control concept on the in-line amplification characteristics of a multi-contact SOA design. The errors in transmission of a pseudo-random bit stream are determined as a function of the bias current applied to the SOA, in order to illustrate the effect of the carrier density control. The characteristics of ultrashort optical pulses after transmission through the SOA is also examined, with the changes in the pulse and spectral shape determined.

Chapter 5 explores the functional applications of the SOA, and how these are affected by the carrier distribution. The use of SOAs as potential wavelength converters and optical switches is explored. The characteristics of cross gain modulation and four wave mixing in the SOA are the presented as a function of the carrier density distribution.

1. SEMICONDUCTOR OPTICAL AMPLIFIERS

1.1. Introduction

1.1.1. SOA technology and historical development

Semiconductor optical amplifiers (SOAs) have been studied for as long as semiconductor lasers, since they are a very similar technology. SOAs are effectively semiconductor lasers with anti-reflection coated facets. An electrical current is injected to the device in order to achieve optical gain for an injected signal. The signal itself is confined through refractive index guiding to an area called the active region, which is where optical gain takes place. The active region is surrounded by doped semiconductor regions called cladding regions, and some of the signal leaks into these areas. The amplification of the optical signal is accompanied by noise, which is an unavoidable aspect of the amplification process. SOAs, like semiconductor lasers, are heavily based on the III-V group of semiconductor materials. Early work on SOAs was carried out on GaAs/AlGaAs material systems, but from the 1990s onwards, research focused on SOAs based on InP with InGaAsP active regions 0. This material was chosen due to its ability to amplify signals in the 1300 – 1600 nm wavelength range, which became the wavelength region of choice for the expanding technology of optical fibre communications. SOAs can be broadly classified into two main categories: Fabry-Perot SOAs (FP-SOA) and travelling wave SOAs (TW-SOA). FP-SOAs have appreciable facet reflectivities and so a cavity resonance is observed, resulting in large ripples in the gain spectrum. TW-SOAs, on the other hand, have much reduced facet reflectivities due to dielectric coatings at the air-semiconductor interface. While typical facet reflectivity values for lasers is ~ 0.3, dielectric coating using SiO_2 and similar materials in SOAs can produce values < 10^{-4} [2]. As a result, the TW-SOA gain spectrum is broad and relatively flat. Some cavity resonance still exists, due to the imperfect nature of the facet coating for a wide range of wavelengths. The SOAs discussed within this thesis are TW-SOAs. SOAs are fabricated using a variety of epitaxial growth techniques, which is the lattice matched growth of one semiconductor on top of another. Such techniques include liquid phase epitaxy, vapour phase epitaxy and molecular beam epitaxy. The most common method used today is metal-organic chemical vapour deposition (MOCVD). In this technique, metal alkyls in gaseous form are passed over an InP substrate, and form an epitaxial layer of InGaAsP [3]. The rate of the gas flow controls the composition of the InGaAsP layer. A basic schematic of an SOA is shown in Fig. 1.1.

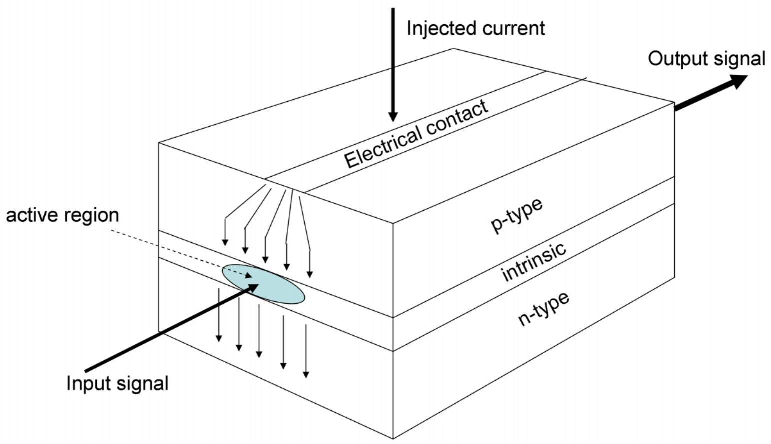

1.1. Schematic of a semiconductor optical amplifier.

1.1.2. SOA structures

The properties of SOAs are dependent on many factors, such as the injected bias current, input optical power, temperature et cetera. In particular, the structure and dimensionality of the active region of the SOA plays a crucial role in determining device parameters. As the size of the active region is reduced, quantum effects begin to have a strong influence. SOA active regions are generally composed of bulk material, quantum wells or quantum dots.

Bulk SOAs

If the SOA active region has dimensions much greater than the de Broglie wavelength λ_B it is a bulk structure. SOAs had only bulk active regions until the late 1980s and the technology is well established. Bulk SOAs have the advantage of a relatively large confinement factor. They also exhibit strong amplitude phase coupling compared with other material systems, which is important for certain dynamic applications such as cross phase modulation.

Quantum well SOAs

In a quantum well SOA (QW-SOA), the active region size is reduced to the point where the carriers are confined to two dimensions, with the scale of the third dimension being on the order of λ_B. As a result, the electron density of states takes the form of a step function, rather than a continuous spread of possible states [4]. This has the effect of reducing the dependency of the SOA gain on the photon energy, and consequently broadens the gain spectrum [5]. The threshold current of a QW-SOA is significantly reduced compared to that of a bulk SOA. The confinement factor of the active region is less than that of a bulk active region due to the small dimensions of a quantum well. In order to compensate for this, stacks of wells as usually grown, with a layer of cladding material between each well. Quantum well SOAs have a lower differential gain coefficient compared with bulk SOAs. This leads to an improvement in the saturation output power.

Quantum dot SOAs

Quantum dots (QD) are semiconductor crystals with all dimensions on the order of nanometers. The carriers in quantum dots are confined in all directions, leading to a zero dimensionality in the density of states. They improve upon the gain bandwidth and saturation power performance exhibited by QW-SOAs [6, 7], while also displaying greatly superior gain recovery properties to other types of SOA. The recovery dynamics of QD-SOAs are accelerated by the capture of carriers from the higher energy wetting layer states into the conduction band ground state, leading to gain recovery times on the order of picoseconds [8]. Pattern free amplification of optical signals has been demonstrated in QD-SOAs at speeds up to 40 GHz [9].

1.1.3. SOAs vs other optical amplifiers

The use of SOAs as in-line amplifiers in optical networks is becoming more common, however their prevalence does not match that of Erbium doped fibre amplifier (EDFA), which is the amplifier technology of choice for modern optical networks in the C-band regime [10]. An EDFA consists of a length of optical fibre that is doped with Er^{+3} ions. EDFAs exhibit high optical gain in the 1550 nm region and thus are widely used in amplification in Dense Wavelength Division Multiplexed (DWDM) transmission schemes in this wavelength region [11, 12, 13]. EDFAs were invented in the mid-1980s and were an integral driver of the optical communications revolution. Their advantages over SOAs for in-line amplification include lower noise figure, higher output saturation power and crucially, slow gain dynamics, which allows them to amplify multiple input signals without crosstalk effects. On the other hand, due to the necessity of a pump laser, EDFAs are generally larger and more expensive than SOAs, and thus cannot be integrated with other photonic devices. Their long lived gain dynamics compared with SOAs mean that they cannot be used for functional applications. SOAs also have an advantage in amplifications windows outside of the C-band, where EDFA technology is still relatively new. An SOAs active region material can be engineered to provide gain in a wide variety of bands.

Another amplification technology in widespread use is Raman amplification. Raman amplifiers use stimulated Raman scattering (SRS) to amplify signals. An intense pump beam propagates in an optical fibre, and through SRS gives up its energy to create another photon at a lower frequency by inelastic scattering. The remaining energy manifests itself in the form of optical phonons. If the wavelength of the pump beam is chosen carefully, energy can be transferred between the pump beam and a signal beam, achieving optical gain. Advantages of Raman amplification include a wide gain bandwidth and the ability to operate in amplification windows that EDFAs cannot [14]. However, like EDFAs, a strong pump beam is required to achieve gain, adding to amplifier complexity and cost. SOAs have an inherent advantage in that they are electrically pumped.

1.2. Semiconductor Physics and Photonic Emission

1.2.1. P-N junction

An SOA is a diode formed from the joining of a material doped with an excess of electron donor ions (n-type), which contributes more electrons, and a material doped with an excess of electron acceptor ions (p-type), which contributes more holes. When the p- and n-type materials are joined, the excess electron concentration begins to diffuse into the p-type material and vice versa [15]. As this diffusion proceeds, an electric field begins to build up due to the positively and negatively charged ions left at the junction. This electric field creates a drift of charges which counteracts the diffusion caused by the material doping and an area called the depletion region forms which is free of charge carriers [16]. If a forward bias greater than a certain magnitude, called the barrier potential V_D, is applied, then this electric field is reduced and current can flow across the junction. This is the basic principle of a homojunction semiconductor diode. SOAs are generally double heterojunction structures.

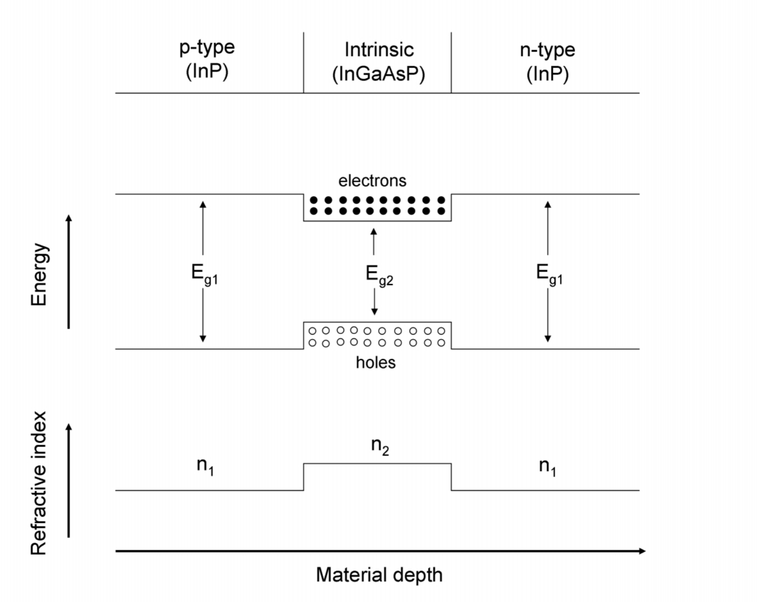

1.2. Illustration of double heterojunction structure, with carrier confinement and index guiding.

A heterojunction is a junction between two semiconductor materials of dissimilar bandgap energy. In a heterojunction diode like an SOA, a layer of intrinsic (undoped) semiconductor material such as InGaAsP is sandwiched between two layers of doped material such as InP. The intrinsic material has a smaller barrier potential, or bandgap, than the doped material. When a forward bias greater than the barrier potential of the doped material is applied, electrons and holes flow into the intrinsic region, but cannot cross the junction at the other side. Thus electrons in the conduction band and holes in the valence band are confined in the one space and recombine in a region called the active region [17]. The active region must be quite narrow so that the SOA supports only a single transverse mode with one of two possible polarizations, transverse electric (TE) or transverse magnetic (TM). The electric field of TE polarized light is oriented in the epitaxial plane. For TM light this is the case for the magnetic field. The concentration of carriers in the active region is what makes optical gain possible. The intrinsic material of the active region has a higher refractive index than the surrounding cladding regions, thus a refractive index step is created across the junction, which acts to confine the light in the active region through total internal reflection. A representation of a heterojunction structure is shown in Fig. 1.2. The amount of confinement created is represented by the confinement factor,

$$\Gamma = \frac{\int_{-w/2}^{w/2} |E|^2 \, dx}{\int_{-\infty}^{\infty} |E|^2 \, dx}, \tag{1.1}$$

which is the ratio of the electric field E within the active region of width w to the total electric field [18, 19].

1.2.2. Radiative Processes and Optical Gain

E-k diagram

We can approximate the radiative processes in the SOA active region with a two level system. This approximation is valid for a bulk material system, which is the system considered. Within the active region, the electrons injected via the applied forward bias occupy the conduction band, leaving holes in the valence band. The electrons in the conduction band can recombine with the holes in the valence band, releasing energy. The band structure of a typical direct bandgap semiconductor is shown in Fig. 1.3, which is an energy momentum diagram [20]. Direct bandgap means that the band edges of the conduction and valence bands coincide in momentum space. The wave-vector k is represented on the x-axis, which is related to the momentum of the carriers. The valence band is split into different bands, depending on the hole effective mass. In a bulk semiconductor, the light hole and heavy hole bands are degenerate at the band maximum, i.e. they have the same energy [21]. Carrier recombination can happen through radiative or non-radiative processes. In order for photonic emission to take place, radiative recombination must occur. The three radiative processes are stimulated absorption, stimulated emission and spontaneous emission [22].

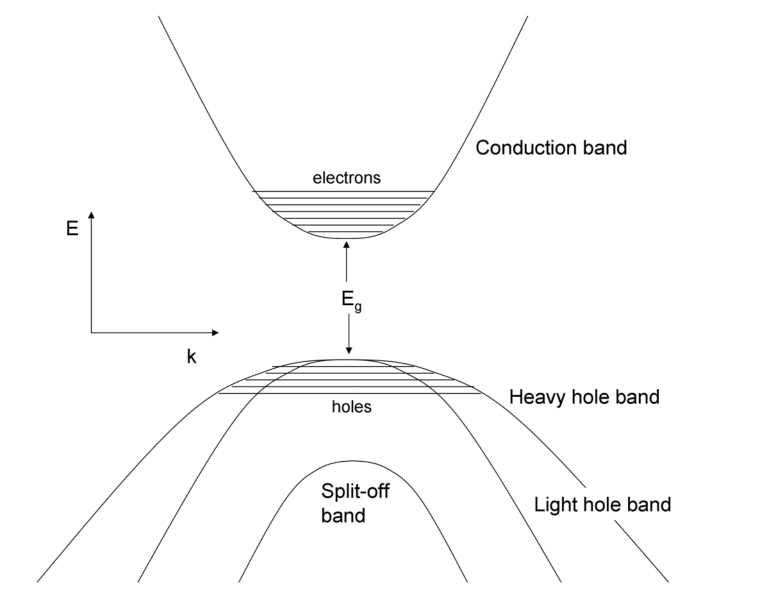

1.3. Band structure of typical direct bandgap semiconductor.

When a photon with energy equal or greater to the bandgap energy is incident on the semiconductor, its energy can cause the transition of an electron from the valence band to the conduction band, extinguishing itself in the process. This is the process of stimulated absorption.

Another process that can occur when a photon is incident on the active region is stimulated emission. Stimulated emission occurs when the incident photon causes the transition of an electron from the conduction band to the valence band, recombining with a hole. The energy lost by the electron in this process is emitted as a photon which has the same phase, frequency and polarisation as the simulating photon, i.e. it is a coherent process.

There is a non-zero probability that a conduction band electron may spontaneously recombine with a hole, emitting a photon. The emitted photon has random phase and direction. The frequency of the emitted photon is dependent on the transition energy and can occur over a wide bandwidth. Spontaneously emitted photons are essentially noise, and are an unavoidable part of the amplification process. In addition to adding noise they reduce the amount of carriers available for stimulated emission.

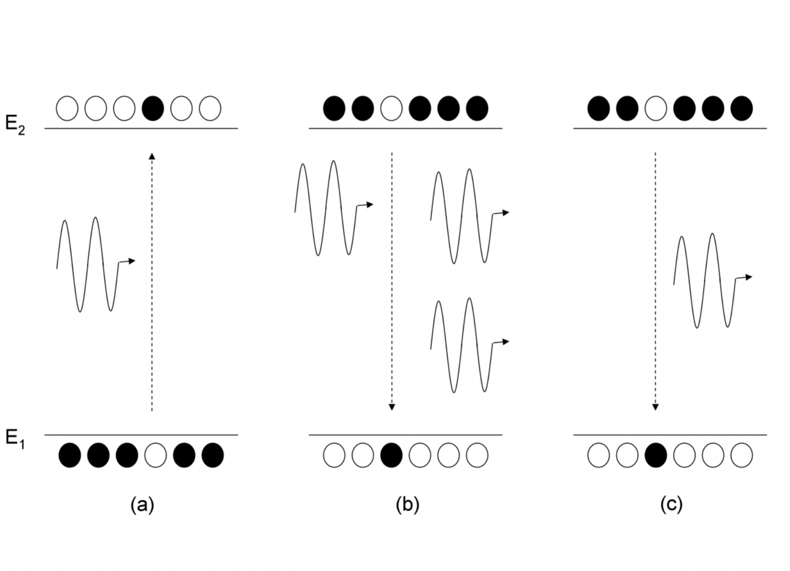

1.4. Band diagram illustration of (a) stimulated absorption, (b) stimulated emission and (c) spontaneous emission.

Population inversion and optical gain

Whether or not a signal is amplified in an SOA is dependent on the relative strength of the various radiative processes. The rate of spontaneous emission is directly proportional to the population of the conduction band N_2 and can be expressed as,

$$R_{21}^{spon} = A_{21} N_2 , \tag{1.2}$$

where *1* and *2* represent the valence and conduction bands respectively and A_{21} is the spontaneous emission probability per unit time from level 2 to level 1. The two processes that mainly determine the optical gain are stimulated absorption and emission. The rate of simulated absorption can be described as a function of the incident photon energy density per unit frequency $\rho(\nu)$ and the population of carriers in the valence band N_1,

$$R_{12} = B_{12} \rho(\nu) N_1 , \tag{1.3}$$

where B_{12} is the stimulated absorption probability per unit time from level 1 to level 2. Similarly, the expression for stimulated emission is,

$$R_{21}^{stim} = B_{21} \rho(\nu) N_2 , \tag{1.4}$$

where B_{21} is the stimulated emission probability per unit time from level 2 to level 1. It can be shown from the Einstein relations that $B_{12} = B_{21}$, i.e. the probability of stimulated absorption equals that of stimulated emission [23]. The spontaneous emission probability is related to the stimulated emission probability by,

$$A_{21} = \left[\frac{8\pi n_r^3 h \nu^3}{c^3}\right] B_{21}, \tag{1.5}$$

where n_r is the material refractive index. Introducing the induced transition lineshape $l(v)$, $\rho(v)$ can be expressed as $\rho l(v)$, where ρ is the energy density of the field inducing the transition. We can then express the inducing field intensity I_v as,

$$I_\nu = \frac{c}{n_r}\rho \tag{1.6}$$

Using Eqs. (1.5) and (1.6), Eq. (1.4) can then be expressed as,

$$R_{21}^{stim} = \frac{A_{21} c^2 l(\nu) I_\nu N_2}{8\pi n_r^2 h \nu^3} \tag{1.7}$$

In the case of a monochromatic plane wave propagating in the z direction through a cross section area A and length increment dz, the change in optical power is given as,

$$\begin{aligned} \frac{dP(z)}{dz} &= \left(R_{21}^{stim} - R_{12}\right) h\nu A \\ &= g_m(\nu) P_\nu \end{aligned} \tag{1.8}$$

where P_v is the initial signal power. Thus the material gain $g_m(v)$ at an optical frequency v is therefore derived as [2],

$$g_m(\nu) = \frac{A_{21} c^2 l(\nu)\left(N_2 - N_1\right)}{8\pi n_r^2 \nu^2} \tag{1.9}$$

From Eq. (1.9) it is clear that in order to achieve a positive gain, the population of the conduction band must exceed that of the valence band. This is called a population inversion and is achieved in SOAs and semiconductor lasers through electrical pumping.

The presence of the spontaneous emission probability term shows how spontaneous emission accompanies the gain process.

1.3. SOA carrier dynamics

1.3.1. Bulk SOA carrier recombination mechanisms

As outlined above, radiative recombination of carriers in the active region is necessary for photonic emission and consequently optical gain. However, carriers in SOAs can also recombine non-radiatively. Non-radiative recombination mechanisms dominate radiative recombination for indirect bandgap semiconductors such as silicon or germanium. Radiative recombination is much more likely for direct bandgap semiconductors. The three main recombination processes in an SOA with no signal injection are non-radiative recombination due to material defects, radiative recombination due to spontaneous emission, and non-radiative Auger recombination [24].

- Defects in the semiconductor material can give rise to "traps" in the active region. Carriers caught at these traps can recombine without the release of a photon because the defects introduce a continuum of energy states. This is called Shockley-Read-Hall recombination. Defects can arise in semiconductor material during the fabrication stage, or as the device ages. The rate of non-radiative recombination due to defects is proportional to the carrier density n and is given as,

$$R_{nr} = A_{nr} n, \tag{1.10}$$

  where A_{nr} is the non-radiative recombination coefficient. A typical value for A_{nr} is $10^7 - 10^8$ s^{-1}.

- Radiative recombination with respect to stimulated emission has been covered to an extent. Spontaneous emission is the spontaneous recombination of an electron and a hole with the subsequent emission of a photon. Since the process depends on the interaction between two particles, an electron and a hole, the radiative recombination rate is dependent on both the carrier (electron) density n

and the hole density *p*. In SOAs *n* is approximately equal to *p*, therefore the recombination rate is,

$$R_{rad} = B_{rad} n^2 , \tag{1.11}$$

where B_{rad} is the radiative recombination coefficient, which usually has a value on the order of 10^{-16} m^3s^{-1}.

- The main non-radiative recombination mechanism is Auger recombination. Considering the case of an n-doped semiconductor, the most prevalent Auger process is the band-to-band CCCH Auger process. In this case, C stands for conduction band and H stands for the heavy hole valence band. It is so called because it involves four particle states, three electron states and a heavy hole state. An electron recombines with a hole but instead of releasing its excess energy and momentum to a photon, it transfers it to a second conduction band electron, which is then excited to a high energy level. This electron can then relax to lower energy levels through the emission of phonons. As the process is dependent on two electrons and a hole, the Auger recombination rate is,

$$R_{aug} = C_{aug} n^3 \tag{1.12}$$

where C_{aug} is the Auger coefficient, which has a value of ~ 10^{-41} m^6s^{-1} in InGaAsP material. Auger recombination is a temperature dependent process, and is stronger in InGaAsP material systems, compared with AlGaAs [25].

1.3.2. SOA gain dynamics

The processes of stimulated and spontaneous emission reduce the optical gain of the SOA because the recombination of carriers means that less are available for further stimulated emission and thus amplification. When an optical signal is injected into an SOA, there is an instantaneous reduction in gain. The gain recovers to its initial value through various processes, each with their own timescale. These timescales determine the dynamic switching speed of the SOA. The processes can be categorized into two types: interband and intraband. The term interband describes processes that involve transitions between the conduction band and the valence band. Intraband describes processes occurring within the bands themselves [26]. The three main processes contributing to gain depletion and recovery in SOAs, in descending order of timescale, are carrier density pulsations, carrier heating and spectral hole burning.

- Carrier density pulsations (CDP) is the name given to the replenishing of carriers from the valence band to the conduction band by electrical pumping. The timescale of CDP is determined by the carrier density and the recombination rates for the radiative and non-radiative processes associated with interband gain recovery, and is given by,

$${}_{2} = \frac{n}{R(n)} = \frac{1}{A_{nr} + B_{rad}\,n + C_{aug}\,n^{3}}\,, \qquad (1.13)$$

  where *n* is the carrier density and *R(n)* is the combined recombination rate for all interband processes. The CDP timescale is called the carrier lifetime. An increase in the carrier density reduces the carrier lifetime and speeds up gain recovery. Typical values for the carrier lifetime in SOAs is 0.1 – 1 ns.

- Carrier heating (CH) can arise from two different processes [27]. When an optical signal is injected into an SOA and causes a stimulated emission event, the electron that recombines is usually one of the conduction band carriers with the least energy, i.e. below the quasi-Fermi level. The removal of this carrier increases the average temperature of the remaining carriers, causing a reduction in the gain. The other process by which this can happen is free carrier absorption (FCA), or the plasma effect. The absorption of an incident photon by a conduction band electron causes it to jump to a higher energy band, again raising the average temperature of the carriers. The temperature of these carriers relaxes back to the lattice temperature by the emission of phonons. This process occurs in a timescale on the order of 1 – 2 ps.

- The final process is spectral hole burning (SHB), which is the localized reduction in the number of carriers at the transition energy of an incident intense optical signal. This causes a “hole” to appear in the gain spectrum of the SOA at the incident photon frequency. The depth of the hole is dependent on the intensity of the optical signal. The gain recovers due to carrier-carrier scattering processes that operate on a timescale on the order of 50 – 100 fs.

1.4. SOA parameters

An SOA can be characterized by a number of measurable parameters that determine its suitability for use in an optical network. These parameters vary from device to device, depending on material composition, active region type, device length et cetera.

1.4.1. Optical gain and saturation

As mentioned in Section 1.2.2, when a population inversion is achieved in the SOA active region, the device exhibits optical gain. This simply means that the output power from the SOA is greater than at the input. The gain of an SOA is dependent on both the input optical power level and the input signal wavelength. The gain G can be expressed as a function of signal power P by,

$$G = \frac{G_0}{1 + P/P_s}, \tag{1.14}$$

where G_0 is the small signal gain value and P_s is the SOA saturation input power. It is clear from this equation that the optical gain reduces drastically as P approaches P_s. This is the phenomenon of gain saturation, which is covered in greater detail in Chapter 2. One of the main objectives of this thesis is to demonstrate control of gain saturation using novel SOA design. P_s is the optical input power at which the gain in the SOA is reduced by half. The gain is also dependent on the signal wavelength. This is a consequence of the band structure of the semiconductor medium. Since the conduction and valence bands in a semiconductor material are not sharp and distinct energy levels but rather bands, the density of states within these bands is spread out over a range of photon energies. Therefore the rate of stimulated and spontaneous emission between these bands will vary depending on the incident photon wavelength. The material gain spectrum is a representation of this dependency and is roughly parabolic in shape. It can be approximated by [28],

$$g_m(N, \lambda) = g_m^{peak}(N) - \gamma(\lambda - \lambda_0)^2, \tag{1.15}$$

where N is the carrier density, λ is the signal wavelength, λ_0 is the gain peak wavelength and γ is a constant related to the width of the material gain spectrum. The peak material gain is given by,

$$g_m^{peak}(N) = a_1 (N - N_0), \tag{1.16}$$

where N_0 is the carrier density at transparency and a_1 is the differential gain coefficient. The gain spectrum of an SOA is said to be homogeneously broadened [29]. This means that a reduction of the carrier density due to spontaneous or stimulated emission does not change the shape of the gain spectrum. If the gain is saturated by a signal at one wavelength, it is saturated for all input signals to the SOA.

1.4.2. Polarisation sensitivity

One of the main disadvantages of SOAs compared with EDFAs is their inherent polarisation sensitivity. Since an EDFA is an optical fibre based system, it is polarisation insensitive, whereas the polarisation sensitivity of an SOA is dependent on, among other factors, its waveguide geometry. Due to the dimensions of the SOA waveguide, the confinement factors for the TE and TM modes are not equal, and therefore they experience different values of gain. The anti-reflection coatings used to suppress cavity resonance can also exhibit polarisation sensitivity. The waveguide of the SOA can be engineered to eliminate most of the confinement factor difference between the modes. In bulk SOAs, square waveguides can be used in order to equalize the geometric factors that affect the TM mode in normal rectangular waveguides. The most common and effective method to reduce polarisation sensitivity is to introduce strain in the active region during the fabrication process [30, 31]. This is done by creating a lattice mismatch between the semiconductor layers. By introducing a tensile strain, the light hole band edge is closer to the conduction band edge than the heavy hole band. This enhances the TM mode gain at the expense of the TE mode gain. In this way the overall optical gain of the modes is balanced.

1.4.3. Non-linear effects

When the input power is high enough and the SOA is in the gain saturation regime, non-linear effects can have a detrimental effect on linear signal transmission. Patterning effects due to the finite gain recovery time lead to problems in distinguishing between transmitted bits, while channel crosstalk limits the number of channels that can be amplified simultaneously in WDM applications. The disadvantages associated with non-linear effects in SOAs for linear amplification have proved to be useful when SOAs are used as functional elements. When operating in the saturation regime, the non-linear gain and refractive index dynamics of SOAs lead to a number of applications in wavelength conversion and optical switching, such as four wave mixing, cross gain modulation, and cross and self-phase modulation. SOAs designed for this purpose exhibit relatively low saturation powers in order to improve the efficiency of the non-linear effects. This enhanced functionality is what makes SOAs a potential key component of future transparent optical networks. These topics are discussed further in Chapters 4 and 5.

1.4.4. Noise figure

The key SOA parameter in low power in-line amplification is the noise due to amplified spontaneous emission. The degradation of the signal-to-noise ratio (SNR) as the signal is amplified is quantified by the noise figure, expressed in decibels as the ratio of the input SNR to the output SNR,

$$NF = 10\log_{10}\left(\frac{SNR_{in}}{SNR_{out}}\right) \tag{1.17}$$

The noise figure is the limiting factor for SOAs in low power transmission compared with EDFAs, which have a noise figure closer to the quantum limit of 3 dB. This topic is discussed further in Chapter 2. One of the main topics of this thesis is the control of the noise figure through carrier density control.

1.5. Summary

In this chapter the physics and functions of a semiconductor optical amplifier were outlined. A brief overview of the main technological advancements contributing to the development of SOAs as a mature technology was followed by a description of the various material systems that are used in the fabrication of these devices, and how the composition of these material systems affect the SOA characteristics. The basic physics of semiconductor heterojunction structures was explained and the origin of optical gain in SOAs was outlined. A brief explanation of the carrier recombination mechanisms in bulk SOAs was given. Finally, the main physical characteristics of SOAs were listed and briefly explained. This chapter will serve as a background to the following work, which further explores the role of both the noise figure and gain saturation on the performance of SOAs, and how these parameters can be controlled.

References

[1] Dutta, N.K; Wang, Q.; “Semiconductor Optical Amplifiers”, World Scientific Publishing Co. Pte. Ltd, 2006.

[2] Connolly, M.J.; “Semiconductor Optical Amplifiers”, Kluwer Academic Publishers, 2002.

[3] Dupuis, R.D.; Temkin, H.; Hopkins, L.C.; "InGaAsP/InP double heterostructure lasers grown by atmospheric-pressure MOCVD," Electronics Letters, Vol. 21, No. 2, Jan. 17, 1985.

[4] Shik, A. Y.; “Quantum Wells: Physics and Electronics of Two-Dimensional Systems”, World Scientific Publishing, 1997.

[5] Seoijin Park, Leavitt, R.; Enck, R.; Luciani, V.; Hu, Y.; Heim, P.J.S.; Bowler, D.; Dagenais, M.; "Semiconductor optical amplifier for CWDM operating over 1540-1620 nm," *IEEE Photonics Technology Letters*, Vol. 17, No. 5, May 2005.

[6] Akiyama, T.; Ekawa, M.; Sugawara, M.; Kawaguchi, K.; Hisao Sudo, Kuramata, A.; Ebe, H.; Arakawa, Y.; "An ultrawide-band semiconductor optical amplifier having an extremely high penalty-free output power of 23 dBm achieved with quantum dots," *IEEE Photonics Technology Letters*, Vol. 17, No. 8, Aug. 2005.

[7] Uskov, A.V.; O’Reilly, E.P.; Laemmlin, M.; Ledentsov, N.N.; Bimberg, D.; “On gain saturation in quantum dot semiconductor optical amplifiers”, *Optics Communications*, Vol. 248, No. 1-3, Apr. 1, 2005.

[8] Akiyama, T.; Kuwatsuka, H.; Simoyama, T.; Nakata, Y.; Mukai, K.; Sugawara, M.; Wada, O.; Ishikawa, H.; "Nonlinear gain dynamics in quantum-dot optical amplifiers and its application to optical communication devices," *IEEE Journal of Quantum Electronics*, Vol. 37, No. 8, Aug 2001.

[9] Akiyama, T.; Sugawara, M.; Arakawa, Y.; "Quantum-Dot Semiconductor Optical Amplifiers," *Proceedings of the IEEE* , Vol. 95, No. 9, Sept. 2007.

[10] Menashe, D.; Shlifer, A.; Ghera, U.; "Optical Amplifiers for Modern Networks," *2006 International Conference on Transparent Optical Networks*, Vol. 1, pp. 115-118, 18-22 June 2006.

[11] Min-Hwan Kim; Sang-Mook Lee; Sil-Gu Mun; Chang-Hee Lee; "A 240 km Reach DWDM-PON of 8-Gb/s Capacity using an Optical Amplifier," *Journal of the Optical Society of Korea*, Vol. 11, No. 3, Sept. 2007.

[12] Kinoshita, S.; Onaka, H; Chikama, T.; "Large Capacity WDM Transmission Based on Wideband Erbium-Doped Fiber Amplifiers," in *Optical Amplifiers and Their Applications*, D. Baney, K. Emura, and J. Wiesenfeld, eds., Vol. 25 of OSA Trends in Optics and Photonics Series (Optical Society of America, 1998), paper CA6.

[13] Kaman, V.; Xuezhe Zheng; Shifu Yuan; Klingshirn, J.; Pusarla, C.; Helkey, R.J.; Jerphagnon, O.; Bowers, J.E.; "A 32×10 Gb/s DWDM metropolitan network demonstration using wavelength-selective photonic cross-connects and narrow-band EDFAs", *IEEE Photonics Technology Letters*, Vol.17, No.9, Sept. 2005.

[14] Senthil Murugan, G.; Suzuki, T.; Ohishi, Y.; “Tellurite glasses for ultrabroadband fiber Raman amplifiers”, *Applied Physics Letters*, Vol. 86, No. 16, 2005.

[15] Wilson, J.; Hawkes, J.F.B.; “Optoelectronics: An Introduction”, Prentice Hall Europe, 1998.

[16] Cooke, M.J.; “Semiconductor Devices”, Prentice Hall, 1990.

[17] Grote, N.; Venghaus, H.; “Fibre Optic Communication Devices”, Springer-Verlag Berlin Heidelberg, 2001.

[18] Visser, T.D.; Blok, H.; Demeulenaere, B.; Lenstra, D.; "Confinement factors and gain in optical amplifiers," *IEEE Journal of Quantum Electronics*, Vol. 33, No. 10, pp. 1763-1766, Oct 1997.

[19] Korkin, A.; Labanowski, J.; Gusev, E.; Luryi, S.; “Nanotechnology for Electronic Materials and Devices”, Springer Science and Business Media, 2007.

[20] Basu, P.K.; “Theory of Optical Processes in Semiconductors: Bulk and Microstructures”, Oxford University Press USA, 2003.

[21] Morgan, D.V.; “Physics and Technology of Heterojunction Devices”, Peter Peregrinus Ltd., 1991.

[22] Numai, T.; “Fundamentals of Semiconductor Lasers”, Springer-Verlag New York, 2004.

[23] Mroziewicz, B.; Bugajski, M.; Nakwaski, W.; “Physics of Semiconductor Lasers”, North-Holland, 1991.

[24] Jia-Ming Liu; “Photonic Devices”, Cambridge University Press, 2005.

[25] Dutta, N.K.; Nelson, R.J.; "Temperature dependence of threshold of InGaAsP/InP double-heterostructure lasers and Auger recombination," *Applied Physics Letters*, Vol. 38, No.6, pp.407-409, Mar 1981.

[26] Occhi, L.; Ito, Y.; Kawaguchi, H.; Schares, L.; Eckner, J.; Guekos, G.; "Intraband gain dynamics in bulk semiconductor optical amplifiers: measurements and simulations," *IEEE Journal of Quantum Electronics*, Vol. 38, No. 1, pp. 54-60, Jan 2002.

[27] Willatzen, M.; Uskov, A.; Mork, J.; Olesen, H.; Tromborg, B.; Jauho, A.-P.; "Nonlinear gain suppression in semiconductor lasers due to carrier heating," *IEEE Photonics Technology Letters*, Vol. 3, No. 7, pp. 606-609, July 1991.

[28] Ghafouri-Shiraz, H.; “The Principles of Semiconductor Laser Diodes and Amplifiers”, Imperial College Press, 2004.

[29] Saleh, B.E.A.; Teich, M.C.; “Fundamentals of Photonics”, Wiley Interscience, 2007.

[30] Koonath, P.; Sangin Kim; Woon-Jo Cho, Gopinath, A.; "Polarization-insensitive quantum-well semiconductor optical amplifiers," *IEEE Journal of Quantum Electronics,* Vol. 38, No. 9, pp. 1282- 1290, Sep 2002.

[31] Silver, M.; Phillips, A.F.; Adams, A.R.; Greene, P.D.; Collar, A.J.; "Design and ASE characteristics of 1550-nm polarization-insensitive semiconductor optical amplifiers containing tensile and compressive wells," *IEEE Journal of Quantum Electronics*, Vol. 36, No. 1, pp.118-122, Jan 2000.

2. CONTROL OF NOISE FIGURE AND SATURATION POWER IN SOAS

2.1. Introduction

Traditionally semiconductor optical amplifiers have suffered from a relatively high noise figure (~ 7 *dB*) compared with erbium doped fibre amplifiers (EDFAs), which generally can achieve noise figures ~ 5 *dB* and below [1]. This feature generally makes them uncompetitive when it comes to long haul transmission applications, where the build up of noise over hundreds or even thousands of kilometres could be very detrimental. At the same time, it is desirable to increase the saturation output power of SOAs. The reason for this is that, whereas EDFAs can and do operate in the saturation regime with no patterning effects, the short carrier recombination time of SOAs means that high bit rate signals can experience significant distortion when the amplifier is operating in the saturation regime. Therefore, arguably the most important factors in determining the suitability of an optical amplifier for use in optical networks, apart from the optical gain, are the noise figure and saturation output power. For example, when SOAs are used as upstream reach-extenders in passive optical networks, the maximum distance permissible between the Optical Network Unit (ONU) and the passive splitter (coupler) is determined by the noise figure, due to the weak transmission power of the ONU and higher losses associated with transmission at 1310nm. Similarly, the maximum distance between the amplifier and the Optical Line Terminal (OLT) is determined by the output power that the SOA can deliver [2].

Put simply, a high noise figure will especially degrade the signal to noise (SNR) ratio of a weak signal, posing problems for detection systems. This can be understood as follows [3]:

- The statistically random nature of spontaneous emission means that an optical transition from the conduction to the valence band can occur at any time.
- This causes fluctuations in the carrier density N which in turn changes the material gain g_m.
- In addition to this, the fluctuations in carrier density induce changes in the refractive index n_g, depending on the value of the linewidth enhancement factor α. Consequently, phase noise is introduced to the signal, in a similar manner to linewidth broadening in semiconductor lasers [4].

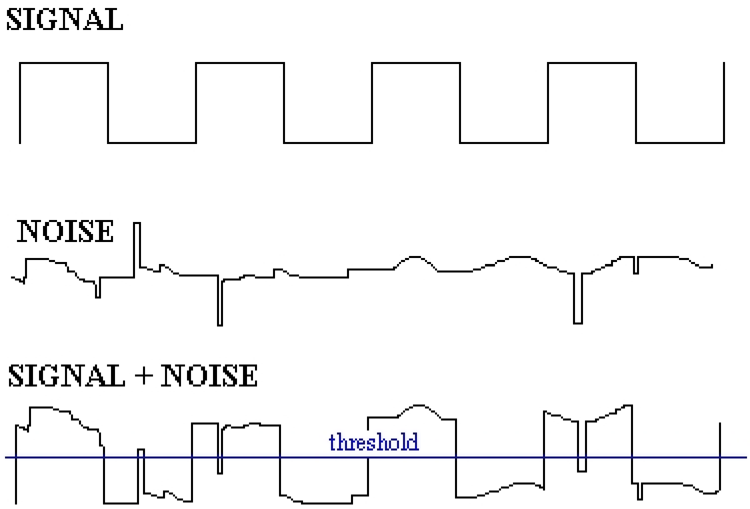

2.1. Degradation of bit stream by optical noise.

All of these effects are exacerbated by the fact that the spontaneously emitted photons experience optical amplification. Most importantly at higher powers, spontaneously emitted photons propagating within the guided mode can beat with the incoming co-polarised signal photons, causing further intensity fluctuations [5]. Other effects include beating between co-polarised spontaneously emitted photons, which dominates at low signal power, and the quantum shot noise of both the signal and spontaneous emission [6]. Combined, the intensity and phase fluctuations caused by these noise components degrade the integrity of individual transmitted bits; with the result that bit error rates increase in receivers whose decision circuits base their deciding criterion on the signal average power (see Fig. 2.1). This effect is further manifested in the closing of eye diagrams.

On the other hand, a low saturation output power will limit the dynamic range of input signal power that can be amplified without distortion. As was previously mentioned, the saturation output power of an SOA is the power that the SOA can produce at the point where its gain has reduced by 3dB due to gain saturation [7]. The input power at this point is called the saturation power. This phenomenon can have a profound effect on in-line amplification operations, particularly at high bit rates, on the order of 20-40Gb/s. Because SOAs have a finite gain recovery time, on the order of hundreds of picoseconds, a transmitted bit can be distorted by the gain saturation caused by a preceding bit [8]. The ensuing patterning effect can give rise to increased bit errors as some bits are amplified more strongly than others. An example of patterning can be seen in Fig. 2.2.

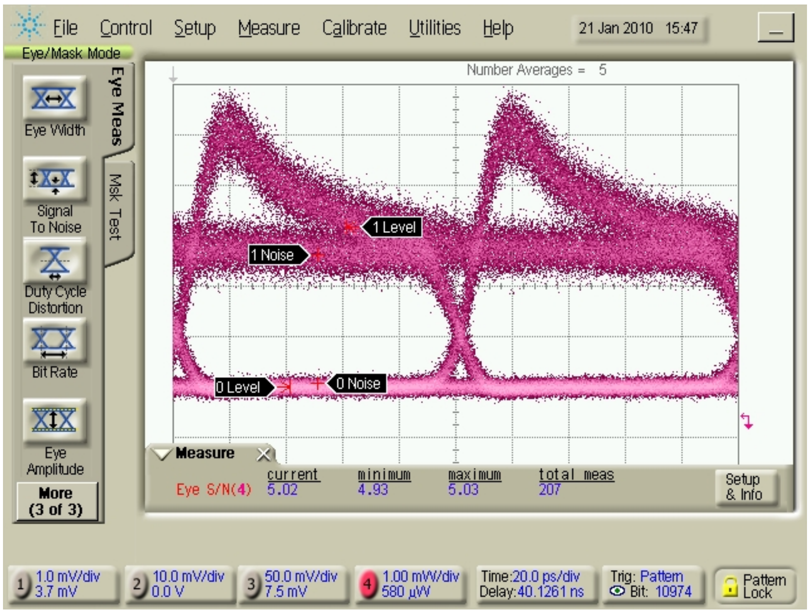

2.2. Bit patterning effects visible on a 10Gb/s PRBS signal. The wavelength of the signal is 1547 nm, with an optical power of 5 dBm.

This is particularly problematic in Optical Time Division Multiplexing (OTDM) schemes. In addition to this, within the saturation regime, non-linear effects such as cross gain modulation (XGM), four wave mixing (FWM), self phase modulation (SPM) and cross phase modulation (XPM) begin to manifest themselves. These phenomena can have deleterious effects on transmission schemes that utilize Dense Wavelength Division Multiplexing (DWDM). XGM, whereby a light signal experiences the gain saturation pattern caused by another data stream, can cause crosstalk between different channels in DWDM systems [9]. FWM, whereby carrier density modulations caused by the beating between two signals gives rise to new frequency components, can have a similar effect [10], where intermodulation distortion can interfere with equally spaced channels. A solution to this problem is to use unequal channel spacing [11], although this is not always possible. XPM is a nonlinear effect where the optical intensity of one beam influences the phase change of another beam through the linewidth enhancement factor leading to an amplitude modulation and power penalty [12]. Finally, SPM, an effect similar to XPM whereby a pulse modulates its own phase due to the change in refractive index induced by gain saturation, can under the right conditions cause both spectral and temporal broadening, making it problematic for OTDM schemes [13].

2.2. State of the art

As can be surmised from the above, there is a clear incentive to develop technology that allows SOAs to compete with fibre amplifiers on all fronts. There have been numerous efforts to improve or ameliorate these debilitating characteristics, with each scheme having inherent advantages and disadvantages. Efforts to improve noise figure have included the use of pump beams in order to change the carrier density profile, to the use of different device structures such as vertical cavity SOAs or devices with reduced confinement. Similarly, pump beams have been used to increase the saturation output power, in addition to gain clamped SOAs, flared waveguides and SOAs with variable contact resistance.

2.2.1. Pump beam schemes

An improvement in steady state NF can be realised through optical injection of a holding beam in both co- and counter-propagation [14, 15]. The beam is injected in the transparency region of the SOA. When injected in co-propagation mode, its main function is to optically pump the carrier density at low bias currents, and to restore a flat spatial carrier distribution at higher currents. A NF improvement of up to 2.5 dB has been realised using such a scheme. The predominant use of pump beam schemes, however, is to increase the saturation output power of the SOA, with an improvement of up to 4.9 dB realised [16]. The function of the beam is to maintain the separation of the quasi-Fermi levels through optical pumping [17]. This has the effect of reducing the spontaneous carrier lifetime [18, 19], which is inversely proportional to the saturation output power. The main drawback with the holding beam approach is that it requires the use of an additional source to serve as a pump beam, which adds to both the cost and the complexity of the setup.

2.2.2. Vertical cavity SOAs

Vertical-cavity semiconductor optical amplifiers (VCSOA) are devices where the input beam is injected perpendicular to the waveguide. A major advantage of this approach is excellent coupling efficiency, which is a result of the fact that the vertical cavity is circularly symmetric, compatible with the modes of optical fibres. It also makes VCSOAs polarisation insensitive. This improvement in coupling efficiency leads directly to a reduction in noise figure [20, 21]. However, because the signal is injected perpendicular to the active region, the gain per pass is very small, and so a feedback mechanism using distributed Bragg reflector mirrors is used to increase the gain. Consequently, the gain bandwidth is restricted to linewidth of the Fabry-Perot mode. While the reduced bandwidth filters any out of bandwidth noise, it also means that VCSOAs are practically limited to single channel amplification.

2.2.3. Confinement factor

Reducing the confinement factor Γ of the active waveguide is another approach to reducing noise figure [22]. For high confinement devices, the interaction between carriers and photons becomes more important, and thus amplification of spontaneous emission is more prominent. As a result the carrier density at the facets of the SOA is reduced due to the increased ASE in these regions. A higher NF results from the lower population inversion at the input facet, due to this carrier density reduction. However, in low confinement SOAs, ASE is not amplified as strongly, which leads to a more uniform carrier density distribution, lowering the NF and increasing the saturation output power at the same time.

2.2.4. Gain clamped SOAs and LOAs

Gain clamped SOAs (GC-SOA) and linear optical amplifiers (LOA) are also used to increase saturation output power. In a gain clamped SOA, a distributed Bragg reflector (DBR) is introduced lateral or perpendicular to the waveguide [23]. The reflection coefficients of the DBR are chosen so that lasing oscillation will occur at a threshold current for a specific wavelength, usually at a wavelength close to the transparency region of the GC-SOA, and clamp the gain at the threshold value. Due to homogenous gain saturation in SOAs, the gain for wavelengths far from the Bragg wavelength is also clamped, and is independent of increasing input signal power until the point where the laser oscillation is switched off due to carrier depletion.

An LOA has a similar functionality, although the gain clamping is achieved not through integrated Bragg reflectors, but through an integrated vertical laser that ensures gain linearity. The overall effect is that deviations in gain are smoothed in the linear regime, and the saturation output power is increased, with a corresponding decrease in the magnitude of the linear gain [24]. GC-SOAs suffer from a higher noise figure than LOAs. This is primarily due to longitudinal spatial hole burning, which occurs because of the inhomogeneous photon density profile along the active later resulting from the relatively high GC-SOA gain [25]. This same phenomenon also occurs in Fabry-Perot and DBR lasers, but is more pronounced in GC-SOAs due to the lower reflectivity of the integrated DBRs compared with lasers. This problem can be minimized through the use of DBRs with unbalanced reflectivity, in order to reduced carrier density variation [26, 27].

2.2.5. Flared waveguides

The use of flared waveguides to increase the saturation output power of an SOA is well known [28, 29]. The saturation output power is directly proportional to the waveguide area, thus exponentially increasing the width of the waveguide from the input to the output facet will allow higher output powers, in addition to maintaining fundamental mode propagation.

2.2.6. Variable contact resistance

An alternative approach to increasing the saturation output power is taken in [30]. The injected carriers are distributed along the waveguide according to a set contact resistance pattern, varied in order to increase the carrier density towards the rear facet of the SOA. Higher carrier density leads to an inverse reduction in the spontaneous carrier lifetime τ. As τ is inversely proportional to the saturation power, in increase in carrier density corresponds to an increase in saturation power.

2.2.7. Choice of gain material

There are fundamental differences between the gain, noise and saturation properties of various gain materials, be they bulk, quantum well (QW) or quantum dot (QD) systems. The basic physics of these differences were covered in the previous chapter. With regards to both noise figure and saturation output power, lower dimensional structures such as QW and QD have inherent advantages over bulk structures. QW SOAs exhibit a lower noise figure than bulk SOA because the low confinement factor of the material means that efficient population inversion is possible at much lower injected currents [31, 32]. QW structures also exhibit a lower waveguide loss, further decreasing the NF [33]. The higher loss in the cladding layers can be reduced by optimizing the doping levels in these regions [34]. Record low noise figure values have been reported for quantum well SOAs, including chip values as low as 3.7dB [35] and packaged SOAs reporting fibre to fibre noise figure values of 4.5dB [36].

The high saturation output power of QW SOAs is a major reason for the high level of research interest in them. Saturation power is inversely proportional to both the confinement factor Γ and the differential gain coefficient a_1. As we have previously seen, the confinement factor of a quantum well SOA is much lower than that of a bulk device. In addition to this, at higher bias currents the differential gain coefficient is lower for QW than for bulk [37]. The reason this is so is because the unsaturated gain does not vary as strongly with carrier density, and therefore the carrier density depletion caused by stimulated emission at high power does not compress the gain to the same extent as a bulk device [7]; therefore QW SOA structures will generally have a higher saturation output power than bulk SOAs. Devices with extremely high output powers have been reported, all utilizing quantum well designs [38, 39].

The high saturation output power and low noise properties of quantum dot SOAs (QD-SOAs) are related to the quasi three-level nature of the QD band structure, similar to an EDFA. Indeed, because of this particular structure, QD-SOAs have more efficient population inversion than QW-SOAs, and in fact can be almost completely inverted. It is predicted that QD-SOA noise figures could approach the quantum limit of 3dB [40]. The relaxation of carriers from the wetting layer to the excited state means that at high input powers, carrier numbers can deplete significantly before the gain is affected. The effect of this is that extremely high output powers can be achieved before gain saturation [41].

2.3. Noise Figure in SOAs

Noise is an unavoidable characteristic of all amplifiers. In any optically amplifying medium, stimulated emission enables the amplification of incoming signal photons. However, carrier relaxation via spontaneous emission will also occur, which is a random and incoherent process. As spontaneous emission events can emit a photon in any direction or phase, and at a range of possible wavelengths, they do not add coherently to the signal, but only add a measurable noise power. In electronics, the noise characteristics of an amplifier are measured by the noise figure (NF). The noise figure is a useful figure of merit. Its basic definition is as a measure of the degradation of the signal to noise ratio of a signal as it is transmitted through the device or system of interest. It is usually measured in decibels (dB). Known NF values are useful to network designers because they can know how much SNR degradation a given signal will suffer by virtue of it being transmitted through the component of interest. In this sense, any absorption of a signal will add linearly to the noise figure. A passive component that attenuates a signal by 2dB will thus have a noise figure of 2dB [42, 43]. NF is also used to quantify the noise characteristics of components in optical systems. In this context, different measurement techniques can be used to determine the NF. A more complete evaluation of the noise characteristics of a system can be obtained through optoelectronic measurements. However, for the purposes of evaluating the noise contribution of a component such as an SOA or EDFA, optical techniques are usually used, and give sufficiently accurate results. The noise figure values presented in this thesis were obtained using optical techniques.

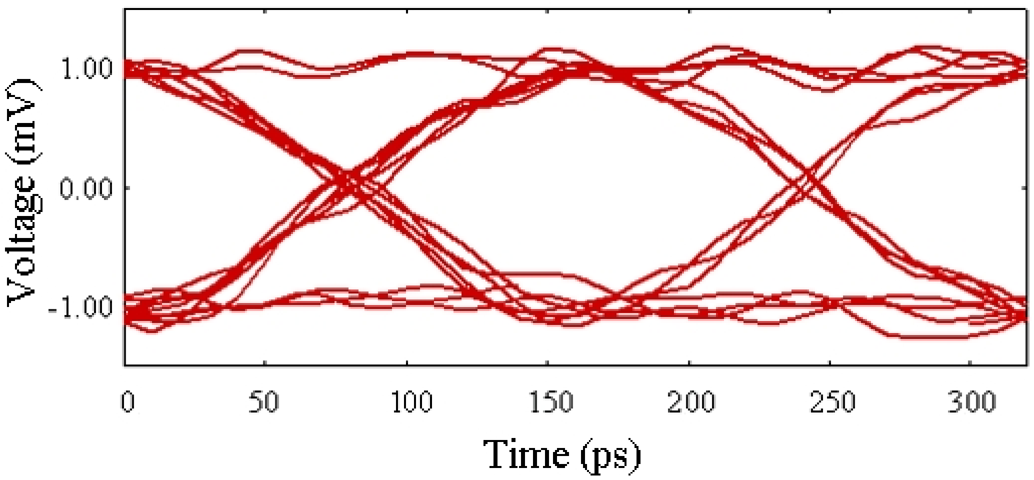

2.3. Eye diagram closure due to optical noise.

2.3.1. Types of optical noise

There are numerous contributing elements to optical noise in semiconductor optical amplifiers, some making more significant contributions than others. The main sources of noise are:

- Signal-spontaneous (sig-sp) beat noise
- Spontaneous-spontaneous (sp-sp) beat noise
- Signal and ASE shot noise
- Multipath interference noise (MPI).

Classically, beat noise from optical sources is considered to appear at the detector because of the fact that the detector photocurrent is proportional to the square of the incident optical fields. The quantum interpretation is that the sources of noise can be explained by fluctuations in the rate of stimulated emission. Both explanations are equivalent in terms of the final calculation of the noise figure.

Signal-spontaneous beat noise

Signal-spontaneous beat noise arises from the beating between the signal photons and spontaneously emitted photons in the same polarization as the signal, when both are incident on a photodiode. Sig-sp beat noise is dependent on the signal photon density, and so at higher input signal powers, or if the amplifier has appreciable gain, this is the most dominant noise contributor. In a polarization independent amplifier, the signal photons beat with half of the detected spontaneously emitted photons, as these photons will be emitted in one of two mutually orthogonal polarizations. The signal is usually passed through an optical filter prior to detection, as the noise contribution of the co-polarized spontaneous emission will then be limited to the detection bandwidth. Fig. 2.4 depicts the spectral density of the signal-spontaneous beat noise photocurrent. The bandwidth of the optical filter is B_0. The noise spectral density stays constant within the frequency interval ($0 - B_0/2$). The reason for this is clear if we consider the beating frequency of the noise power. The maximum frequency of the beat is determined by the frequency interval between the signal and the spontaneous emission, which extends to a maximum of $\pm B_0/2$, either side of the signal. An in-depth derivation of the signal-spontaneous beat noise is given by Olsson [44].

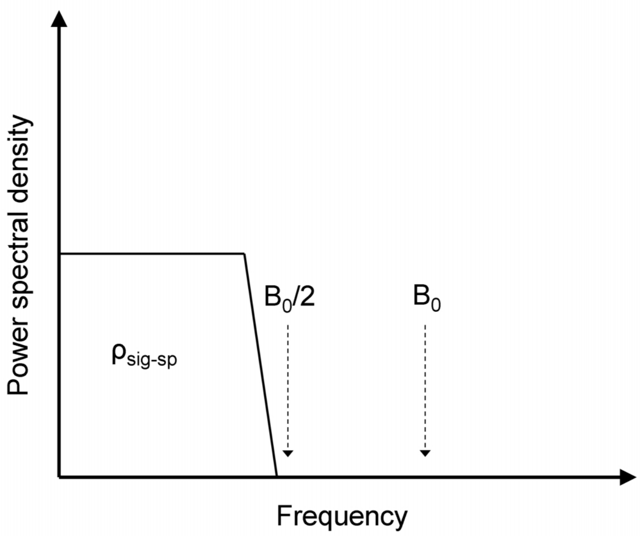

2.4. Power spectral density of signal-spontaneous beat noise as measured on an electrical spectrum analyzer. B_0 indicates the bandwidth of the optical filter.

Spontaneous-spontaneous beat noise

Spontaneous-spontaneous beat noise is caused by the beating between different frequency components of the spontaneous emission within the same state of polarization. Like signal-spontaneous beat noise, it manifests itself during the detection process in a photodiode [45]. Beating between photons of different frequencies can give rise to new RF components at the frequency difference between them. Sp-sp noise at the detector can be reduced with the use of a narrowband filter and a polarizer. The purpose of the polarizer is to pass the optical signal unchanged and to filter out half of the spontaneously emitted photons (assuming polarization-independent amplification). However, this technique is not necessarily useful in practical receivers as the polarization of the input signal may not be known. Fig. 2.5 shows the spectral density of the spontaneous-spontaneous beat noise photocurrent. The spectrum extends from 0 to B_0, with a triangular shape. The sp-sp noise beats within the entire bandwidth, since any spontaneous photon may beat with any other. The reason for the triangular shape is that smaller frequency intervals are more numerous than large frequency intervals, within a bandwidth B_0. If we define B_0 as the maximum frequency interval in the optical spectrum, only one such interval can occur between set photon frequencies at the band edges. Conversely, the DC component of the noise can contain a number of terms equal to $B_0/\delta v$, where δv is a unit division of bandwidth. The derivation of sp-sp beat noise is discussed in more detail in [44].

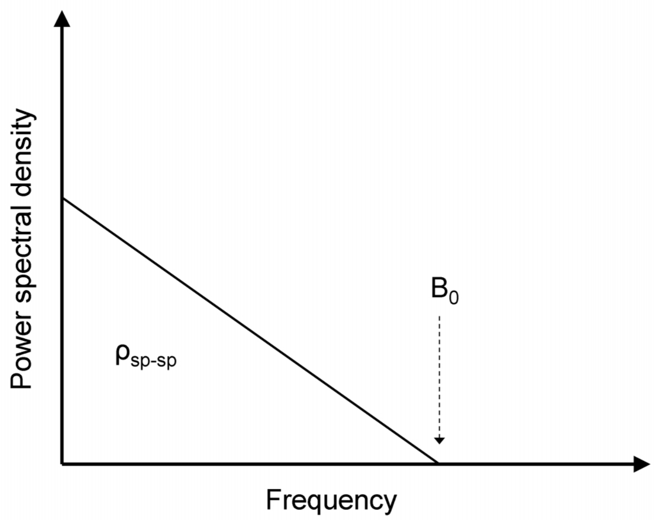

2.5. Power spectral density of spontaneous-spontaneous beat noise as measured on an electrical spectrum analyzer. B_0 indicates the bandwidth of the optical filter.

Shot noise

Shot noise is a form of intensity noise caused by fundamental quantum limits. It arises due to the independent, random nature of the detection of incoming photons, although it applies to any quantum particle. It manifests itself as a statistical fluctuation in detected power levels, and is exacerbated when the detector used has a lower than unity quantum efficiency. Shot noise is independent of the noise frequency and so may be thought of as a kind of “white” noise. The magnitude of shot noise increases with the square root of the expected number of detection events, although since the strength of the signal increases more rapidly, the contribution of shot noise becomes relatively insignificant at higher powers or optical gains. Shot noise from both the signal and the amplified spontaneous emission contribute to noise in SOAs.

Multipath interference noise

Multipath interference noise (MPI) arises from multiple reflections in the signal path. If an optical isolator is not used at the SOA output, reflections of ASE power back into the active region can enhance sig-sp and sp-sp noise. This is normally taken into account by multiplying the signal-spontaneous noise (the dominant term) by a factor, taking into account the reflectivity and the optical gain. When an isolator is used, the main source of this noise is the reflectivity of the SOA facets. MPI noise can thus be a problem for vertical cavity SOAs [20]. However, for travelling wave amplifiers, where facet reflectivities are generally very low, MPI noise can safely be neglected.

2.3.2. Derivation of optical noise figure

The optical definition of noise figure can be derived from the original electrical definition, given certain constraints [46, 47]. The following derivations are based on [46]. The equations for optical NF are basically a special case of noise figure where all sources of noise except signal-spontaneous beat noise and shot noise can be ignored. We need to begin the derivation by first defining what we mean by a signal to noise ratio. SNR is a measure of the quality of a signal. It is measured in terms of the received signal photocurrent i_{sig} and the received noise photocurrent i_n in a detector. Another way of thinking about it is as the ratio between the mean value of the signal power to the standard deviation of the noise power. In this sense we can write SNR as,

$$SNR = \frac{\langle i_{sig} \rangle^2}{\langle \Delta^2 i_n \rangle}. \qquad (2.1)$$

The noise variance $<\Delta^2 i_n>$ is obtained by integrating the received noise spectral density S_n over the bandwidth of interest. It is assumed that the input signal is shot-noise limited, which is a reasonable assumption for good quality optical sources. Rewriting this equation in terms of electrical power rather than squared photocurrent, we define the signal to noise ratio of the input signal to be,

$$SNR_{in} = \frac{\langle i_{sig} \rangle^2}{\langle \Delta^2 i_n \rangle} = \frac{R^2 P_{in}^2}{2eRP_{in} B_e} = \frac{\eta P_{in}}{2h\nu B_e}, \qquad (2.2)$$

where P_{in} is the signal input power, e is electric charge, v is the optical frequency, η is the photodetector quantum efficiency, B_e is the bandwidth of the noise and $R = \eta e / hv$ is the responsivity of the detector in amps/watt. For the sake of simplicity, we shall assume and ideal receiver and take the quantum efficiency to be unity. Assuming negligible thermal noise, the input SNR becomes,

$$SNR_{in} = \frac{P_{in}}{2h\nu B_e}. \qquad (2.3)$$

An equivalent approach can be taken for the output SNR, which is the ratio of the detected signal power to the variance of the detected noise power,

$$SNR_{out} = \frac{\langle i_{out} \rangle^2}{\langle \Delta^2 i_{out} \rangle}, \qquad (2.4)$$

where in this case,

$$\langle i_{out} \rangle^2 = R^2 G^2 P_{in}^2, \qquad (2.5)$$

where G is the optical gain of the component being characterised. Unlike in the case of the input signal SNR, the variance of the output noise power depends on a number of contributing sources. Therefore the power spectral densities of all of these sources must be added up in order to take them into account when calculating the noise power variance. The output SNR then becomes,

$$SNR_{out} = \frac{R^2 G^2 P_{in}^2}{B_e R^2 \left[S_{sig-sp} + S_{sp=sp} + \eta^{-1} S_{sig-shot} + \eta^{-1} S_{sp-shot} + S_{MPI} \right]}, \tag{2.6}$$

where the power spectral densities in the denominator represent the contributions from signal-spontaneous beat noise, spontaneous-spontaneous beat noise, shot noise from the signal and the ASE, and multipath interference noise. Now that the signal to noise ratios at both the input and the output are defined, we can introduce the definition of the noise factor. The noise factor is the ratio of the SNR of the input signal to the SNR of the output signal. The noise figure is ten times the base 10 logarithm of the noise factor. In the electrical domain, the noise factor would therefore be the ratio of Eq. (2.3) to Eq. (2.6). This is a complete characterisation of the noise taking all components into account.

In the optical domain, where optical measurement techniques are used, the expression for the output SNR can be simplified. Firstly, we will assume a detector with a quantum efficiency of unity, so that the η term in the shot noise spectral densities in Eq. (2.6) disappears. Secondly, we can see that both the numerator and the denominator of Eq. (2.6) depend on the value of the detector responsivity. Therefore, these terms will cancel. In the case of an optical signal that is amplified by an amplifier with appreciable gain ($G >> 1$), signal-spontaneous beat noise and the shot noise of the signal will dominate over the other terms, and so spontaneous-spontaneous beat noise and the ASE shot noise can be safely ignored. In an amplifier with very low or negligible facet reflectivity, multipath interference noise can also be discounted. Thus, Eq. (2.6) then becomes,

$$SNR_{out} = \frac{G^2 P_{in}^2}{B_e \left[S_{sig-sp} + S_{sig-shot} \right]}. \tag{2.7}$$

We can now write the noise factor of an optical amplifier with appreciable gain as the ratio of Eq. (2.3) to Eq. (2.7),

$$F = \frac{S_{sig-sp} + S_{sig-shot}}{2h\nu G^2 P_{in}}. \tag{2.8}$$

The signal-spontaneous beat noise power spectral density can be expressed as,

$$S_{sig-sp} = 4\rho_{ASE} G P_{in} , \tag{2.9}$$

where ρ_{ASE} is the ASE power spectral density. The signal shot noise can be written as,

$$S_{shot} = 2h\nu G P_{in} . \tag{2.10}$$

Eqs. (2.9) and (2.10) are derived in [44]. By substituting Eqs. (2.9) and (2.10) into Eq. (2.8), we are left with the final expression for the noise factor of an optical system, defined in terms of optically measureable parameters,

$$F = \frac{2\rho_{ASE}}{Gh\nu} + \frac{1}{G} . \tag{2.11}$$

By definition, the noise figure is ten times the base 10 logarithm of this expression,

$$NF = 10\log\left(\frac{2\rho_{ASE}}{Gh\nu} + \frac{1}{G}\right). \tag{2.12}$$

2.4. Gain Saturation and Output Power

Gain saturation is a phenomenon that will occur in any amplifying medium. In the case of optical amplifiers in steady state conditions, it can be observed that as the power injected into the system is increased, the optical gain remains approximately linear only up to a point. After this point, the gain will decrease with increasing input power. Gain saturation can be intuitively understood by approximating the amplifying medium as a simple two level system. As was previously mentioned, there are a number of carrier excitation and recombination processes occurring in SOAs. For the sake of argument, we shall consider only carrier excitation resulting from electrical pumping, and carrier recombination via stimulated emission. As input powers are increased, stimulated emission becomes more prominent and thus in this example we can neglect the influence of spontaneous emission, although at higher biases this effect cannot be overlooked. In this simplified example, electrical pumping excites carriers from the valence to the conduction band. Conversely, incoming signal photons cause stimulated emission, with the result that excited carriers recombine in the valence band. Due to conservation of energy, as the input power to the amplifier is increased, the rate of stimulated emission exceeds the rate of the pumping, and thus the upper state population decreases, along with the optical gain. When the gain has reduced to half of its unsaturated value, the input power at that point is the saturation power. The saturation output power of an amplifier, as opposed to the saturation power, is defined as the power that is emitted from the amplifier when the input power is at the saturation point. Both the saturation power and the saturation output power are fundamental characteristics of an amplifier and are important limiting factors when considering an amplifier's suitability for in-line applications. The saturation output power of an SOA can be determined by plotting the optical gain as a function of the output power, as the input power is increased, and determining the point where the gain is reduced by 3dB, as shown in Fig. 2.6.

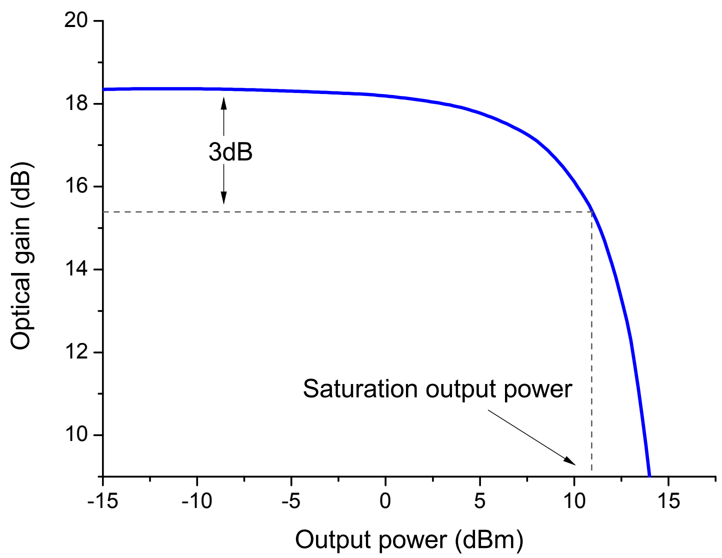

2.6. Output power of an SOA plotted against optical gain. Indicated is the 3dB saturation point, where the gain is reduced by half. The output power at this point is the saturation output power.

2.4.1. Saturation output power in linear transmission

EDFAs are very suitable for applications in linear amplification for two reasons. Firstly, for non-burst data transmission, they can be and usually are operated in the saturation regime without signal non-linearities. This is because of the relatively long carrier lifetime of EDFAs with respect to SOAs, on the order of milliseconds. This means that carrier density modulations caused by amplification of signals can be smoothed out over thousands of bits, effectively averaging the gain available to a data stream. In addition, the slow modulation speed of the carrier density means that beating effects between closely spaced signal channels are almost non-existent [48]. Secondly, because the transition cross-section in an EDFA is generally quite small, the saturation energy is relatively high. SOAs in general have a lower saturation output power than EDFAs. As SOAs are best described as a two level system, the maximum output power is limited to not much more than the saturation output power. This is not necessarily the case with EDFAs, since they can be strongly pumped to give output powers larger than their saturation output power, due to the three level nature of the Erbium ion. SOAs cannot be operated in the saturation regime when being used as an in-line amplifier, as their carrier lifetimes are much shorter than EDFAs, on the order of hundreds of picoseconds. When SOAs amplify a long, high bit rate data stream in the saturation regime, patterning effects occur that distort the signal. The first bit amplified saturates the gain, which begins to recover. If however the data rate is on the order of 10-20GHz or above, the gain does not have time to recover before the next bit arrives. This bit experiences a reduction in gain due to the saturation caused by the first bit. The result of these pattern effects is that bit errors can accumulate in detection systems, as the extinction ratio between logical 1 and 0 levels for some of the affected bits can be too low. For this reason, if SOAs are to be competitive as linear in-line amplifiers, and especially as power amplifiers, a high saturation output power is essential. This parameter will determine the transmission distance of a given SOA, constrained to operate in the linear regime.

2.4.2. Non-linear effects in the saturation regime

In addition to patterning effects, non-linear effects such as cross gain modulation and four wave mixing cause power penalties in multichannel transmission schemes such as WDM due to channel crosstalk and intermodulation distortion. These non-linear effects arise because of the short carrier lifetime of SOAs, and also because the gain medium of SOAs is homogeneously broadened. A consequence of this broadening is that the saturation of the gain by any signal in a multichannel system will saturate the gain for all other signals being amplified. Saturation occurs homogeneously because it depends on the total number of photons in the cavity for all wavelengths. Therefore, for linear multichannel amplification the sum of the power of the individual signals cannot exceed the saturation power. Channel crosstalk occurs because of cross gain modulation, which is the imprint of a gain compression pattern of one channel onto another. When a given bit pattern saturates the SOA gain, a second bit pattern in another channel will experience the same gain saturation because of homogeneous broadening. Unless the bit stream is identical to the first channel, patterning effects occur. This process can be useful for wavelength conversion if a CW beam is used as the second channel. Four wave mixing is the principle cause of intermodulation distortion. When two closely spaced channels interact with each other in a saturated SOA, the beating between them causes sidebands to appear at the sum and difference frequencies between them. Amplitude modulations caused by these sidebands distort the input channels. Again, as with cross gain modulation, four wave mixing employed in a wavelength converter scheme can be very useful. These effects will be studied further in later chapters. Other non-linear effects in SOAs are caused by the accompanying refractive index change resulting from a compression of the gain. An example of such an effect is self phase modulation, in which the phase of an optical pulse is modified by the refractive index change caused by the relation between the real (index) and imaginary (absorption) components of the complex refractive index [49]. Self phase modulation results in a frequency shift in the spectrum of the pulse, and can result in spectral spreading or narrowing, depending on whether the pulse is positively or negatively chirped. For the purposes of linear amplification in WDM schemes, in particular DWDM where the channel spacing is small, non-linear effects in the saturation regime of SOAs are serious impediments to their usage [50].

2.4.3. Mathematical description

The conservation of energy basis for the explanation of gain saturation can be inferred from the carrier density rate equation for a slice of the active region with thickness *d*,

$$\frac{dn}{dt} = \frac{i}{ed} - R(N) - a_1(n - n_0)\left(\frac{I_s}{h\nu} + \frac{I_{sp}}{h\nu}\right), \tag{2.13}$$

where n is the carrier density, n_0 is the carrier density at transparency, i is the bias current, e is the electronic charge, $R(N)$ represents the carrier density dependent recombination rates, a_1 is the differential gain coefficient, I_s is the signal intensity, I_{sp} is the spontaneous emission intensity and v is the optical frequency of the signal. The material gain is represented as,

$$g_m = a_1(n - n_0). \tag{2.14}$$

As the signal intensity is increased, the carriers depleted according to the intensity dependent term outnumber the carriers added by the bias current dependent term, and so *dn/dt* becomes negative. This in turn reduces the material gain. The propagation of the signal intensity can be represented by the travelling wave equation,

$$\frac{dI}{dz} = \left(\Gamma g_m - \alpha\right) I \,, \tag{2.15}$$

where z is the propagation direction, Γ is the optical confinement factor and α is the waveguide loss coefficient. If we now introduce the concept of the saturation intensity I_{sat}, the material gain as a function of I_{sat} is,

$$g_m = \frac{g_0}{1 + \frac{I}{I_{sat}}} \,, \tag{2.16}$$

where g_0 is the unsaturated material gain given by Eq. (2.14) where the carrier density n depends only on the bias current and spontaneous recombination rates. We can now rewrite Eq. (2.15), using Eq. (2.16) as the expression for material gain,

$$\frac{dI}{dz} = \left(\Gamma \frac{g_0}{1 + \frac{I}{I_{sat}}} - \alpha \right) I \,. \tag{2.17}$$

If, for simplicity, we assume that $\alpha = 0$, then Eq. (2.17) is a first order differential equation with the solution,

$$I_L \exp\left(\frac{I_L - I_0}{I_{sat}} \right) = I_0 \exp\left(\Gamma g_0 L\right), \tag{2.18}$$

where I_L and I_0 are the signal intensity at the output and input of the SOA, respectively. The gain of the amplifier is the ratio of the signal intensity at the output to the intensity at the input. Therefore Eq. (2.18) can be rearranged to give an expression for the single pass gain,

$$G = \exp\left[\Gamma g_0 L - \left[\frac{(I_L - I_0)}{I_{sat}}\right]\right] = G_0 \exp\left[\frac{(G-1)I_L}{GI_{sat}}\right], \tag{2.19}$$

where the identities $G = I_L/I_0$ and $G_0 = exp(\Gamma g_0 L)$ are used. From this equation we can now define the saturation output intensity $I_{L,\mathrm{sat}}$, where the gain is equal to half of the unsaturated gain, as,

$$I_{L,sat} = \frac{\ln(2) G_0 I_{sat}}{G_0 - 2}, \tag{2.20}$$

where the identity $G = G_0/2$ is used. This is now an expression for determining the saturation output intensity of an amplifier with the saturation intensity and the unsaturated single pass gain as parameters. The saturation intensity itself can be calculated from the rate equation and is defined as [51],

$$I_{sat} = \frac{h\neg}{a_1^{2}}, \tag{2.21}$$

where τ is the spontaneous carrier lifetime. Now, knowing the expression for $I_{L,sat}$, we can derive an expression for the saturation output power of an SOA. As power is equal to the intensity multiplied by the area, we are left with,

$$P_{L,sat} = \frac{AI_{L,sat}}{\Gamma}, \tag{2.22}$$

where A is the waveguide area. It is clear from this expression and the expressions for saturation intensity and saturation output intensity that the saturation output power can be increased by having a larger waveguide area, a smaller confinement factor or increasing the saturation output intensity. This in turn can be increased by having a larger gain, or by reducing either the differential gain or the spontaneous carrier lifetime. Various methods for achieving all of the above were outlined in section 2.2.

2.5. Concept for parameter control

In section 2.2, various techniques that have been published for reducing noise figure or for increasing saturation output power in SOAs were outlined. It is the intention of this work to examine two techniques that aim to accomplish the same goal. Key to both of these techniques is the concept of manipulation of the carrier density distribution within the active region of the SOA. The techniques differ in terms of the method of achieving this control, with one being an indirect shaping of the carrier density profile and the other being direct. The indirect technique has been designed with the aim of reducing noise figure, while the direct technique is more flexible in that it aims to achieve either NF reduction or increased saturation output power, depending on the application desired. The following sections will outline the theoretical basis for these concepts. All results presented in this section have been obtained using the simulation outlined in Chapter 3.

2.5.1. Reducing noise figure

Dependence of noise figure on population inversion factor

Key to reducing the noise figure of an SOA is the reduction of the population inversion factor, or spontaneous emission factor, n_{sp}. This parameter is a measure of the population of the excited state compared with the ground state in semiconductor photonic devices, given by,

$$n_{sp} = \frac{N_2}{N_2 - N_1}, \tag{2.23}$$

where N_1 and N_2 are the population levels of the ground state and the excited state respectively. Thus, as the name suggests, the population inversion factor is a measure of the efficiency of population inversion in the SOA. Clearly, the magnitude of n_{sp} depends on the amount of electrical pumping applied to the device, such as this process increases the rate of excitation of carriers from the valence to the conduction band. The effect of this electrical pumping is to reduce n_{sp}. The minimum value of n_{sp} is 1, where the ground state is empty of carriers, and the SOA is completely inverted.

At this point, the question of nomenclature should be resolved. In this thesis, n_{sp} shall be referred to as the population inversion factor, whereas spontaneous emission factor shall be neglected so as to avoid confusion with the *effective* spontaneous emission factor introduced by Adams [52], which quantifies the proportion of spontaneous emission coupled to the guided mode in an SOA. The term population inversion factor also more intuitively illustrates the mechanism for NF reduction that is outlined herein. We can show the dependency of the noise figure on the population inversion factor by realizing the relation between spontaneous emission and n_{sp}. The additive noise power in an SOA (power added that is not part of the amplified signal) is given by,

$$P_{ASE} = n_{sp}(G-1)h\nu B_0 , \tag{2.24}$$

where G is the amplifier gain, v is the optical frequency, and B_0 is the measurement bandwidth. This equation illustrates the advantage of using a narrowband optical filter when using SOAs in optical networks, as reducing the bandwidth will reduce the noise power proportionately. The noise power spectral density, which is the noise power per unit of bandwidth, is,

$$\rho_{ASE} = n_{sp}(G-1)h\nu \, . \tag{2.25}$$

Recalling that the expression derived for the optical noise figure is dependent on the ASE power spectral density, we can combine Eq. (2.11) and Eq. (2.25) to derive an expression for the noise factor in terms of the population inversion factor,

$$F = \frac{2n_{sp}(G-1)}{G} + \frac{1}{G} \, . \tag{2.26}$$

As before, the noise figure is then simply,

$$NF = 10\log\left(\frac{2n_{sp}(G-1)}{G} + \frac{1}{G}\right). \tag{2.27}$$

In the case where the amplifier gain is significantly greater than 1, the shot noise term on the right hand side of the equation can be neglected, and the noise factor is determined exclusively by the signal-spontaneous beat noise term, which reduces to,

$$F = 2n_{sp} \, . \tag{2.28}$$

Eq. (2.28) clearly demonstrates that the noise factor (and noise figure) is dependent on the population inversion factor. NF decreases as n_{sp} decreases. What is more, it shows that there is a fundamental lower limit for the noise figure of high gain ($G>>1$) amplifiers, both semiconductor and fibre based. As the minimum value for n_{sp} is 1, which is the case when N_1 is 0 (full population inversion), then the noise factor quantum limit is 2, with the corresponding noise figure limit being 3dB [53]. The relations outlined above suggest that to achieve a low noise figure, the electrical pumping of the device needs to be high, and consequently increase the carrier density N in the active region. The dependence of n_{sp} on N is illustrated in Fig. 2.7.

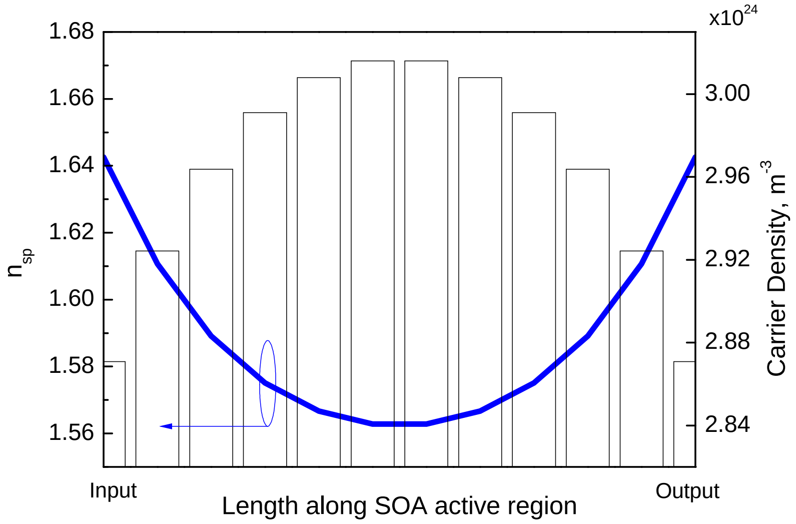

2.7. Population inversion factor plotted against carrier density as a function of position in active region for a typical SOA. Inverse relationship is clearly shown. No signal is injected into the SOA.

The population inversion factor is plotted against the carrier density as a function of position along the length of the SOA active region. The data used for this plot comes from a model that is described in detail in Chapter 3. The carrier density profile depicted is a typical profile for an SOA. There is some depletion of carriers at the facets due to the increased amplified spontaneous emission at the extremes of the waveguide. This phenomenon gives the carrier density profile a parabolic shape overall. What is interesting to note is that the population inversion factor shows an inverse parabolic shape, reflecting the inverse relationship between n_{sp} and the valence band population N_2.

The problem of amplified spontaneous emission

It would seem that the solution to reducing the noise figure is therefore to increase the bias current supplied to the SOA. However, recombination processes responsible for the decay of carriers from the conduction band to the valence band become more important at higher bias. As detailed in chapter 1, non-radiative, radiative and Auger processes reduce the population of the excited state at a rate governed by their dependency on the carrier density. Non-radiative recombination, caused by defects in the crystal lattice structure, depends linearly on the carrier density. Auger recombination, while weak at low bias currents, varies with N^3 as it is a three particle process. Both of these effects reduce the excited state population and thus prevent complete inversion. Of particular importance, however, is the rate of radiative recombination, which results in spontaneous emission. Radiative recombination is a two particle process and so varies with N^2. The problem is compounded by the amplifier gain and the facet reflectivity. The higher the bias current, the greater the magnitude of the amplified spontaneous emission, due to the increased gain. At high enough bias, the ASE can actually saturate the gain, which is a problem for SOAs with lengths greater than ~ 1 *mm* [54]. The depletion of carriers depicted in Fig. 2.7. illustrates the effect clearly. The problem of ASE is compounded by residual reflectivity from the SOA facets. While anti-reflection coated SOAs can achieve reflectivity as low as 10^{-5}, a portion of the ASE produced will reflect from the facets back into the active region, where it will be re-amplified and can contribute to carrier depletion. This problem is only exacerbated at higher biases. Therefore, for the reasons outlined above, simply increasing the bias indefinitely cannot reduce the NF to its optimal level.

Noise figure of a chain of amplifiers

The carrier density within the active region of an SOA is considered to be constant when operating at steady state conditions at a constant bias current. However, this is true only for the *total* carrier number in the excited state. As was shown in Fig. 2.7, even in an SOA with constant bias, the carrier density within the active region can vary as a result of depletion of carriers by ASE or signal. As such, while for the purposes of practical usage of SOAs it makes sense to talk only of the total noise figure of the SOA, it can still be considered that the noise figure at any one point in the active region will vary as a result of the local carrier density distribution. This reasoning can apply not just to the noise figure, but to any parameter that depends on the level of carrier density, such as the optical gain, refractive index and spontaneous carrier lifetime. When we think of an

SOA not as a monolithic block with set parameters but as a structure of individual components, each with their own parameters, we can draw an analogy between this situation and that of a chain of optical or RF amplifiers. The total noise figure of an amplifier chain and how it is related to the individual components is derived as follows [46]; consider a chain of three amplifiers, each with their own gain G_m and noise photon density ρ_m, where *m* denotes the individual amplifiers 1-3, depicted in Fig. 2.8.

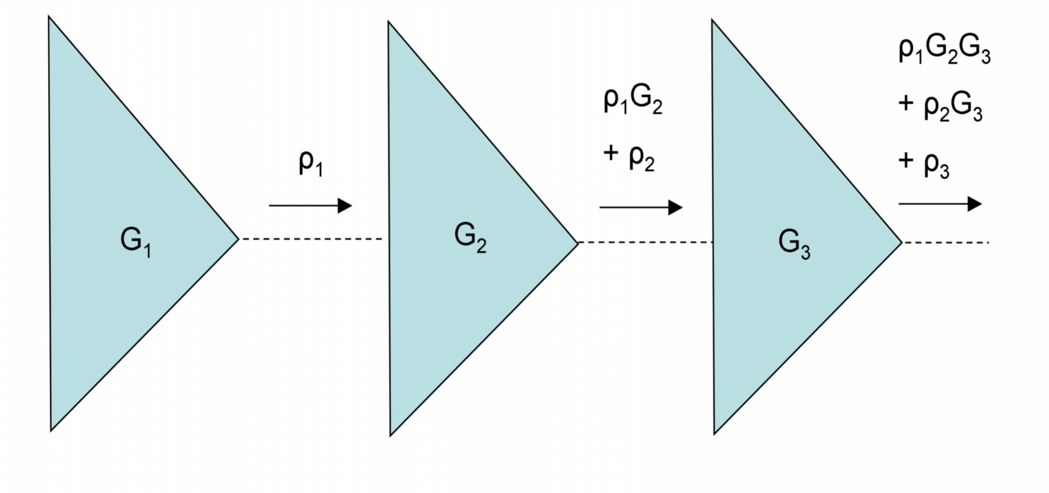

2.8. Chain of amplifiers along with respective gain (G_m) and noise densities (ρ_m).

In this figure, the noise from each amplifier is equal to the noise from the previous components in the chain, plus the amplifiers own noise density multiplied by its gain. This figure is illustrative of how high levels of noise can build up in cascaded amplifier chains, and must be carefully controlled. The result of this setup is that the total noise photon density of the amplifier chain, generalized to *n* components, is,

$$\rho_{tot} = \rho_1 G_2 G_3 G_4 ... G_n + \rho_2 G_3 G_4 ... G_n + \rho_3 G_4 ... G_n .. + \rho_n G_n . \tag{2.29}$$

Assuming that in an optical amplifier, the noise photon density is represented by the signal-spontaneous beat noise density, we can use Eq. (2.11), neglecting the shot noise term, to calculate the noise factor of each component and thus the overall noise figure, and noise figure, of the chain. Inserting the expressions for ρ_{tot} into Eq. (2.11) instead of ρ_{ASE}, and taking the total gain $G_{tot} = G_1 G_2 G_3 \ldots G_n$, we get,

$$F_{tot} = \frac{2\rho_{tot}}{h\nu G_{tot}} = \frac{2\rho_1}{h\nu G_1} + \frac{2\rho_2}{h\nu G_1 G_2} + \frac{2\rho_3}{h\nu G_1 G_2 G_3} + \ldots + \frac{2\rho_n}{h\nu G_1 G_2 \ldots G_n} . \tag{2.30}$$

Again, using Eq. (2.11), Eq. (2.30) can be expressed in terms of the noise factors of the individual components,

$$F_{tot} = F_1 + \frac{F_2}{G_1} + \frac{F_3}{G_1 G_2} + \ldots + \frac{F_n}{G_1 G_2 \ldots G_{n-1}}. \tag{2.31}$$

It follows from this equation that, in a chain of amplifiers, the components contributing the majority of the noise in the system is the component at the beginning of the chain, simply because the noise power that it produces is amplified by every other amplifier that follows it. Each successive term in the equation is divided by an additional factor *G*, where *G* is the gain of the previous amplifier in the chain. It should be noted that all values used in the equation are linear, rather than logarithmic. Fig. 2.9 visualizes this concept, showing a chain of amplifiers and their relative contributions to the total NF.

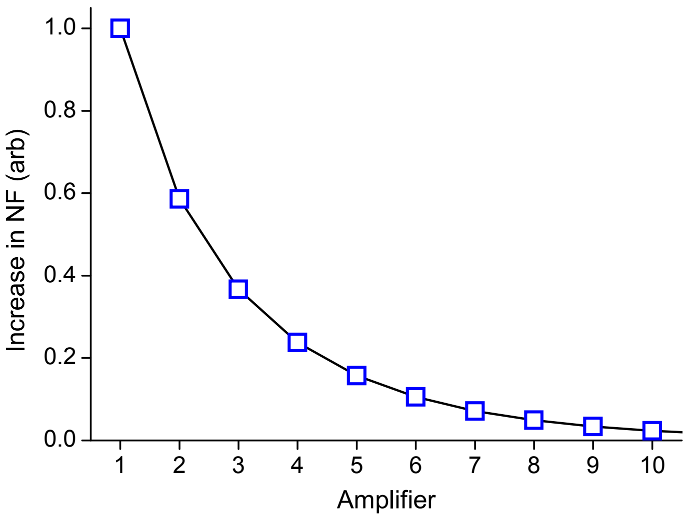

2.9. Contribution to increase in NF for a series of amplifiers, relative to the first amplifier.

This is the reason that low noise amplifiers are place first in a cascaded system. If we consider again our analogy of a single SOA being equivalent to a chain of amplifiers, it should be reasonable to assume that if a carrier density profile could be created such that the input region of the SOA had a low noise figure, then the overall noise figure of the SOA should be reduced.

Optimal carrier density profile

As discussed above, the most important aspect of reducing the noise in an SOA should be to ensure low noise operation at the input facet region. It has been established already that NF is proportional to the population inversion factor, which in turn is inversely proportional to the level of carrier density in the active region. Therefore, in order to reduce the noise in the input region of the SOA, the carrier density in that area must be kept at a high level. On the basis that the intrinsic noise figure contributions of the non-input regions of the SOA are not as important, the control of the carrier density in these areas is not as much of a concern. However, when amplified spontaneous emission is taken into account, the situation becomes more complicated. If the carrier density at the input regions of the SOA is increased, ASE is amplified by an additional factor, and can deplete the carriers at this facet. This is unavoidable if a high N is to be maintained. However, as previously mentioned ASE can also emanate from the output region and reflect from the output facet, travel backwards through the active region being amplified on the way, and then further reduce the carrier density at the input facet. However, if the carrier density in the region at the output facet is kept to a low level, three objectives are achieved. Firstly, ASE emanating from the input region of the SOA experiences less amplification than if the output region had a normal carrier density distribution, and may even be attenuated. Secondly, this attenuation means that the magnitude of the reflected ASE from the output facet is very small, and experiences very little amplification. Most importantly, the magnitude of ASE emanating from the output region is greatly reduced due to the low carrier density. As a result, the carrier density at the input of the SOA is not depleted as it might have been given a normal carrier density distribution.

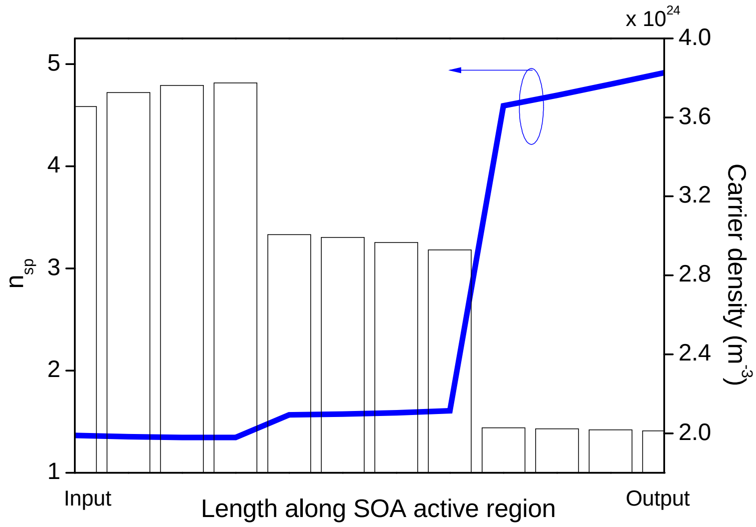

2.10. Optimal carrier density profile and population inversion factor for low noise figure, as a function of position along SOA active region.

Fig. 2.10 shows this optimal carrier density profile, along with the population inversion factor for illustration, as a function of position along the SOA active region. Of note is the low value for n_{sp} when the carrier density is at its highest level and the rapid increase of this parameter as the carrier density decreases. Further evidence for this is presented in Figs. 2.11a and 2.11b. Fig. 2.11a shows the carrier density distribution of a standard SOA as a function of the position along the active region, for a range of input signal powers. The effect of the injected signal is clear. At low input powers, the signal has an insignificant effect on the carrier density distribution, and the profile we see is identical to that shown in Fig. 2.7. As the input power is increased, the carrier density towards the output facet of the SOA is depleted by the amplified signal. This effect becomes much stronger at higher powers, and the peak of the carrier density distribution is shifted to the input facet. The depletion of carriers at the output facet as the power is increased is also responsible for the fact that the input facet carrier density is higher for the 0 dBm case than for lower powers. This is because less ASE is emitted from the output of the device that would otherwise deplete carriers at the input facet. Fig. 2.11b shows a standard noise figure versus input power curve for the same SOA.

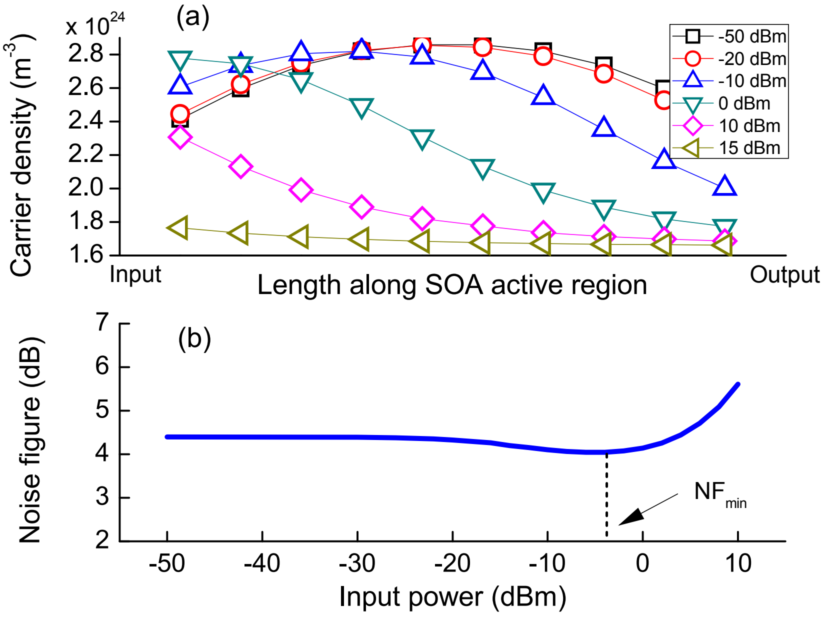

2.11. (a) Carrier density profiles for a standard SOA, for a range of input powers, and (b) noise figure vs input power for the same SOA.

What is significant is that the noise figure minimum observed on this curve is between 0dBm and -10dBm input power. Interestingly, the corresponding carrier density profiles for both 0dBm and -10dBm input powers in Fig. 2.11a are similar to the optimal profile described in this section. Chapter 3 will outline the structure of the simulation used to model this concept and will describe SOA designs that aim to achieve this carrier density profile, along with simulated and experimental results of this approach.

2.5.2. Increasing saturation output power

Dependence of saturation output power on spontaneous carrier lifetime

It has previously been stated in this chapter that the saturation intensity of an SOA is indirectly proportional to the spontaneous carrier lifetime τ. The relation between τ and the saturation intensity of the SOA is given by Eq. (2.21). It follows from this that one way to increase the saturation output power is to decrease the spontaneous carrier lifetime. The spontaneous carrier lifetime is defined as the average time it takes carriers in the conduction band to recombine with holes in the valence band through spontaneous processes. In a semiconductor medium with non-radiative, radiative and Auger recombination mechanisms, the total recombination rate is expressed as [55],

$$R(N) = AN + BN^2 + CN^3 \, , \tag{2.32}$$

where N is carrier density and A, B and C are the non-radiative, radiative and Auger recombination coefficients, respectively. Therefore the spontaneous carrier lifetime is inversely dependent on the carrier density, as demonstrated by,

$$^{2} = \frac{N}{R(N)} = \frac{1}{A + BN + CN^2} \, . \tag{2.33}$$

This suggests that increasing bias current supplied to the SOA and thus the carrier density, the saturation power should be indirectly improved through an increase in the saturation intensity. Similarly, according to Eq. (2.20), increasing the gain should accomplish the same goal, as it is directly proportional to the saturation intensity. A crucial difference between the methodology of reducing noise figure and increasing saturation output power is that the ASE plays the opposite role in each process. As has been demonstrated with long (> 1 *mm*) SOAs [56], a large ASE power increases the rate of stimulated emission recombinations, reducing the carrier lifetime. At high enough ASE power, the gain recovery dynamics are dominated by the ASE induced stimulated emission rate [57], minimizing the depleting effect of the input signal. In a way the ASE acts in a similar manner to a holding beam [17].

Optimal carrier density profile

Obviously the optimal carrier density to increase the saturation output power would be as high as possible, limited by increased non-radiative and Auger recombination effects. However, in the situation where the total bias current in the SOA is restricted to a certain value, as it is in this case (see Chapter 3 for details), a specific carrier density profile must be created that maximizes the saturation output power under the restrictions of a fixed total bias. If we assume that the total bias limit is the same as that of the low noise case, then the optimal carrier density profile should be the inverse of the low noise case. The reason for this is that as the signal propagates through the SOA, it exponentially increases in magnitude due to optical gain. Therefore, as it increases it converges on the saturation intensity value. The saturation intensity of any one point in the SOA waveguide, therefore, needs to be tailored to reflect the intensity of the signal being amplified at that point. Recalling that to increase the saturation intensity, the spontaneous carrier lifetime needs to be reduced through a higher carrier density, it stands to reason that higher carrier densities would be needed for the more strongly amplified signals towards the rear facet of the amplifier. The optimal carrier density profile is shown in Fig. 2.12, along with the corresponding spontaneous carrier lifetime values, as a function of position along the SOA active region. A clear inverse trend is observed. The decrease of τ along the propagation direction is the key to keeping the saturation intensity higher than the intensity of the propagating signal.

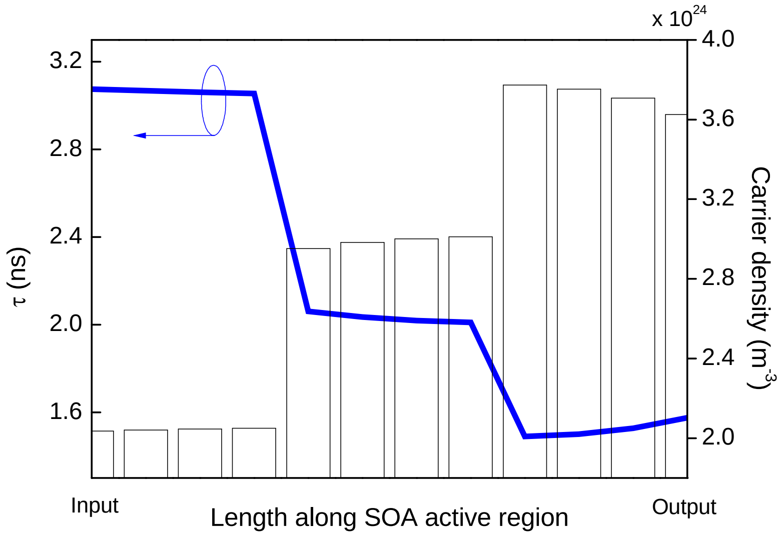

2.12. Spontaneous carrier lifetime and carrier density as a function of position along the SOA active region.

2.5. Summary

In this chapter, the concepts of optical noise and gain saturation in semiconductor optical amplifiers were outlined. The problems of optical noise and gain saturation with respect to linear amplification applications in optical networks were explored, and following on from this, various efforts to improve both the noise figure and the saturation output power of SOAs were detailed. An in-depth derivation and explanation of optical noise figure was shown, along with a discussion about the types of optical noise in SOAs, as well as their relative importance in optical systems. The effect of gain saturation on high bit rate and multichannel amplification was outlined, as well as a derivation of the saturation output power, an important parameter of SOAs. The central concept of this thesis, the control of device parameters through the reshaping of the SOA carrier density profile, was described, and an explanation as to the optimal carrier density profiles to achieve control over noise figure and saturation power was given. In Chapter 3, we will look at a case study of these concepts, as applied to two SOA designs that will be outlined in detail. Simulated and experimental characterization in the steady state regime will be presented, along with a detailed explanation of the model used to simulate the SOA designs.

References

[1] Giles, C.R.; Desurvire, E.; Zyskind, J.L.; Simpson, J.R.; "Noise performance of erbium-doped fiber amplifier pumped at 1.49 μm, and application to signal preamplification at 1.8 Gbit/s," *IEEE Photonics Technology Letters*, Vol.1, No.11, pp. 367-369, Nov 1989

[2] Spiekman, L.; Piehler, D.; Iannone, P.; Reichmann, K.; Han-Hyub Lee; "Semiconductor Optical Amplifiers for FTTx,", *International Conference on Transparent Optical Networks 2007*, Vol.2, pp.48-50, 1-5 Jul 2007.

[3] Kikuchi, K.; Zah, C.-E.; Lee, T.-P.; "Measurement and analysis of phase noise generated from semiconductor optical amplifiers," *IEEE Journal of Quantum Electronics*, Vol.27, No.3, pp.416-422, Mar 1991.

[4] Henry, C.; "Phase noise in semiconductor lasers," *Journal of Lightwave Technology*, Vol.4, No.3, pp.298- 311, Mar 1986.

[5] Mukai, T.; Yamamoto, Y.; "Noise characteristics of semiconductor laser amplifiers," *Electronics Letters*, Vol.17, No.1, pp.31-33, Jan 8 1981.

[6] Shtaif, M.; Tromborg, B.; Eisenstein, G.; "Noise spectra of semiconductor optical amplifiers: relation between semiclassical and quantum descriptions," *IEEE Journal of Quantum Electronics*, Vol.34, No.5, pp.869-878, May 1998.

[7] In Kim; Uppal, K.; Dapkus, P.D.; "Gain saturation in traveling-wave semiconductor optical amplifiers ," *IEEE Journal of Quantum Electronics*, Vol.34, No.10, pp.1949-1952, Oct 1998.

[8] Saleh, A.A.M.; Habbab, I.M.I.; "Effects of semiconductor-optical-amplifier nonlinearity on the performance of high-speed intensity-modulation lightwave systems," *IEEE Transactions on Communications*, Vol.38, No.6, pp.839-846, Jun 1990.

[9] Durhuus, T.; Mikkelsen, B.; Stubkjaer, K.E.; “Detailed dynamic model for semiconductor optical amplifiers and their crosstalk and intermodulation distortion”, *Journal of Lightwave Technology*, Vol.10, No.8, pp.1056-1069, Aug 1992.

[10] Agrawal, G.P.; Habbab, I.M.I.; “Effect of a four-wave mixing on multichannel amplification in semiconductor laser amplifiers”, *IEEE Journal of Quantum Electronics*, Vol.26, No.3, pp.501-505, Mar 1990.

[11] Forghieri, F.; Tkach, R.W.; Chraplyvy, A.R.; Marcuse, D.; "Reduction of four-wave mixing crosstalk in WDM systems using unequally spaced channels," *IEEE Photonics Technology Letters*, Vol.6, No.6, pp.754-756, Jun 1994.

[12] Shtaif, M.; Eiselt, M.; Garrett, L.D.; "Cross-phase modulation distortion measurements in multispan WDM systems," *IEEE Photonics Technology Letters*, Vol.12, No.1, pp.88-90, Jan 2000.

[13] Stern, M.; Heritage, J.P.; Thurston, R.N.; Tu, S.; "Self-phase modulation and dispersion in high data rate fiber-optic transmission systems," *Journal of Lightwave Technology*, Vol.8, No.7, pp.1009-1016, Jul 1990.

[14] Crottini, F.; Salleras, P.; Moreno, M. A.; Dupertuis, B.; Deveaud, B.; Brenot, R.; “Noise figure improvement in semiconductor optical amplifiers by holding beam at transparency scheme”, *IEEE Photonics Technology Letters*, Vol.17, No.5, pp.977-979, May 2005.

[15] Enbo Zhou; Xinliang Zhang; Dexiu Huang; "Evaluating characteristics of semiconductor optical amplifiers using optical pumping near the transparency", *Journal of the Optical Society of America B*, Vol.24, No.10, pp.2647-2657, Oct 2007.

[16] Yoshino, M.; Inoue, K.; "Improvement of saturation output power in a semiconductor laser amplifier through pumping light injection", *IEEE Photonics Technology Letters*, Vol.8, No.1, pp.58-59, Jan 1996.

[17] Manning, R.J.; Davies, D.A.O.; "Three-wavelength device for all-optical signal processing," *Optics Letters*, Vol.19, No.12, pp.889-991, Jun 1994.

[18] Talli, G.; Adams, M.J.; “Gain recovery acceleration in semiconductor optical amplifiers employing a holding beam”, *Optics Communications*, Vol.245, No.1-6, Jan 2005.

[19] Hill, M.T.; Tangdiongga, E.; de Waardt, H.; Khoe, G.D.; Dorren, H. J. S.; “Carrier recovery time in semiconductor optical amplifiers that employ holding beams”, *Optics Letters*, Vol.27, No.18, pp.1625-1627, September 2002.

[20] Bjorlin, E.S.; Bowers, J.E.; “Noise Figure of Vertial-Cavity Semiconductor Optical Amplifiers”, *IEEE Journal of Quantum Electronics*, Vol.38, No.1, pp.61-66, Jan 2002.

[21] Wen, P.; Sanchez, M.; Gross, M.; Esener, S.C.; “Noise and noise figure of vertical-cavity semiconductor optical amplifiers (VCSOAs) operated in reflection mode”, *Proc. SPIE*, 5111, 506 (2003).

[22] Brenot, R.; Pommereau, F.; Le Gouezigou, O.; Landreau, J.; Poinet, F.; Le Gouezigou, L.; “Experimental Study of the Impact of Optical Confinement on Saturation Effects in SOA”, *Proc. Optical Fiber Communications Conference*, 3 pp., Vol. 1, 6-11 Mar 2005.

[23] Doussiere, P.; Jourdan, A.; Soulage, G.; Garabedian, P.; Graver, C.; Fillion, T.; Derouin, E.; Leclerc, D.; "Clamped gain travelling wave semiconductor optical amplifier for wavelength division multiplexing applications," *14th IEEE International Semiconductor Laser Conference*, pp.185-186, 19-23 Sep 1994.

[24] Verspurten, S.; Morthier, G.; Baets, R.; "Experimental and numerical small-signal analysis of two types of gain-clamped semiconductor optical amplifiers," *IEEE Journal of Quantum Electronics*, Vol.42, No.3, pp.302- 312, Mar 2006.

[25] Chao-Yuan Jin; Yong-Zhen Huang; Yu, L.-J.; Shen-ling Deng; "Detailed model and investigation of gain saturation and carrier spatial hole burning for a semiconductor optical amplifier with gain clamping by a vertical laser field," *IEEE Journal of Quantum Electronics*, Vol.40, No.5, pp. 513- 518, May 2004.

[26] Pleumeekers, J.L.; Dupertuis, M.-A.; Hessler, T.; Selbmann, P.E.; Haacke, S.; Deveaud, B.; "Longitudinal spatial hole burning and associated nonlinear gain in gain-clamped semiconductor optical amplifiers," *IEEE Journal of Quantum Electronics*, Vol.34, No.5, pp.879-886, May 1998.

[27] Guiliani, G.; D'Alessandro, D.; "Noise analysis of conventional and gain-clamped semiconductor optical amplifiers", *Journal of Lightwave Technology*, Vol.18, No.9, pp. 1256, Sep 2000.

[28] Bendelli, G.; Komori, K.; Arai, S.; Suematsu, Y.; "A new structure for high-power TW-SLA [Travelling wave semiconductor laser amplifier]," *IEEE Photonics Technology Letters*, Vol.3, No.1, pp.42-44, Jan 1991.

[29] Donnelly, J.P.; Walpole, J.N.; Betts, G.E.; Groves, S.H.; Woodhouse, J.D.; O'Donnell, F.J.; Missaggia, L.J.; Bailey, R.J.; Napoleone, A.; "High-power 1.3-μm InGaAsP-InP amplifiers with tapered gain regions," *IEEE Photonics Technology Letters*, Vol.8, No.11, pp.1450-1452, Nov 1996.

[30] Saini, S.S.; Bowser, J.; Enke, R.; Luciani, V.; Heim, P.J.S.; Dagenais, M.; "A semiconductor optical amplifier with high saturation power, low noise figure and low polarization dependent gain over the C-band", *Proc. Lasers and Electro-Optics Society*, Vol. 1, pp. 102-103, 7-11 Nov 2004.

[31] Saitoh, T.; Suzuki, Y.; Tanaka, H.; "Low noise characteristics of a GaAs-AlGaAs multiple-quantum-well semiconductor laser amplifier," *IEEE Photonics Technology Letters*, Vol.2, No.11, pp.794-796, Nov 1990.

[32] Tauber, D.; Nagar, R.; Livne, A.; Eisenstein, G.; Koren, U.; Raybon, G.; "A low-noise-figure 1.5 μm multiple-quantum-well optical amplifier," *IEEE Photonics Technology Letters*, Vol.4, No.3, pp.238-240, Mar 1992.

[33] Komori, K.; Arai, S.; Suematsu, Y.; "Noise study of low-dimensional quantum-well semiconductor laser amplifiers," *IEEE Journal of Quantum Electronics*, Vol.28, No.9, pp.1894-1900, Sep 1992.

[34] Morito, K.; Tanaka, S.; Tomabechi, S.; Kuramata, A.; "A broadband MQW semiconductor optical amplifier with high saturation output power and low noise

figure”, *IEEE Photonics Technology Letters*, Vol. 17, No. 5, pp. 974-976, May 2005.

[35] Hasegawa, H.; Funabashi, M.; Yokouchi, N.; Kiyota, K.; Maruyama, K.; "Design and fabrication of semiconductor optical amplifier with low noise figure," *2010 15th OptoeElectronics and Communications Conference (OECC)*, pp.204-205, 5-9 Jul 2010.

[36] Loh, W.; Plant, J.J.; Klamkin, J.; Donnelly, J.P.; O'Donnell, F.J.; Ram, R.J.; Juodawlkis, P.W.; "Noise Figure of Watt-Class Ultralow-Confinement Semiconductor Optical Amplifiers," *IEEE Journal of Quantum Electronics*, Vol.47, No.1, pp.66-75, Jan. 2011.

[37] Connolly, M.J.; “Semiconductor Optical Amplifiers”, Kluwer Academic Publishers, 2002.

[38] Juodawlkis, P.W.; Plant, J.J.; Huang, R.K.; Missaggia, L.J.; Donnelly, J.P.; "High-power 1.5-μm InGaAsP-InP slab-coupled optical waveguide amplifier," *IEEE Photonics Technology Letters*, Vol.17, No.2, pp.279-281, Feb. 2005.

[39] Morito, K.; Tanaka, S.; "Record high saturation power (+22 dBm) and low noise figure (5.7 dB) polarization-insensitive SOA module," *IEEE Photonics Technology Letters*, Vol.17, No.6, pp.1298-1300, June 2005.

[40] Mørk, J; Nielsen, M.L.; Berg, T.W.; “The Dynamics of Semiconductor Optical Amplifiers: Modeling and Applications”, *Optics and Photonics News*, Vol. 14, No. 7, pp. 42-48, Jul 2003.

[41] Berg, T.W.; Mørk, J.; "Saturation and noise properties of quantum-dot optical amplifiers," *IEEE Journal of Quantum Electronics*, Vol.40, No.11, pp. 1527- 1539, Nov 2004.

[42] Connor, F.R.; “Noise”, Edward Arnold, 1982.

[43] Friis, H.T.; “Noise Figures of Radio Receivers”, *Proc. of the IRE*, Vol. 32, No. 7, pp. 419-422, Jul 1944.

[44] Olsson, N.A.; “Lightwave systems with optical amplifiers”, *Journal of Lightwave Technology*, Vol. 7, No. 7, pp. 1071-1082, Jul. 1989.

[45] Hui, R; O’Sullivan, M; “Fibre optic measurement techniques”, Elsevier Academic Press, 2009.

[46] Baney, D.M.; Gallion, P.; Tucker, R.S.; “Theory and Measurement Techniques for the Noise Figure of Optical Amplifiers”, *Optical Fibre Technology*, Vol. 6, No. 2, pp. 122-154, Apr. 2000.

[47] Haus, H.A., “The Noise Figure of Optical Amplifiers”, *IEEE Photonics Technology Letters*, Vol. 10, No. 11, pp. 1602-1604, Nov. 1998.

[48] Desurvire, E.; Giles, C.R.; Simpson, J.R.; "Gain saturation effects in high-speed, multichannel erbium-doped fiber amplifiers at λ = 1.53 μm," *Journal of Lightwave Technology*, Vol.7, No.12, pp.2095-2104, Dec 1989.

[49] Hutchings, D.C.; Sheik-Bahae, M.; Hagan, D.J.; Stryland, E.W.; “Kramers-Kronig relations in nonlinear optics”, *Optical and Quantum Electronics*, Vol. 24, No. 1, pp. 1-30, 1992.

[50] Inoue, K.; "Crosstalk and its power penalty in multichannel transmission due to gain saturation in a semiconductor laser amplifier," *Journal of Lightwave Technology*, Vol.7, No.7, pp.1118-1124, Jul 1989.

[51] Yamamoto, Y.; Saito, S.; Mukai, T.; "AM and FM quantum noise in semiconductor lasers--Part II: Comparison of theoretical and experimental results for AlGaAs lasers," *IEEE Journal of Quantum Electronics*, Vol.19, No.1, pp. 47-58, Jan 1983.

[52] Adams, M.J.; Collins, J.V.; Henning, I.D.; “Analysis of semiconductor laser optical amplifiers”, *IEE Proceedings J Optoelectronics*, Vol. 132, No. 1, pp. 58-63, Feb 1985.

[53] Desurvire, E.; “On the Physical Origin of the 3dB Noise Figure Limit in Laser and Parametric Optical Amplifiers”, *Optical Fibre Technology*, Vol. 5, No. 1, p. 40-61, January 1999.

[54] Occhi, L.; “Semiconductor optical amplifiers made of ridge waveguide bulk InGaAsP/InP: experimental characterisation and numerical modelling of gain, phase, and noise, Doctoral thesis (2002).

[55] Agrawal, G.P.; Dutta, N.K.; “Long wavelength semiconductor lasers”, Springer, 1986.

[56] Liu, T.; Obermann, K.; Petermann, K.; Girardin, F.; Guekos, G.; "Effect of saturation caused by amplified spontaneous emission on semiconductor optical amplifier performance," *Electronics Letters*, Vol.33, No.24, pp.2042-2043, 20 Nov 1997.

[57] Valiente, I.; LaBlonde, L.; Simon, J.C.; Billès. L.; “Effect of amplified spontaneous emission on gain recovery dynamics of semiconductor optical amplifier”, *OAA*, Monterey, CA, Paper SaB2-1, pp. 224-227 July 1996.

3. SIMULATED AND EXPERIMENTAL STEADY-STATE CHARACTERIZATION OF SOA DESIGNS

3.1. Introduction

As mentioned previously in Chapter 2, various schemes for reducing noise figure and increasing saturation output power have been proposed and implemented [1, 2]. A number of advantages and disadvantages of these ideas were outlined. It is the purpose of this chapter to describe the practical implementation of the concepts for parameter control, introduced in the previous chapter, in two SOA designs [3, 4]. The proposed designs are simulated in the steady state using a travelling wave model. Experimental characterization of the steady state parameters such as noise figure, gain and saturation output power are then compared to the model in order to determine the effect of the carrier density reshaping. The opening sections of this chapter will be dedicated to describing the physical functioning of the two SOA designs. The first design, which is primarily intended to reduce noise figure, is based on a lateral cavity implemented over a portion of the waveguide, lateral to the axis of propagation. The second design, which has the advantage of flexibility in its functionality, is based on the injection of bias current through multiple electrical contacts, with the aim of directly controlling the carrier density distribution within the active region. The two SOAs described herein are prototype units. A thorough characterization can reveal potential for improvement in future designs.

3.2. SOA designs

3.2.1. Lateral cavity semiconductor optical amplifier

The concept of gain clamped and linear SOAs has been discussed in Chapter 2 [5, 6, 7]. Central to the physical mechanisms of these designs is the ability to clamp the carrier density, in order to smooth out any variations caused by changes in the input signal power. The objective of these designs is to increase the linear dynamic range of the SOA, and thus increase the saturation output power. GC-SOAs achieve this through the use of DBR mirrors, usually situated in the axis of the epitaxial growth. LOAs, are similar except that they use integrated lasers. In both methods, the carrier density throughout the entire device is clamped. The first SOA design, that is the subject of this thesis, differs from the aforementioned gain clamped SOAs in a fundamental way. Like GC-SOAs, the lateral cavity SOA, or LC-SOA, utilizes DBR mirrors in order to achieve lasing in the cavity thus formed, clamping the carrier density and gain [8]. These DBR mirrors are placed lateral to the waveguide axis, rather than vertical. Unlike the GC-SOA, the DBR reflectors in the LC-SOA do not extend the full length of the waveguide, but occupy only the output section. The reason why this is so is elaborated further on in the chapter.

Device structure

The LC-SOA design is a multi-quantum well InP/InGaAsP MOCVD grown semiconductor optical amplifier. It is designed to operate in the 1.5 μm window. To minimize internal reflections of signal and ASE, the waveguide is tilted at 22^0 and is anti-reflection coated. The entire device, shown in Fig. 3.1, is 1 mm long, with an 800 μm long active region and two 100 *μm* tapered regions at the facets. The active waveguide is 1.6 μm in width in order to ensure single mode operation. The lateral DBR cavity is implemented at the output region of the SOA over 450 μm, or 55% of the SOA active region. The guided ASE mode is 73% polarised in the TE axis, making the LC-SOA quite polarisation dependent. A number of LC-SOA designs were fabricated within the same batch, each having different placement of the lateral cavity or different cavity lengths. In addition to the LC-SOAs in this batch, a control device, lacking a lateral cavity, was also fabricated. Of the devices with lateral cavities, only the LC-SOA under investigation in this study had appreciable output power and gain. It is suspected that the reason for this lies in the placement of the DBR grating close to the active waveguide in the other LC-SOA designs, with the possible consequence of damage to the waveguide. The DBR grating in the LC-SOA under test was placed further from the waveguide, relative to the other LC-SOAs.

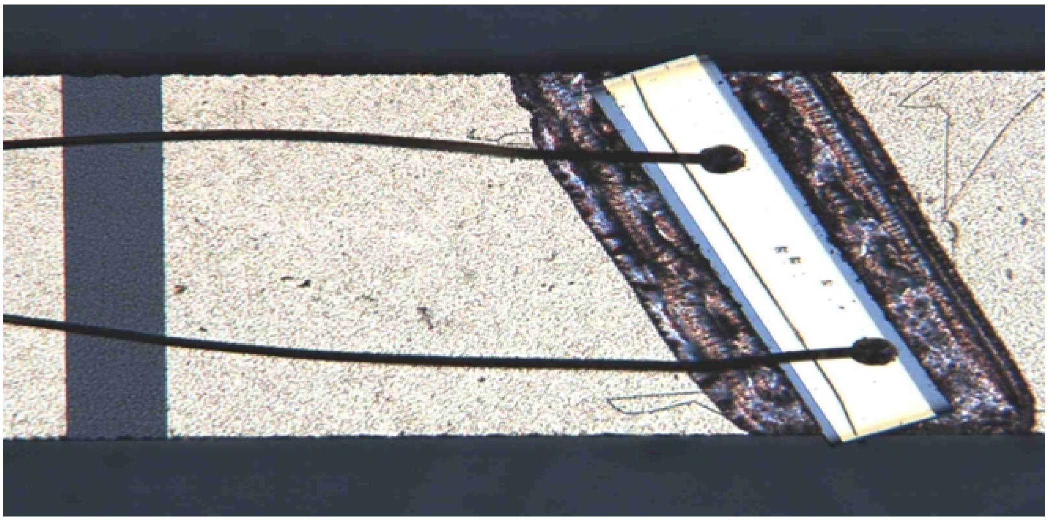

3.1. Microscope view of LC-SOA, showing the waveguide and electrical contacts.

Lateral cavity design

As previously mentioned, the LC-SOA employs distributed Bragg reflectors (DBR). DBRs are constructed of alternating layers of material with different refractive indices. Assuming normal angles of incidence, the optical layer thickness is chosen to be one quarter of the wavelength for which the DBR is intended to reflect. Each interface between layers will contribute a Fresnel reflection when encountering an optical wave. The optical path length difference between the forward travelling wave and the reflected wave will be half the wavelength. In addition to this, the amplitude reflection coefficients for each successive boundary have opposite signs. Therefore constructive interference occurs at the chosen Bragg wavelength, which in a device such as a DBR laser, amounts to a laser cavity. The reflections build up until the cavity gain equals the loss, creating the condition for lasing. The same process occurs in gain clamped SOAs. In the LC-SOA, the DBR grating is created by etching a slot pattern in the InP cladding around the InGaAsP active region. The InP layer thickness is chosen to be 208 nm, with an 80 nm air gap, giving a lasing wavelength of 1450 nm, according to the first order Bragg condition [9],

$$\lambda_0 = 2 n_e \Lambda \tag{3.1}$$

where λ_0 is the central wavelength of the DBR bandwidth, n_e is the effective refractive index and Λ is the grating period.

Lateral cavity function

The basic schematic of the LC-SOA is shown in Fig. 3.2. The DBR grating is introduced at the output half of the waveguide, encompassing approximately 450 μm. At a certain threshold bias current, the lateral cavity formed by the DBR grating starts to lase, and the carrier density is subsequently clamped to the threshold value. As the bias current is increased, the carrier density in the output clamped region does not increase. The additional injected carriers translate directly into strengthening the intensity of the lasing mode. It is important to note the carrier density for the entire SOA is *not* clamped to that value. The input section of the SOA experiences a variable carrier density depending on the bias current supplied. Consequently, as the bias is increased above the threshold value for the DBR grating, the carrier density profile begins to resemble that of the low noise case outlined in Chapter 2.

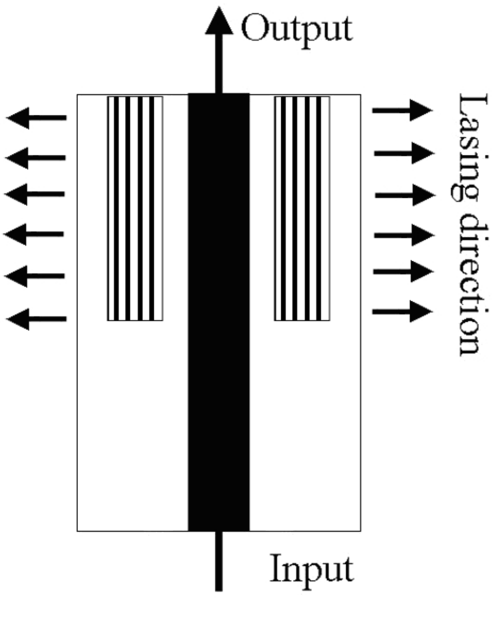

3.2. Schematic of the LC-SOA. Distributed Bragg reflector grating is positioned at the output of the SOA.

In a normal SOA, as the bias is increased there is a corresponding rise in ASE power, which eventually saturates the gain through depletion of carriers. As this effect is more pronounced at the SOA facets, the noise figure is heavily affected, because of the dependence of NF on the input section carrier density. The novel aspect of the LC-SOA is that the low carrier density in the clamped region of the SOA has an attenuating effect on amplified spontaneous emission. ASE emanating from the clamped region towards the input facet is greatly reduced, and does not increase with increasing bias. As an additional effect, ASE emanating from the high carrier density input region towards the output facet experiences much reduced amplification in the clamped region, making the effect of reflected ASE from the output facet almost negligible. As a result of this process, the carrier density at the input of the SOA is not depleted as it would be in a normal SOA, and so the noise figure remains low.

3.2.2. Multi-contact semiconductor optical amplifier

The second design that will be discussed is that of a multi-contact semiconductor optical amplifier. The later-cavity SOA controls the carrier density distribution with the active region both directly, through gain clamping, and indirectly, through the reduction of ASE travelling to the input region. The multi-contact SOA, or MC-SOA, achieves this goal through directly shaping the carrier density profile [10]. The device is electrically separated into a number of sections, and each section is independently electrically pumped, allowing the direct control of the carrier density within. Multi-contact SOAs have been studied before for a number of purposes. Control of gain bandwidth through the use of MC-SOAs has been demonstrated [11]. Other applications include use as interferometric devices, utilizing the ability to dynamically vary the phase change experienced by input signals [12]. MC-SOAs have also been studied as potential solutions for low chirp remote modulators in passive optical networks [13]. The key advantage of MC-SOAs is their ability to dynamically alter device parameters depending on the bias current injected.

Device structure

An image of the MC-SOA is shown in Fig. 3.3. The device is a bulk InP/InGaAsP SOA, angled and anti-reflection coated, with a length of approximately 700 μm. Three electrodes are used for current injection into three sections of length 236 μm, 254 μm and 210 μm. The 236 μm side is nominally taken to be the input facet. Electrical isolation between the contacts is provided by a 10μm slot, and resistance between sections is measured to be 300 Ω. The waveguide is slightly flared at the facets. The SOA is nearly polarization independent. For manufacturing reasons, the current in each contact is limited to 100 mA. It has been experimentally observed that the gain of the MC-SOA rapidly diminishes at overall bias currents > 150mA. Increased heating of the device is a possible cause. Consequently, the total bias current for the three sections, in all experiments, is restricted to 150 mA.

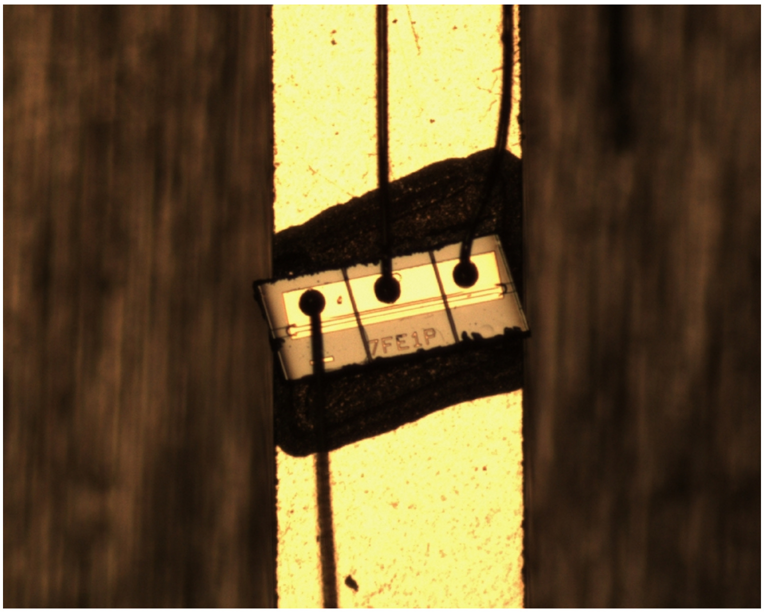

3.3. Top-down view of multi-contact SOA, showing individually biased sections.

Function of multi-contact design

The individual sections in the MC-SOA share a common ground, and can be connected to multiple current sources or a single source with a resistor network controlling the distribution of current (see Fig. 3.4). The device presented in this thesis was biased using three separate current sources. The key advantage of using a multi-contact design is that there is complete flexibility regarding the choice of SOA operating conditions. The carrier density profile achieved by the lateral cavity SOA by using gain clamping can be created simply by injecting a higher bias current into the input section than the output section. Similarly, the carrier density profile for achieving a higher saturation output power, discussed in Chapter 2, can be obtained using the same total bias current, but with a higher bias applied to the output section compared to the input.

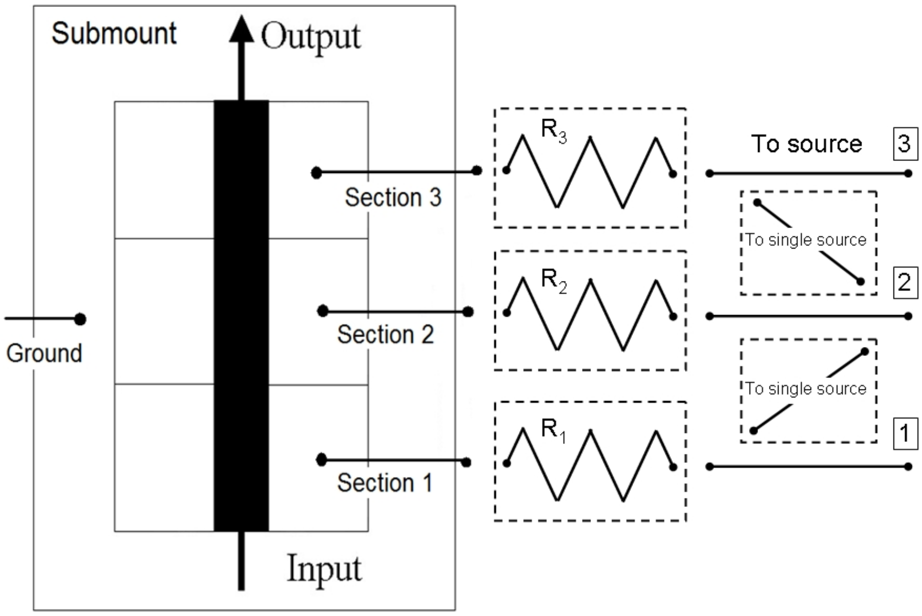

3.4. Schematic of MC-SOA. Sections can be pumped with multiple sources or single source with resistor network.

3.3. SOA model

The SOA designs described above and the concepts for parameter control outlined in the previous chapter are elaborated in this chapter using simulations. The simulations have been developed based on a travelling wave description of an SOA [14, 15]. In order to accurately model the variation of electric fields and carrier density along the waveguide length, the SOA is modelled in *n* subsections, with values for all variables assumed to be constant for each subsection and calculated for each one [16]. The carrier density is set at an initial value and is updated from the determined values of the ASE and signal fields. This process continues over a defined number of iterations. Values for carrier density as well as ASE and signal fields are used as initial conditions for the next iteration. The structure of the simulation is outlined in a flowchart in Appendix A.2. An overview of the concept of the simulation is shown in Fig. 3.5 below. This depicts the sectioning of the SOA, as well as the carrier density and forward and backward travelling spontaneous emission fields.

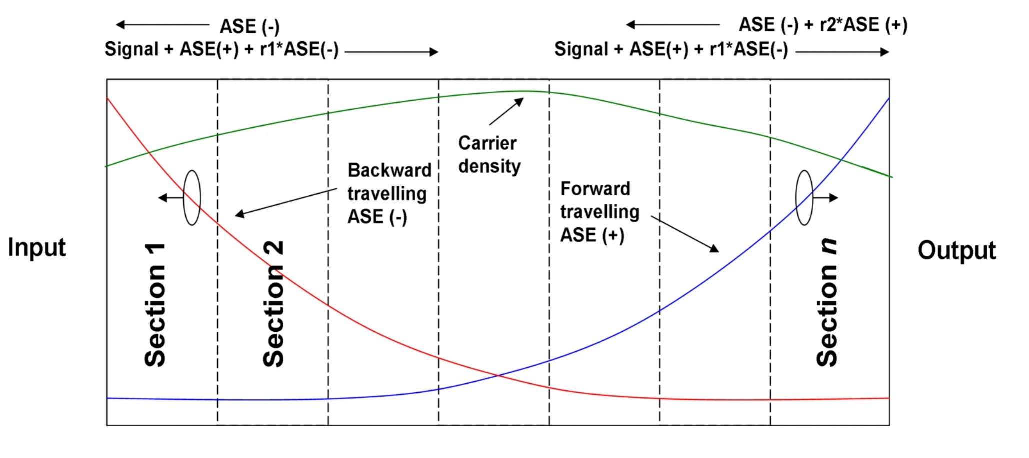

3.5. Schematic of simulated SOA, indicating carrier density (green) and forward (blue) and backward (red) travelling spontaneous emission, for the case with no injected signal.

The ASE intensity and the signal intensity along the waveguide (z axis) are described as a function of angular frequency ω by slowly varying envelope functions, and calculated using the set initial value of the carrier density and the material gain, which is itself determined from the physical properties of the SOA specified in the simulation. The material gain function used in this model is physical [17] rather than phenomenological [18] and is outlined in Appendix A.1. The values of the ASE intensity *I*, for each successive subsection are determined by the values in the previous subsection according to boundary conditions. These boundary conditions govern how the facet reflectivity affects the propagation of the ASE, and are given as,

$$\begin{aligned}
&I^{+}_{m,sp}(\mu, z^{-}_{m}) = I^{+}_{m-1,sp}(\mu, z^{+}_{m-1}), && m \neq 1 \\
&I^{-}_{m,sp}(\mu, z^{+}_{m}) = I^{-}_{m+1,sp}(\mu, z^{-}_{m+1}), && m \neq n \\
&I^{+}_{1,sp}(\mu, z^{-}_{1}) = r_1^2 I^{-}_{1,sp}(\mu, z^{-}_{1}), && m = 1 \\
&I^{-}_{n,sp}(\mu, z^{+}_{n}) = r_2^2 I^{+}_{n,sp}(\mu, z^{+}_{n}), && m = n
\end{aligned}, \tag{3.2}$$

where *m* indicates subsection number. The relations above determine the behaviour of the ASE intensity travelling in both the positive and negative directions at the subsection boundaries and the facets, where $r_{1,2}$ is the reflectivity of facet 1 or 2. A similar equation set determines the behaviour of the signal intensity with respect to time *t* and position, *z*. The boundary conditions for the signal envelope functions are,

$$
\begin{aligned}
F_{k,m}^{+}(t, z_m^{-}) &= F_{k,m-1}^{+}(t, z_{m-1}^{+}), & m \neq 1 \\
F_{k,m}^{-}(t, z_m^{+}) &= F_{k,m+1}^{-}(t, z_{m+1}^{-}), & m \neq n \\
F_{k,1}^{+}(t, z_1^{-}) &= r_1 F_{k,1}^{-}(t, z_1^{-}) + F_k^{in}(t) e^{i(\omega_{po} - \omega_{ko})t}, & m = 1 \\
F_{k,n}^{-}(t, z_n^{+}) &= r_2 F_{k,n}^{+}(t, z_n^{+}), & m = n
\end{aligned}
, \tag{3.3}
$$

where ω_{p0} and ω_{k0} are the gain peak angular frequency and signal angular frequency respectively. Using the values for the ASE envelope function, modified by the boundary conditions above, the spontaneous emission photon density is obtained as,

$$
\begin{aligned}
S_{m,spon} &= \frac{4\beta n_{g,o}}{\hbar \omega_{po} c} \\
&\times \left[\left(I_{m,sp}^{+}(z_m^{-}) + I_{m,sp}^{-}(z_m^{+}) + \frac{R_r(N_m).\hbar\omega_{po}}{2\beta\,(\Gamma g(\omega_{po}, N_m) - \alpha_i)} \right) . \frac{G_m - 1}{\ln(G_m)} \right] \\
&\qquad - \frac{2\,R_r(N_m).n_{g,o}}{(\Gamma g(\omega_{po}, N_m) - \alpha_i).c}
\end{aligned}
\tag{3.4}
$$

where N_m is the carrier density in subsection m, G_m is the single pass gain (expressed in linear scale) in subsection m calculated from the carrier density and material gain, $R_r(N_m)$ is the radiative recombination rate, α is the internal loss coefficient and is the effective spontaneous emission factor, a measure of the spontaneous emission coupled to the travelling mode. The photon density for the signal is also obtained in a similar way using the signal envelope function:

$$
\begin{aligned}
S_{m,sig} &= \frac{G_m - 1}{\ln(G_m)} \frac{\beta n_{g,0}}{c.\P} \\
&\times \left(\left| \sum_{k=1} \frac{1}{\sqrt{h\omega_k}} F_{k,m}^{+}(t, z_m^{-}) \right|^2 + \left| \sum_{k=1} \frac{1}{\sqrt{h\omega_k}} F_{k,m}^{-}(t, z_m^{+}) \right|^2 \right) .
\end{aligned}
\tag{3.5}
$$

The values for the spontaneous emission photon density and the signal photon density are then used to solve the carrier density rate equation. The program algorithm attempts to find a solution for carrier density N_m such that the derivative equals zero,

$$
\frac{dN_m}{dt} = \frac{i_m}{qV} - R(N_m) \\
- \quad v_g \left[g(\mu_{sig}, N_m) S_{m,sig} + a_1 (N_m - N_0) S_{m,spon} \right] , \tag{3.6}
$$

where i_m is the bias current injected at an individual subsection m, q is the charge of the carriers, V is the volume of the active region in subsection m, a_1 is the differential gain coefficient and N_0 is the transparency carrier density. $R(N_m)$ represents the total recombination rate equal to $AN_m+BN_m^2+CN_m^3$, where A is the non-radiative recombination coefficient, B is the radiative recombination coefficient, and C is the Auger recombination coefficient. The simulation is modified in the case of modelling the lasing that occurs in the lateral cavity SOA, which introduces a change in the carrier density distribution. An additional term S_{las}, representing the laser photon density, is added to the carrier density rate equation to take this into account. The evolution of the lateral laser photon density with time is determined by,

$$
\frac{dS_{las}}{dt} = v_g . \Gamma_L \left[g(\mu_{las}, N_m) - \gamma_l \right] . S_{m,las} + \Gamma_L . R_{sp}(N_m) , \tag{3.7}
$$

where Γ_L is the optical confinement factor of the lateral laser cavity, γ is the photon lifetime and R_{sp} the spontaneous emission rate coupled to the lasing mode. This entire process comprises a single iteration of the model. The solved value of the carrier density is used to calculate the ASE and signal fields for the next iteration. Once convergence is reached, the gain and the noise figure are then obtained. The noise figure of each subsection in the SOA is determined from the population inversion factor for that subsection, $n_{sp,sub}$, in accordance with the relationship between the two parameters that was established in Chapter 2. Following on from this, the noise factor F_{sub} for a single subsection is given by,

$$
F_{sub} = \frac{2n_{sp,sub}(G_{sub} - 1)}{G_{sub}} + \frac{1}{G_{sub}} , \tag{3.8}
$$

where G_{sub} is the single pass gain of the relevant subsection. The model presented takes into account the shot noise of the signal in order to improve accuracy. The total noise factor of the SOA, taking into account the individual noise contributions of each subsection, must be described as equivalent to a chain of amplifiers, and is thus calculated by the formula established in [19]. This formalism can be derived from the formalism given in [20] and described by Eq. (2.31) by taking into account the shot noise term. If we define F_{tot} as described in Eq. (2.31) as equal to the noise factor due to the signal spontaneous beat noise only, $F_{sig\text{-}sp,tot}$, then the total noise factor for a chain of amplifiers, or in this case, subsections, is given by,

$$F_{sig-sp+shot,tot} = F_{sig-sp,tot} + \frac{1}{G_1 G_2 \ldots G_m G_{n-1} G_n}, \tag{3.9}$$

where G_m is the single pass gain of the m^{th} subsection out of n subsections. Replacing the individual noise factor terms F_m in Eq. (2.31) with the equation used in the model, given in Eq. (3.8), and correcting for the extra shot noise terms, Eq. (3.9) becomes,

$$\begin{aligned} F_{sig-sp+shot,\,tot} = & \left(\left[\frac{2n_{sp,1}(G_1-1)}{G_1}+\frac{1}{G_1}\right]-\frac{1}{G_1}\right)+\left(\left[\frac{2n_{sp,2}(G_2-1)}{G_2}+\frac{1}{G_2}\right]-\frac{1}{G_2}\right)\Big/G_1 \\ & +\left(\left[\frac{2n_{sp,3}(G_3-1)}{G_3}+\frac{1}{G_3}\right]-\frac{1}{G_3}\right)\Big/G_1G_2+\ldots \\ & \ldots+\left(\left[\frac{2n_{sp,n}(G_n-1)}{G_n}+\frac{1}{G_n}\right]-\frac{1}{G_n}\right)\Big/G_1G_2\ldots G_{n-1}+\frac{1}{G_1G_2\ldots G_{n-1}G_n} \end{aligned} \tag{3.10}$$

Multiplying out this expression and combining Eqs. (3.8) and (3.10), we are left with an expression for the total noise factor F of an amplifier (or subsection) chain that takes into account sig-sp noise and shot noise,

$$F = F_1 + \frac{F_2 - 1}{G_1} + \frac{F_3 - 1}{G_1 G_2} + \ldots + \frac{F_n - 1}{G_1 G_2 \ldots G_{n-1}}, \tag{3.11}$$

The noise model used in the simulation is a deterministic model, rather than a stochastic model that takes the full noise bandwidth and random nature into account. The noise is determined for the signal wavelength only, and so the model is used primarily for determining the behaviour of the parameter control schemes, rather than for accurately predicting the SOA noise figure. Results from the simulation are presented further on in the chapter in sections 3.5.1 and 3.6.1. The parameters used in the simulation and their values are given in Appendix A.3.

3.4. Measurement techniques

The determination of the gain and noise figure for the modelled SOA designs is governed by the equations outlined in the previous section. For the experimental characterization, certain factors need to be taken into account, such as the optical losses in the setup and the polarization of the input signal and ASE, both of which strongly affect the measured NF.

3.4.1. Experimental setup

Shown in Fig. 3.6 below is the basic setup used to characterise the SOAs. Both SOA designs are characterized using the same setup. The continuous wave injected signal comes from a tabletop tuneable external cavity laser (ECL). The maximum wavelength emitted from this laser with at least 0 dBm optical power is 1590 nm, and thus, experiments are restricted to this extent. The output from this source is fiberized and the polarisation of the signal is controlled through the use of fiberized polarisation controller (PC). The signal is then propagated through free space by coupling to a lens. The use of mirrors allows additional angular adjustment to the beam, allowing the improvement of the coupling. The signal is linearly polarised using a free space polariser (POL) and the beam is then coupled to the SOA via a 0.5 NA anti-reflection coated aspheric lens. Polarization is set along the TE eigenmode of the waveguide for both SOA designs. The collection side of the setup is similar, save for the absence of a polariser and a polarisation controller, and the output signal is finally coupled to an optical spectrum analyzer (OSA) with a resolution bandwidth of 0.06 nm. For the accurate determination of the noise figure when not using an output polariser, it is necessary to know the magnitude of the ASE that is co-polarised with the signal [21]. To achieve this, the free space polariser is set to the polarisation of the input signal and is then placed at the output of the SOA in the absence of an input signal. The ASE is then measured both with the polariser and without, using a free space power meter. The ratio of the two measurements is the percentage of co-polarised ASE. The absorption loss due to the polariser is also taken into account.

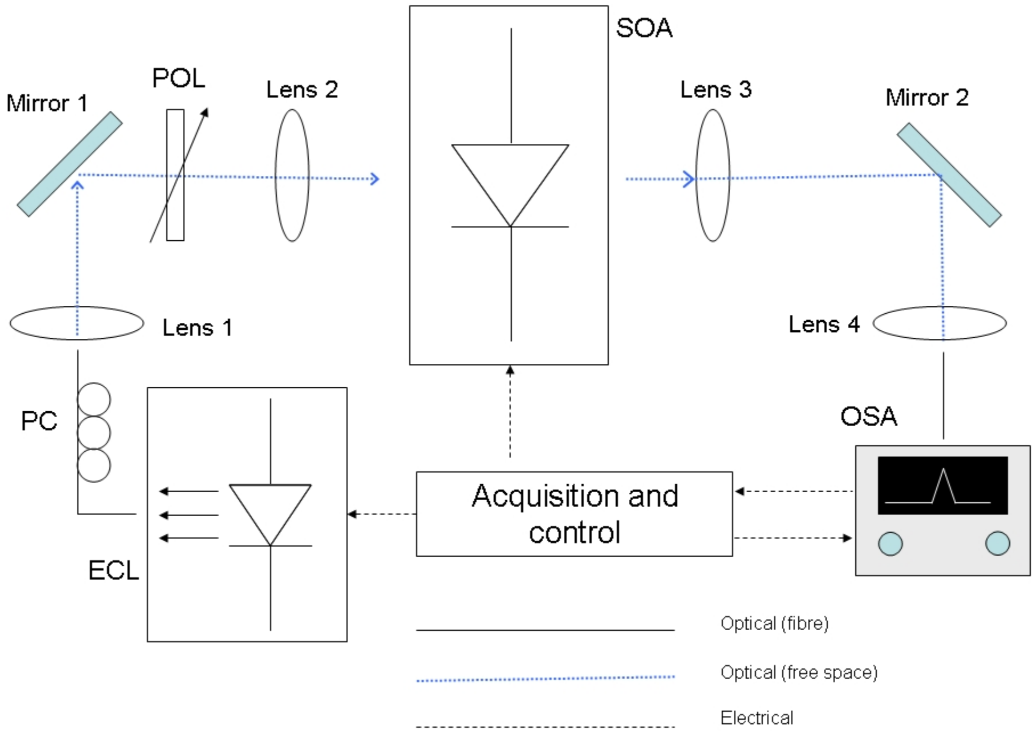

3.6. Experimental setup for characterizing SOAs in CW regime. ECL - external cavity laser; PC – polarization controller; POL – polarizer; SOA – semiconductor optical amplifier; OSA – optical spectrum analyzer.

3.4.2. Determination of losses

To accurately determine the noise figure of an SOA, it is vital to have a good estimation of the coupling losses in the experimental setup. In particular, input losses affect the noise figure to a large extent. When signal-spontaneous beat noise dominates over other sources of noise, which it normally does in the case of a moderate to high gain SOA, the relation between the fibre to fibre noise factor F_{ff} and the intrinsic noise factor F_i can be approximated to:

$$F_{ff} = \frac{F_i}{c_{in}}, \tag{3.12}$$

where c_{in} is the input coupling coefficient. The main source of loss when launching a signal into an SOA is mode coupling loss. This occurs because the mode profile of a light beam emerging from an optical fibre is circular, whereas the mode profile of the spontaneous emission at the facet of an SOA is generally elliptical. The mismatch between these two shapes causes a coupling loss at the input and at the output if a fibre is used to collect the output signal. Other sources of loss in the setup can come from losses in the fibre itself, absorption and reflection in the free space polariser, the mirrors and reflection from the coupling lenses. A wide aperture integrating sphere and power meter is used to measure the power at various points in the experimental setup. In doing so, the loss due to each element can be calculated.

1) Output losses

- The modal mismatch between the circular mode of the fibre and the elliptical mode of the SOA is measured first. The ASE power is measured just after *lens 3* using the integrating sphere. Power is measured using the OSA. The difference between these readings is the output modal coupling loss + the losses from the mirror and *lens 4* + fibre just before the OSA.
- The ASE is measured after *mirror 2*. The difference between this reading and the measurement after *lens 3* gives the mirror loss for the ASE. This is subtracted from the modal coupling loss to give pure modal coupling loss + fibre and *lens 4* loss.
- Mirror reflectivity is not necessary the same for signal and ASE. A signal is injected at the output arm of the setup and power is measured before and after *mirror 2*. The difference is the mirror loss for signal.

2) Input losses

- The modal mismatch at the input side of the setup is determined in the same way as the output side. Because we assume that the optical path can be reversed, this measurement should be valid to describe the modal mismatch of the signal coupling to the SOAs elliptical mode. The polariser is removed from the setup while calculating the modal loss. The mirror loss is also determined in the same way.
- To calculate the loss from the polariser, a signal is injected into the SOA and maximized (TE polarised) using the polariser. It can be observed on the OSA when the maximum signal has been reached. The injected power is measured before and after the polariser. This gives the loss associated with the polariser.

3) Lens losses

- To find losses due to reflections at the coupling lenses (*lenses 2 and 3*), a signal is injected through a lensed fibre in order to approximate the SOA output mode. This signal is measured before and after the coupling lens (the integrating sphere is placed in the setup instead of the SOA).

3.4.3. Measurement of gain and noise figure

Fig. 3.7 below shows a typical output spectrum of an SOA with an input signal injected. The spectra are recorded over a wavelength span of 1nm and are corrected for the resolution of the OSA, which is set at 0.06 nm for the measurements. The peak value of each spectrum, i.e. the peak of the signal, is found. The area around this peak is then integrated, within a set bandwidth, giving the total signal power. Using these same limits, a line is extrapolated across the peak, indicating the level of noise or ASE in the received signal. Integration under this line gives this value, which is then subtracted from the calculated total signal power. The same process is applied to the input signal spectrum in order to determine the contribution of source spontaneous emission (SSE), which is noise associated with the laser source. This is sufficient information to calculate the noise figure. The gain is first determined by comparing the total output signal power measured with the input signal, the power of which is already known. Both of these values are corrected for losses. The noise figure can then be calculated from the optical noise figure formula give in Eq. (2.12). Here, ρ_{ASE} is the ASE power spectral density that is *co-polarised* with the signal.

$$\rho_{ASE} = \frac{cP_{ASE}}{B}, \tag{3.13}$$

where P_{ASE} is the measured ASE power and B is the noise bandwidth, which in this case is taken to be the bandwidth of the signal. The correction factor *c* takes into account the percentage of ASE that is polarised in the same direction as the signal and the loss associated with the free space polariser.

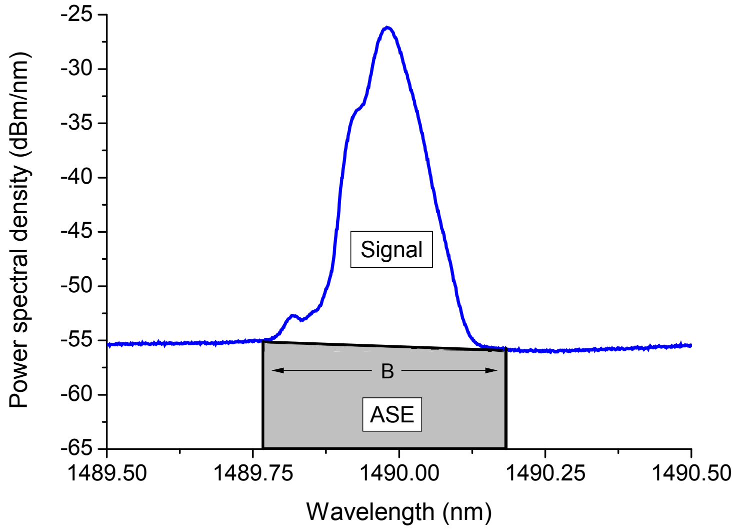

3.7. Output spectrum from SOA with signal injection recorded on optical spectrum analyzer. Indicated are the signal and the extrapolated ASE noise within bandwidth B.

3.5. Simulated and experimental characterization of LC-SOA

This section presents the results of both a simulated and experimental characterization of the lateral cavity SOA design in the static regime. The gain, saturation output power and noise figure of a CW input signal after amplification is determined and the device characteristics that are affected by the carrier density shaping are compared to the model.

3.5.1. Simulated characterization

In order to take into account the lateral lasing and its effect on the carrier density profile of the SOA, the carrier density rate equation Eq. (3.6) is modified to include a term to describe the interaction of the carriers with the laser photons, such that the rate equation can be written as,

$$\frac{dN_m}{dt} = \frac{i_m}{qV} - R(N_m) - v_g\left[g(\mu_{sig}, N_m) S_{m,sig} + g(\mu_{spon}, N_m) S_{m,spon} + \frac{L_{las}}{W} g(\mu_{las}, N_m) S_{m,las} \right] \tag{3.14}$$

where L_{las} is the length of the laser cavity, W is the active region width and $S_{m,las}$ is the laser photon density.

Reduction of ASE

Fig. 3.8 shows the effect of the gain clamping caused by the lateral laser. Two carrier density profiles are simulated, using a simulation with 20 subsections, both for a standard SOA and for the LC-SOA with the output half of the waveguide clamped by the lateral laser. The bias current supplied to each SOA is set to 250 mA. There is no signal injected in the SOA. The standard SOA exhibits the familiar symmetric carrier density profile, with some depletion of carriers at the facets due to higher ASE intensity in these regions. For the LC-SOA, the carrier density in the gain clamped regions is much reduced due to the consumption of carriers by the lateral laser. The level of this clamping is set by the reflection coefficient of the cavity. Conversely, the carrier density at the input of the LC-SOA has been increased relative to the standard SOA, although it is still possible to observe depletion due to ASE. This profile therefore is analogous to that in Fig. 2.10, which is designed to reduce the noise figure.

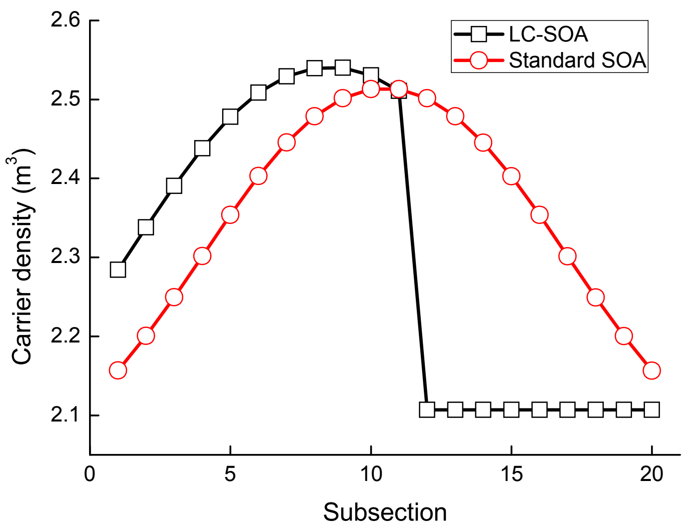

3.8. Carrier density profiles of LC-SOA and standard SOA, showing effect of gain clamping technique.

The carrier density at the input of the device is higher than that of the standard SOA because of the reduction in backward travelling ASE, which would otherwise deplete the carriers. This concept is illustrated in Fig. 3.9, which depicts the forward and backward travelling ASE intensity for both the standard SOA and the LC-SOA. The ASE for the standard SOA is symmetrical at both facets. However it is clear to see that in both forward and backward directions, the ASE is reduced for the LC-SOA as a result of the gain clamped output region. The ASE from the output facet of the LC-SOA is also reduced compared with the ASE emitted from the input facet.

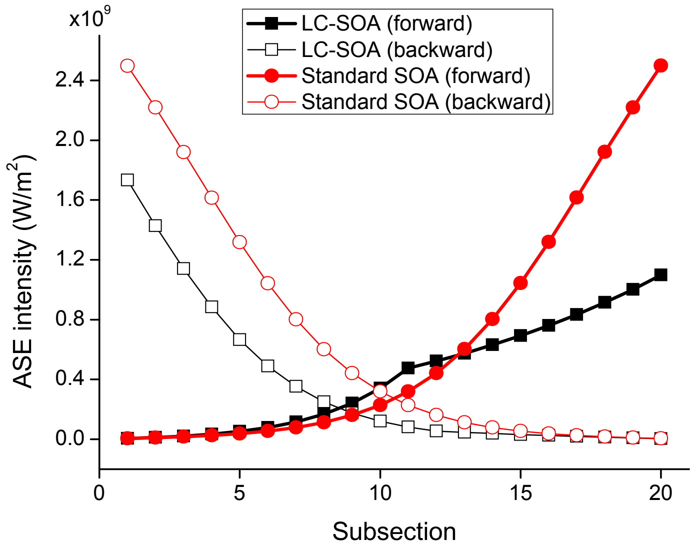

3.9. Evolution of forward and backward travelling ASE, for LC-SOA and standard SOA. ASE is reduced in both directions for LC-SOA. The bias current used in the simulation was 250 mA.

Steady state characterization

The extent of the lateral cavity over the length of the SOA has a significant effect on both the noise figure and gain properties. Fig. 3.10 (a) shows the variation of the noise figure as a function of the percentage of the SOA length under gain clamping conditions. It has been found that the best NF performance can be obtained with 40 - 70% of the waveguide clamped. The gain variation as a function of the cavity extent is also plotted, in Fig. 3.10 (b). The gain steadily reduces from its maximum when none of the waveguide is clamped (standard SOA) to its minimum when the entire waveguide is clamped, as in the case of a linear optical amplifier (LOA). The LC-SOA used in these experiments has a cavity extent of 55% of the active waveguide, which provides an acceptable trade-off between appreciable gain and low noise figure. As a portion of the waveguide is not clamped, and the carrier density within this region is free to increase with bias current, the LC-SOA displays a higher gain than the LOA.

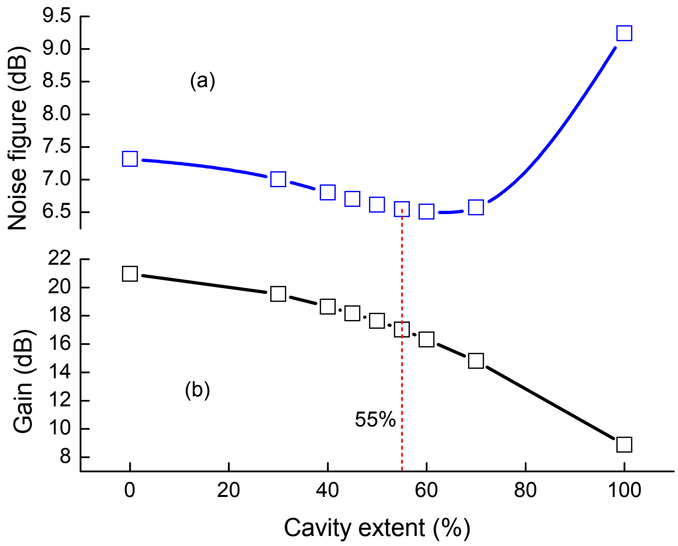

3.10. (a) NF for LC-SOA (input injection) for various values of cavity length (% of active region length) and (b) gain variation as a function of cavity extent. Input signal at 1500 nm, -30 dBm.

Fig. 3.11 depicts the noise figure of the LC-SOA, for both the input and output injection directions, and the standard SOA as a function of SOA output power. The characteristic shape of the NF curve for the standard SOA, as depicted in Fig. 2.12(a) in the previous chapter, can be seen here. Notably, at lower input powers, the NF of the modelled LC-SOA is much reduced compared with that of the standard SOA when the signal is injected at the facet with no cavity, with a difference in magnitude of about 0.8 dB, or almost 20%. Also interesting to note is that the NF of the LC-SOA is much higher when the signal is injected at the facet with the cavity. This is due to the low carrier density, and thus low population inversion factor, at the input of the device, increasing the overall NF in the SOA. The increase of NF at higher input powers is due to the depletion of carriers at the input facet. The subsequent increase in n_{sp} leads to a higher overall NF for the SOA.

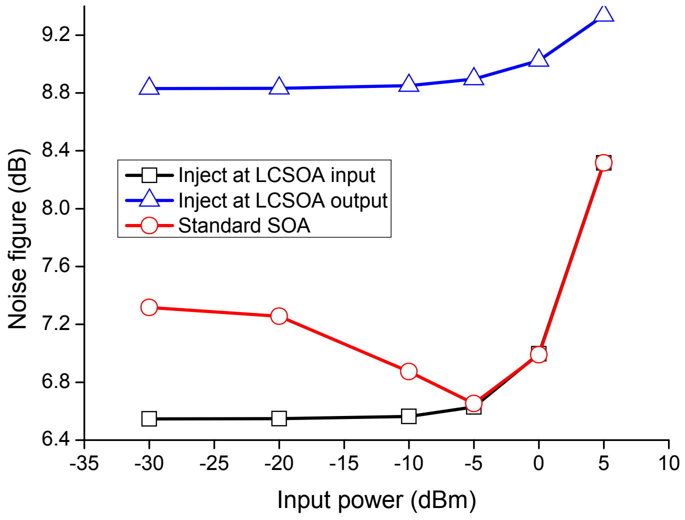

3.11. Noise figure as a function of input power for simulated SOA at 250 mA. Injected signal wavelength is 1500mA.

3.5.1. Experimental characterization

Non-injection characterization

The output ASE power of the SOA is measured, using an optical power meter, as a function of the bias current supplied. These data are plotted on an L-I curve, which is shown in Fig. 3.12. The power is measured from both the input facet and the output facet, which is the side with the embedded lateral cavity.

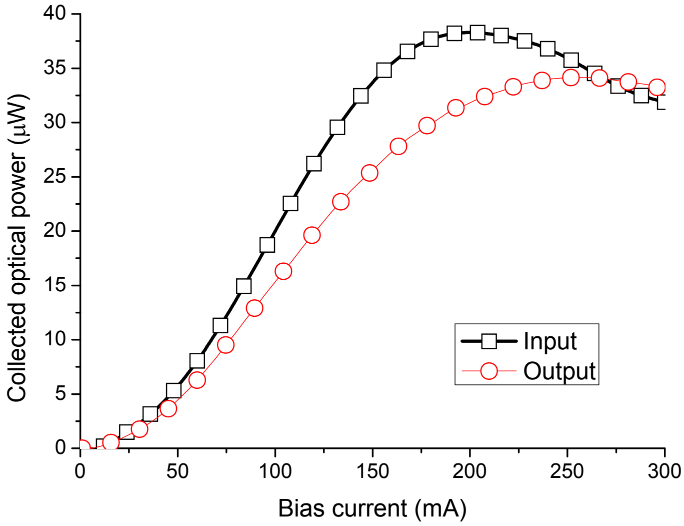

3.12. L-I curve of LC-SOA, measured from both input (no cavity) and output (cavity).

It is clear to see from Fig. 3.12 that the output ASE power from the facet without the lateral cavity is higher, indicative of the higher carrier density in this unclamped region of the SOA. This result corroborates the simulated data in Fig. 3.9. Also of note is the reduction of the ASE power measured at the input side as the bias current is increased past 200mA. Increased heating of the device is thought to be responsible for a reduction in gain, due to poor thermal bonding between the chip and the submount. Am additional cause of device heating could be that of excess heat trapped in the air between the Bragg layers. For this reason, the experimental characterization of the LC-SOA is performed at a maximum bias current of 250mA. Another important characteristic of the SOA in the non-injection regime is the amplified spontaneous emission spectrum. The ASE spectrum indicates the power spectral density of the ASE as a function of the wavelength. The peak of the ASE spectrum generally corresponds to the maximum of the material gain spectrum. To characterize the ASE, the output of the SOA was coupled to an optical spectrum analyzer with a resolution bandwidth of 0.06nm. Fig. 3.13 presents these results, taken at a bias current of 175mA, again measured from both the input and output facets. There is a measurable power difference between the spectra measured from the input facet compared to that of the output facet. In addition to this, the greater carrier density at the input facet leads to a wider ASE bandwidth. The ASE peak wavelength is 1497nm.

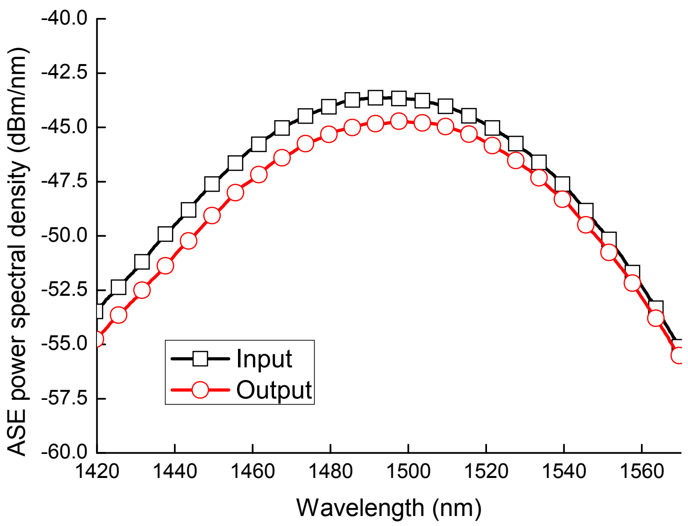

3.13. ASE spectra for LC-SOA, measured from input (no cavity) and output (cavity) facets at 175 mA bias current.

Steady state characterization

The gain spectrum of the LC-SOA as a function of the input signal wavelength is presented in Fig. 3.14. An input signal of -10dBm was injected to the SOA. The input modal mismatch was measured using the methodology described in Section 3.4.2, and was found to be ~ 5.5dB, which is relatively high for an SOA, where modal mismatches on the order of 3 dB are expected. The input modal losses as well as other setup losses added up to a total input loss of ~ 8 dB. The input coupling coefficient, defined in Eq. (3.12), is therefore 0.15. Consequently the input signal at the SOA facet is reduced to ~ -18dBm. The output modal mismatch is measured to be 5 dB, with the total loss equal to ~ 7 *dB*, a coupling coefficient of 0.19. The presented gain and noise figure values are corrected for the system losses and so represent chip values.

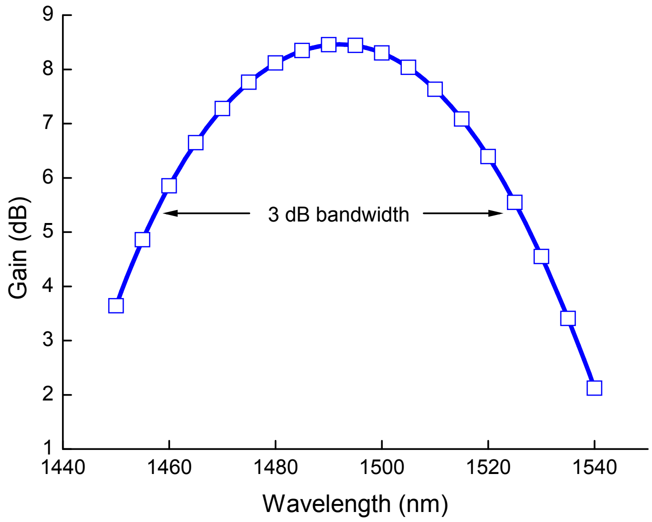

3.14. Gain spectrum of LC-SOA with respect to wavelength. Input signal power at SOA facet is -18 dBm, injected at input facet (no cavity).

The maximum gain measured is 8.5 dB at a central wavelength of 1492 nm, 5 nm from the ASE peak wavelength. The 3 dB bandwidth is measured as ~ 70 nm. The saturation power characteristics are shown in Fig. 3.15 below. The gain is plotted as a function of the input power for a wavelength of 1490 nm in Fig. 3.15a. The most obvious feature of this plot is the gain difference between input and output injection schemes. A possible explanation is that the presence of the slots reduces the refractive index immediately surrounding the active region. This could increase the confinement factor in this area and potentially introduce a directional dependent discrepancy in the facet loss. When the signal is injected at the input facet, the larger confinement in the area of the cavity increases the efficiency of the output coupling to the lens. This effect is absent when injecting from the output facet, where the signal experiences a lower confinement as it travels through the device. This discrepancy in output coupling causes a difference in the gain. When measuring the loss factors present in the setup, as per Section 3.4.2, this extra loss would not be measured and accounted for, as it occurs between the SOA and the coupling lens. As the extra loss occurs for the output coupling, it should not affect the noise figure measurement, which is dependent only on the input coupling loss.

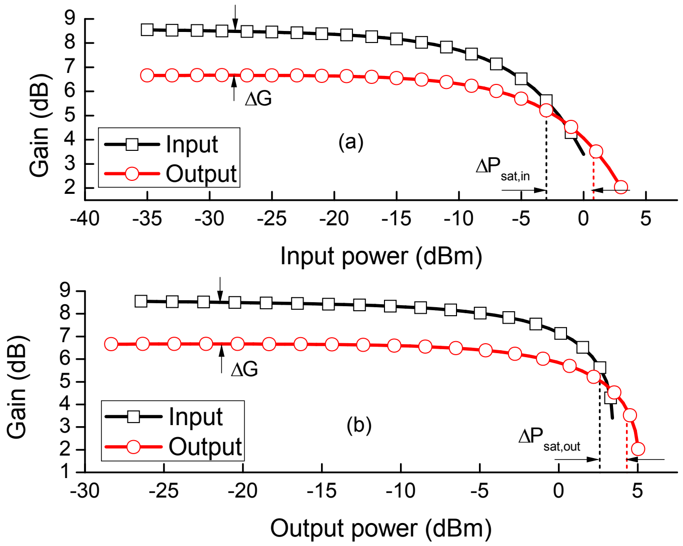

3.15. (a) Gain as a function of input signal power at 1490 nm and (b) gain as a function of SOA output power. 3 dB saturation powers are indicated by colour-coded dashed lines.

In order to examine the dimensions of the output beams from the SOA facets, a large area photodiode was used to measure the power from the SOA. It was placed on a 3-D translation stage which allowed it to obtain a profile of the output beam in both x and y directions. The step size of the stage is 2 µm. The photodiode was place at a working distance of 200 µm from the SOA facet. This distance was measured using a microscope with a calibrated micrometer scale. The starting point was set as the position of maximum signal in both axes. The results can be seen in Fig. 3.16. The probability density function (PDF) of the beam profile along the horizontal axis for both SOA facets is shown in the figure on the left, while that along the vertical axis is shown on the right. The beam profile from side 1, which is nominally the input facet, is shown in blue. The beam profile from side 2, which is the output facet, is shown in red. The lateral cavity is placed closest to the output facet. It is clear to see that the profile from the output facet is narrower than that of the input facet. The FWHM of the side 2 beam profile in the horizontal axis is 28.2 µm, compared with 31.1 µm for the side 1 profile. Similarly, the FWHM of the side 2 beam profile in the vertical axis is 17.5 µm, compared with 24.2 µm for the side 1 profile. These results indicate the possibility of a coupling loss discrepancy when coupled to the lens.

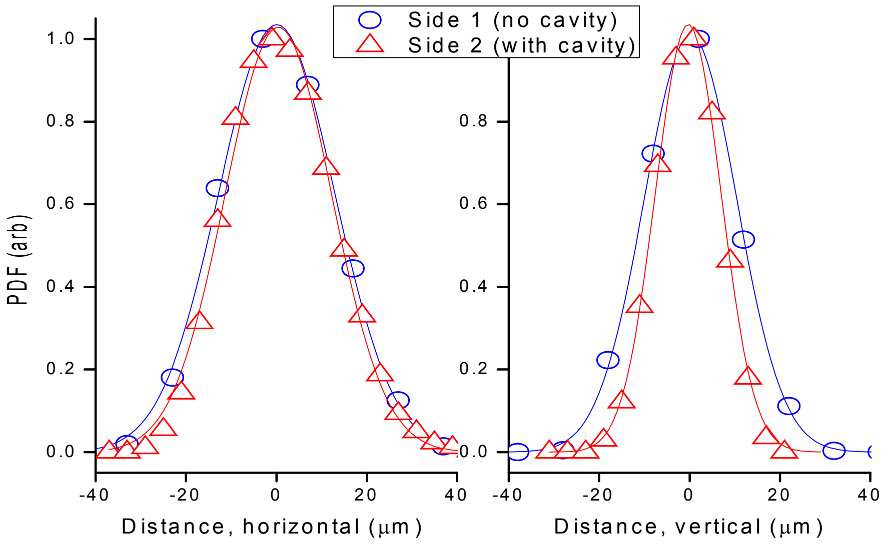

16. Probability density functions of beam profiles, measured at both SOA facets for both horizontal and vertical axes.

It can be seen from this Fig. 3.15 that the saturation power of the SOA is increased when the signal is injected at the output facet. The reason for this is that the carrier density profile experienced by the signal injected at the output is the high saturation power profile explained in Chapter 2. In the case of the LC-SOA, the input signal does not saturate the gain-clamped section of the amplifier, and the high carrier density at the input facet of the SOA created by the gain clamping scheme ensures that the signal can be linearly amplified in the this section as well. The effects combined increase the input power required to saturate the SOA, measured to be -3 dBm and 0.8 dBm for input injection and output injection, respectively. Similarly, in Fig. 3.15b, the saturation output powers are measured to be 2.54 dBm and 4.31 dBm, respectively. These results demonstrate a 1.77 dB increase depending on injection direction.

The key goal of the LC-SOA is to achieve control over the noise figure. Fig. 3.17 shows the noise figure plotted as a function of the signal wavelength, for signal injection at both the input and the output facet. The injected signal power is the same as that for Fig. 3.14, which was -18 dBm. Of particular note is the reduction in NF achieved through injection at the input. This discrepancy is due to the particular carrier density profile created by the lateral cavity scheme, as explained in the previous chapter. The minimum NF measured for the input injection scheme is 8.2 dB at 1500 *nm*, which is quite high. This value could possibly be explained by higher internal losses than expected, in addition to explaining the low gain value. The minimum NF of the output injection direction is 10.75 dB, which is 2.55 dB higher than that of the input injection direction. This is direct evidence of the effect of the lateral cavity on device parameters.

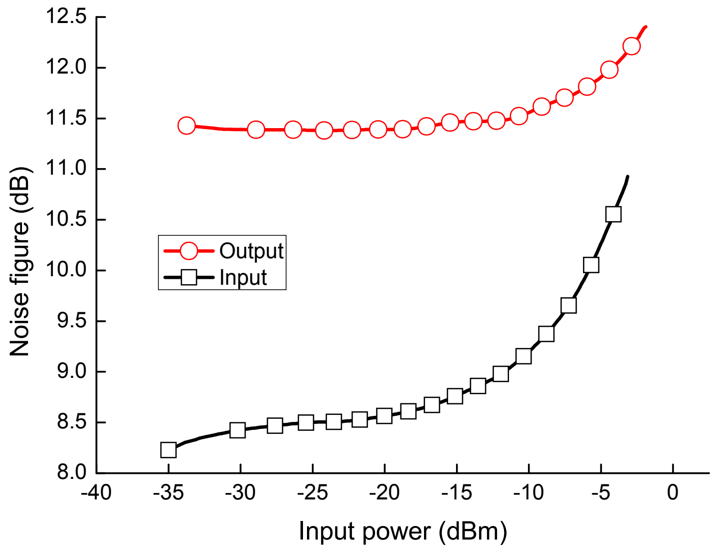

3.17. Noise figure of LC-SOA as a function of input signal power for both injection directions. Signal wavelength is 1490 nm.

Control SOA

In order to assess the noise figure performance of the LC-SOA vis-à-vis a standard SOA, an identical SOA from the same batch was characterized. This SOA does not have a lateral cavity embedded. The chip gain spectrum of the SOA with respect to wavelength is shown in Fig. 3.18a. The input power to the SOA is -18 dBm. As can clearly be seen, the performance of this SOA is not comparable to the LC-SOA. The maximum gain observable is 4.53 dB at a wavelength of 1487 nm. In addition to this, the minimum noise figure value of 11.54 dB seen in Fig. 3.18b is higher than that of the output injection scheme in the LC-SOA, which is counter to expectations from the simulated data. As a result of these measurements, the control SOA cannot be used for an accurate validation of the NF reduction achieved by the LC-SOA.

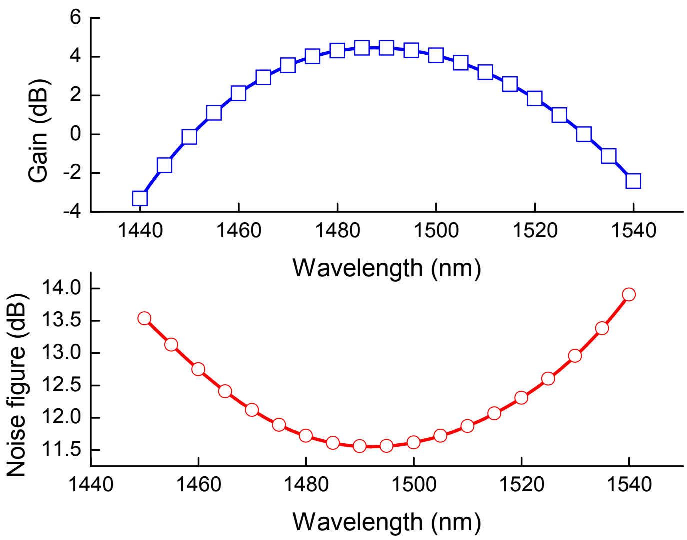

3.18. (a) Gain of control SOA as a function of input wavelength. (b) Noise figure of control SOA as a function of input wavelength. Input signal power is -18 dBm.

In conclusion, the results from both the simulated and experimental characterisation of the LC-SOA indicate that the NF can be varied through control of the carrier density distribution within the SOA. This is done through gain clamping with a lateral laser cavity. The experimental characterisation also indicates that saturation output power of the device can be improved by signal injection at the output facet. The overall values for gain and noise figure were below expectations, although it should be noted that the SOA is a prototype design. It is possible that the proximity of the Bragg structure to the active layer introduces a direction dependent loss due to altering the mode confinement. Other LC-SOA devices from the same batch with narrower lateral cavity exhibited performance worse than that of the presented device. This problem could potentially be addressed by further increasing the width of the lateral cavity.

3.6. Simulated and experimental characterization of MC-SOA

This section presents a study through simulation of the multi-contact SOA concept and its effect on the noise figure and saturation power of an SOA. Experimental results from the MC-SOA are then presented and the device characteristics are compared to those determined by the simulation. For the following data, the following terminology will apply. The carrier density profile for lowering noise figure is referred to as *low noise*, and indicates 80 mA, 50 mA, and 20 mA in the input, middle and output sections of the SOA for the simulated data, and 90 mA, 50 mA and 10 mA for the experimental data. The reason for the discrepancy in the bias current between the simulation and the real data is due to a difference in the transparency current in the low bias section between the simulation and the real device. The objective of the simulation is to identify the physical mechanisms of the parameter control process. The carrier density profile for increasing the saturation output power is referred to as *high* P_{sat}. The bias conditions for this profile are the opposite of the low noise profile. The third profile referred to is the *standard SOA* profile, which is created by injecting 50 mA into each contact.

3.6.1. Simulated characterization

Simulating separate contacts

An important difference between simulating the LC-SOA and the MC-SOA is that multiple injection currents must be taken into account. As the simulation models the SOA in subsections, an individual bias current can be specified for each one. Following on from this, groups of subsections are assigned to represent individually modelled electrical contacts / sections.

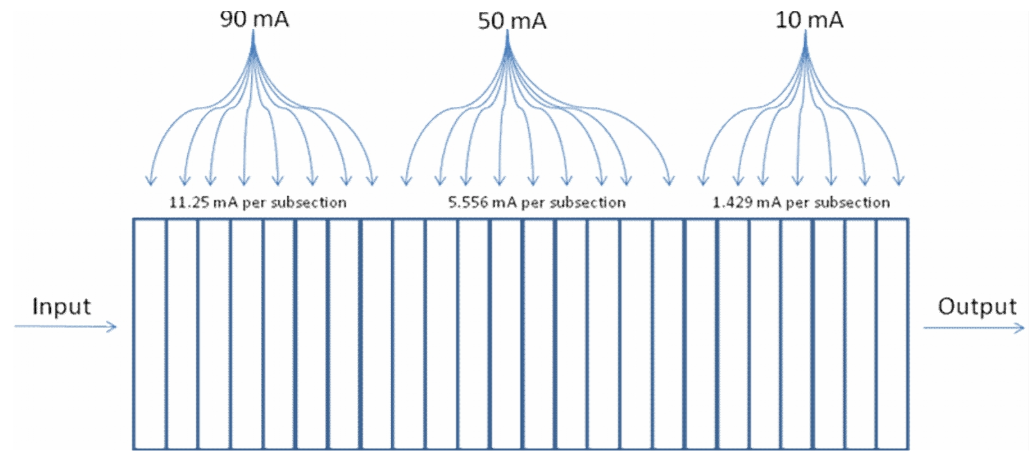

3.19. Schematic of bias current injection for 24 subsection model, assuming differing MC-SOA section sizes. 90 mA, 50 mA and 10 mA are the bias currents injected into the input, middle and output sections respectively in this example.

For example, in the case of modelling a 3 contact MC-SOA, with each contact being of equal size, a simulation that uses 12 subsections would assign 4 subsections to represent each contact. In the case of the MC-SOA under test in this work, the SOA sections are not of equal size. This fact has an important bearing on the characteristics of the device, relative to an SOA with equal section sizes, and must be accurately modelled. To do this, the number of subsections modelled is increased to 24. In this case, the 236 µm section is represented by 8 subsections, the 254 μm section by 9 subsections and the 210 μm section by 7 subsections. A schematic of this approach is shown in Fig. 3.19, above.

Evidence from model for parameter control

It has been predicted in the previous chapter that the carrier density profile used to achieve a low noise figure should lead to lower levels of ASE in the SOA, relative to a normal SOA, because the gain clamped / low bias sections cause an attenuation in the propagating spontaneous emission. An indication of this effect in the simulation is presented in Fig. 3.20, which shows both the forward and backward evolution of the spontaneous emission intensity within the SOA for the three bias configurations in question. The backward travelling ASE shown is representative of the spontaneous emission emanating from the output facet, and not the reflected forward travelling ASE, which is relatively low. The ASE is clearly attenuated for both the low noise and high P_{sat} configurations within their respective low bias sections, while the evolution of the ASE is symmetric for the standard SOA case. Of particular note is that in both the forward and backward directions, the total ASE intensity is reduced for both low noise and high P_{sat} profiles compared with the standard SOA profile. This phenomenon is a result of both the attenuation of the ASE in the low bias sections and the lower optical gain in these two configurations.

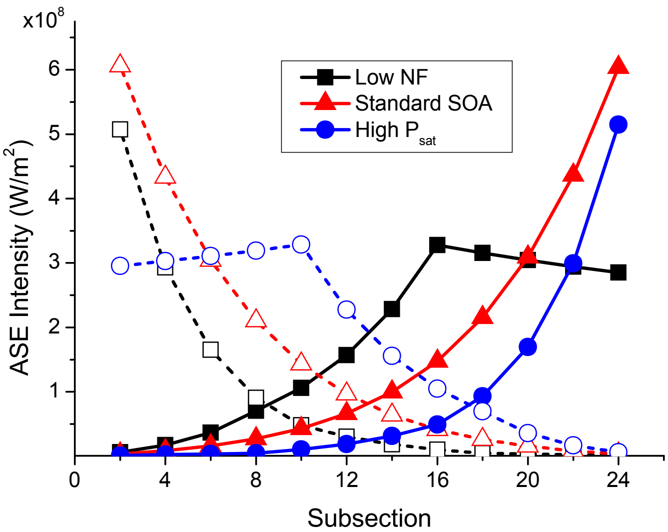

3.20. Evolution of ASE intensity along waveguide for both forward (solid) and backward (dash) traveling ASE, for 3 simulated bias conditions.

To achieve the lowest possible noise figure, the input section must be as highly pumped as possible. For this reason the input section of out modelled SOA is set to 80 mA injected current, and the middle and end sections are varied from 5 mA to 90 mA in steps of 5 mA. The resulting noise figure values are plotted on a colour map graph (Fig. 3.21) in order to illustrate the effect of the spontaneous emission.

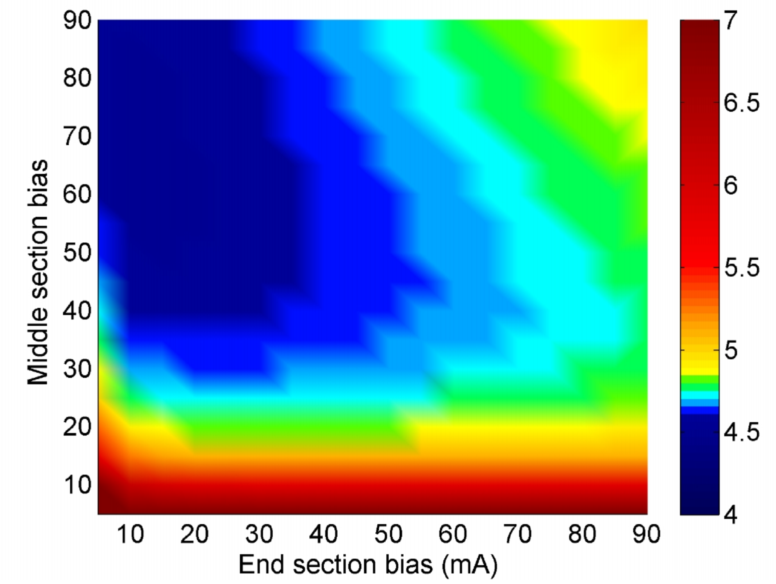

3.21. Colour map of noise figure values, given in colour coded scale on the right. Blue areas indicate lower NF, whereas red areas indicate higher NF. Input section bias is 80 mA.

The colour map indicates that for an input section bias current of 80 mA, the lowest noise figure values are obtained when the middle section bias is ~ 40 – 90 mA and the output section bias is ~ 10 – 30 mA. For a set total bias current of 150 mA, a reasonable configuration would seem to be 50 mA in the middle section and 20 mA in the output, which corresponds to the low noise configuration mentioned previously. The reason for this result has been covered in Chapter 2. As the bias current is increased, the role of spontaneous emission becomes more important. At high bias currents, backward travelling ASE, whether due to reflections or otherwise, depletes the carrier density of the input sections of the SOA, increasing the population inversion factor n_{sp} and thus increasing the NF.

The data shown in Fig. 3.22 shows the simulated evolution of the signal photon density for the three bias conditions as it propagates through the waveguide, in a similar manner to Fig. 3.20. The signal power and wavelength are 5 dBm and 1570 nm, respectively, in order to saturate the SOA. The optical gain in this figure can be imagined as the slope of the photon density. The reduction of the signal for the low noise profile is clearly evident in the final subsections as the signal photon density drops rapidly, indicative of the low carrier density in this region resulting in optical loss. A reduction in the slope of the standard profile curve is visible towards the output of the SOA, whereas for the high P_{sat} profile, the signal photon density increases sharply in the highly pumped final subsections, indicating that the gain remains unsaturated in this configuration.

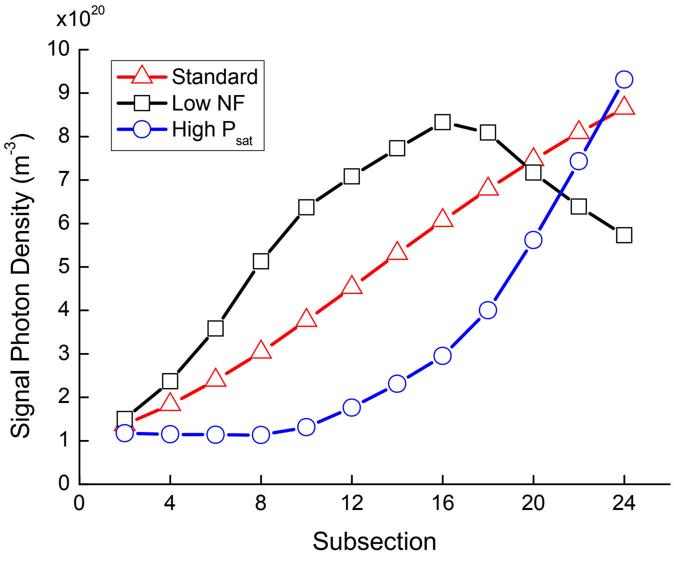

3.22. Photon density of input signal of 5 dBm as it propagates through waveguide, for three bias configurations.

Fig. 3.23 shows the simulated gain, noise figure and saturation power values for various bias conditions, again modelling an SOA with 3 contacts. The middle contact bias is held constant, and the bias conditions in the other two contacts are varied. A simulated signal of -15dBm power and 1570nm wavelength is injected for the gain and NF calculations. The maximum gain is observed while operating in the standard condition, i.e. that replicating a single contact SOA with equal current injection to all contacts. The magnitude of the gain decreases as the carrier density profile becomes less symmetrical. This effect is due to gain saturation at high bias, which is explained further on in this section. As expected, the NF is observed to decrease as the bias condition approaches that of the previously discussed low noise profile, and equivalently the saturation power increases for the opposite case. For the saturation power calculations, the signal power is increased to 5 dBm.

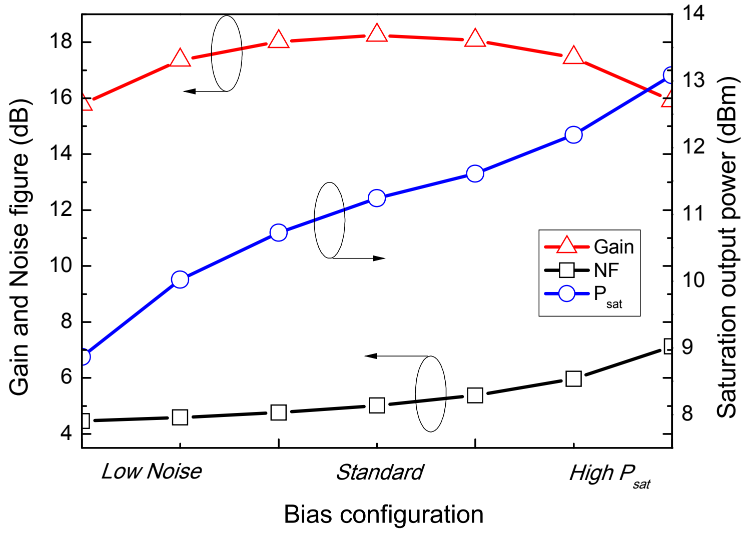

3.23. Simulated gain, noise figure and saturation power for various bias configurations.

Simulated steady state characterization

The steady state gain and noise figure values were calculated for the modelled multi-contact SOA for a range of input power, signal wavelengths and for the 3 bias current distributions under investigation. All values given for gain and NF are considered to be chip values and not fibre to fibre, as the model does not account for sources of optical coupling loss. In order to determine the gain spectrum of the MC-SOA as a function of the input wavelength, the signal wavelength was varied from 1540 nm to 1590 nm, given that the SOA is designed to operate in the 1550 nm region. The input signal power was chosen to be -15 dBm, which is within the linear amplification region of the SOA. The resultant gain spectra for the 3 bias configurations of interest are presented in Fig. 3.24. The maximum gain is observed with the standard SOA profile and is measured as 18 dB at a wavelength of 1550 nm. The maximum gain of the low noise and high P_{sat} configurations is 16.06 dB and 15.54 dB respectively at 1570 nm, a difference in gain of 0.52 dB. At low input power, it would be expected that the gain should be equal. This discrepancy is explained by the difference in the size of the individual contacts of the SOA, as explained further on in this section. These gain values were calculated at 1570nm.

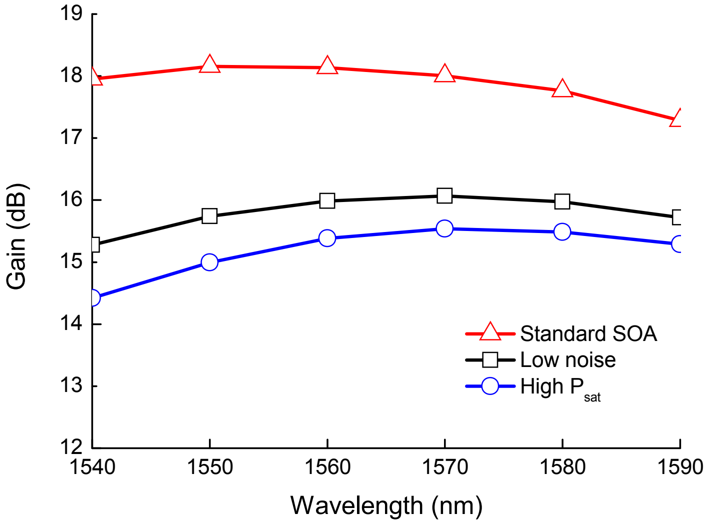

3.24. Simulated gain spectra for investigated bias conditions as a function of input signal wavelength. Input power is set to -15 dBm.

The blueshift of the gain peak in the standard SOA configuration relative to the other two is caused by the relative increase in band filling at this bias configuration. As the bias current is increased, the parabolic nature of the conduction band E-k diagram means that the lowest energy states are filled before higher energy states. Hence in low bias current conditions, such as those seen in the low noise and high P_{sat} configurations in the output and input sections respectively, the gain is more significant at longer wavelengths.

The noise figure spectra of the modelled SOA are shown in Fig. 3.25. The operating conditions are identical to those used to obtain the optical gain data in Fig. 3.24. The minimum NF determined by the simulation is 4.47 dB at 1570nm, for the low noise bias configuration. A reduction in the noise figure of 0.6 – 0.7 dB between the low noise configuration and the standard configuration is visible over the entire wavelength range in the simulated data, which corresponds to a reduction of over 12%. The noise figure for the high P_{sat} configuration is approximately 2.5 dB higher than that of the low noise case. The reason for this increase is due to the small bias current injected into the input facet, causing a high NF and thus increasing the NF of the whole device.

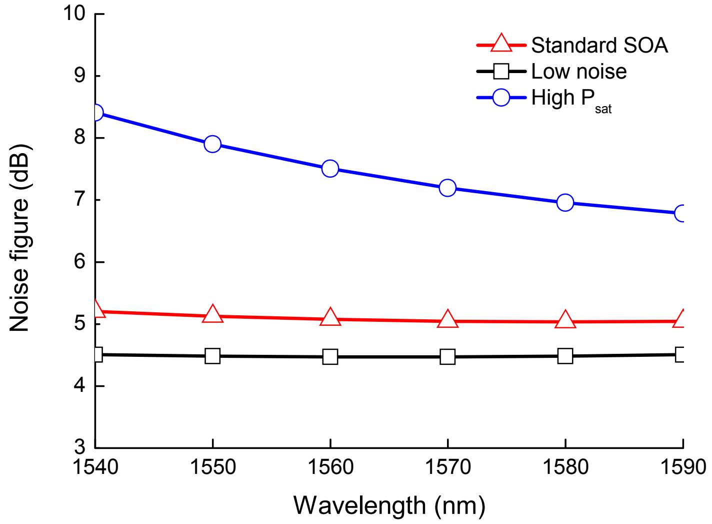

3.25. Simulated noise figure spectra as a function of signal wavelength.

The saturation input and output powers were obtained by calculating the gain as a function of input signal power. The signal wavelength was chosen to be 1570 nm, which is the gain peak wavelength for the low noise and high P_{sat} cases. The input power was varied from -30 dBm to 5 dBm. The results can be seen in Fig. 3.26a, which plots the optical gain as a function of the input signal power. According to the data presented here, the saturation of the gain occurs at much lower powers for both the standard and the low noise configuration compared with the high P_{sat} configuration. The input saturation powers are indicated on the graph in colour-coded dashed lines, and are calculated to be -5.44 dBm, -4.39 dBm, and -0.16 dBm for the low noise, standard and high P_{sat} configurations, respectively. The large difference in the saturation power is a strong indication that the linear increase in carrier density along the waveguide allows the gain to stay linear for a larger range of input powers. The difference in saturation input power is large enough such that the smaller gain experienced by the high P_{sat} configuration is not enough to diminish the saturation output power below that of the other two configurations. These data are presented in Fig. 3.26b, and follow a similar trend to that of Fig. 3.26a.

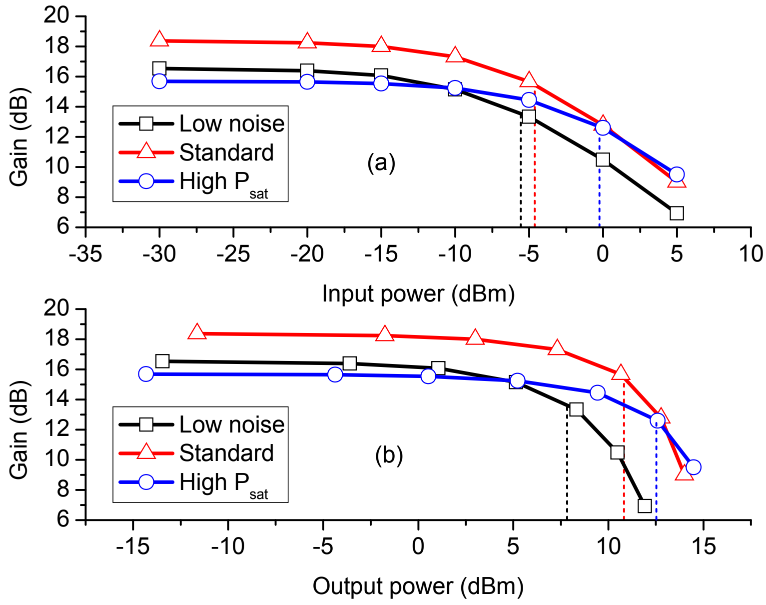

3.26. (a) Simulated optical gain as a function of input signal power, for three bias configurations; (b) Simulated optical gain as a function of SOA output power, for three bias configurations. For both figures, 3 dB saturation powers are indicated.

From Fig. 3.26b we can determine the saturation output powers to be 7.83 dBm, 10.82 dBm and 12.53 dBm for the low noise, standard and high P_{sat} bias configurations, respectively. This shows an increase in saturation output power of the high P_{sat} case of 1.72 dB, or 48%, over the standard case.

Effect of Contact Size

In addition to the magnitude of the current injected into the device, the relative size of the individual contacts impacts significantly on the characteristics of the SOA. As described previously, the multi-contact SOA under investigation has three contacts of slightly varying length. The consequence of this feature is that for a given injected bias current, average carrier density at a particular contact will vary depending on its size, and thus affect the gain and saturation properties of the overall device. The simulated results presented in Figs. 3.24 and 3.26 exhibit a similar trend with regard to the difference in gain observed between the low noise and high P_{sat} cases at low input power. In both cases the small signal gain for the low noise case is ~ 0.52dB higher than that of the high P_{sat} case. Fig. 3.27 demonstrates the explanation for this phenomenon.

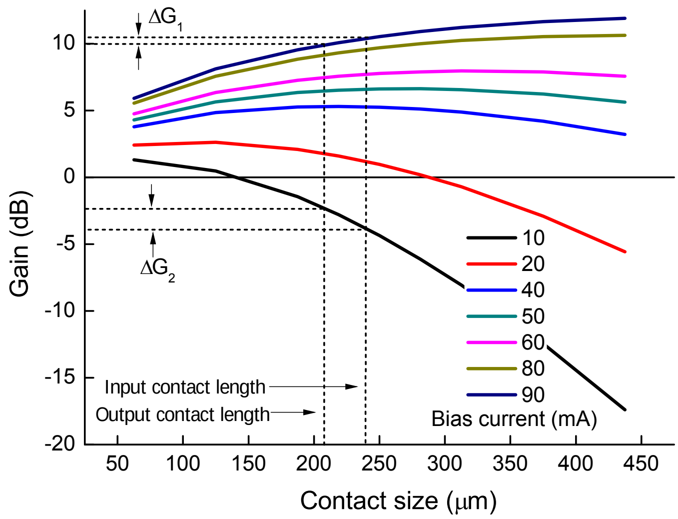

3.27. Gain vs contact size for various bias currents.

It is observed in simulation that as the size of the modelled contact increases, the gain is reduced for low bias currents, whereas for higher bias currents it is increased, as seen in Fig 3.27. For large contact sizes, a low injected bias current can mean that the carrier density is below transparency, that is, gain is below 0 dB. Conversely, the same bias current injected into a small contact leads to a larger average carrier density and thus larger gain. At the other end of the bias scale, gain saturation due to ASE as well as Auger and bi-molecular non-radiative recombination processes occurs sooner in small contacts. This is due to their higher average carrier density, whereas the lower average carrier density in the large contacts prevents saturation from occurring until far larger bias currents are injected.

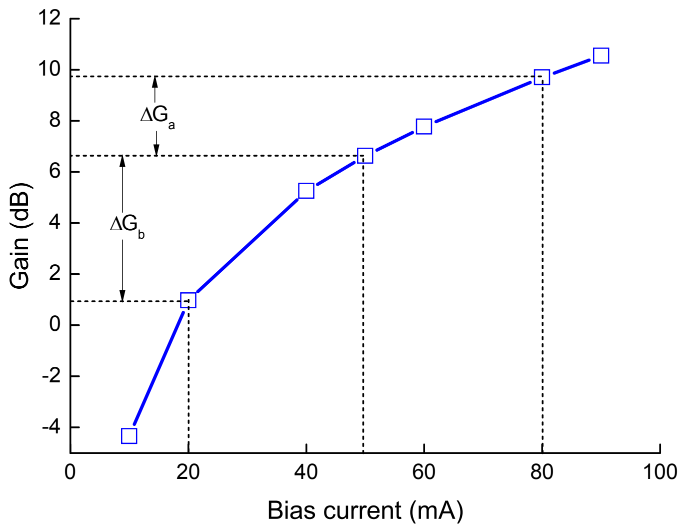

3.28. Gain vs bias current for a single contact.

The result of this behaviour can be seen in the SOA under investigation. For the low noise case, a large current is injected into the larger of the facet contacts, and thus leads to a higher gain than the equivalent high current contact in the high P_{sat} case, where this current is injected into the opposite, smaller contact. In Fig. 3.27 this difference in represented by ΔG_1. Similarly, for the low noise case, the small current is injected into the small facet contact, producing a higher average carrier density than for the equivalent low current contact in the P_{sat} case. This difference is represented by ΔG_2. Consequently, the gain for the low noise case is higher. The effect of the contact size on the characteristics of the SOA provides an additional flexibility in the design of the device. It should be noted that the non-linear variance in gain with bias in a single contact shown in Fig. 3.28 is due to the previously explained processes, and is the reason why the gain is higher for the standard bias configuration. As the bias current increases, recombination processes limit the increase in gain at high bias currents. Consequently, in either the low noise or high P_{sat} configurations, the larger gain experienced by the highly pumped area is not enough to compensate for the lower gain in the low bias portion of the device, and thus the overall gain is lower than that of an SOA with equally distributed current, i.e. $\Delta G_a < \Delta G_b$, as per Fig. 3.28.

.

3.6.2. Experimental characterization

Non-injection characterization

Before signals are injected into the MC-SOA in order to determine gain and noise figure, the basic non-injection characterization of the SOA is performed. Fig. 3.29 shows both the L-I and V-I characteristics of the MC-SOA. For this plot, the 3 individual sections are pumped in parallel from a single source, equivalent to a single contact SOA. The bias current indicated is therefore the total bias supplied to the device, while the voltage measured is that across all sections. The characteristic turn-on behaviour of the voltage can be seen as current begins to flow in the device. As the current is increased, the optical power rises steadily. However, between 100 and 150 mA, the power begins to drop off rapidly. As previously mentioned, this is thought to be due to increased heating of the device, resulting from poor thermal bonding of the chip to the submount.

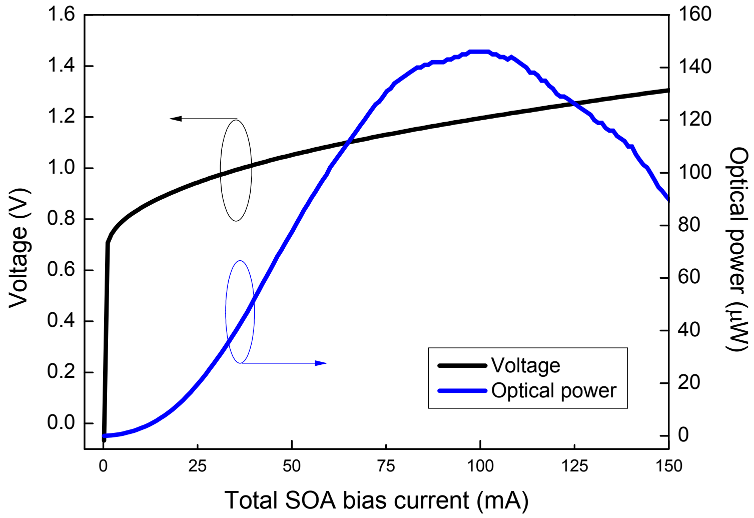

3.29. L-I and V-I curves for MC-SOA with all electrical contacts wired in parallel.

In Fig. 3.30, L-I and V-I curves are presented where the bias current in both the input and output sections is held constant at 33 mA, while the bias in the middle section is varied. In this case, the voltage across the middle section is non-zero at 0 mA bias current. This is likely due to a combination of the voltage applied across the input and output sections and the imperfect electrical isolation between the contacts. As the middle section bias is increased towards 80 mA, the total current in the device approaches 150 mA and the measured optical power begins to decrease, similar to the trend seen in Fig. 3.29.

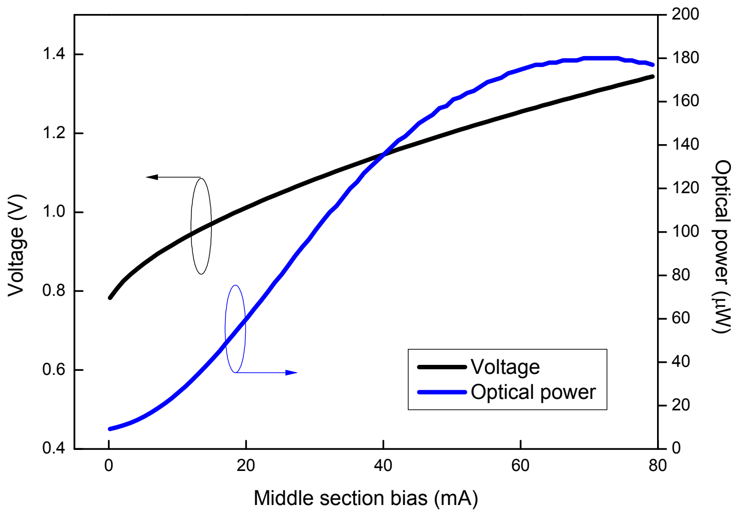

3.30. L-I and V-I curves for MC-SOA with input and output section biases of 33 mA and middle section bias varied from 0 – 80 mA.

Fig. 3.31 shows the ASE spectra for the 3 bias configurations. The standard configuration results in the largest emission of ASE, as is to be expected from the simulations which indicate that it should result in the highest gain. This dependence on gain is also supported by the fact that the ASE is consecutively lower for the low noise and high P_{sat} configurations. Inset in Fig. 3.31 is a close view of the ASE spectrum showing the Fabry-Perot ripples caused by the residual facet reflectivity. These ripples are approximately 0.2 dB peak to peak, so effectively the MC-SOA can be considered a travelling wave amplifier. The OSA resolution bandwidth for measuring the ASE ripples was 0.02 nm.

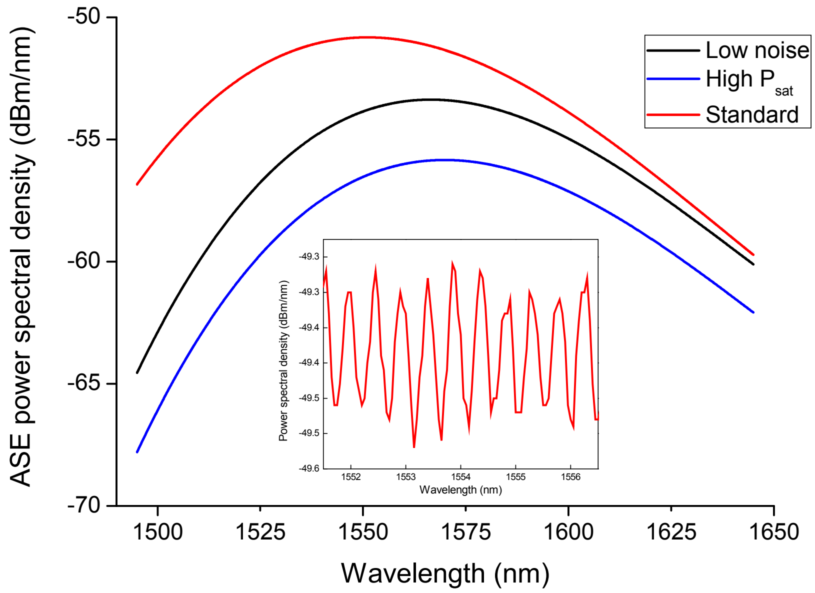

3.31. ASE spectra of MC-SOA for 3 bias configurations. Inset: Fabry Perot ripples in ASE spectra, taken at 0.02 nm resolution bandwidth.

Steady state characterization

The gain and noise figure of the MC-SOA are experimentally determined for a range of input signal wavelengths and powers. The input and output coupling coefficients are measured using the technique outlined in Section 3.4.2. The input loss due to the modal mismatch between the fibre and SOA modes is calculated as ~ -3 dB. The additional losses in the setup increase the input loss, the final input coupling loss determined to be ~ -5 dBm. The input coupling coefficient, defined in Eq. 3.12, is therefore 0.32. Similarly, the total output losses are determined to be -6 dBm, giving a coupling coefficient of 0.25. The chip gain characteristics are measured as a function of the input signal wavelength, which is varied, as in the simulated characterization, from 1540 nm to 1590 nm. The signal power is set to -10 dBm, giving an input power at the SOA facet of -15 dBm. The results are presented in Fig. 3.32. Similarly to the simulated data, the maximum gain is observed in the standard bias configuration, and is measured to be 17.5 dBm at a wavelength of 1562 nm. The maximum gain measured for the low noise and high P_{sat} configurations is 15.05 dB and 14.25 dB, respectively, at 1570 *nm*. As with the simulated characterization, there is a difference in gain between the low noise and high P_{sat} configurations, in this case 0.8 dB. This discrepancy has been explained previously as a result of the difference in the SOA section sizes. The difference in the maximum gain wavelengths for the individual bias configurations can be explained by the blueshift in the material gain spectra at higher carrier density. This blueshift is also visible in the ASE spectra in Fig. 3.31. The 3 dB bandwidth of the gain in the standard bias configuration is measured to be 57 nm.

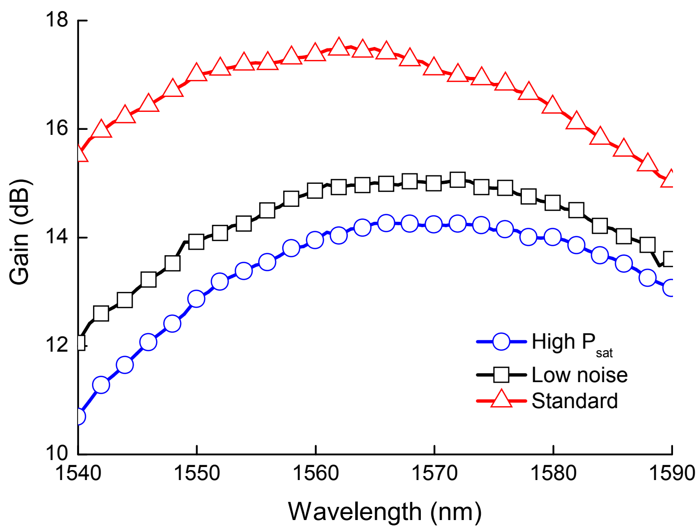

3.32. Chip gain as a function of input signal wavelength for 3 bias configurations.

The chip noise figure spectra as a function of input signal wavelength is shown in Fig. 3.33. Of particular note in this plot is that lack of significant difference between the NF of the low noise configuration and that of the standard configuration. The measured difference of 0.2 dB is within experimental error. This unexpected result is thought to be caused by the leakage of carriers between sections due to the small resistance of the slots between the contacts, which is 300 Ω. It is anticipated that an increase in the slot resistance could produce a measureable reduction in the noise figure of the low noise configuration. The measured chip NF of the low noise case is 5 dB at 1568 nm, which is comparable and superior to many commercial SOAs. Additionally, the difference in NF between the low noise configuration and the high P_{sat} configuration is measured to be 1.5 dB at 1570 nm.

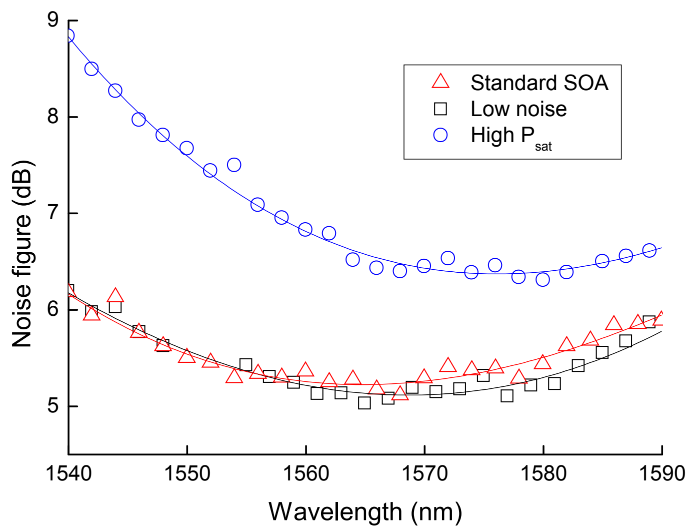

3.33. Chip noise figure spectra as a function of input signal wavelength.

This result demonstrates the effect of the carrier density profiles on the SOA noise figure. The tunability of the device characteristics depending on the carrier density profile is evident in Fig. 3.34, which plots the saturation characteristics of the MC-SOA.

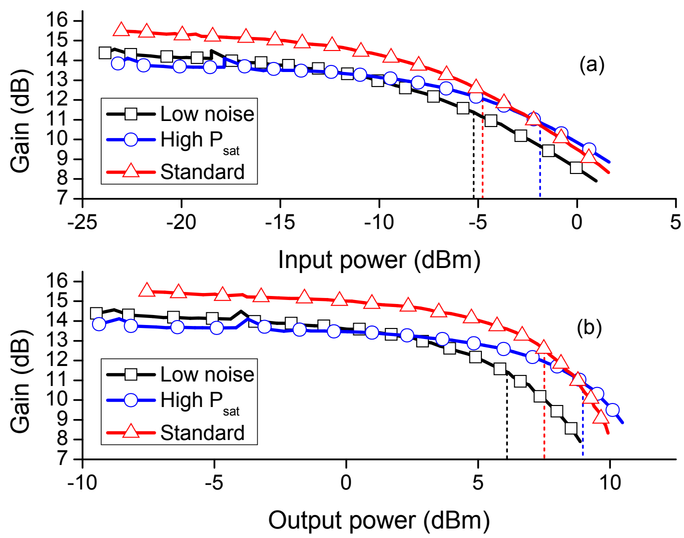

3.34. (a) Chip gain as a function of input signal power, at input wavelength 1570 nm; (b) Chip gain as a function of SOA output power, at input wavelength 1570 nm. For both figures, 3 dB saturation powers are indicated by dashed lines.

Fig. 3.34a shows the chip gain as a function of the input power. The input signal wavelength is 1570 nm. The 3 dB saturation input powers are indicated by the colour-coded dashed lines. It should be noted that the gain of the standard configuration in this plot is lower than the peak gain, as the peak gain wavelength in this bias configuration is closer to 1550 nm. The trend observed is identical to that of the simulated data. The low noise configuration saturates at the lowest input power, -5.23 dBm, due to the small bias current in the output section, where the signal intensity is highest. The standard configuration saturates at a similar input power, -4.75 dBm, mainly due to the increased gain in this configuration causing saturation in the output sections of the SOA. However, due to the high carrier density in the final sections, which reduces the carrier lifetime, the high P_{sat} configuration saturates at an input power of -1.83 dBm. The input saturation power is dependent on the SOA gain in that a higher gain causes the strongly amplified signal to saturate the SOA earlier along the waveguide. Accordingly, at a wavelength of 1540 nm, which is closer to the standard bias gain peak, the input saturation power of the low noise and high P_{sat} configurations are increased to -3.32 dBm and 0.71 dBm, respectively. Conversely, the input saturation power of the standard bias configuration is reduced slightly to -4.88 dBm. Fig. 3.34b shows the saturation output power for injection at 1570 nm. The measured powers are 6.08 dBm, 7.53 dBm and 9 dBm for the low noise, standard and high P_{sat} configurations, respectively. It should also be noted that the greater negative slope of the gain curve of the standard bias configuration suggests that gain saturation for this case would be greatest at higher input powers than were used in this experiment. Although the saturation input powers measured in the experimental characterization are similar to those in the simulation, the lower gains measured for the experimental data reduce the saturation output power relative to the simulation. Nonetheless, an increase of ~ 1.5 dB, or 40%, has been achieved by shaping the carrier density profile in the device.

3.7. Summary

In this chapter, two proposed SOA designs for controlling noise and saturation parameters were outlined. The devices in question, namely an SOA employing a lateral laser cavity for clamping the carrier density at the SOA output (LC-SOA), and an SOA with multiple electrical contacts (MC-SOA) were characterized both experimentally and theoretically. The structure of the simulation that was used to model the SOAs was outlined. The SOA characteristics and the processes behind the parameter control were simulated and presented. A description of the experimental characterization of the SOAs was then given, along with the results from this characterization. It has been found theoretically that the LC-SOA concept has the potential to reduce the NF as compared to a standard SOA. Experimentally, injecting a signal from either facet of the LC-SOA yielded different values for the noise figure, suggesting that the carrier density engineering has an effect. However, the characteristics of the control SOA used for comparative purposes were not comparable to the LC-SOA in terms of gain, which is not what was expected. Thus, it was not possible to experimentally verify the expected reduction in noise figure. With regards to the MC-SOA, simulated results suggested that great flexibility could be achieved in terms of controlling the parameters of the device. By varying the bias current distribution, the noise figure could be reduced, or conversely the saturation output power increased. The experimental characterization revealed that the noise figure reduction over a standard SOA was less than expected. A possible reason for this might lie in an inadequate slot resistance between the SOA sections, leading to carrier leakage. A large increase in saturation power over a standard SOA was observed in the experimental characterization. These results, combined with potential improvements to the SOA design, suggest that the MC-SOA could be a flexible low noise or high saturation power component for in-line amplification.

References

[1] Manning, R.J.; Davies, D.A.O.; "Three-wavelength device for all-optical signal processing," *Optics Letters*, Vol.19, No.12, pp.889-991, Jun 1994.

[2] Brenot, R.; Pommereau, F.; Le Gouezigou, O.; Landreau, J.; Poinet, F.; Le Gouezigou, L.; “Experimental Study of the Impact of Optical Confinement on Saturation Effects in SOA”, *Proc. Optical Fiber Communications Conference*, 3 pp., Vol. 1, 6-11 Mar 2005.

[3] Landais, P.; Surre, F.; “A semiconductor optical amplifier for amplifying an optical signal,” UK patent GB0821602.0, Nov. 26, 2008.

[4] Landais, P.; Surre, F.; “A semiconductor optical amplifier for amplifying an optical signal,” US patent 2010/0134877A1, Jun. 3, 2010.

[5] Doussiere, P.; Jourdan, A.; Soulage, G.; Garabedian, P.; Graver, C.; Fillion, T.; Derouin, E.; Leclerc, D.; "Clamped gain travelling wave semiconductor optical amplifier for wavelength division multiplexing applications," *14th IEEE International Semiconductor Laser Conference*, pp.185-186, 19-23 Sep 1994.

[6] Guiliani, G.; D’Alessandro, D.; “Noise analysis of conventional and gain-clamped semiconductor optical amplifiers”, *Journal of Lightwave Technology*, Vol.18, No.9, pp. 1256, Sep 2000.

[7] Francis, D.A.; DiJaili, S.P.; Walker, J.D.; “A single-chip linear optical amplifier”, *Optical Fiber Communication Conference*, 2001 OSA Technical Digest Series, paper PD13.

[8] Carney, K.; Lennox, R.; Maldonado-Basilio, R.; Philippe, S.; Bradley, A.L.; Landais, P.; “Noise Controlled Semiconductor Optical Amplifier based on Lateral Cavity Laser”, *Electronics Letters*, Vol. 46, No. 18, pp. 1288-1289, Sep. 2010.

[9] Hill, K.O.; Meltz, G.; “Fiber Bragg Grating Technology Fundamentals and Overview”, *Journal of Lightwave Technology*, Vol. 15, No. 8, pp. 1263-1276, Aug. 1997.

[10] Lennox, R.; Carney, K.; Maldonado-Basilio, R.; Philippe, S.; Bradley, A.L.; Landais, P.; “Impact of Bias Current Distribution on the Noise Figure and Saturation Power of a Multi-Contact Semiconductor Optical Amplifier”, *Optics Letters*, Vol. 36, No. 13, pp. 2521-2523, Jul. 1, 2011.

[11] Shanshan Zhu, Lirong Huang, Yu Chen, “Gain spectrum control in Multi-Electrode Semiconductor Optical Ampifiers”, *Proc. SPIE* 7278, 72781V (2008).

[12] Moll, E.; Chai, Y.J.; Williams, K.A.; Penty, R.V.; White, I.H.; “Optimization of twin-contact semiconductor optical amplifiers for use in integrated interferometric devices”, *Proc. SPIE* 5723, 209 (2005).

[13] de Valicourt, G.; Maké, D.; Landreau, J.; Lamponi, M.; Duan, G.H.; Chanclou, P.; Brenot, R.; “High Gain (30 dB) and High Saturation Power (11 dBm) RSOA Devices as Colorless ONU Sources in Long-Reach Hybrid WDM/TDM-PON Architecture”, *IEEE Photonics Technology Letters*, Vol. 22, No. 3, Feb. 1, 2010.

[14] Tromborg, B., Olesen, H., Xing Pan, Saito, S., “Transmission line description of optical feedback and injection locking for Fabry-Perot and DFB lasers”, *IEEE Journal of Quantum Electronics*, Vol. 23, No. 11, pp. 1875-1889, Nov. 1987.

[15] Adams, M.J.; Collins, J.V.; Henning, I.D.; “Analysis of Semiconductor Laser Optical Amplifiers”, *IEE Proceedings Journal of Optoelectronics*, Vol. 132, No. 1, pp. 58-63, Feb. 1985.

[16] Durhuus, T.; Mikkelsen, B.; Stubkjaer, K.E.; “Detailed Dynamic Model for Semiconductor Optical Amplifiers and their Crosstalk and Intermodulation Distortion”, *Journal of Lightwave Technology*, Vol. 10, No. 8, pp. 1056-1069, Aug. 1992.

[17] Connolly, M.J.; “Wideband Semiconductor Optical Amplifier Steady-State Numerical Model”, *IEEE J. Quantum Electron.*, Vol. 37, No. 3, pp. 439-447, Mar. 2001.

[18] Leuthold, J.; Mayer, M.; Eckner, J.; Guekos, G.; Melchior, H.; Zellweger, Ch.; “Material gain of bulk 1.55μm InGaAsP/InP semiconductor optical amplifiers

approximated by a polynomial model", *Journal of Applied Physics*, Vol. 87, No. 1, pp. 618-620, Jan. 2000.

[19] Friis, H.T.; "Noise Figures of Radio Receivers", *Proc. of the IRE*, Vol. 32, No. 7, pp. 419-422, Jul 1944.

[20] Baney, D.M.; Gallion, P.; Tucker, R.S.; "Theory and Measurement Techniques for the Noise Figure of Optical Amplifiers", *Optical Fibre Technology*, Vol. 6, No. 2, pp. 122-154, Apr. 2000.

[21] Briant, T.; Grangier, P.; Tualle-Brouri, R.; Bellemain, A.; Brenot, R.; Thedrez, B.; "Accurate Determination of the Noise Figure of Polarization Dependent Optical Amplifiers: Theory and Experiment", *Journal of Lightwave Technology*, Vol. 24, No. 3, pp. 1499-1503, Mar. 2006.

4. CHARACTERISTICS OF MULTI-CONTACT SOA FOR IN-LINE AMPLIFICATION

4.1. Introduction

4.1.1. SOAs as amplifiers in optical networks

The previous chapters outlined the theoretical basis for the SOA designs under investigation in this thesis, as well as a study of their experimental characteristics. These characteristics are important indicators of how the SOA will perform in a real-life linear transmission system. SOAs have been shown to be viable as amplifiers in certain wavelength division multiplexed (WDM) networks, when the total input power is kept below the saturation power of the SOA [1]. While SOAs generally do not compete with EDFAs when it comes to high channel count long haul WDM transmission, their lower cost makes them attractive for use in shorter distance, metro and access networks, that may have a much reduced channel count compared to long haul networks [2]. SOAs also have an important advantage over EDFAs in terms of in-line amplification of packet switched data, as their gain dynamics take place at the speed of the bitrate, and so exhibit none of the transient effects displayed by EDFAs. The desired attributes of the SOA depend on the function that it is used for, whether that is amplifying weak or strong signals, single or multiple channels, et cetera. For example, a potential application for in-line amplification by SOAs is in reach extension for passive optical networks (PON), which is a type of network design in which a single optical line terminal in a central office serves multiple end users via a single fibre and a network of passive splitters [3]. The downstream transmission wavelength of PONs is generally in the 1550 nm window, whereas upstream transmission takes place in the 1310 nm window. SOAs are ideally suited to both wavelength ranges, due to the tunability of their material composition. An SOA with a high saturation power would be suitable for extending the range of the PON downstream transmitter, whereas SOAs with low noise figure are necessary for effective amplification of weaker upstream signals. The effect of the multi-contact SOA in both the low power and high power amplification regimes is characterized in this chapter.

The effects of SOA gain saturation in particular are especially important when amplifying short optical pulses. Due to the strong coupling between gain and refractive index changes, gain saturation in SOAs can lead to significant spectral distortion of optical pulses. The impact of the bias current distribution on both the temporal and spectral characteristics of these pulses is characterized in the Section 4.3.

4.1.2. SOA requirements for in-line amplification

In linear transmission systems, unlike when SOAs are used for wavelength conversion applications, the limiting factors are the noise figure and the saturation power [4]. The influence of one or the other depends on the whether the SOA is used as an in-line amplifier, a preamplifier or a booster amplifier.

In-line repeaters

Before the development of optical amplifiers, the attenuation of optical signals transmitted over long distances had to be compensated for by terminating the signal at a photodiode, amplifying it electrically, and then retransmitting. This process, in addition to having transparency issues, has a major disadvantage in that the equipment needed for it is inherently expensive. The advent of optical amplifiers made these electrical repeaters obsolete, as the optical signal could now be amplified instantaneously in the optical domain. As has been mentioned previously, the amplifier of choice for long haul transmission has been the EDFA, due to its long lived gain dynamics and low noise figure. As well as EDFAs, Raman amplifiers and linear optical amplifiers (LOAs) have been studied for WDM transmission [5, 6]. SOAs have also been shown to fulfil this role [7], for single channel and multichannel amplification, either through keeping the total injected power below the SOA saturation point, or through the use of novel schemes such the use of an optical reservoir channel [8]. Because of the ability to tune the operating bandwidth by altering the material composition of the device, SOAs are the most suitable technology for in-line amplification in Coarse Wavelength Division Multiplexing (CDWM) schemes, where the signal wavelengths are outside the amplification bandwidth of EDFAs [9]. In the case of a long haul transmission link, numerous amplifiers would be used in a cascade. In this case, the Friis transmission equation for noise figure (Chapter 2 and Chapter 3) would apply, whereby the amplifier with the lowest noise should be placed first in the chain. In the case where noise power builds up from multiple cascaded SOAs, the gain can saturate due to ASE. The total number of SOAs can be used in an amplifier cascade before noise saturation is given by [10],

$$k_{\max} = \frac{P_{o,sat}}{2n_{sp}h\nu\eta_{out}\left(\frac{G}{\eta_{in}\eta_{out}} - 1\right)B_0} \tag{4.1}$$

where $P_{o,sat}$ is the saturation output power of the amplifiers, n_{sp} is the population inversion factor, G is the gain of the SOAs, B_0 is the optical filter bandwidth, and η_{in} and η_{out} are the input and output coupling losses. The dependence on both $P_{o,sat}$ and n_{sp} suggests that both the noise figure and the saturation output power are important parameters for in-line amplifiers, depending on where the are placed in the amplifier chain.

Pre-amplifiers

SOAs can be used to boost the power of a weak signal prior to detection by a photodetector [11, 12, 13]. A key advantage is that they can be integrated with photodetectors in one package [14, 15], saving on cost and footprint. Receiver sensitivity can be greatly improved when the signal is optically preamplified, compared to an avalanche photodiode (APD) alone, when used in non-coherent direct detection schemes. The crucial parameter for an SOA preamplifier is the noise figure. Since the optical signals being amplified have a low power, there is little to no suppression of the ASE, and thus signal spontaneous beat noise plays an important role. The lack of ASE suppression means that an optical filter must be used in order to block the broadband noise from the SOA. If the polarization state of the signal is known, a polarizer may be used to pass only the co-polarized ASE, improving the photodetector sensitivity by 3 dB. However, this is usually not the case. The fact that low power signals are being amplified means that SOA preamplifiers should have an appreciable gain.

Booster amplifiers

Booster amplifiers are typically used immediately following a laser transmitter, in order to boost the power prior to transmission [16]. This allows the deployment of greater stretches of fibre without the need for optical or electrical repeaters, cutting down on costs and increasing reliability. Due to the high input powers encountered by booster SOAs, the saturation output power is a crucial design factor [17]. The greater this parameter, the greater the distance the signal can travel, unamplified. The use of SOAs in WDM transmission applications is reliant on the SOA having a high saturation power.

This is because the saturation of the SOA is determined by the *total* power injected into it, i.e. the sum of the powers of the individual WDM channels. It is necessary to operate the SOA in the linear regime for amplifying WDM signals in order to avoid non-linear distortions, such as intermodulation distortion due to four wave mixing of the WDM channels. Quantum dot SOAs have attracted a significant amount of attention as booster amplifiers due to the high saturation output powers that they display [18, 19].

4.2. Data transmission using MC-SOA

4.2.1. Introduction

Errors can occur in the detection of optically transmitted signals because of a number of factors. As previously stated, the limiting factors with regard to SOAs in linear transmission systems are noise figure and saturation power. Generally, at low optical power, the noise figure of the SOA is the critical factor. When an optical signal is incident on a photodiode, a small current is generated. This current is subject to distortions arising from various factors such as the photodiode dark current, thermal noise and statistical gain fluctuations for avalanche photodiodes. Importantly, in the case of SOAs, they are subject to beat noise due to the interaction of spontaneous and signal photons in the SOA itself (Chapter 2). A decision circuit after the photodiode compares the received electrical signal to a reference voltage, known as the threshold voltage. The level of the received signal with respect to this voltage determines whether a 1 or a 0 was transmitted. The various sources of noise in the system give rise to fluctuations in the signal. If these fluctuations are strong enough, a transmitted 1 can be detected as a 0, and vice versa. In the case of a high power signal amplified through an SOA, gain saturation causes inter-symbol interference (ISI), which generally can cause a transmitted 1 to be detected as a 0, since it has been compressed in the SOA due to the reduction in gain. In this section the impact of the bias distribution in the multi-contact SOA on the detected errors in a linear transmission system will be examined, for both low optical power and high optical power. The data to be used in the experiment is coded in non-return to zero (NRZ) format, which is an amplitude modulation scheme whereby the transmitted bit occupies an entire bit time slot.

4.2.2. Analysis of signal quality

It is necessary to assess the quality of an optical transmission system in order to identify faults and sources of noise in the link. This can be done by tapping the signal at a point along the line and analyzing it using an oscilloscope or network analyzer, or by analyzing it at the receiver end of the line. In order to analyze the impact of the MC-SOA on the integrity of the transmitted signal, the eye diagrams of the signal is examined and the bit errors are counted using a bit error rate tester.

Eye diagram

A convenient way to assess the quality of a data signal is the eye diagram. An eye diagram consists of a series of oscilloscope traces of a modulated signal, repetitively sampled, and then superimposed on top of one another. It is an intuitive way to visualize the various factors that impair data transmission [20]. The centre region of the eye diagram (the "eye") is a measure of the signal integrity.

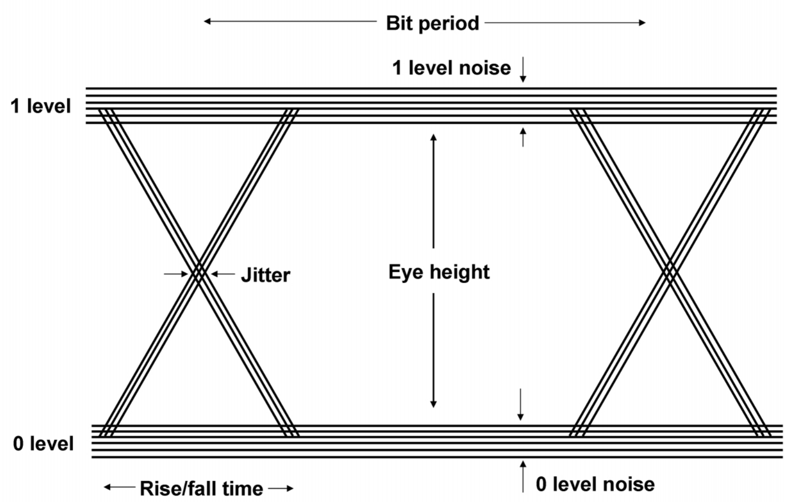

4.1. Illustration of NRZ eye diagram indicating measurements obtained.

Fig. 4.1 is an illustration of a typical eye diagram of an NRZ pulse stream. The extent of the eye opening is measured by the eye height, which is defined as the separation between the upper and lower 3σ points, where the 3σ point is the point that is three standard deviations σ from a mean upper or lower level. If the top and bottom levels, or "rails", are distorted or spread out, as in this case, it is indicative of intensity noise in the signal. The signal to noise ratio can be obtained directly from the eye diagram by measuring the extent of this distortion. The timing jitter between measurements is also visible as a spreading out of the transition between bits at the crossing point. All of these effects contribute to a closure of the eye and a corresponding rise in errors.

Bit error rate testing

The bit error rate (BER) of a transmission system is an end-to-end type of signal quality assessment that incorporates all of the potential sources of error in a link. It is the best way to determine the actual performance of a system in its entirety, rather than testing individual component parts. The signal detected at the receiver end of the link is compared to the transmitted signal, with any discrepancies between the two counted as errors. The BER is simply defined as,

$$BER = \frac{number\ of\ errors}{total\ number\ of\ bits\ sent}\ . \tag{4.2}$$

A generally accepted value of BER for error free transmission is 10^{-9}, although certain standards such as 40/100 Gb Ethernet have even more stringent requirements, demanding BER of 10^{-12} and below [21]. A BER of 10^{-9} for a transmission bit rate of 10 Gb/s corresponds to 10 detected errors every second. In the case of a BER of 10^{-12}, a bit rate of 10 Gb/s yields one error every 100 seconds. In order to make an accurate estimation of the BER, the measurement would have to be performed over a significant period of time. Data errors occur in a random fashion because most of the noise sources in the optical link are random processes. Therefore in a real non-random data transmission, it could take too long to detect sufficient errors for an accurate assessment to be made. In testing bit error rates on a system, a pseudo random binary sequence (PRBS) can be used instead of the data signal. A PRBS is an approximation of a random bit pattern, such that a more accurate appraisal of the error introduced by random noise sources can be made. For the BER analysis performed with the MC-SOA, a 10 Gb/s signal was transmitted and the errors counted over a 90 second period. This gives an error count of 900 at a BER of 10^{-9}, which is sufficient to make an accurate assessment.

Analysis of the Q-factor

Each of the transmitted “1” and “0” signal levels has its own associated noise power, and consequently its own signal to noise ratio (SNR). As such it is required to define a parameter that takes into account both SNR values, incorporating them into an overall measure of the quality of the signal. The Q-factor is such a measure [22] and is defined as,

$$Q = \frac{v_1 - v_0}{\sigma_1 + \sigma_0}, \tag{4.3}$$

where v_i and σ_i are the average signal and noise powers of the "1" level ($i = 1$) and the "0" level ($i = 0$) level, respectively. The Q-factor is related to the bit error rate, for thermal noise limited signals with Gaussian noise distributions, by,

$$BER = \frac{1}{2} erfc\left(\frac{Q}{\sqrt{2}}\right) \tag{4.4}$$

A BER of 10^{-9} corresponds to a Q factor of ~ 6 dB.

4.2.3. Measurement of bit error rates in MC-SOA transmission

Experimental setup

In order to demonstrate the effect of the carrier density distribution in a practical transmission system, the detection of a pseudo random binary sequence (PRBS) was performed using the MC-SOA, which was biased in the relevant configurations of interest. The setup for this experiment is shown in Fig. 4.2.

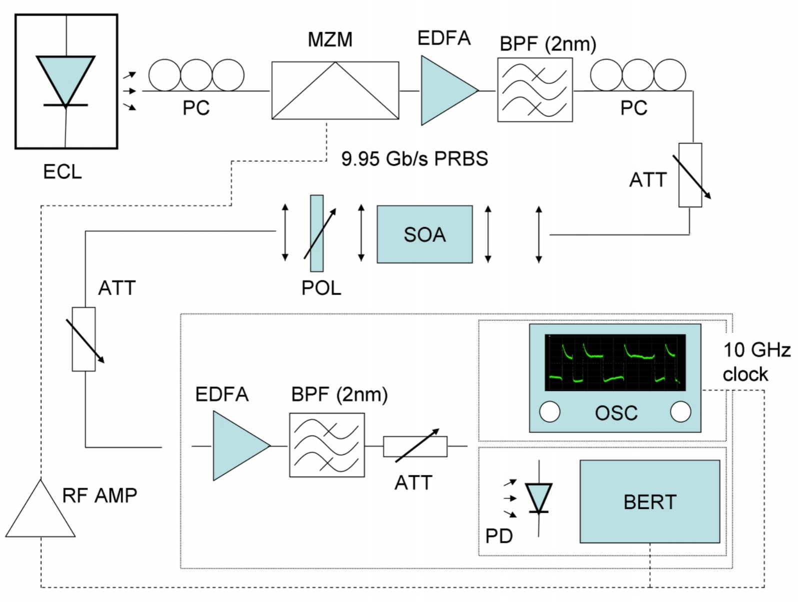

4.2. Setup diagram of BER measurement experiment. ECL – external cavity laser, PC – polarisation controller, MZM – Mach-Zehnder modulator, EDFA – erbium doped fibre amplifier, BPF – bandpass filter, ATT – variable attenuator, POL – polariser, RF AMP – electrical amplifier, PD – photodiode, OSC – sampling oscilloscope, BERT – bit error rate tester.

The optical source used was an external cavity laser (ECL), of the same type as that used in the CW characterization of the SOA in Chapter 3. The output signal power was 4 dBm, which was the highest optical power the ECL could sustain. The signal was then coupled to a Mach-Zehnder intensity modulator (MZM) via a polarization controller (PC). The MZM is biased at 2.2 V. An RF signal (0.5 Vp-p) coupled to the MZM, via an electrical amplifier with a gain of 25 dB, modulated the optical carrier with a 9.95 Gb/s PRBS non-return to zero (NRZ) signal, which had a bit pattern length of 2^7-1. The optical signal was amplified using an erbium-doped fibre amplifier (EDFA), with a gain ~ 25 dB and a noise figure ~ 5.5 dB, before being filtered by a 2 nm tuneable bandpass filter and passed through a polarisation controller. A variable attenuator allowed monitoring of the optical power prior to injection to the SOA. The pulses were injected into the SOA via a free space setup similar to that outlined in Fig. 3.6, with the exception of the mirrors. The lenses used were also different, with a numerical aperture of 0.68. The coupling losses were estimated to be ~ 4 dB per facet, using the method described in Section 3.4.2. A polariser was used at the SOA output in order to filter out orthogonally polarised ASE and reduce spontaneous-spontaneous beat noise and shot noise. In addition to this, the polariser functioned as a quality control, in combination with the attenuator/power meter at the SOA output, in order to determine if the signal polarisation had changed in the SOA. An attenuator at the output of the SOA allowed measurement of the SOA output power. The detection scheme consisted of an EDFA (gain ~ 22 dB, NF ~ 4.5 dB), a 2 nm bandpass filter and a variable attenuator in order to keep the optical power to the photodetector at a constant level, well above the detection threshold. The optical signal was coupled to a 10GHz photodetector (PD) and bit error rate tester (BERT). The detection threshold power of the PD is approximately -15 dBm. Separately, the signal waveforms were recorded using a sampling oscilloscope with an electrical bandwidth of 80 GHz. The BERT consists of a pattern generator, for outputting the PRBS test signal to the MZM, and an error detector, to count the errors generated by the system. The 10 GHz clock signal for the sampling oscilloscope was provided by the BERT unit. The clock signal was also internally wired in the BERT in order to synchronize the pattern generator and the error detector. For this experiment, the temperature of the SOA was held at 23^0C.

BER at low input power

In order to determine the effect of the SOA noise figure on the sensitivity performance of the detection system, signals with a very low average power were injected into the SOA. The output signal from the SOA was amplified by the EDFA to a detector power of 60 μW, for all values of SOA input power, in order to determine the effect of the SOA. The back-to-back sensitivity of the detector, i.e. in the absence of the SOA, was also determined in order to illustrate the extent of the sensitivity improvement obtained in each bias configuration. Fig. 4.3 shows the eye diagrams of a signal with an average power of ~ -26 dBm, measured at the SOA output, for the low noise and high P_{sat} bias configurations, as well as the back to back case.

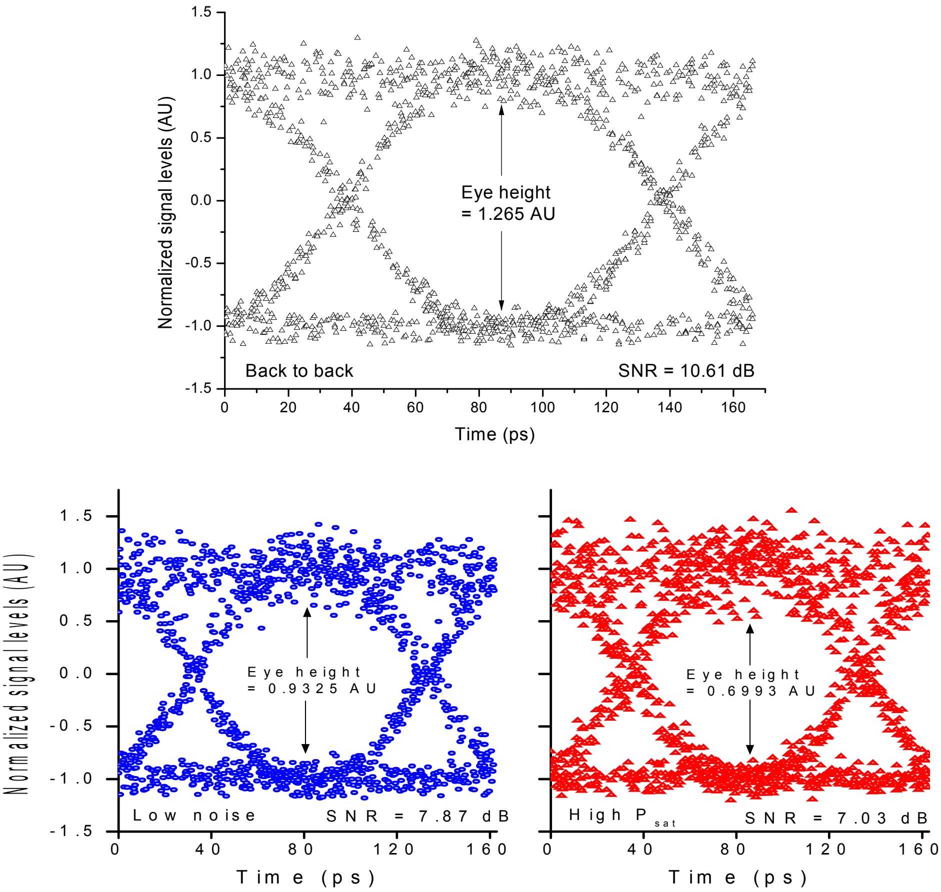

4.3. Eye diagrams of -26 dBm signal at 1550 nm at SOA output for low noise (left) and high Psat (right) bias configurations. Also shown is the back to back eye diagram (top). The wavelength of the injected signal is 1550 nm.

The signal levels are normalized and displayed in arbitrary units (AU). The increased noise in the high P_{sat} configuration is evident in the value of the measured signal to noise ratio (SNR). The SNR measured on the sampling oscilloscope for the low noise case is 7.87 dB, whereas for the high P_{sat} case it is 7.03 dB, illustrating the effect of the SOA noise figure on the injected signal. The SNR of the back to back signal is measured as 10.61 dB. The eye opening amplitudes were measured by fitting a Gaussian distribution function to a histogram of the eye diagram, and finding the 3σ points, as detailed in Section 4.2.2. Fig. 4.4 shows a plot of the bit error rate detected by the BERT as a function of the input power injected to the SOA. The bit errors were counted by the BERT over a 90 second period and the rate was then calculated. The optical power at the photodetector was kept at a constant 60 μW by the combination of the EDFA and variable attenuator. The back to back measurement was also taken as a reference. The input power in the back to back case was measured at the attenuator before the SOA input (with SOA removed), as shown in Fig. 4.2. The wavelength of the input signal was 1550 nm.

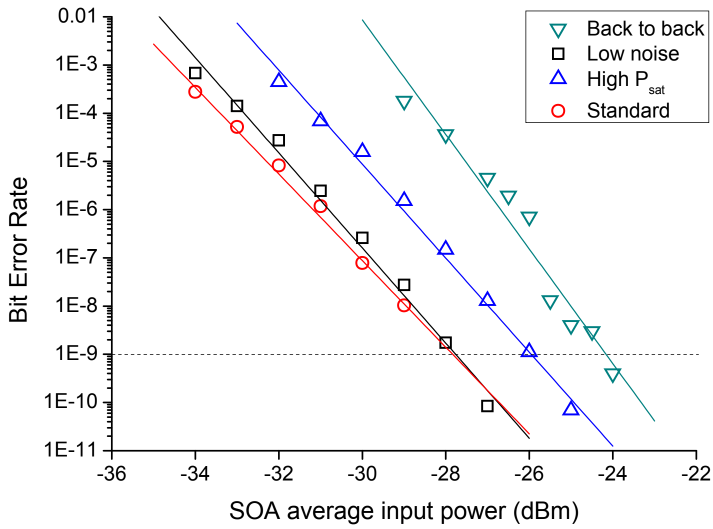

4.4. BER curves for low power signal transmission at 1550 nm, for various bias configurations. Minimum BER for error free transmission is indicated.

A clear difference in the detected BER is visible between the low noise and high P_{sat} bias configurations. At a BER of 10^{-9}, the minimum BER for error free transmission, the power penalty for the high P_{sat} configuration compared with the low noise configuration is ~ 1.8 dB. This indicates a clear effect of the carrier density distribution. The back to back measurements indicate a receiver sensitivity at a BER of 10^{-9} of -24.1 dBm average power. This compares with receiver sensitivities of -25.94 dBm, -27.76 dBm and -27.83 dBm for the high P_{sat}, low noise and standard bias configurations, respectively. The low noise configuration does not lead to an improved receiver sensitivity relative to the standard bias configuration. This is due to the low noise figure and higher gain values displayed by the standard bias configuration.

BER at high input power

In order to measure the impact of gain saturation on the bit error rate in transmission through the MC-SOA, the injected signal power was increased into the SOA saturation regime. Fig. 4.5 shows the eye diagram of an input signal of ~ 6 dBm average power and the resultant signal at the output of the SOA, biased in the low noise configuration. The effects of gain saturation are clearly visible in the output signal eye diagram, causing a closure of the eye.

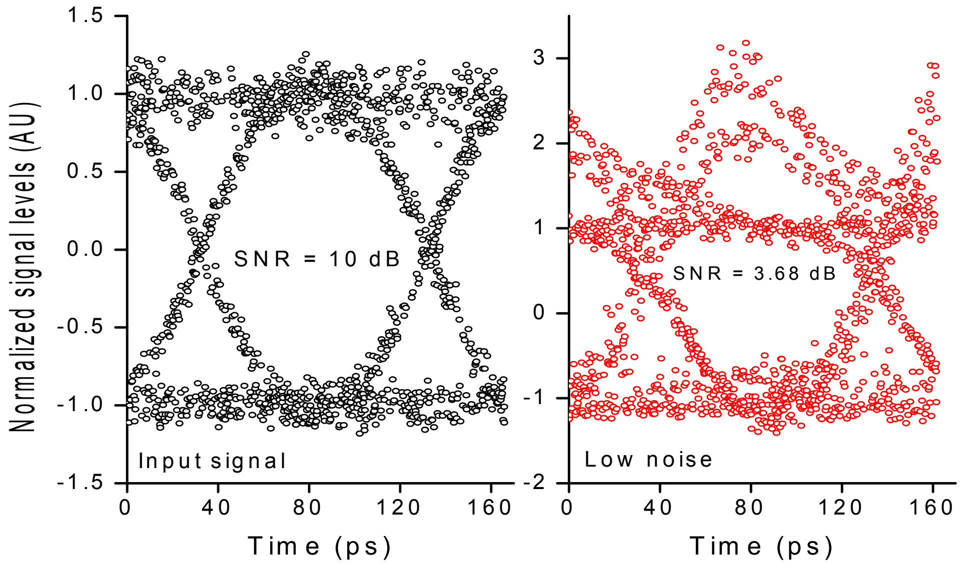

4.5. Eye diagrams for 6 dBm signal at 1550 nm (left) before injection and (right) after injection into SOA. Bias current is set to low noise configuration.

The SNR values measured by the sampling oscilloscope were 10 dB for the input signal and 3.68 dB for the output signal, indicating the extent of the penalty imposed by the gain saturation. Fig. 4.6 shows the detected bit error rate as a function of the average input power to the SOA, for the three studied bias configurations. The SOA is well within the saturation regime before errors in transmission are detected. Appreciable errors are detected for the standard bias configuration at ~ 2.5 dBm average input power. The equivalent powers for the low noise and high P_{sat} cases are 4.8 dBm and 6.4 dBm, respectively. These results confirm that the higher saturation power enabled by the high P_{sat} bias configuration leads to decreased bit errors at high input power, relative to other bias configurations. Interestingly, the standard bias configuration leads to the largest error count. This is because the signal is injected at the gain peak wavelength of this bias configuration, 1550 nm, and consequently the input saturation power is reduced. In contrast, the gain peak wavelength of the low noise and high P_{sat} cases is 1570 nm, and thus the saturation power for these cases is relatively high at 1550 nm. The results of the high power BER characterization indicate the potential suitability of the multi-contact SOA as a power booster SOA.

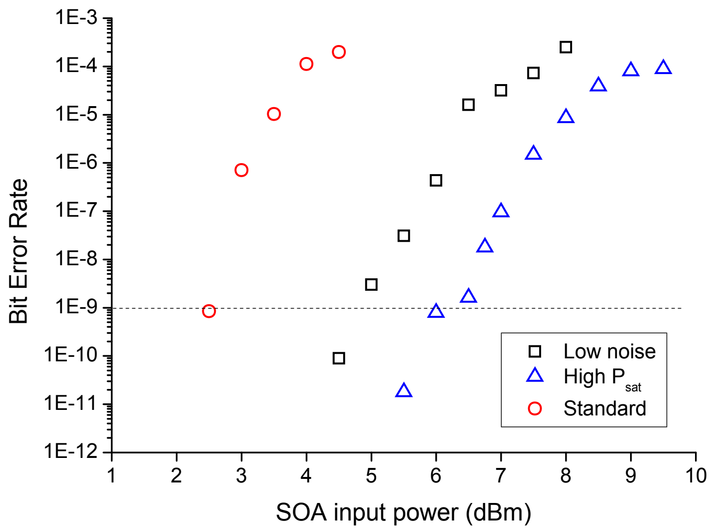

4.6. BER curves for high power signal transmission at 1550 nm, for various bias configurations. Minimum BER for error free transmission is indicated.

4.3. Picosecond Pulse Amplification in MC-SOA

4.3.1. Ultrashort pulse generation for optical communications

As data rates in optical communications networks exceed 40 Gb/s, pulsed optical sources are becoming indispensible components of transmission systems. The narrow pulsewidth obtainable with mode locked laser diodes [23] allows efficient utilization of the available bandwidth within a single fibre. For example, the bit spacing for a channel multiplexed to 160 Gb/s is only 6.25 ps, requiring pulsewidths much smaller than this. Optical pulses are inherently Return to Zero (RZ) in format. RZ is distinguished from NRZ in that the signal level drops to zero between each bit. RZ pulses lead to increased receiver sensitivity when compared to NRZ signals [25, 26], for a given energy per pulse. Comparative studies of RZ and NRZ formats have shown that at high bit rates, RZ signals suffer less from optical non-linearities [27], with the main limiting factor being dispersion, due to the short optical pulsewidth [28].

Optical pulses for data transmission can be generated through numerous means. Semiconductor laser diodes are the most common devices used in modern communications systems. The multiple modes generated by a laser diode can generate optical pulses if a fixed phase relationship is maintained between them, through the process of mode locking [29]. The laser modes will all constructively interfere at a fixed interval, generating a short, intense burst of light. Mode locking can be achieved through active, passive, or hybrid means.

- Semiconductor lasers employing active mode locking are frequently used in optical communications as they can be synchronized to an external electrical modulation signal [30]. This signal modulates the loss of the laser cavity, allowing the transmission of an optical pulse if the modulation period is matched to the resonator round trip time. Active mode locking can be achieved through amplitude modulation (AM), frequency modulation (FM) or synchronous pumping of the laser medium with another optical source.

- Passively mode locked lasers have an advantage over actively mode locked lasers in that they can generate shorter pulses [31]. This is due to the use of a saturable absorber section in order to generate mode locking. The absorber can be engineered so that the absorption bleaches at the peak of the mode intensity, thus transmitting a pulse. The attenuation of the leading edge of the pulse causes the pulse to temporally compress. The faster response time of saturable absorbers compared to modulation speeds achieved by active mode locking is the reason for the shorter pulses created by passive mode locking.

- Hybrid mode locking combines elements from both active and passive mode locking, for example, the use of a saturable absorber and modulation of the electrical injection to the laser [32]. This approach has the advantage of generating short pulses due to the saturable absorber section, while also allowing for synchronization with an external electrical signal.

Another technique for the generation of pulses in laser diodes is gain switching. The principle behind gain switching is that the laser is DC biased just below threshold, and the optical gain is modulated through the application of high amplitude electrical pulses. In this way, optical pulses are generated that can be of considerably shorter duration than the electrical switching pulses. CW lasers can also be used to generate optical pulses through the use of an external modulator such as a Mach-Zehnder interferometer or an electro-absorption modulator (EAM). In a MZI, when a voltage is applied, the refractive index in one of the two waveguides changes, resulting in a phase change in that arm. This leads to destructive interference, and thus modulation of the beam.

4.3.2. Effects of SOA dynamics on picosecond pulses

SOAs are suitable devices for use in pulse amplification schemes due to their wide amplification bandwidth (> 5 THz). This allows them to amplify pulses on the order of a few picoseconds in duration without distortion due to gain dispersion and other effects. The penalizing effect of dispersion that affects ultrashort pulses in long stretches of fibre does not have a significant effect in SOAs due to the short length of the devices, however non-linear phenomena such as gain saturation and self phase modulation can cause pulse distortions, depending on the pulse energy injected into the SOA. An optical pulse with energy below the saturation energy of the SOA is generally amplified with few distortions, but non-linear effects come into play once the pulse energy reaches this limit.

Propagation of a pulse in an SOA

The propagation of an optical pulse in an SOA is governed by the following set of equations. The evolution of the pulse amplitude *A* is expressed as [33],

$$\frac{\partial A}{\partial z} + \frac{1}{v_g}\frac{\partial A}{\partial t} = \frac{1}{2}(1 - i\alpha)gA\,, \tag{4.5}$$

where z represents distance along the propagation axis, v_g is the group velocity, t is absolute time and α is the linewidth enhancement factor. A itself is represented in terms of the power P and the phase Φ by,

$$A = \sqrt{P(z,t)}\,e^{i\Phi(z,t)} \tag{4.6}$$

Neglecting the spontaneous emission term, and using the phenomenological approximation for the gain coefficient, Eq. (1.16), the carrier density rate equation of Eq. (3.6) can be expressed as,

$$\frac{\partial g}{\partial t} = \frac{g_0 - g}{\tau_c} - \frac{gP}{E_{sat}}\,, \tag{4.7}$$

where g_0 is the unsaturated steady state gain coefficient, τ_c is the effective carrier recombination time, P is the power of the pulse and E_{sat} is the saturation energy of the SOA.

Effect of gain saturation on pulseshape

As the pulse propagates through the SOA, it experiences an energy and time dependent gain. We can substitute the absolute time t for a time frame τ moving with the propagating pulse by the transformation $\tau = t - z / v_g$. Using this frame of reference, and using Eq. (4.6), the following equations can be obtained from Eqs. (4.5) and (4.7),

$$\frac{\partial P}{\partial z} = g(z,\tau)P(z,\tau) \tag{4.8}$$

$$\frac{\partial \phi}{\partial z} = -\frac{1}{2}\alpha g(z,\tau)) \tag{4.9}$$

$$\frac{\partial g}{\partial \tau} = -g(z,\tau)P(z,\tau)/E_{sat} \tag{4.10}$$

If Eq. (4.8) is integrated over the length of the amplifier, the output power can be obtained,

$$P_{out}(\tau) = P_{in}(\tau)e^{h(\tau)}, \tag{4.11}$$

where P_{in} is the input pulse power, and $h(\tau)$ is the integrated gain at each point of the pulse profile, given as,

$$h(\tau) = \int_0^L g(z,\tau)dz \tag{4.12}$$

By using this identity in the gain rate equation given in Eq. (4.7), and then integrating this equation in the special case where the width of the pulse is much less than τ_c (which is true in the case of picosecond scale pulses), we have,

$$\frac{dh}{d\tau} = -\frac{P_{in}(\tau)}{E_{sat}}\left(e^{h(\tau)} - 1\right) \tag{4.13}$$

This equation can be solved to obtain *h(τ)*. The instantaneous amplifier gain is related to *h(τ)* as *G(τ) = exp[h(τ)]*, giving,

$$G(\tau) = \frac{G_0}{G_0 - (G_0 - 1)\exp(-E(\tau)/E_{sat})}, \tag{4.14}$$

where G_0 is the unsaturated gain of the SOA and *E(τ)* is the energy of the pulse integrated up to time *τ*. When a pulse propagates in an SOA, it is assumed that the leading edge of the pulse will experience the maximum unsaturated gain G_0. This implication is clear from Eq. (4.14), where if we assume that only a fraction of the total pulse energy has passed, the exponent can be approximated to zero. The corollary of this result is that the trailing edge of the pulse experiences the least amount of amplification, due to the saturation of the gain by the leading edge. In this case *E(τ)* is replaced in Eq. (4.14) by E_{in}, the total input energy of the pulse. This saturation temporally broadens the pulse, as the reduced gain experienced by the trailing edge causes it to "stretch out" [34], . In addition to this, the leading edge of the pulse is sharpened. The peak of the pulse is also shifted to earlier times with increasing pulse energy, due to the saturation of the gain occurring earlier for a given pulse energy. This behaviour is assuming a Gaussian pulse shape. For rectangular pulses, temporally compression can occur. The broadening of pulses can pose problems for OTDM transmission schemes where pulses are interleaved so that the spacing between them is small. Pulse broadening can lead to inter-symbol interference (ISI), meaning that detection systems could experience problems distinguishing between the successive pulses.

Spectral effects of gain saturation

Dynamic carrier density variations in SOAs not only cause a change in the gain characteristics, but also lead to a phase variation in the SOA. A change in the carrier density results in a corresponding change in the imaginary part of the complex refractive index. This in turn is accompanied by a change in the real part of the refractive index, inducing a fluctuation in phase. Small changes in the optical gain can lead to large variations in the phase, depending on the strength of the coupling between the gain and the refractive index. This is governed by the linewidth enhancement factor [35], defined as,

$$\alpha = -\frac{4\pi}{\lambda}\frac{dn_e/dN}{dg/dN}, \tag{4.15}$$

where λ is the signal wavelength, N is the carrier density, g is the material gain and n_e is the SOA effective refractive index. The linewidth enhancement factor was originally proposed to account for linewidth broadening in semiconductor lasers. It is essentially the ratio between the change in the real part of the refractive index to the change in the imaginary part of the refractive index with respect to the carrier density. Thus, a reduction in the carrier density will lead to an increase in the real part of the complex refractive index, and cause a corresponding change in phase.

When an optical pulse propagates through an SOA, the intensity variation along the pulse, translated into a variation in the carrier density due to gain saturation, leads to a corresponding modulation of the phase. In this sense, the optical pulse affects its own phase through the process of self phase modulation (SPM). SPM can cause large distortions in the spectral shape of a pulse through frequency chirping. Frequency chirping is the variation of the instantaneous frequency of a pulse caused by the change in phase, and is given as,

$$\Delta v = -\frac{1}{2\pi}\frac{d\phi}{dt} \tag{4.16}$$

The chirp resulting from SPM in SOAs has the opposite sign to that imposed on directly modulated semiconductor lasers. The relatively large value of the linewidth enhancement factor in bulk SOAs (~ 5 or higher [36]) means that significant frequency chirp can occur as a result of SPM when the gain saturation is quite small.

The overall effect of SPM is to asymmetrically shift the pulse spectrum to longer wavelengths, often with the formation of multiple peaks [37]. This is due to interference between different points in the pulse profile that may have the same instantaneous frequency. SPM also leads to a broadening of the pulse spectrum, for initially unchirped and positively chirped pulses (increasing in frequency across the pulse), by effectively transferring pulse energy to spectral components that are further from the central frequency. The dynamics of SPM in SOAs depends to a large extent on the duration of the pulse. For pulses on the order of 1 ps or less, intraband effects can come into play. The thermalization of hot carriers through the carrier heating process rapidly replenishes the carrier density reduction resulting from non-linear gain compression after the peak of the pulse. A blue chirp (increase in frequency) on the trailing edge of the pulse results from this process [38]. For pulses longer than a few picoseconds, this effect is not as significant.

SPM has been used in optical fibres to temporally compress pulses [39, 40]. The SPM process in optical fibres is due to the intensity dependent optical Kerr effect, rather than a dependence on carrier density. In optical fibres with anomalous dispersion, higher frequencies propagate faster than lower frequencies. The reduction of the frequencies at the leading edge of the pulse caused by SPM allows the trailing edge to “catch up” with it, thus compressing the pulse. The SPM dynamics of SOAs have also been used instead of fibres, as the required pulse energy is much less than that required in fibre based schemes [41, 42]. If the effects of self phase modulation and dispersion are balanced, a soliton can propagate in the fibre. An optical soliton is a pulse that can propagate while maintaining its shape, without dispersive broadening.

In a similar manner to the broadening of positively chirped pulses, SPM can also cause a compression of the pulse spectrum if the pulse is initially negatively chirped; that is, reducing in frequency from the leading to the trailing edge of the pulse [43, 44]. SPM causes a transfer of pulse energy to spectral components closer to the central frequency of the pulse. This effect has been demonstrated for femtosecond pulses propagating in a standard single mode fibre [45, 46], and transform limited spectral compression has been demonstrated in photonic crystal fibre [47].

4.3.3. Characterization of pulses by SHG-FROG

The optical pulses in this work are characterized both in the spectral domain and the temporal domain. The temporal profile of relatively long, repetitive pulses can be measured using a wide bandwidth sampling oscilloscope with a fast photodiode. The oscilloscope should have a bandwidth large enough to detect the modulation frequency of the signal. Despite having a potentially low sampling rate compared with the bit rate of the signal, the oscilloscope can build a complete trace of the pulse using multiple delayed triggering events from an external trigger signal. Alternatively, a real time oscilloscope can be used in order to record single or repetitive pulses, by taking advantage of a high sampling rate. The upper limit on the detectible bit rate is lower than that of a wide bandwidth sampling oscilloscope. Both types of oscilloscope are ultimately limited in the duration of the pulses they can measure by their resolution. In the spectral domain, an optical spectrum analyzer can be used to measure the frequency spectrum of a pulse. The aforementioned measurement techniques characterize either the temporal or spectral profile of the pulse. In order to determine the complete characteristics of the electric field of a pulse, both temporal and spectral information must be obtained simultaneously. Frequency resolved optical gating is a technique whereby both the amplitude and the phase of the pulse can be measured [48].

Autocorrelation and SHG-FROG

The most common technique for measuring ultra-short pulses is autocorrelation. The principle of autocorrelation is that the pulse is used to measure itself. A beamsplitter is used to replicate the original pulse. The replica is delayed relative to the original and then recombined in a non-linear medium that exhibits second harmonic generation (SHG). The SHG signal displays a frequency twice that of the input signal used to generate it, and requires a strong optical power for an efficient conversion. The SHG signal is focused onto a detector that integrates the resultant signal over a long timeframe relative to the pulse length. The magnitude of the SHG signal can be related to the input pulse by,

$$E_{SHG} = E(t)E(t-\tau), \tag{4.17}$$

where τ is the time delay introduced onto the replica pulse. Due to the slow response of the detector, the actual structure of the pulse cannot be resolved, so the measurement produces an autocorrelation,

$$A(\tau) = \int_{-\infty}^{+\infty} I(t)I(t-\tau)dt\,, \tag{4.18}$$

where I is the detected pulse intensity. Autocorrelation traces are symmetric around the point $\tau = 0$, and any phase information in the pulse is lost, since no spectral measurements are made.

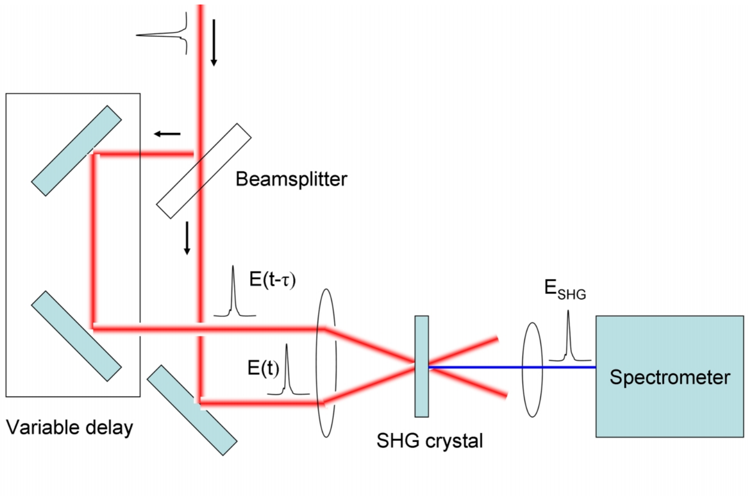

4.7. Basic schematic of FROG setup using second harmonic generation.

Frequency resolved optical gating (FROG) resolves this issue through a combination of spectral and temporal measurements [49]. Similar to an autocorrelation measurement, the pulse to be measured is split using a beamsplitter, and the replica pulse is time delayed. The pulses are again recombined in a non-linear medium (like a SHG crystal). In contrast to an autocorrelator, the resultant signal focused onto a spectrometer. In this way, traces of intensity versus frequency *ω* as a function of the time delay are measured. A basic schematic of a second harmonic generation FROG (SHG-FROG) setup is shown in Fig. 4.7. The result of this measurement is the spectrogram,

$$S_E(\mu,{}^2) = \left| \int_{-\infty}^{\infty} E(t) g(t - {}^2) \exp(-i\mu t) dt \right|^2 , \tag{4.19}$$

where *E(t)* is the field of the pulse to be measured and *g(t-τ)* is the field of the gate pulse that is used to measure the original pulse. In this case, the gate pulse is simply the replica of the original pulse. An example of spectrogram of a 2 ps pulse is shown in Fig. 4.8. The different colours on the plot indicate the intensity of the pulse. Note that the signal field determined by Eq. (4.17) is invariant with respect to the sign of the time delay *τ*. This leads to an ambiguity in the electric field with respect to time. The phase and pulse temporal structure can be obtained from the spectrogram measurements through the use of a two dimensional phase retrieval algorithm [50]. An initial estimate of the electric field is made, and the SHG signal field is constructed from Eq. (4.19) for this. The constructed field is Fourier transformed to find the frequency domain signal. The experimental FROG trace is compared with this signal and an improved signal field is generated. By inverse Fourier transforming this improved field back to the temporal domain, a new estimate for the electric field is made. This process continues over successive iterations until the error between the measured FROG trace and the retrieved trace is a minimum.

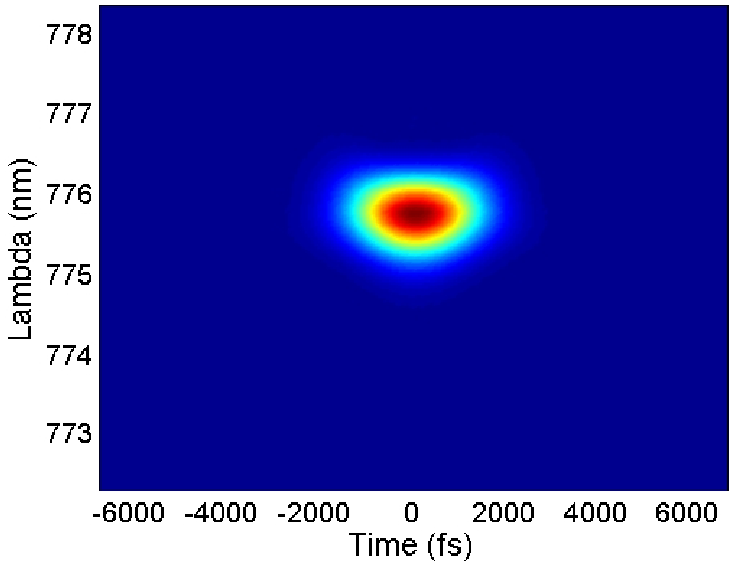

4.8. Spectrogram of SHG signal generated from a 2 ps optical pulse.

It should be noted that due to the time ambiguity in the FROG trace, the sign of the retrieved phase and thus the frequency chirp can be difficult to determine. This can be resolved by introducing a known phase distortion onto the pulse, for example, running it through a length of fibre with a known dispersion sign. This should affect the chirp of the pulse in a measureable way and the relative signs of the chirp before and after the phase distortion should remove the ambiguity.

Experimental setup

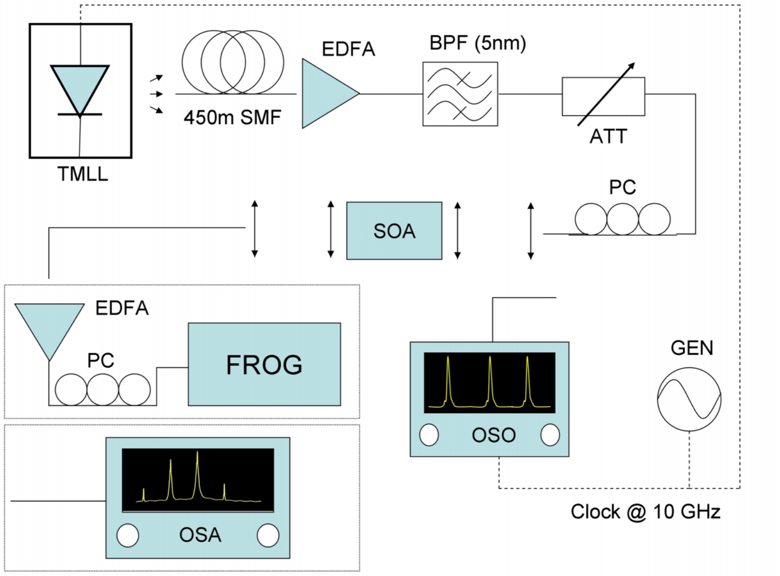

4.9. Schematic of pulse characterization experimental setup. OSA or FROG setup are alternately used to measure pulses after SOA. OSO is used to measure pulses before and after SOA.

The setup for characterizing the optical pulses after amplification by the MC-SOA is shown in Fig. 4.9. The pulses are generated by a tuneable mode locked laser diode (TMLL) at a wavelength of 1550 nm and have a $sech^2$ shape. They have a pulsewidth of approximately 1.5 ps and a time-bandwidth product of approximately 0.34, close to the limit for $sech^2$ pulses which is ~ 0.315. The TMLL has a saturable absorber section that enables passive mode locking within a range of 9.8 to 10.8 GHz. Hybrid mode locking is also possible and this is the technique used in this experiment. A 10 GHz clock from a signal generator is applied to the TMLL to enable mode locking. The power of the clock signal is 12 dBm at the output of the signal generator. A 50:50 splitter is used to separate the clock signal so that it can also be used to trigger an optical sampling oscilloscope (OSO) in order to confirm the mode locking of the laser. The OSO has a temporal resolution of 1 ps. The TMLL is biased at ~ 50 mA, which is slightly above the turn-off current. The reason for this is because at higher biases, satellite pulses can appear next to the main pulse peak.

In order to account for the time ambiguity in the FROG traces, the pulses are first passed through 450 m of single mode fibre (SMF). The anomalous dispersion in the SMF introduces a negative chirp on the pulses, and also causes the temporal width to broaden to 4.3ps. The pulses then are amplified with an EDFA (gain ~ 25 dB, NF ~ 5.5

dB) before being passed through a wide band optical filter (5 nm bandwidth), a variable attenuator and a polarisation controller. The mode locking procedure is monitored on the optical sampling oscilloscope, which has a temporal resolution of 1 ps, before coupling to the SOA. The pulses are injected into the SOA using the same free space setup that was used for the BER characterization. The coupling loss at each facet is again estimated to be ~ 4 dB. At the output of the SOA, an EDFA (gain ~ 30 dB, NF ~ 5.5 dB) amplifies the pulses so that the optical power is at a suitable level for efficient second harmonic generation. A polarisation controller is also necessary as the FROG is polarisation sensitive. The temporal and spectral resolution of the FROG is 26.66 fs and 0.05 nm, respectively. In addition to the FROG, the spectral characteristics of the pulses are measured using an optical spectrum analyzer with a resolution of 0.02 nm. In order to obtain an accurate measurement using the FROG, the error between the measured pulse field and the estimated signal field must be on the order of ~ 10^{-6}.

4.3.4. SOA gain characteristics in pulsed amplification

The average power of the signal is varied from -25 dBm and 10 dBm. Accounting for the input facet coupling loss, these powers correspond to pulse energies between 1 fJ and 400 fJ at a 10 GHz repetition rate. The optical gain of the MC-SOA as a function of the input pulse energy is shown in Fig. 4.10, as measured by the optical spectrum analyzer. The input saturation energy for the standard, low noise and high P_{sat} bias configurations are measured to be 34 fJ, 40 fJ and 80 fJ, respectively. These energies correspond to average signal powers of -4.68 dBm, -3.98 dBm and -0.96 dBm, respectively. These values are slightly higher than those measured for the CW case. The low power gain values are broadly in agreement with the measured CW values. The values measured for both the low noise and high P_{sat} configurations are slightly lower because the pulses are generated at 1550 nm, which is redshifted from the peak gain wavelength for these biases. The higher saturation energy of the high P_{sat} bias configuration can be visualized from the slope of the gain curve with respect to the other bias configurations.

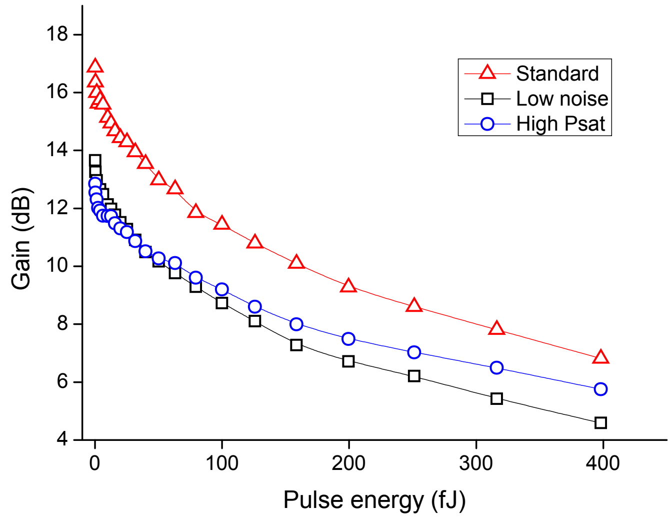

4.10. Optical gain as a function of injected pulse energy. Pulses have a wavelength of 1550 nm.

The gain characteristics of SOAs can be very different when amplifying short optical pulses, compared to CW signals [51]. For a single pulse being amplified in a SOA, the saturation energy is greater than that of a CW beam of similar energy, due to the effect of carrier recovery. At repetition periods on the order of the carrier recovery time and below, however, the saturation energy approaches that of the CW case as the gain does not have sufficient time to recover between pulses. This is the reason for the relatively small difference between the saturation power of the 10 GHz pulses and the CW signal.

The distortion of pulses due to gain saturation and SPM is also reduced at high repetition rates because the amount of gain compression experienced by each pulse is greatly reduced. Fig. 4.11 shows the amplification of a stream of pulses from the TMLL, multiplexed to a repetition rate of 160 GHz. The bias configuration of the SOA is set to the standard configuration. These pulses have not been passed through the SMF and have a pulsewidth on the order of 2 ps. They are amplified before being coupled to the multiplexer. The process of multiplexing the 10 GHz pulses four times to a repetition rate of 160 GHz significantly weakens the optical power. A second EDFA is used after the multiplexer to compensate for this. The remainder of the setup up to the SOA input is identical to that shown in Fig. 4.9, after the first EDFA. At the output of the SOA another 5 nm bandpass filter is used to eliminate SOA and EDFA noise, and the signal is detected at the optical sampling oscilloscope. The OSO has a detection bandwidth of 500 GHz and a time resolution of 0.8 ps. The average power of the pulses before injection is ~ 5 dBm, which reduces to ~ 1 dBm at the facet due to coupling losses.

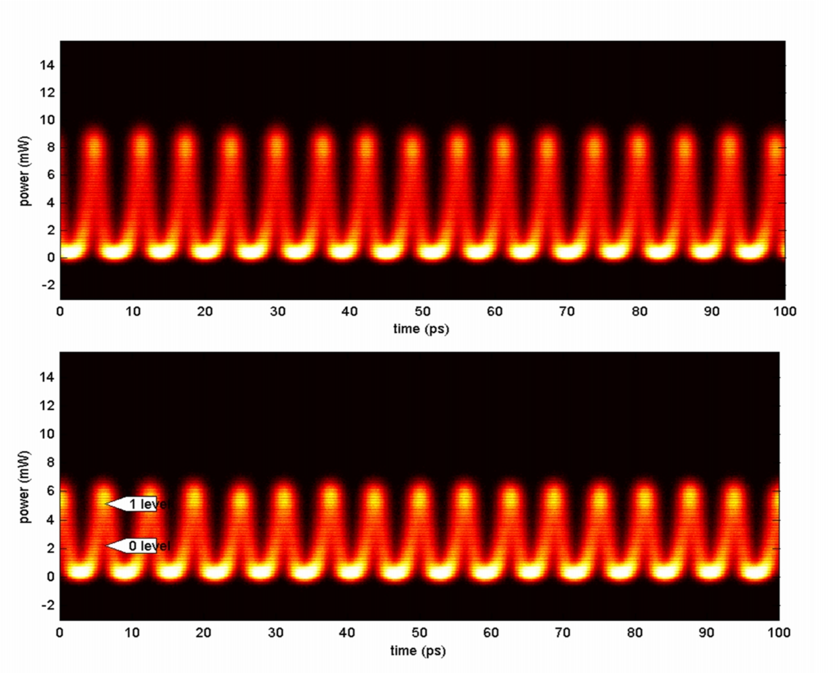

4.11. Eye diagram of 10 GHz, 2 ps pulses multiplexed to 160 GHz. Pulses before SOA are shown in top figure, while pulses at SOA output are shown in bottom figure.

The output pulses are well separated and show very little distortion due to gain saturation effects. The lower peak power of the detected output pulses is indicative of the coupling losses at both SOA facets. The calculated gain for this pulse stream is ~ 7.7 dB, assuming coupling losses of 4 dB per facet. This is similar to the CW gain calculated for 1 dBm input power of 8.7 dB. At very high repetition rates such as this, the gain of the SOA responds to the average power of the pulse stream, rather than the individual pulses.

4.3.5. Temporal characteristics of pulses

Using the setup shown in Fig. 4.9, pulses from the TMLL, mode locked at a 10 GHz repetition rate, are injected into the SOA at a wavelength of 1550 nm. The pulse energy was varied from ~ 1 fJ to 400 fJ. The pulsewidth was measured at the FROG as a function of the injected pulse energy and also as a function of the SOA bias current. The broadening of the pulsewidth can be clearly seen in Fig. 4.12, which plots the temporal pulse profile as a function of the injected pulse energy for the standard bias configuration, as measured at the output of the SOA.

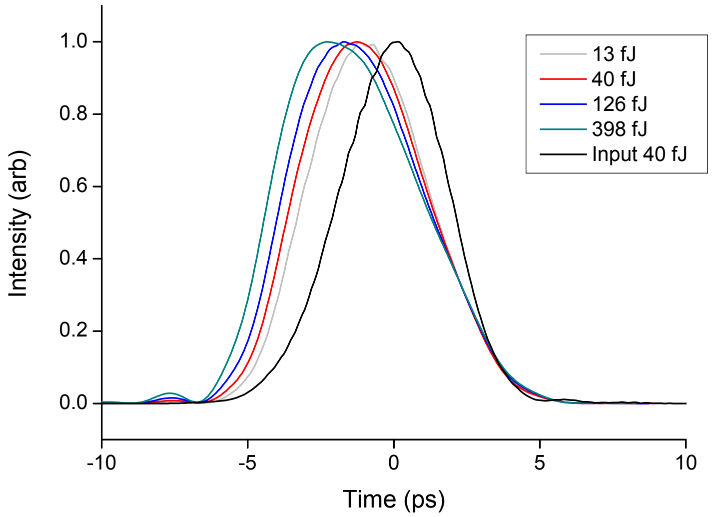

4.12. Temporal profiles of pulses as a function of pulse energy, for standard bias configuration.

A 40 fJ pulse before injection to the SOA is plotted for comparison. The measured pulsewidth for the input pulse is 4.3 ps, which indicates the temporal broadening introduced by the 450 m SMF reel. The pulse intensity is normalized for all profiles. The broadening of the pulses can be clearly seen as the injected pulse energy is increased. Additionally, the peak intensity is shifted to earlier times as the saturation of the gain occurs further towards the front of the pulse. The small ripple feature at the leading edge of the pulse is a pedestal pulse produced by the TMLL. It was minimized by using the low bias region of operation of the TMLL. The effect of the SOA bias configuration is summarized in Fig. 4.13, which shows the increase in the width of the injected pulses as a function of the pulse energy for the three bias configurations studied. The higher saturation energy of the high P_{sat} bias configuration leads to a less significant effect on the pulsewidth as the pulse energy is increased. By contrast, the lower saturation energy of the other two bias configurations is manifested in a more pronounced increase of the pulsewidth. The standard bias configuration shows the greatest increase in pulsewidth. This is due to the larger unsaturated gain [37] and lower input saturation power at 1550 nm compared with the other bias configurations. Also plotted is the calculated pulsewidth for the pulses before injection.

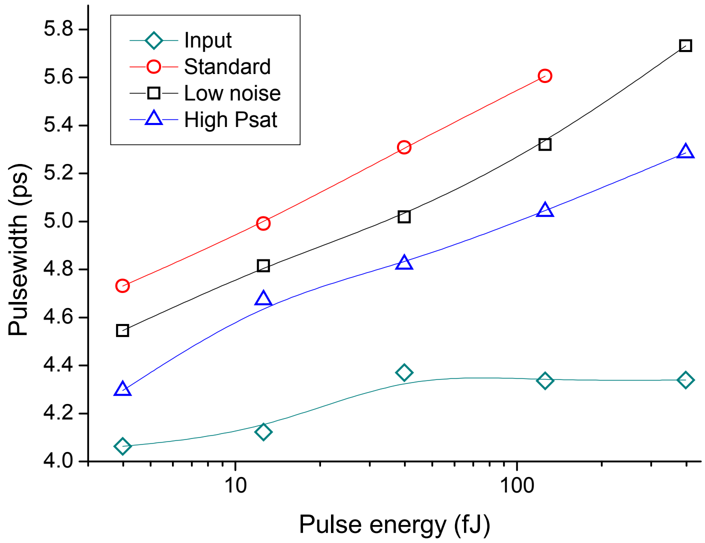

4.13. Measured temporal width as a function of pulse energy, for various bias configurations. Also plotted for reference is the temporal width of pulses before SOA injection.

A potential useful application for the MC-SOA is illustrated in the following results and in Fig. 4.14. The middle contact of the SOA is biased at 90 mA and the end contact at 50 mA. The input contact bias is varied from 0 mA to 4 mA. A reduction in pulsewidth is measured at low input energy when the input contact bias is less than 2 mA. This can be explained by saturable absorption in the input, low bias section. As the pulse propagates through this section, the leading edge is attenuated by this absorption. The absorption is saturated at or near the peak intensity of the pulse, thus allowing greater transmission of the trailing edge of the pulse. This narrows the temporal width of the pulse. Another effect of the leading edge attenuation is the shifting of the intensity peak to later times, in contrast to the gain saturation process. The increase in pulsewidth at higher powers is due to the pulse saturating the gain in the highly pumped middle and end sections. This broadening effect dominates over the pulsewidth narrowing in the input section at high input powers, and vice versa. This is a similar reason for the increase in pulsewidth observed with the increase in bias. The increased electrical pumping of the input section reduces the amount of carriers available for absorption, and thus the absorption is bleached earlier along the temporal profile of the pulse. As a result, less of the leading edge is attenuated and the pulse compression effect is reduced.

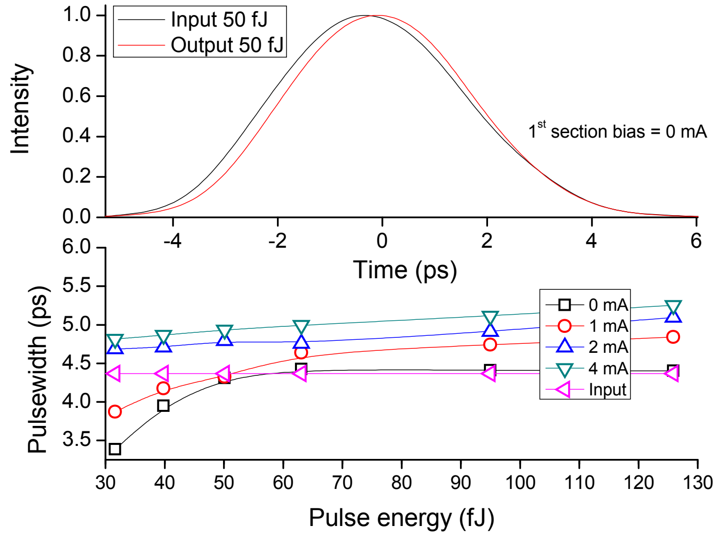

4.14. Intensity profiles (top) of 50 fJ pulse before and after SOA, showing reduction in width, and evolution of pulsewidth (bottom) with respect to pulse energy, for various values of input contact bias.

4.3.6. Spectral characteristics of pulses

The phase and chirp characteristics of the optical pulses are measured using the FROG, and the corresponding optical spectra are measured separately on the OSA. The intensity profiles and the frequency chirp of the input signals taken before and after the 450 m SMF reel are shown in Fig. 4.15. The initial pulse has a very slight up-chirp, although the absolute sign of the chirp remains ambiguous when taken in isolation. Since the operating wavelength used in the experiment takes place in the anomalous dispersion regime of the SMF, it is already known that a negative chirp should be imposed on the initial pulses. In this way, the time ambiguity of the SHG-FROG is resolved. It can then be assumed that the negative chirp attributed to the broadened pulse in Fig. 4.15 is a correct representation. The dispersion in the SMF also increases the pulsewidth. The width of the initial pulse was measured to be 1.62 ps. This was broadened to 4.3 ps by the SMF.

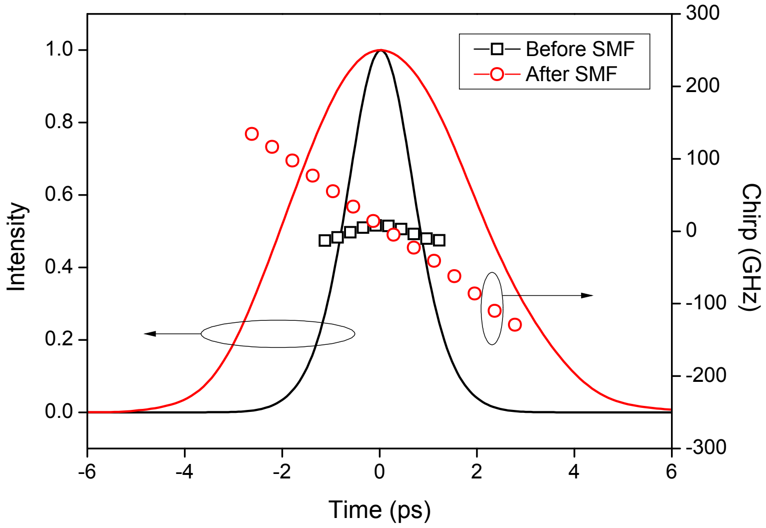

4.15. Intensity profiles and frequency chirp for pulse before and after 450 m SMF.

The spectra of a pulse both before and after injection to the SOA are shown in Fig. 4.16. The pulse energy for this figure is 398 fJ, with the SOA bias current set to the standard configuration. The main feature of the plot is the redshift of the spectrum of the pulse at the SOA output relative to the pulse before the SOA. The change in the peak wavelength of the pulse for this pulse energy is measured as ~ 0.45 nm, which is equivalent to a frequency shift of ~ 55 GHz. A multipeak structure is also visible in the spectrum of the output pulse, due to interference effects. Both of these results are due to self phase modulation in the SOA brought about by gain saturation. Fig. 4.17 shows the frequency chirp imposed by SPM on the same output pulse, compared with the input pulse. The downshift in frequency, and thus the shift to longer wavelengths, is clear. Also plotted for reference is the input pulse intensity profile. Downshift in frequency at the leading edge of the pulse is ~ 55 GHz, which is in agreement with the result obtained from the OSA spectral measurements.

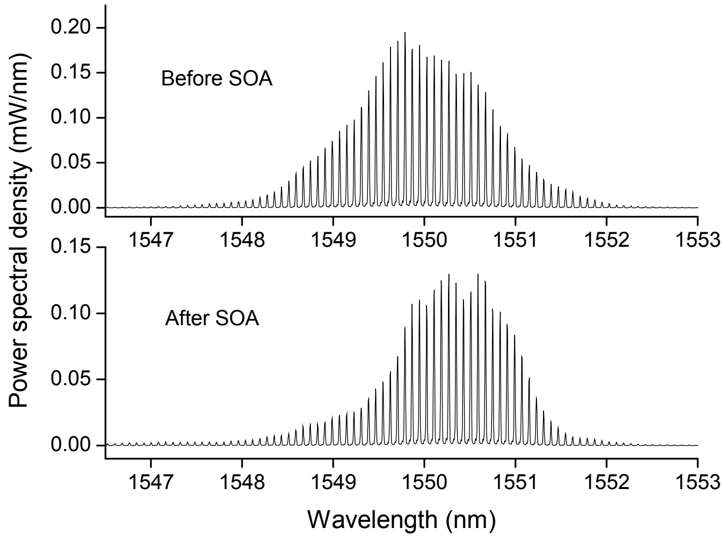

4.16. Optical spectra of 398 fJ pulse before and after injection in SOA, bias in standard configuration. Power at output is measured as lower than input due to coupling losses to SOA.

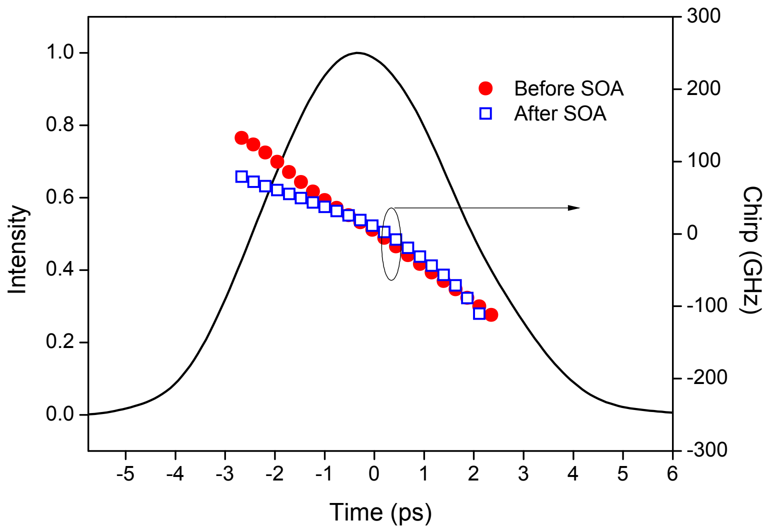

4.17. FROG trace showing frequency chirp of 398 fJ pulse before and after injection into SOA, which is biased in standard configuration. Intensity profile of input pulse plotted for reference.

The extent to which SPM affects the spectral characteristics of the pulses is dependent on the SOA bias configuration, as illustrated in Fig. 4.18. This shows the change in peak wavelength of the pulses as a function of the input pulse energy. The smallest wavelength shift is seen in the high P_{sat} bias configuration, indicating that the strength of the SPM effect is reduced due to the relatively low saturation of the gain.

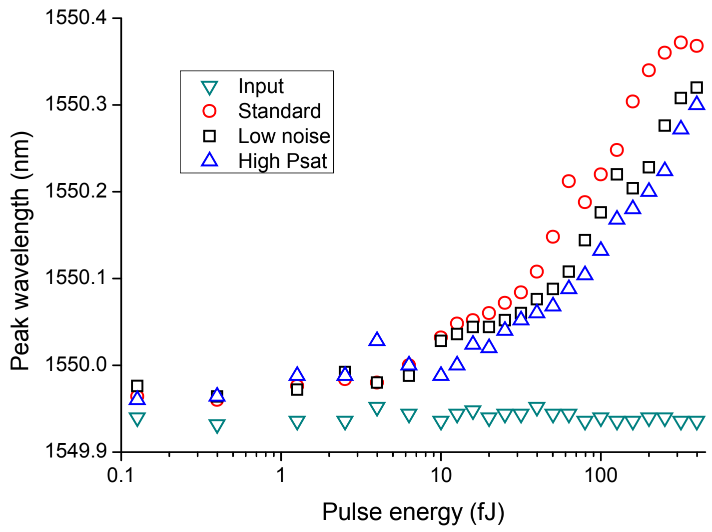

4.18. Wavelength of pulse spectrum peak as a function of input pulse energy, for different bias configurations. Input pulse spectral peak position is also plotted for reference.

Another notable feature of the optical spectra shown in Fig. 4.16 is that the spectral width of the output pulse is narrower than that of the input pulse. This is a direct consequence of SPM, combined with the negative chirp of the pulse before injection into the SOA. The standard bias configuration shows a more significant effect, with a reduction in spectral width of up to 25 GHz at input pulse energy of 398 fJ. The smallest effect is seen in the high P_{sat} bias configuration, due to the weaker SPM process in this case. It is expected that for initially up-chirped pulses, the resultant spectral broadening would be least detrimental in the high P_{sat} bias configuration. These results are shown in Fig. 4.19.

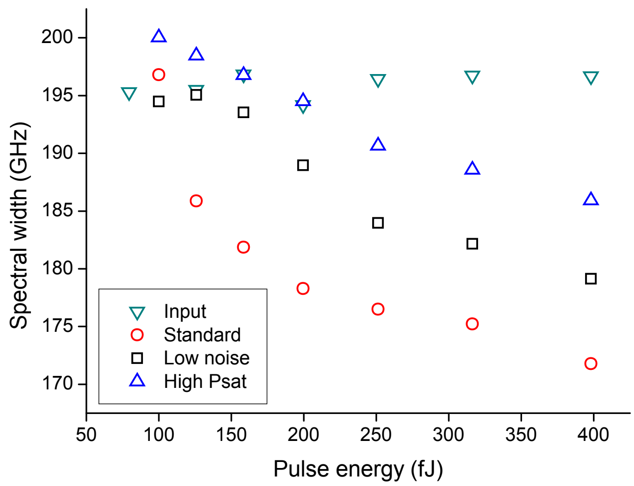

4.19. Spectral width of pulses at output of SOA as a function of input pulse energy. Spectral width of pulses at input of SOA also plotted for comparison.

4.4. Summary

The effects of the bias current distribution in the multi-contact SOA on signal amplification have been demonstrated. Analysis of the measured eye diagrams of an NRZ PRBS signal showed the increased noise evident on the signal in the high P_{sat} bias configuration, when compared with the low noise bias configuration, in the low power regime. This is clearly manifested in a reduced sensitivity improvement over the back to back case at a bit error rate of 10^{-9}, compared with the other bias configurations. The sensitivity improvement over back to back was almost identical for the low noise and standard bias configurations, which is consistent with the measured noise figure results from Chapter 2. In the case of high optical power transmission, the improved saturation power of the high P_{sat} configuration enables much higher optical powers to be transmitted error free compared with the standard bias configuration. An improvement of almost 4 dB was achieved. The standard configuration, despite having the largest unsaturated gain, has the lowest saturation power of the three configurations at 1550 nm, and thus patterning effects impact more strongly in this case. The amplification of picosecond scale optical pulses in the multi-contact SOA indicated similar results to the high power data transmission experiment. Again, the standard bias configuration exhibited the greater temporal broadening of pulses, while the high P_{sat} configuration suffered from a less significant penalty. The spectral distortions induced by self phase modulation showed a similar trend. It is expected that, in the case of positively chirped optical pulses, the standard bias configuration would suffer significant temporal and spectral broadening compared with both the low noise and high P_{sat} bias configurations. The results of this chapter indicate the advantage of flexible control of the SOA carrier density for minimizing non-linear effects when SOAs are used for in-line amplification.

References

[1] Spiekman L.H. et. al.; “Recent advances in WDM applications of semiconductor optical amplifiers,” *ECOC 2000*, Vol. 1, pp. 35 – 38, 2000

[2] Iannone P.; Frigo, N.J.; " Applications of SOAs in Optical Access and Metro Networks," in *Optical Amplifiers and Their Applications*, OSA Technical Digest Series (Optical Society of America, 2001), paper OTuC1.

[3] Michie, C.; Kelly, T.; Andonovic, I.; McGeough, J.; "Reach extension of passive optical networks using semiconductor optical amplifiers," *10th Anniversary International Conference on Transparent Optical Networks*, 2008. Vol.1, No., pp.194-197, 22-26 June 2008

[4] Spiekman, L.H.; Gnauck, A.H.; Wiesenfeld, J.M.; Garrett, L.D.; , "WDM transmission using semiconductor optical amplifiers," *13th Annual Meeting IEEE Lasers and Electro-Optics Society*, 2000, Vol.1, No., pp.271-272 vol.1, 2000

[5] Islam, M.N.; , "Raman amplifiers for telecommunications," *IEEE Journal of Selected Topics in Quantum Electronics*, Vol.8, No.3, pp.548-559, May/Jun 2002

[6] Tangdiongga, E.; Crijns, J.J.J.; Spiekman, L.H.; van den Hoven, G.N.; de Waardt, H.; "Performance analysis of linear optical amplifiers in dynamic WDM systems," *IEEE Photonics Technology Letters*, vol.14, no.8, pp. 1196- 1198, Aug 2000

[7] Spiekman, L.H.; Wiesenfeld, J.M.; Gnauck, A.H.; Garrett, L.D.; Van Den Hoven, G.N.; Van Dongen, T.; Sander-Jochem, M.J.H.; Binsma, J.J.M.; "Transmission of 8 DWDM channels at 20 Gb/s over 160 km of standard fiber using a cascade of semiconductor optical amplifiers," *IEEE Photonics Technology Letters*, vol.12, no.6, pp.717-719, Jun 2000

[8] Sun, Y.; Srivastava, A.K.; Banerjee, S.; Sulhoff, J.W.; Pan, R.; Kantor, K.; Jopson, R.M.; Chraplyvy, A.R.; "Error-free transmission of 32×2.5 Gbit/s DWDM channels over 125 km using cascaded in-line semiconductor optical amplifiers," *Electronics Letters* , vol.35, no.21, pp.1863-1865, 14 Oct 1999

[9] Seoijin Park; R. Leavitt; R. Enck; V. Luciani; Y. Hu; P.J.S. Heim; D. Bowler; M. Dagenais; , "Semiconductor optical amplifier for CWDM operating over 1540-1620 nm," *IEEE Photonics Technology Letters*, vol.17, no.5, pp.980-982, May 2005

[10] Connolly, M.J.; “Semiconductor Optical Amplifiers”, Kluwer Academic Publishers, 2002.

[11] LaViolett, K.D.; "The use of semiconductor-optical-amplifiers for long optical links in the CATV upstream optical network," *IEEE Photonics Technology Letters*, vol.10, no.8, pp.1165-1167, Aug 1998

[12] Mikkelsen, B.; Jorgensen, C.G.; Jensen, N.; Durhuus, T.; Stubkjaer, K.E.; Doussiere, P.; Fernier, B.; "High-performance semiconductor optical preamplifier receiver at 10 Gb/s," *IEEE Photonics Technology Letters*, vol.5, no.9, pp.1096-1097, Sep 1993

[13] T. Kimura; S. Bjorlin; Hsu-Feng Chou; Qi Chen; Shaomin Wu; J.E. Bowers; "Optically preamplified receiver at 10, 20, and 40 Gb/s using a 1550-nm vertical-cavity SOA," *IEEE Photonics Technology Letters*, vol.17, no.2, pp.456-458, Feb. 2005

[14] Tauke-Pedretti, A.; Dummer, M.; Barton, J.S.; Sysak, M.N.; Raring, J.W.; Coldren, L.A.; "High saturation power and high gain integrated photoreceivers," *IEEE Photonics Technology Letters*, vol.17, no.10, pp. 2167- 2169, Oct. 2005

[15] Ducellier, T.; Goix, M.; Hebert, J.P.; Legouezigou, O.; N'Go, R.; Pommereau, F.; Tscherptner, N.; Pasquier, J.; Gaborit, F.; Pagnod, P.; Grard, E.; Artigaud, S.; Blanconnier, P.; Giraudet, L.; "Compact high sensitivity 10 Gbit/s SOA-filter-pin receiver module ," *Electronics Letters*, vol.33, no.6, pp.509-510, 13 Mar 1997

[16] Yonggyoo Kim, Hodeok Jang, Yonghoon Kim, Jeongsuk Lee, Donghoon Jang, and Jichai Jeong; "Transmission Performance of 10-Gb/s 1550-nm Transmitters Using Semiconductor Optical Amplifiers as Booster Amplifiers," *Journal of Lightwave Technology*, vol.21, no.2, pp.476, 2003

[17] Borghesani, A.; Fensom, N.; Scott, A.; Crow, G.; Johnston, L.M.; King, J.A.; Rivers, L.J.; Cole, S.; Perrin, S.D.; Scrase, D.; Bonfrate, G.; Ellis, A.D.; Crouzel, G.; How Kee Chun, L.S.; Lupu, A.; Mahe, E.; Maigne, P.; Lealman, I.F.; "High Saturation Power (>16.5dBm) and Low Noise Figure (<6dB) Semiconductor Optical Amplifier for C-band Operation," in *Optical Fiber Communication Conference*, Technical Digest (Optical Society of America, 2003), paper ThO1.

[18] Akiyama, T.; Ekawa, M.; Sugawara, M.; Kawaguchi, K.; Hisao Sudo; Kuramata, A.; Ebe, H.; Arakawa, Y.; "An ultrawide-band semiconductor optical amplifier having an extremely high penalty-free output power of 23 dBm achieved with quantum dots," *IEEE Photonics Technology Letters*, vol.17, no.8, pp.1614-1616, Aug. 2005

[19] Berg, T.W.; Mork, J.; , "Saturation and noise properties of quantum-dot optical amplifiers," *IEEE Journal of Quantum Electronics*, vol.40, no.11, pp. 1527- 1539, Nov. 2004

[20] Keiser, G.; "Optical Fiber Communications", McGraw-Hill, 1991.

[21] http://www.ieee802.org/3/ba/PAR/P802.3ba_Objectives_0709.pdf.

[22] Bergano, N.S.; Kerfoot, F.W.; Davidsion, C.R.; , "Margin measurements in optical amplifier system," *IEEE Photonics Technology Letters*, vol.5, no.3, pp.304-306, Mar 1993

[23] Latkowski, S.; Maldonado-Basilio, R.; Landais, P.; "Sub-picosecond pulse generation by 40-GHz passively mode-locked quantum-dash 1-mm-long Fabry-Pérot laser diode," *Optics Express*, vol.17, no.21, pp.19166-19172, 2009

[24] Tucker, R.S.; Eisenstein, G.; Korotky, S.K.; "Optical time-division multiplexing for very high bit-rate transmission," *Journal of Lightwave Technology*, vol.6, no.11, pp.1737-1749, Nov 1988

[25] Personick, S.D.; , "Receiver design for optical fiber systems," *Proceedings of the IEEE* , vol.65, no.12, pp. 1670- 1678, Dec. 1977

[26] Boivin; L.; Nuss; M.C.; Shah, J.; Miller; D.A.B.; Haus, H.A.; "Receiver sensitivity improvement by impulsive coding," *IEEE Photonics Technology Letters*, vol.9, no.5, pp.684-686, May 1997

[27] Breuer, D.; Petermann, K.; "Comparison of NRZ- and RZ-modulation format for 40-Gb/s TDM standard-fiber systems," *IEEE Photonics Technology Letters*, vol.9, no.3, pp.398-400, March 1997

[28] Hayee, M.I.; Willner, A.E.; "NRZ versus RZ in 10-40-Gb/s dispersion-managed WDM transmission systems," *IEEE Photonics Technology Letters*, vol.11, no.8, pp.991-993, Aug 1999

[29] Smith, P.W.; "Mode-locking of lasers," *Proceedings of the IEEE*, vol.58, no.9, pp. 1342- 1357, Sept. 1970

[30] Bowers, J.E; Morton, P.A.; Mar, A.; Corzine, S.W.; "Actively mode-locked semiconductor lasers", *IEEE Journal of Quantum Electronics*, vol.25, no.6, pp.1426-1439, 1989

[31] Silberberg, Y.; Smith, P.W.; Eilenberger, D.J.; Miller, D.A.B.; Gossard, A.C.; Wiegmann, W.; "Passive mode locking of a semiconductor diode laser," *Optics Letters*, vol.9, no.11, pp.507-509, 1984

[32] Delfyett, P.J.; Lee, C.-H.; Florez, L.T.; Stoffel, N.G.; Gmitter, T.J.; Andreadakis, N.C.; Alphonse, G.A.; Connolly, J.C.; "Generation of subpicosecond high-power optical pulses from a hybrid mode-locked semiconductor laser," *Optics Letters*, vol.15, no.23, pp.1371-1373, 1990

[33] Agrawal, G.P.; "Fiber Optic Communications Systems", John Wiley & Sons, 1997.

[34] Tang, J.M.; Spencer P.S.; Shore, K.A.; "The influence of gain compression on picosecond optical pulses in semiconductor optical amplifiers", *Journal of Modern Optics*, vol.45, no.6, 1998.

[35] Henry, C.; "Theory of the linewidth of semiconductor lasers," *IEEE Journal of Quantum Electronics*, vol.18, no.2, pp. 259- 264, Feb 1982

[36] Storkfelt, N.; Mikkelsen, B.; Olesen, D.S.; Yamaguchi, M.; Stubkjaer, K.E.; "Measurement of carrier lifetime and linewidth enhancement factor for 1.5 μm ridge-waveguide laser amplifier," *IEEE Photonics Technology Letters*, vol.3, no.7, pp.632-634, July 1991

[37] Agrawal, G.P.; Olsson, N.A.; "Self-phase modulation and spectral broadening of optical pulses in semiconductor laser amplifiers," *IEEE Journal of Quantum Electronics*, vol.25, no.11, pp.2297-2306, Nov 1989

[38] Delfyett, P. J.; Silberberg, Y.; Alphonse, G. A.; "Hot-carrier thermalization induced self-phase modulation in semiconductor traveling wave amplifiers," *Applied Physics Letters*, vol.59, no.1, pp.10-12, Jul 1991

[39] Tomlinson, W.J.; Stolen, R.H.; Shank, C.V.; "Compression of optical pulses chirped by self-phase modulation in fibers," *Journal of the Optical Society of America B*, vol.1, no.2, pp.139-149, 1984.

[40] Gomes, A.S.L.; Gouveia-Neto, A.S.; Taylor, J.R.; "Optical fibre-grating pulse compressors", *Optical and Quantum Electronics*, vol. 20, no. 2, pp.95-112, Mar 1988.

[41] Agrawal G.P.; Olsson, N.A.; "Amplification and compression of weak picosecond optical pulses by using semiconductor-laser amplifiers," *Optics Letters*, vol.14, no.10, pp.500-502, 1989

[42] Watanabe, T.; Sakaida, N.; Yasaka, H.; Koga, M.; "Chirp control of an optical signal using phase modulation in a semiconductor optical amplifier," *IEEE Photonics Technology Letters*, vol.10, no.7, pp.1027-1029, Jul 1998

[43] Planas, S.A.; Pires Mansur, N.L.; Brito Cruz, C.H.; Fragnito, H.L.; "Spectral narrowing in the propagation of chirped pulses in single-mode fibers," *Optics Letters*, vol.18, no.9, pp.699-701, 1993

[44] Washburn, B.R.; Buck, J.A.; Ralph, S.E.; "Transform-limited spectral compression due to self-phase modulation in fibers," *Optics Letters*, vol.25, no.7, pp.445-447, 2000

[45] Shuai Shen; Cheng-Chun Chang; Sardesai, H.P.; Binjrajka, V.; Weiner, A.M.; "Effects of self-phase modulation on sub-500 fs pulse transmission over dispersion compensated fiber links," *Journal of Lightwave Technology*, vol.17, no.3, pp.452-461, Mar 1999

[46] Cundiff, S.T.; Collings, B.C.; Boivin, L.; Nuss, M.C.; Bergman, K.; Knox, W.H.; Evangelides, S.G., Jr.; "Propagation of highly chirped pulses in fiber-optic communications systems," *Journal of Lightwave Technology*, vol.17, no.5, pp.811-816, May 1999

[47] Andresen, E.R.; Dudley, J.M.; Oron, D.; Finot, C.; Rigneault, H.; "Transform-limited spectral compression by self-phase modulation of amplitude-shaped pulses with negative chirp," *Optics Letters*, vol.36, no.5, pp.707-709, 2011

[48] Kane, D.J.; Trebino, R.; "Characterization of arbitrary femtosecond pulses using frequency-resolved optical gating," *IEEE Journal of Quantum Electronics*, vol.29, no.2, pp.571-579, Feb 1993

[49] Trebino R.; Kane, D.J.; "Using phase retrieval to measure the intensity and phase of ultrashort pulses: frequency-resolved optical gating," *Journal of the Optical Society of America A*, vol.10, no.5, pp.1101-1111, 1993

[50] DeLong, K.W.; Trebino, R.; Hunter, J.; White, W.E.; "Frequency-resolved optical gating with the use of second-harmonic generation," *Journal of the Optical Society of America B*, vol.11, no.11, pp.2206-2215, 1994

[51] Saitoh, T.; Mukai, T.; "Gain saturation characteristics of traveling-wave semiconductor laser amplifiers in short optical pulse amplification," *IEEE Journal of Quantum Electronics*, vol.26, no.12, pp.2086-2094, Dec 1990

5. Effect of Carrier Distribution on Wavelength Conversion Characteristics

5.1. Introduction

Previous chapters have focused on the applications of SOAs, and in particular the SOAs under investigation in this thesis, for in-line amplification and data transmission. The technologies available for this functionality are relatively mature, with widespread use of EDFAs in long-haul transmission and increasing adoption of SOAs and other technologies in metro and access networks. The use of SOAs in optical networks allows added functionality not possible with fibre amplifiers due to the non-linear interaction of photons in the semiconductor medium that give rise to potentially useful effects, including signal processing, switching and wavelength conversion. In the last two decades, the augmentation and improvement of communications networks by utilizing the nearly limitless bandwidth of optical fibre has proceeded at a rapid pace [1]. In order to maximize this enormous potential and properly implement higher speed networks, a transparent network is required [2, 3]. Transparency in this sense means that the network is able to deal with and process any data format, bit rate or modulation scheme in the optical domain. A transparent network would incorporate all wavelength conversion and cross-connects in an all-optical format, that is, without recourse to opto-electro-optical (OEO) conversion [4].

In order to provide a clear optical path between the source and destination of a particular channel in a Wavelength Division Multiplexed (WDM) network, switching wavelengths is necessary to allow the full utilization of the available network bandwidth. At present the most common method of signal processing and wavelength conversion is to detect the input optical signal and convert it to electronic format using a photodetector, and retransmit the signal at the same or another wavelength by modulating a laser [5]. The technologies used for the electro-optical (EO) technique are mature and it has distinct advantages, including the ready implementation of 3R regeneration (retiming, reshaping, reamplification), and the detection of the optical signal can accommodate a wide range of input power levels and any signal polarization state. However it suffers from a number of disadvantages. The components of an EO wavelength converter can be expensive, and their power consumption can be considerably higher than that of other technologies, with the power required increasing for higher bit rates [6]. Upgradability is another serious issue; generally, the sensitivity of an EO wavelength converter is optimized for the highest bit rate it will encounter, and as such higher bit rates could pose problems for such systems. The primary disadvantage with EO switching, however, is the issue of transparency, which was mentioned above [7]. There are two main issues regarding transparency. Firstly, when the optical signal is terminated at a photodiode, all phase, polarization and wavelength information is lost. Secondly, the maximum switching speed of an EO converter will always be limited when compared to all-optical approaches, since the conversion to an electrical signal is slower than an optical signal, and as bit rates increase beyond 40Gb/s [8], the “electronic bottleneck” becomes more of a problem. Therefore, for future optical networks, the development of optical switching solutions is of particular importance.

5.2. Switching and wavelength conversion in WDM networks

5.2.1. Wavelength Division Multiplexing

In order to utilize the full bandwidth capacity of optical fibre, wavelength division multiplexing was developed, multiplying the capacity of optical networks [9]. Previously, to increase the capacity of a network beyond what was possible using Time Division Multiplexing (TDM), additional fibre would have to be laid to carry extra channels. WDM solves this problem by transmitting multiple channels within the same fibre, each channel having a separate wavelength [10]. These individual channels in turn may service multiple users through TDM. The aggregate bit rate passing through a WDM node could potentially be on the order of multiple Terabits per second [11]. For example, a WDM scheme with 40 channels, each modulated at 40 Gb/s, gives an aggregate bit rate of 1.6 Tb/s [12]. WDM schemes are classified into categories depending on the number of channels that are transmitted. Coarse WDM (CWDM) utilizes a channel spacing of 20 nm, within a wavelength range of 1271nm to 1611nm [13]. The wide spacing allows for the use of cheaper and less capable receivers and other equipment. Dense WDM (DWDM) on the other hand provides for channel spacing down to 12.5 GHz, or ~ 0.1 nm, with central wavelengths generally contained within the C-band in order to avail of optical amplification by EDFAs [14]. A DWDM transmission system consists of a number of components, as seen in Fig. 5.1.

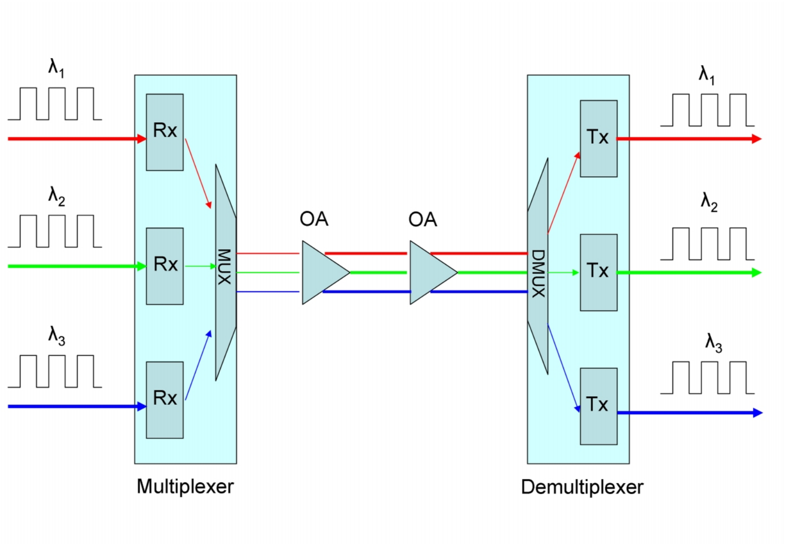

5.1. Schematic of a WDM system. Rx – receiver; MUX – multiplexer; DMUX – demultiplexer; OA – optical amplifier; Tx – transmitter.

A multiplexer at the Optical Line Terminal (OLT) terminates multiple channels from different fibres and retransmits the electrical signals into a single fibre using a 1550nm band laser. The transmitter can be combined with an optical amplifier to extend the range. The signal may be amplified at some point along the signal path by EDFAs before it reaches the terminal demultiplexer, which separates the combined channels into individual fibres.

5.2.2. Applications of wavelength conversion

Key to maximizing the efficiency of a WDM network is the ability to change the transmission wavelength of a particular channel depending on the network requirements [15]. This process is called wavelength conversion. There are numerous applications where wavelength conversion is necessary in an optical network; cross connects, which switch optical channels within a mesh network; add/drop multiplexers, which filter out or add specific channels; and in optical signal monitoring.

Optical cross-connects

Optical cross-connects (OXCs) are used where bandwidth management is important, such as where multiple WDM transmission routes converge in a mesh network. They have they ability to switch channels from one fibre to another at a basic level. This is a vital function to enable a clear channel to be opened up between the source and end user. OXCs also allow the optical network to reconfigure to bypass failures in a particular node or fibre. More advanced cross-connects add the capability of wavelength conversion [16, 17]. OXCs incorporating this capability are important network elements in terms of reducing blocking caused by wavelength contention. This problem can arise when two channels at the same wavelength are to be routed to the same output node. In this case, one of the channels must be converted to another wavelength. By doing so, the wavelength contention is resolved.

Optical add/drop multiplexers

Optical add/drop mutiplexers (OADMs) perform a similar task to cross-connects in that they involve rerouting particular optical channels. In the case of an OADM however, it is usually only one channel, or a limited number, that need to be rerouted. OADMs are used when a wavelength channel needs to be added and/or dropped from the multiplexed signal [18, 19]. This is accomplished through demultiplexing and filtering technologies. OADMs are categorized according to their capabilities. Fixed OADMs do not utilize switching. They are concerned with adding or dropping a particular wavelength. Reconfigurable OADMs (R-OADMs) on the other hand have the capability, through wavelength conversion, to add or drop arbitrary wavelengths, and in this sense most resembles an OXC.

Advantages of optical wavelength conversion

As mentioned previously, there are numerous drawbacks to wavelength conversion and switching when using EO conversion, namely the lack of transparency and the "electronic bottleneck" that results from the limited speed of electronics. The ultimate end goal is that all wavelength conversion tasks in optical networks would be performed in the optical domain [20]. As the signal is not terminated and converted to electrical form, information such as the phase and polarization of the signal are preserved. Most importantly, an optical switching system is inherently upgradeable in terms of increasing bit rates, which in the long term greatly decreases the cost of the network.

5.2.3. All-optical wavelength converters

There are numerous techniques used to achieve wavelength conversion in the optical domain, each with their own benefits and drawbacks. Key goals to be achieved by an optical wavelength converter include:

- Optical transparency
- High switching speeds
- Good conversion efficiency
- Low SNR
- Simplicity

Optical wavelength converters can be grouped into different categories depending on the physical mechanism involved in the conversion process, as outlined below.

Optical gating wavelength converters

1) **Non-linear optical loop mirror (NOLM)** – A NOLM consists essentially of a Sagnac interferometer, using a non-linear medium such as a dispersion shifted fibre instead of free space mirrors. In a Sagnac interferometer, a beam is split using a half silvered mirror, with the two resultant beams traversing an optical path in opposite directions. Asymmetry in the paths of the two beams causes an interference pattern to appear, while no asymmetry causes destructive interference, with no output beam appearing. In a NOLM, an additional modulated signal is coupled to the fibre, propagating in a certain direction. This modulates the refractive index of the non-linear fibre due to the optical Kerr effect. As a result, the phase of the probe beam propagating in the same direction as the signal increases, and the resultant asymmetry causes the modulated probe beam to appear at the output [21, 22].
2) **Saturable absorption and intensity modulation in semiconductor lasers –** For the saturable absorber technique, a modulated signal saturates the absorption when a "1" is transmitted, allowing the simultaneous transmission of a probe signal at a different wavelength [23, 24]. The bandwidth of this method is restricted due to the time taken for carrier recombinations. The bandwidth can be increased in laser diodes by modulating the intensity of the lasing mode through the injection of a modulated signal. In this way, the signal can be converted to the wavelength of the lasing mode. The bandwidth is increased due to the role of the stimulated emission in the laser diode reducing the effective carrier lifetime.
3) **Cross gain modulation in SOAs –** Cross gain modulation (XGM) is a technique that utilizes the homogeneously broadened gain of an SOA. A pump data stream modulates the gain of the SOA, and this modulation is imprinted onto a probe beam at another wavelength. This topic is discussed in more detail in the following section.

4) **Cross phase modulation in SOAs –** When the gain of an SOA is modulated by a pump beam, such as in XGM as described above, it is accompanied by a simultaneous modulation of the refractive index. If a probe beam is injected into the SOA, it experiences a phase shift due to this refractive index modulation. If an interferometer is used, this phase modulation can be translated to an intensity modulation [25, 26, 27]. Fig. 5.2 shows a basic symmetric Mach-Zehnder interferometer incorporating two SOAs.

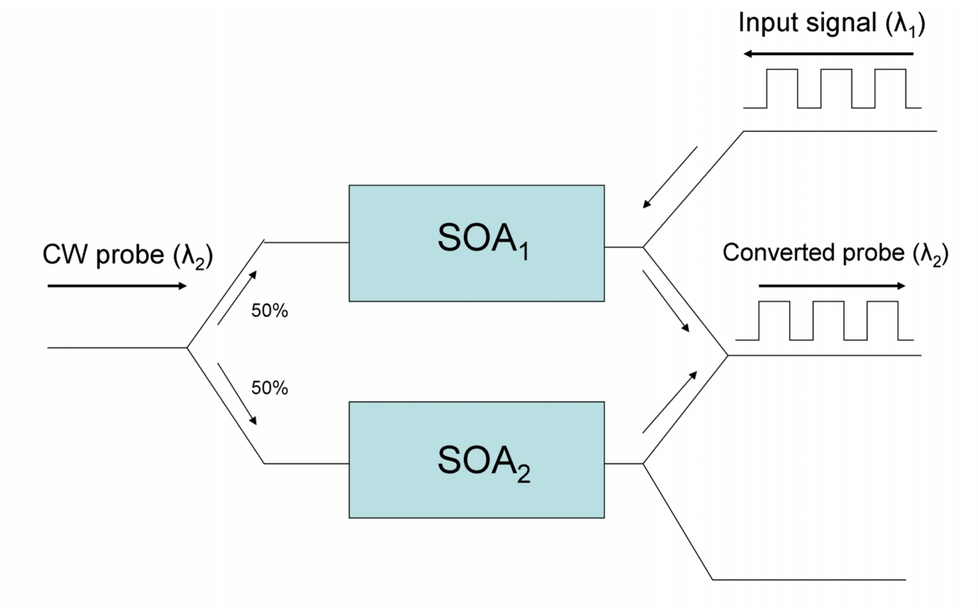

5.2. Symmetric Mach-Zehnder interferometer incorporating XPM in SOAs.

A CW probe beam at λ_2 is coupled to the two SOAs through a 50:50 coupler. Simultaneously a modulated pump signal at λ_1 is coupled to SOA_1 at the output facet. The refractive index modulation introduced by the pump changes the phase of the probe beam in SOA_1 relative to SOA_2. When the probe beams are recombined, they can interfere either constructively (outputting a logical “1”) or destructively (logical “0”). In this way, a XPM wavelength converter can act as an effective switch, tunable through both the bias current of the SOA (controlling the magnitude of the carrier density modulation) and the power of the input signal. XPM converters have been shown to have higher conversion efficiency than XGM converters. A lower input power is required to achieve the necessary phase shift of π radians than is required for XGM, leading to a lower frequency chirp. Additionally, the converted signal remains non-inverted, with no difference in extinction ratio for up- or down-converted wavelengths. One disadvantage of XPM conversion schemes is the requirement for strict bias current control, due to the strong dependency of the induced phase shift on bias current.

Wave-mixing wavelength converters

1) **Difference frequency generation in passive waveguides** – Difference frequency generation (DFG) is the non-linear interaction of two waves, a pump and a probe wave, in a non-linear medium such as a $LiNbO_3$ or AlGaAs passive waveguide [28]. The advantage of this technique over other techniques such as four wave mixing (FWM) in SOAs is that the conversion process in passive waveguides adds no excess noise to the converted signal, and the satellite signals that occur in FWM are absent. DFG is an optically transparent process, maintaining phase and modulation information at any bit rate. The main issue with DFG is the difficulty of maintaining phase matching over the interaction length. There is also the challenge of fabricating low loss waveguides with high conversion efficiency. Typical conversion efficiencies are on the order of -6 dB.
2) **Four wave mixing in SOAs** – FWM in SOAs results from the interaction between a pump beam and a probe beam in the non-linear medium of the SOA. It allows relatively efficient wavelength conversion through gain enhancement, albeit with the addition of optical noise. This topic is discussed in more detail in section 5.4.

There are different degrees of transparency offered by the various optical wavelength converters. The only techniques offering full transparency are the wave mixing techniques, although a balance has to be struck between this feature and other considerations, such as conversion efficiency and signal to noise ratio. In this chapter the focus will be on an optical gating technique, XGM, and a wave mixing technique, FWM. The goal of this work is to demonstrate the effect of the carrier density distribution in the MC-SOA on the characteristics of each wavelength conversion process.

5.3. Cross gain modulation in MC-SOA

5.3.1. Introduction

As previously discussed, cross gain modulation (XGM) is an example of an optical gating wavelength conversion technique. It is the most conceptually and practically simple design that has been discussed herein. It takes advantage of the non-linear gain suppression mechanism in semiconductor optical amplifiers.

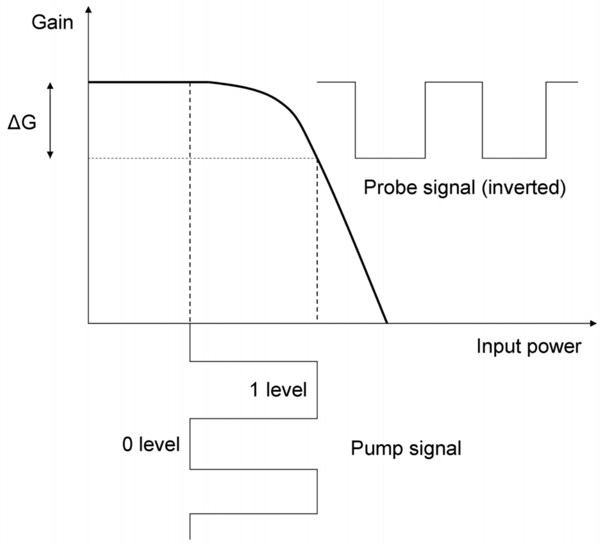

5.3. Visualization of non-linear gain reduction in SOA due to pump signal saturation.

As the input power to an SOA is increased, the optical gain is decreased due to the stimulated recombination of carriers, which is proportional to the input signal photon density. For a modulated pump signal, when the optical power is high ("1" level), the carrier density is depleted, while for low optical power, no depletion occurs. Because the material gain spectrum of an SOA is homogeneously broadened, the gain of the SOA at all wavelengths is compressed when saturated by the pump signal. Therefore, when a CW probe signal at the converted wavelength is injected simultaneously into the SOA, as per Fig. 5.3, the gain modulation caused by the pump signal is imprinted onto the probe, modulating it with the inverse bit pattern to that of the pump signal. The probe signal can be injected at the same facet as the pump (co-propagation) or at the opposite facet (counter-propagation). When injected in co-propagation mode, as in Fig. 5.4, an optical band-pass filter must be used at the output of the SOA in order to pass the converted probe signal and block the pump.

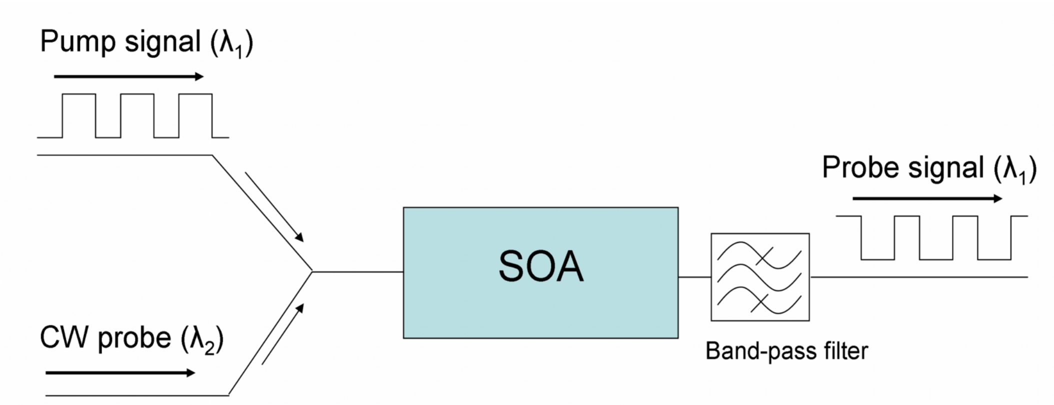

5.4. Co-propagating XGM wavelength conversion scheme.

The modulation bandwidth of an XGM converter is determined by the carrier recovery time. If the data rate is high enough such that the conduction band population, and hence the gain, does not have time to recover, patterning effects begin to appear. Another limitation on XGM wavelength converters is the amount of wavelength chirp experienced by the converted signal. This can make transmission over long distances difficult in the absence of dispersion shifted fibre. Despite these impairments, impressive performance of XGM wavelength converters has been demonstrated. The fast gain recovery properties of quantum dot SOAs have been utilized to achieve pattern free wavelength conversion at up to 160Gb/s [29, 30, 31, 32]. The use of optical filters to select the blue chirped components of the modulated output probe signal allows for a significant improvement in the modulation bandwidth, with the consequence of a loss of signal to noise ratio [33, 34, 35, 36]. Another successful approach is that of the turbo switch, in which the gain dynamics of a second SOA placed after the wavelength converter are used to compensate for the slow “tail” of the converted probe signal. Error free performance was observed at over 170Gb/s [37].

For the characterization of XGM in the MC-SOA, the setup shown in Fig. 5.5 was used. The pump and probe signals, both generated using external cavity lasers (ECLs) of the same type used in the previous experiments, were arranged in co-propagation mode. The CW probe signal was set at 0 dBm input power. The pump signal was modulated at 2.5 Gb/s using a pseudo random binary sequence (PRBS) source with a bit pattern length of 2^7-1 binary symbols. The PRBS signal was amplified using an electrical amplifier with 25 dB gain, and a splitter was used in order to allow both modulation of the pump signal and to trigger a sampling oscilloscope. The wavelength of the pump signal was initially set to 1570 nm, which is the peak gain wavelength of the SOA in the low noise and high P_{sat} bias configurations. The pump signal power was varied between 2 dBm and 10 dBm (prior to SOA injection). Both pump and probe were amplified using EDFAs (gain ~ 25 dB) before injection into the SOA. Filters and attenuators were used subsequent to amplification in order to control the final input power and to reduce the noise emanating from the EDFAs. The signals were coupled to the SOA using the free space setup utilized in Chapter 4. The coupling losses at the SOA input and output facet were measured to be ~ 4 dB per facet, which reduced the probe signal power at the input facet to -4 dBm. A polarizer was used at the SOA output in order to reduce the contribution from spontaneous beat noise. The detection scheme consisted of an additional EDFA (gain ~ 22 dB, NF ~ 4.5 dB), a tuneable filter and a sampling oscilloscope with optical input. The optical detection bandwidth of the OSO is 63 GHz. The EDFA was used in order to maintain a constant detector power of 4 dBm.

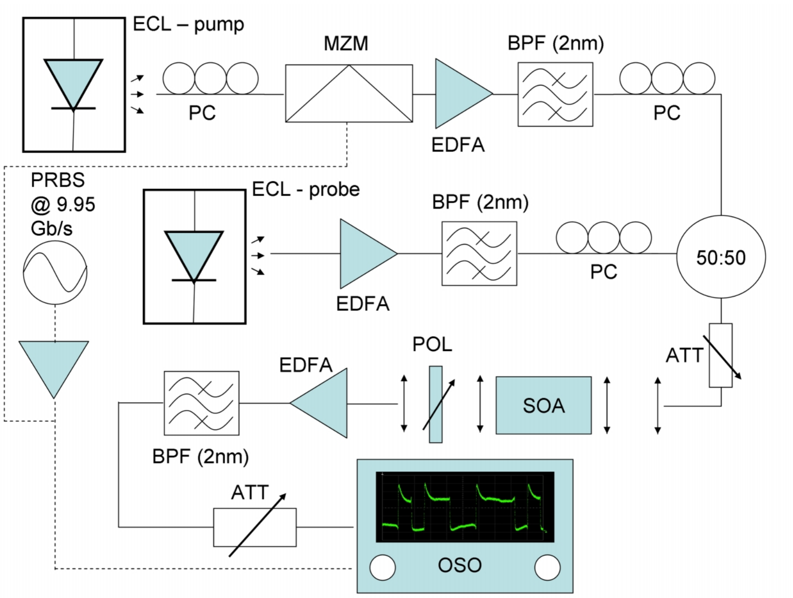

5.5. Setup diagram for XGM experiment. ECL – external cavity laser; MZM – Mach-Zehnder modulator; BPF – bandpass filter; PC – polarisation controller; EDFA – Erbium doped fibre amplifier; ATT – variable attenuator; POL – free space polariser; OSO – optical sampling oscilloscope. Optical and electrical paths are represented by solid and broken lines, respectively.

5.3.2. Noise in XGM wavelength conversion

Sources of noise in XGM wavelength converters

A key parameter in the characterization of a wavelength converter is the noise imparted to the converted signal. This noise can be described using a small-signal analysis applied to the SOA rate equation [38],

$$2\,\frac{dN_{av}}{dt} = N - N_{av}(t) - \sum_{i=s,p} \frac{x_i(L) - x_i(0)}{\Gamma g_{N_i} L}\,, \tag{5.1}$$

where N is the unsaturated carrier density, N_{av} is the average carrier density integrated over the length of the waveguide at time t, g_N is the differential gain at carrier density N, Γ is the mode confinement factor, τ is the spontaneous carrier lifetime and L is the length of the waveguide. The symbols p and s denote the pump signal and probe signal, respectively. Finally, the normalized optical power is represented by,

$$x_i(z) = \frac{P_i(z)}{P_i^{sat}}\,, \tag{5.2}$$

where $P_i(z)$ is the optical power at position z, and P_i^{sat} is the saturation power. The rate equation is solved for $i = s$ at position L, i.e. the converted output probe, with the solution given as,

$$x_s(L) = G_s\left\lfloor a(\mu)x_s(0) + b(\mu)x_p(0)\right\rfloor, \tag{5.3}$$

where G_s is the optical gain experienced by the normalized probe signal and ω is the modulation frequency of the pump signal. The coefficients a and b are defined as,

$$a(\mu) = 1 - \frac{(G_s - 1)x_s(0)}{(\mu_B + j\mu)2}\,, \tag{5.4}$$

$$b(\mu) = -\frac{(G_p - 1)x_s /}{(\mu_B + j\mu)2}\,, \tag{5.5}$$

where β is the ratio of the differential gain at the pump wavelength to that at the probe wavelength. The quantity ω_B is defined as the 3 dB bandwidth,

$$\mu_B = \frac{(1 + G_p x_p + G_s x_s)}{2}\,, \tag{5.6}$$

Thus, the noise within the bandwidth of the converted probe signal has two origins, according to Eqs. (5.3) – (5.5). The last term in Eq. (5.4) as well as the coefficient *b* describe the non-linear interaction of the pump and probe waves with the carrier density. In effect this describes the gain fluctuations caused by signal spontaneous beating on the pump signal being converted onto the output probe wave. The pump noise is "modulated" onto the converted signal. The other contribution to the noise comes from the direct transmission of the input probe noise, degraded further due to signal spontaneous beat noise from the SOA.

5.3.3. XGM noise characterisation of MC-SOA

The Q values for the converted probe signal of -4 dBm were measured for a pump signal at 1570 nm, with the pump power varied from -2 dBm to 6 dBm. All optical power values quoted in the setup are considered to be after coupling losses are taken into account. The results are shown in Fig. 5.6 for two negatively detuned probe wavelengths, 1566 nm and 1564 nm, and for two bias configurations, the low noise and high P_{sat} cases. The corresponding BER values for the 1564 nm probe wavelength are shown in Fig. 5.7. The evolution of the Q-factor shows two separate trends for both probe wavelengths and both bias configurations. At moderate pump power levels, the Q-factor increases with pump power, and then at a certain point begins to decrease. In addition to this trend, a clear difference in the magnitude of the Q-factor is observed between the two bias configurations.

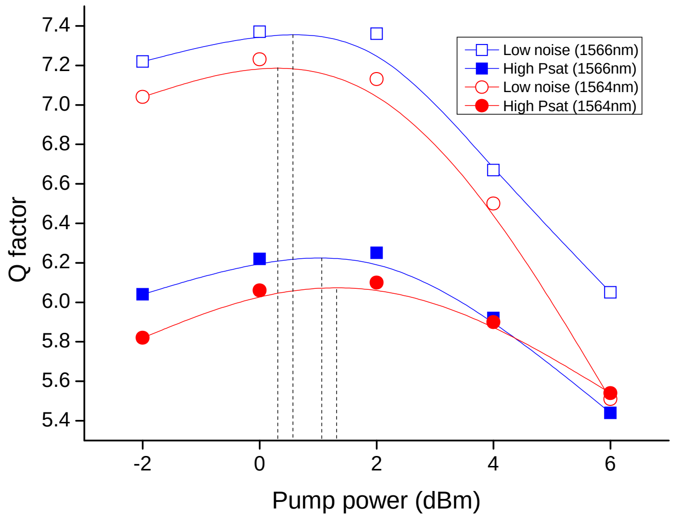

5.6. Q factor of converted probe signal, at two separate wavelengths, as a function of the injected pump power for both bias configurations under investigation. Inflection points are indicated by dashed lines. Pump wavelength is set to 1570 nm. Connecting lines are eye-guides.

The initial increasing trend in Q-factor can be explained with reference to Eqs. (5.3)-(5.5). It is clear that as x_p is increased, and G_p and G_s subsequently decreased due to gain saturation, the coefficients a and b will tend towards 1 and 0, respectively. This indicates is that the conversion of the intensity fluctuations caused by the pump noise onto the probe wavelength is suppressed at higher powers [39, 40]. The predominant source of noise at the probe wavelength in this case is the transmission noise of the input probe itself, as well as the noise of the SOA within the bandwidth of the probe. This noise suppression effect is further illustrated in Fig. 5.8. This figure shows a histogram of the measured converted probe signal eye diagram. The SOA is in the low noise bias condition. The optical power on the x-axis is normalized to the binary signal levels. This plot gives an indication of the relative magnitude of the noise (σ) at the “1” or “0” levels. Plot (a) is a histogram of the converted probe signal at -2 dBm pump power, whereas plot (b) is a histogram of the converted signal at 6 dBm pump power. This figure shows the reduction in magnitude of the noise at the “0” level when the pump power is 6 dBm, relative to the lower pump power.

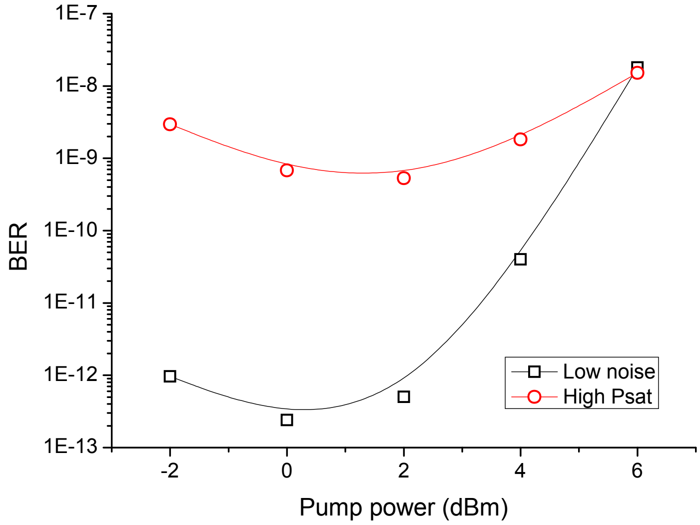

5.7. Bit error rate curves as a function of pump power for input probe wavelength of 1564 nm, for two bias configurations. Connecting lines are eye-guides.

This result illustrates the explanation given above for the suppression of noise by a strong pump signal. This noise suppression directly translates to the converted signal in terms of the "0" level noise, due to the fact that the signal waveform is inverted in XGM. The Q-factor begins to show a decreasing trend at higher pump powers [39, 41]. While the suppression of the "1" level noise is still in effect at this point, gain saturation due to the higher SOA input powers reduces the power of the output probe signal, thus degrading the SNR. This trend is illustrated in Fig. 5.9, which shows the normalized probe output power with respect to the pump power, for both bias configurations. This figure indicates that conversion efficiency of the pump signal to the probe is better in the high P_{sat} bias configuration.

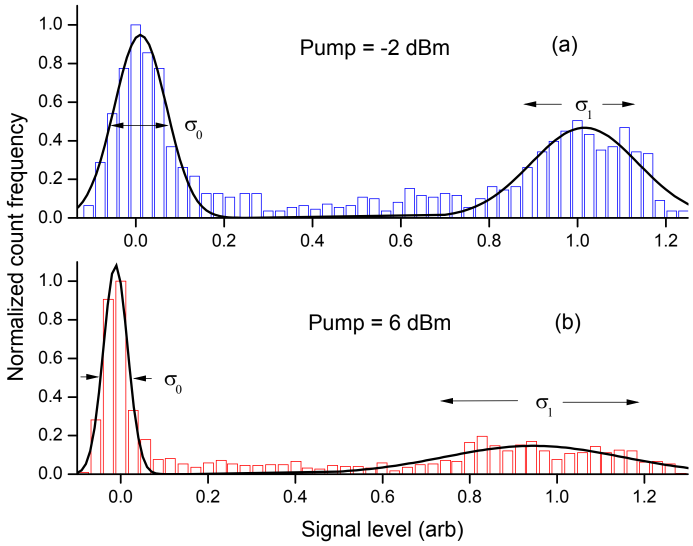

5.8. Demonstration of pump signal noise suppression and its effect on probe signal. Histograms illustrate change in probe noise levels for (a) -2 dBm pump and (b) 6 dBm pump.

A key point to note is that the gain saturation for the low noise case is more significant at a lower pump power than for the high P_{sat} case, as is to be expected. The positions of the inflection points, indicated by dashed lines, and convergence of the Q-factor curves in Fig. 5.6, as well as the convergence of the BER curves in Fig. 5.7 is evidence of the stronger effect of gain saturation on the low noise bias case. Simultaneously, as the pump "0" noise level continues to rise with pump power, gain fluctuations due to beating between the ASE photons from the pump EDFA give rise to increased noise on the converted signal "1" level. This is shown by the increase in σ_0 at the higher pump power in Fig. 5.8 (b). Gaussian fits to the histogram data indicate a reduction in σ_0 of 50 % due to the noise suppression and an increase in σ_1 of 70 %. The EDFA noise is visible on the pump "0" level in Fig. 5.10 (a), which shows the 6 dBm pump signal at the SOA output. Fig. 5.10 (b) shows, as an example, the corresponding probe signal for the low noise bias case at 1566 nm, where the noise on the "1" level is clearly seen.

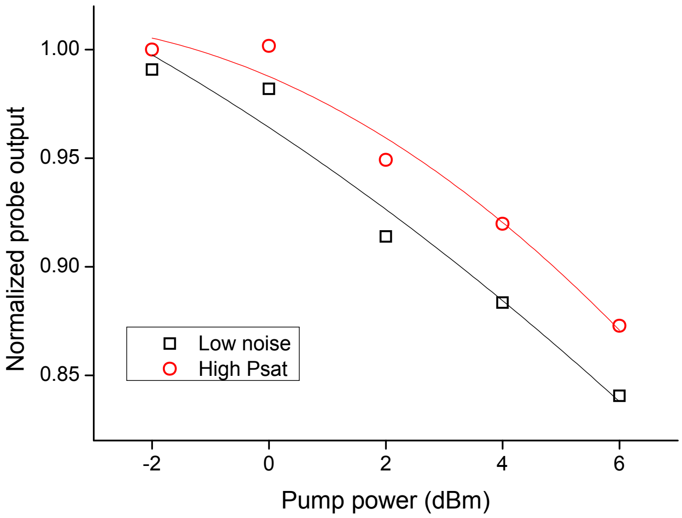

5.9. Normalized probe output power with respect to pump power for two bias conditions at a probe wavelength of 1560 nm.

The overall effect is that at the inflection points in Fig. 5.6, the reduction of the signal due to gain saturation, combined with the added EDFA noise imprinted onto the converted “1” level begins to outweigh the effect of the noise suppression caused by the strong pump signal. These results, along with the BER values from Fig. 5.7, would suggest that an optimum pump power exists in order to achieve the minimum bit error rate for a given bias configuration.

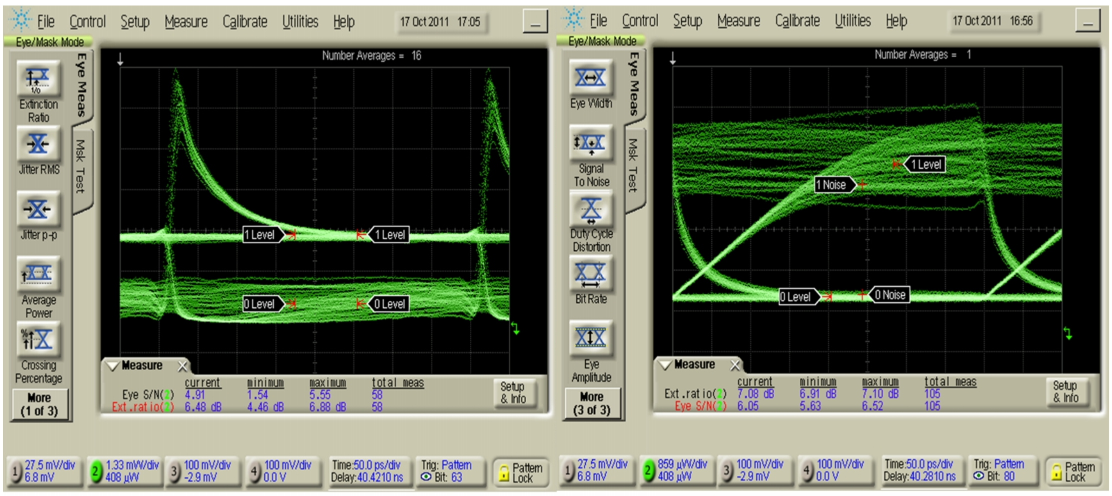

5.10. Eye diagrams of pump and probe signals at 6 dBm pump power. The waveform on the left (a) is the pump signal at the SOA output, while the waveform on the right (b) is the output probe signal at 1566 nm.

The large discrepancy between bias conditions in the Q-factor at moderate pump powers is due to the same reason that co-propagating pump and probe signals yield a larger SNR than counter-propagating signals [42]. In the case of co-propagating signals in a normal SOA, the pump signal depletes carriers as it traverses the waveguide, creating a carrier density profile similar to the low noise profile under investigation in this work. Conversely, when the pump signal is injected at the output of the SOA, the opposite carrier density profile results, and thus the probe signal experiences a higher population inversion factor at the SOA input, increasing the overall noise figure. Both situations are replicated in the MC-SOA depending on the bias current distribution, assuming that the saturation of the SOA due is mainly determined by the pump signal. This particular result suggests that the main influence on the Q-factor of the converted probe signal is the ASE at the output of the SOA.

5.3.4. Variation in extinction ratio

The extinction ratio of a wavelength converter is defined simply as the ratio of the logical "on" power to the logical "off" power, i.e.

$$ER = \frac{P_1}{P_0}. \tag{5.7}$$

In an ideal transmission system, the "off" state would correspond to zero power, in which case the extinction ratio would be infinite. However in practical transmission systems, this is not the case. For the "0" state, directly modulated lasers are usually biased near the threshold current, with the consequent emission of a limited optical power, while intensity modulators for externally modulated schemes always have a finite extinction ratio. The extinction ratio in a XGM wavelength converter is heavily dependent on the pump signal power. As the pump signal is increased, the gain is compressed more strongly, creating a larger differential between the saturated and unsaturated gain [43]. The level of the saturated gain is what determines the extent of compression of the CW probe signal and thus directly determines the extinction ratio. The evolution of the ER with respect to pump power can be seen in Fig. 5.11. The measured extinction ratio for the low noise configuration is higher than that of the high P_{sat} configuration. This is as a result of the lower saturation power of the low noise configuration. Also plotted is the extinction ratio of the input pump signal, indicating a problem with XGM wavelength converters, that of extinction ratio degradation. The values obtained for the ER at higher pump powers are sufficient for error free detection.

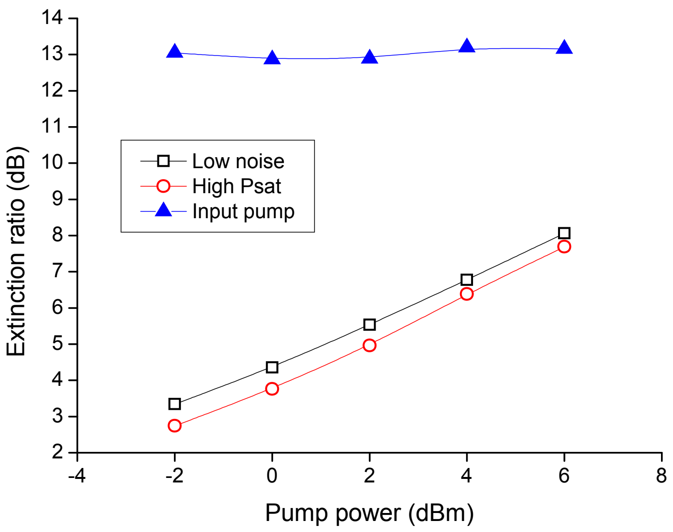

5.11. Evolution of extinction ratio as a function of input pump power. Injected pump wavelength is 1570 nm, probe wavelength 1560 nm.

Another problem with XGM in SOAs is that it is impossible to accomplish symmetric extinction ratio conversion with a single SOA. This problem is illustrated in Fig. 5.12, which shows the evolution of the extinction ratio as a function of the injected probe wavelength. The wavelength of the injected pump signal is 1560 nm, while the optical power is 0 dBm. The extinction ratio shows a decreasing trend when the probe moves to longer wavelengths. For XGM, wavelength down-conversion always yields a higher extinction ratio [44]. This is due to the dependence of the extinction ratio on the differential gain. When the SOA is saturated, the peak of the differential gain shifts to longer wavelengths resulting in down-converted signals experiencing a greater differential gain, and thus a higher extinction ratio. In effect the greater the negative detuning of the probe signal, the larger the extinction ratio. The extinction ratio is also higher when the pump signal is injected at the gain peak of the SOA, due to the increased depletion of carriers at this wavelength.

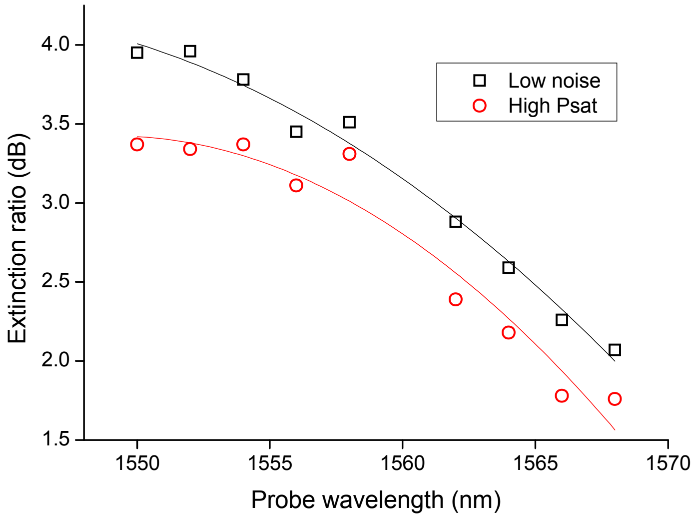

5.12. Extinction ratio of output probe signal as a function of probe wavelength. Pump signal injected at 1560 nm, 0 dBm optical power.

5.3.5. Change in rise/fall times

The main factor in determining the maximum bit rate achievable in an XGM wavelength converter is the rise time of the converted signal. The rise time as it is used in this work is defined as the time taken for the probe signal to increase from 10% of the logical "1" power level, to 90% of this level. The fall time is the inverse of this. The physical mechanism affecting this time is the slow gain recovery of the SOA, which is determined by the effective carrier lifetime, τ_{eff}. This can be understood if we imagine the transition from a pump "1" to a "0", where the gain, which had been saturated to give a converted "0", begins to recover. The effective carrier lifetime is reduced according to the following [45, 46],

$$\tau_{eff} = \frac{\tau}{1 + \sum_i \frac{P_i^{out}}{P_{sat}}}, \tag{5.8}$$

where $i = 1,2$ denotes pump and probe respectively, τ is the differential carrier lifetime, P_{sat} is the saturation output power and P_i^{out} is the output pump or probe power. An increase of the input power to the SOA should lead to a smaller τ_{eff}, due to the interaction of signal photons increasing the rate of stimulated emissions. Eq. (5.8) assumes that the differential carrier lifetime is constant over the length of the SOA. In the MC-SOA, this is clearly not the case. This behaviour is modelled in Fig. 5.13, which plots the average effective carrier lifetime over the entire length of the SOA as a function of the input CW power, using the simulation parameters listed in Appendix A.3. It should be noted that the values obtained are intended as a qualitative description of the behaviour of τ_{eff}. The value for P^{out} in Eq. (5.8) is taken as the power in the cavity at a particular point along the waveguide. The reduction of τ_{eff} is more pronounced for the low noise bias configuration.

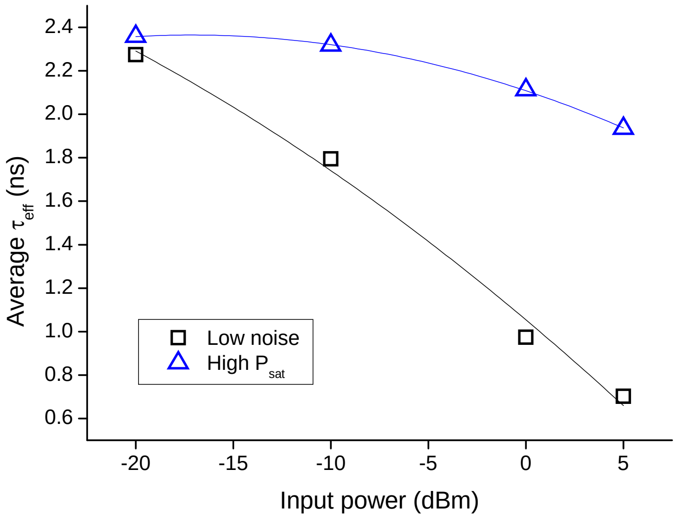

5.13. Simulated effective carrier lifetime, averaged over the length of the SOA, as a function of input CW power.

The reduction of τ_{eff} causes both the rise time and the fall time of the converted signal to decrease. This behaviour is to be observed in Fig. 5.14, which shows the rise times (open symbols) and fall times (filled symbols) measured experimentally for both bias configurations as a function of the input probe power. Of particular note are the smaller times measured for the low noise bias case. This is as a result of the greater gain compression in this state, leading to a greater carrier-photon interaction and consequently reducing τ_{eff}. The rise time of the converted signal is influenced not by the pump "1" level, but by the "0" level, which contains a substantial amount of power when the overall pump power is increased.

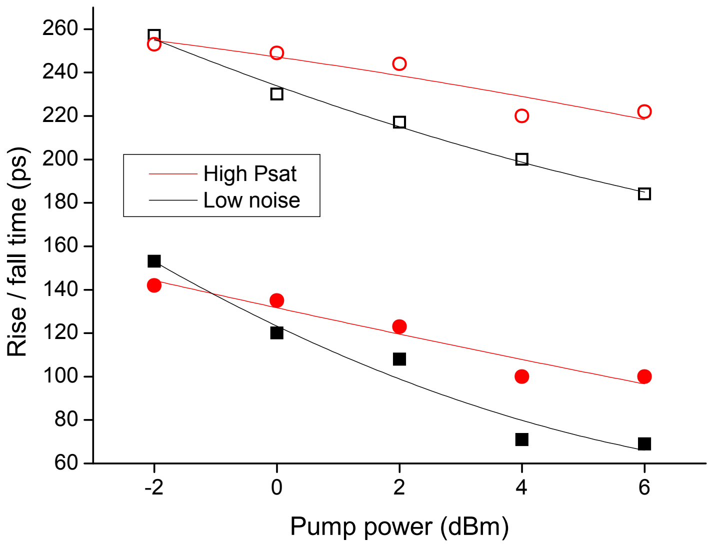

5.14. Rise (open symbols) and fall (closed symbols) times for converted output probe as a function of input pump power. Pump and probe wavelengths were 1570 nm and 1560 nm respectively.

The measured rise times are on the order of 200 ps, whereas the fall times are closer to 100 ps. The fall times are considerably shorter because of the extra reduction in effective carrier lifetime induced by the strong pump "1" level. The rise times are the limiting factor in terms of the wavelength conversion bit rates that can be achieved. If the probe signal does not have time to increase to its full CW level due to the arrival of a pump pulse, then a power penalty is introduced. Using the values of rise time obtained in Fig. 5.14, the maximum bit rates achievable as a function of the average pump power is shown in Fig. 5.15. The low noise bias configuration has an advantage over the high P_{sat} configuration with regards the maximum penalty free conversion bit rate, with a value of 5.4 GHz for a pump power of 6 dBm, compared with 4.5 GHz for the high P_{sat} configuration.

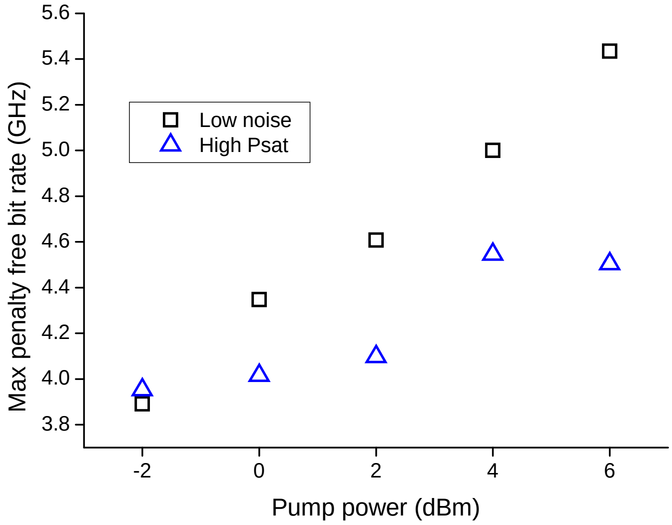

5.15. Maximum bit rate with no power penalty, as a function of the input pump power. Probe power is -4 dBm.

5.4. Four wave mixing in MC-SOA

5.4.1. Introduction

Four wave mixing (FWM) in semiconductor optical amplifiers is a non-linear effect that couples two input waves in a semiconductor medium to produce additional signals. Two waves are incident on a non-linear medium with third order susceptibility, such as in an SOA. A strong pump wave at an angular frequency ω_0 saturates the gain of the SOA in order to produce a noticeable third order non-linear effect. A weaker probe wave at a second angular frequency ω_1 is also injected. Consequently, a modulation of the light intensity in the medium is caused by the beating between the two input waves, with the modulation speed determined by the detuning frequency Ω between them [47]. The intensity modulation in turn leads to a modulation of the complex refractive index with the formation of dynamic gain and index gratings. The pump and probe waves diffract from these gratings, resulting in sidebands to both waves. The diffraction of the probe signal gives rise to a new field at the frequency $\omega = 2\,\omega_1 - \omega_0$, although the wave of most interest, and that which is defined as the conjugate signal, is the result of the diffraction of the pump wave, with the resultant new wave having an angular frequency,

$$\mu_2 = 2\mu_0 - \mu_1 . \tag{5.9}$$

The newly generated waves can be seen in Fig. 5.16, which shows the injection of a strong pump and weak probe beam into the SOA, measured at the SOA output. The individual waves are highlighted, along with the frequency detuning. The input pump power is 3.5 dBm and the probe power is -6.5 dBm, while the low noise bias configuration is used.

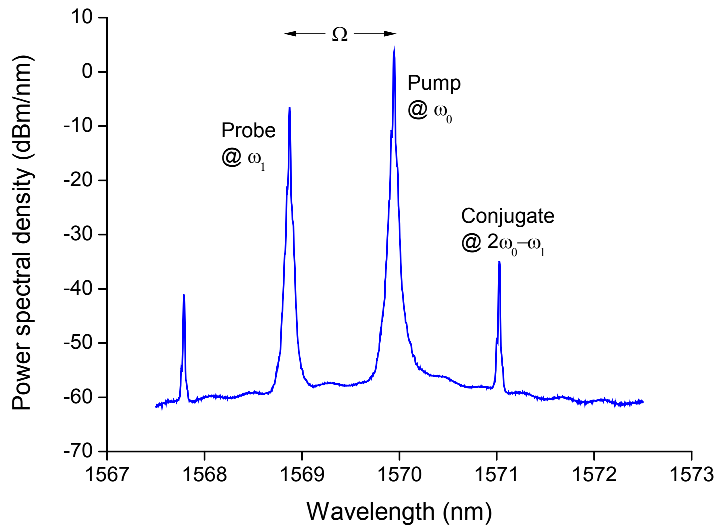

5.16. Optical spectrum of SOA output with injected signals and resulting four wave mixing products. Frequency detuning Ω is highlighted.

The newly generated wave is known as the conjugate because it is a phase inverted replica of the probe signal. FWM in SOAs is an efficient process compared to that of difference frequency generation in passive waveguides. As such, the interaction length can be reduced, hence the viability of FWM in short devices such as SOAs. An additional benefit to the use of a short interaction length is that phase matching conditions are easier to achieve. The phase matching condition is achieved whenever,

$$\Delta kL \approx 0\,, \tag{5.10}$$

where L is the interaction length, usually the length of the SOA active region, and Δk is the wavevector mismatch whereby,

$$\Delta k = 2k_0 - k_1 - k_2\,, \tag{5.11}$$

where *0, 1, 2* denote pump, probe and conjugate signals, respectively, and k_i is the wavevector for each signal. The conjugate signal intensity is proportional to a phase matching factor $G(\Delta kL)$ which in turn tends towards 1 as $\Delta kL \rightarrow 0$. Therefore, FWM in

SOAs is a polarization dependent process, unlike XGM in polarization independent SOAs. However schemes exist whereby the injection of two pump beams, either co-polarized or orthogonally polarized in a polarization insensitive SOA, can yield a FWM signal that is polarization independent.

Experimental setup

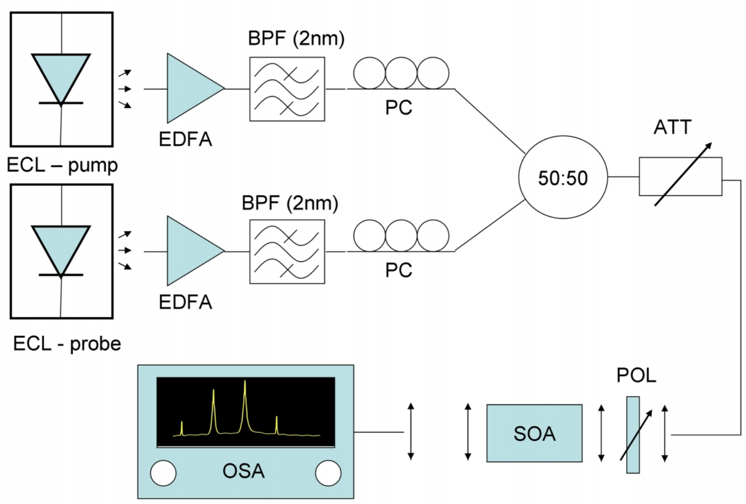

5.17. Experimental setup for FWM characterisation. ECL – external cavity laser; EDFA – Erbium doped fibre amplifier; BPF – bandpass filter; PC – polarisation controller; ATT – variable attenuator; POL – free space polariser; OSA – optical spectrum analyzer.

The experimental setup for the FWM characterization of the MC-SOA, shown in Fig. 5.17, involves the injection of two CW signals, provided by two external cavity lasers (ECLs). The power difference between the pump and probe optical power was kept at 10 dB, ensuring that the SOA saturation was due to the pump signal. The pump wavelength was set to 1570 nm, which is the peak gain wavelength of the SOA. The probe wavelength was downtuned from this value. Uptuned values of the probe wavelength were not used due to restrictions in the spans of both the ECLs and optical filters. Both signals were amplified by EDFAs and then filtered. The EDFAs had gain values between 22 and 25 dB, with noise figures on the order of 5 dB. A tuneable filter was used for the probe signal and the central wavelength was synchronized with the output wavelength of the ECL using Labview™ software. The bandwidth of the filter was set to 2 nm. A second 2 nm filter was used for the pump signal. The signals were polarization controlled before being coupled together via a 50:50 coupler. An optical attenuator was used prior to injection in order to ensure accurate measurement of the input power. The signals were coupled to the SOA via the free space setup outlined in the previous section and also in Chapter 4. A free space polarizer at the SOA input, set to the polarization maximum of the SOA (marginally TE) ensured that the injected signals were linearly and most importantly co-polarized, to ensure efficient FWM. Finally, the signals were analyzed on an optical spectrum analyzer (OSA) with a resolution bandwidth of 0.02 nm. The OSA was also synchronized to the probe signal ECL and optical filter.

5.4.2. Efficiency of FWM conversion process

Dependence on non-linear gain mechanisms

As previously mentioned, the efficiency of the conversion process in FWM in SOAs is better than that of other techniques such as difference frequency generation in fibres. However, the conversion efficiency is still low compared with optical gating techniques such as XGM and XPM. In FWM, the conversion efficiency is dependent on the ability of the material parameters in the SOA to follow the optical beating of the pump and probe signals. The material parameters involved in this process depend on the detuning of the signals. We can define two types of FWM, depending on the detuning: nearly degenerate FWM and non-degenerate FWM. Nearly degenerate FWM occurs when the signal detuning is on the order of megahertz to a few gigahertz. Non-degenerate FWM occurs with detuning frequencies from 10GHz up to a few THz. In nearly degenerate FWM, the physical process affected by the beating modulation is carrier density pulsations (CDP). CDP are caused by the modulation of the carrier density between the conduction and valence bands. The relaxation of the carrier density for this process takes place on the order of the spontaneous carrier lifetime, i.e. ~ 200 ps. This corresponds to a frequency detuning of ~ 5 GHz. The speed of the carrier density pulsations can follow the modulation caused by the optical beating up to this frequency region. Beyond 5 – 10 GHz, however, the CDP can no longer follow the speed of the optical beating, and thus the power of the converted signal caused by the CDP gain and index grating drops rapidly, along with the efficiency.

At frequency detunings > 100 GHz, within the regime of non-degenerate FWM, the effect of carrier heating (CH) becomes significant. The CH process as it pertains to gain recovery in SOAs occurs when the carrier distribution within an energy band relaxes to equilibrium temperature through the emission of optical phonons, usually after free carrier absorption or stimulated emission has increased the temperature of the band relative to the lattice temperature. The lifetime of this process is on the order of 1 – 2 ps. The second process in effect in the non-degenerate FWM regime is spectral hole burning

(SHB), which is where quasi-Fermi equilibrium is established within a band due to carrier-carrier scattering, with a timescale on the order of ~ 100 fs. CDP is an interband process, whereas CH and SHB occur within the band and as such are intraband processes. All three gain relaxation processes described herein have been covered in greater detail in Chapter 1.

The efficiency of each process is determined by the strength of the gain or index grating produced. The large linewidth enhancement factor for the CDP process in SOAs (on the order of 5 – 10) means that the modulation of the carrier density also produces a large modulation of the refractive index. The scattering of the input waves to form the conjugate signals is mainly governed by the index grating formed by these refractive index modulations. For SHB, the modulation of the carrier distribution within the band structure is a much weaker effect than modulation of carriers between bands; as the linewidth enhancement factor for this process is small [48], the index modulation is small and thus SHB mainly produces a gain grating. CH contributes both index and gain gratings, with an index grating being predominant.

Measured FWM efficiency

The conversion efficiency of the FWM wavelength converter is defined as,

$$\eta = \frac{P_2(L)}{P_1(0)}, \tag{5.12}$$

where $P_2(L)$ and $P_1(0)$ are the measured conjugate power at the SOA output and probe power at the SOA input, respectively. The theoretical conversion efficiency can be modelled as,

$$\eta_{th} = S_0^2(L)\left| f_{CDP}(\Omega) + f_{CH}(\Omega)\right|^2, \tag{5.13}$$

where $S_0^2(L)$ is the pump signal photon density measured at the SOA output, and the contributions from carrier density pulsations and carrier heating, respectively, are given as [49],

$$f_{CDP}(\Omega) = -\frac{1}{S_{sat}}\frac{1 - j\alpha_{CDP}}{2\left(1 - j2\pi\Omega\tau_s\right)} \tag{5.14}$$

$$f_{CH} = -\frac{1}{S_{CH}} \frac{1 - j\alpha_{CH}}{\left(1 - j2\pi\Omega\tau_{CH}\right)\left(1 - j2\pi\Omega\tau_{SHB}\right)}, \tag{5.15}$$

where S_{sat} is the saturation photon density of the SOA, S_{CH} is the characteristic saturation photon density for the carrier heating process, Ω is the detuning frequency in Hz, α_{CDP} and α_{CH} are the linewidth enhancement factors for CDP and CH respectively, and τ_s, τ_{CH} and τ_{SHB} are the characteristic times for CDP, CH and SHB respectively.

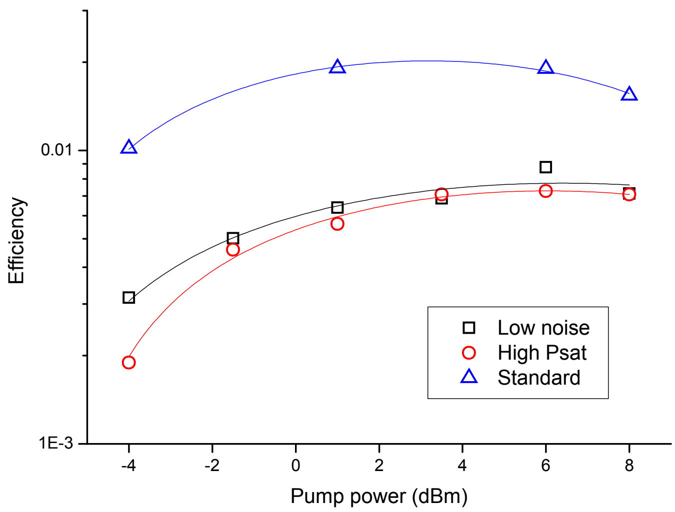

5.18. FWM efficiency as a function of input pump power. The frequency detuning is 100GHz.

Fig. 5.18 shows the measured FWM efficiency as a function of the input pump power. The probe power is kept at a constant difference of 10 dB from the probe signal. The frequency detuning is set to 100 GHz. Immediately obvious is the larger efficiency achieved for the standard bias configuration. The reason for this is that the higher gain in this configuration leads to a larger value for S_0^2 in Eq. (5.13), while the relatively low value for S_{sat} increases the contribution from f_{cdp}. This same inverse dependency on the saturation photon density means that the efficiency for the low noise case is higher than that of the high P_{sat} case. This is to be expected, as the SOA should be saturated in order to observe appreciable third order non-linear effects. It has been shown that the FWM efficiency is roughly dependent on the cube of the amplifier gain and the square of the pump power [50], i.e.

$$\eta \propto G^3 I_0^2, \tag{5.16}$$

As the input power to the SOA increases, the efficiency also increases along with I_0, but only up to a point. When the input power has compressed the gain by a factor of approximately e^{-2}, this reduction in G outweighs the contribution from I_0 and the efficiency starts to reduce [51]. This effect is visible in the efficiency curve for the standard bias configuration, indicative of the greater gain saturation for that bias case at very high input powers. Another indication of this behaviour is the convergence of the curves for the low noise and high P_{sat} cases, where the reduction in G from Eq. (5.16) is less severe in the case of the high P_{sat} configuration.

Fig. 5.19 shows the FWM efficiency as a function of the detuning frequency. The pump powers used are (a) -4 dBm and (b) 6 dBm, in order to demonstrate the behaviour of the FWM efficiency at low and high pump powers. All plotted curves show a similar trend. At a detuning up to ~ 100 GHz, the curve exhibits the characteristic shape determined by Eq. (5.14). At this point a shoulder appears as the effects of carrier heating become predominant. The curve follows the trend of Eq. (5.15). The detuning efficiency drops off sharply around 1 – 2 THz. Within the nearly degenerate and most of the non-degenerate FWM regimes, the magnitude of the FWM efficiency displays the same qualitative behaviour as that exhibited in Fig. 5.16, whereby the maximum efficiency is seen in the standard bias configuration. A clear difference emerges in the plots at a frequency detuning > 1 THz, however. In this region, for high pump power, it is observed that the efficiency drops off far more rapidly for the standard SOA case, followed by the low noise configuration, with the high P_{sat} configuration having the highest conversion bandwidth. In comparison, the opposite behaviour with regards to the conversion bandwidth is observed in the low pump power case. This suggests that at such high pump powers, the high P_{sat} bias configuration has the largest gain bandwidth due to the reduction in gain saturation.

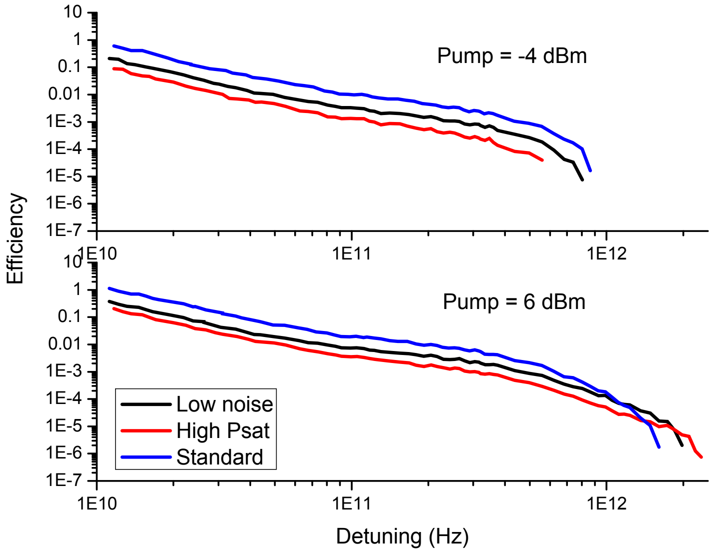

5.19. FWM efficiency as a function of detuning frequency for low and high pump powers. Probe power = pump power – 10 dB. The probe wavelength is downtuned from the pump.

5.4.2. Curve fitting and parameter extraction

An application for CW FWM efficiency characterisation is the calculation of the spontaneous carrier lifetime and the carrier heating lifetime, as well as the linewidth enhancement factors for the interband and intraband processes. The efficiency vs detuning curves were fitted with the functions defined in Eq. (5.13) and (5.14) .The contribution in Eq. (5.13) from f_{CH} is neglected for the calculation of τ_s and α_{CDP}. In this case, Eq. (5.13) is a low pass filter function. The values for S_{sat} were calculated using the saturation output power values measured in Chapter 2. The parameters τ_s and α_{CDP} were set as variables, and a fitting algorithm was used to find the values for these parameters that gave the optimum fit to the FWM efficiency curve. For the calculation of the carrier heating lifetime and α_{CH}, the contribution from f_{CDP} in Eq. (5.15) is neglected and the contribution from f_{CH} is incorporated. For this calculation, as it was not previously known, S_{CH} was also set as a variable in the fitting algorithm. The results of both fittings are shown in Fig. 5.20. The separate fittings for the CDP and CH regions are visible. Of note is the tail-off in the fit compared with the experimental data at high detuning frequencies. This is due to the omission of the spectral hole burning term from Eq. (5.15) when fitting. The calculated spontaneous carrier lifetimes for CDP and CH are plotted in Fig. 5.21 (a) and (b), respectively. As the input pump power is increased, the gain saturation resulting from this leads to a reduction in the carrier density. This is reflected in the upward trend in the spontaneous emission lifetime. The values are quite low but not uncommon in the literature [52].

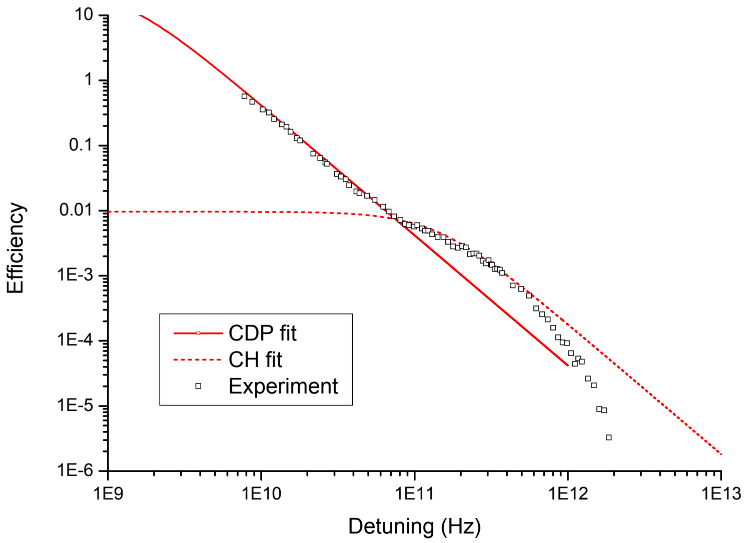

5.20. FWM efficiency vs detuning frequency for low noise bias condition, at pump power of 6 dBm. Also plotted are fitted curves.

Significantly, the larger carrier density at high powers that exists in the high P_{sat} bias condition is reflected in the lower carrier lifetimes calculated for it. This result correlates well with the explanation for the increased saturation power observed in this bias state that was proposed in Chapter 2.

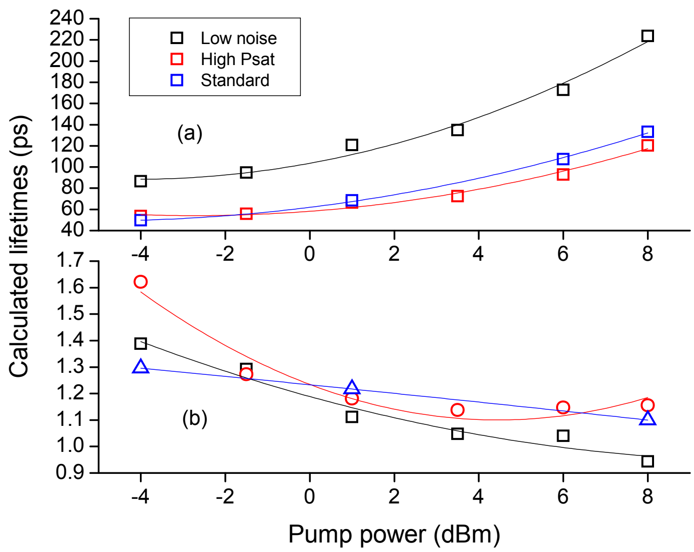

5.21. (a) Calculated spontaneous carrier lifetimes and (b) carrier heating lifetimes as a function of pump power.

The values obtained for the CH lifetimes are on the order of 1 – 2 ps, which is in general agreement with the literature. The downward trend in values of τ_{CH} with increasing pump power is an indication that the gain recovery time associated with intraband effects becomes slower with increased carrier density [53].

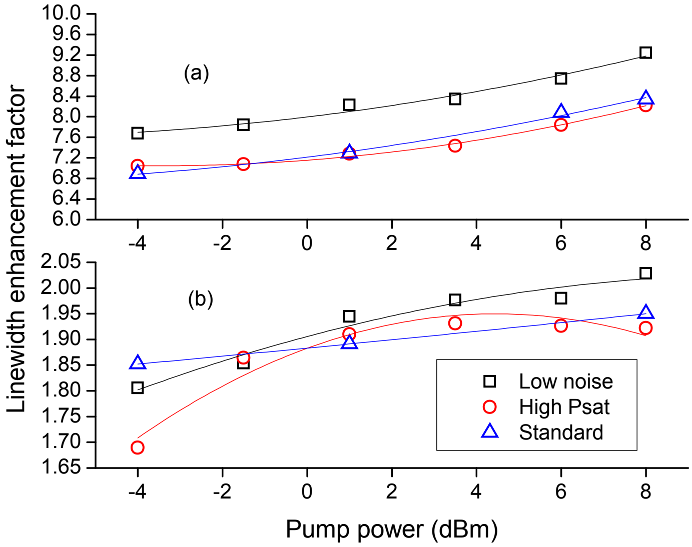

5.22. Calculated linewidth enhancement factors for (a) CDP and (b) CH processes, as a function of input pump power.

The calculated linewidth enhancement factors for both the CDP and CH processes are shown in Fig. 5.22. The upward trend of α with pump power can be explained with reference to [54], as pertaining to semiconductor lasers. The linewidth enhancement factor is enhanced by the non-linear gain of the SOA according to,

$$\alpha = \alpha_0 \sqrt{1+I} - \frac{I}{1+1/\sqrt{1+I}}, \tag{5.17}$$

where α_0 is the low intensity linewidth enhancement factor, I is the intracavity intensity normalized to the saturation intensity and β is a parameter defined as,

$$= \frac{2(\omega_0 - \omega_p)}{\tau_{in}^2 \Delta\omega_g^2}, \tag{5.18}$$

where ω_0 is the pump signal frequency, ω_p is the linear gain peak frequency $\Delta\omega_g$ is the gain bandwidth and τ_{in} is the intraband polarisation relaxation time. The numerator in

Eq. (5.18) disappears if the pump signal is injected at the gain peak, as it is in our experiment. In that case, the linewidth enhancement factor is dependent on the mode intensity.

5.4.4. Noise in FWM wavelength conversion

Due to the inherent inefficiencies of the FWM conversion process, the noise performance of FWM wavelength converters is generally poor compared to in-line amplification applications. This is a serious drawback as wavelength converters are likely to be cascaded when in operation due to the need to perform multiple wavelength conversions. Solutions to this problem include the use of long SOAs, to take advantage of high conversion efficiency [55], or preamplification using a low noise EDFA, so that the total system noise figure is determined by the noise figure of the EDFA (assuming that the gain of the EDFA is greater than the NF of the SOA). Two measures used to quantify noise performance in FWM wavelength converters are signal to ASE background ratio (SBR) and noise figure. SBR is defined as the ratio of the output converted signal power to the ASE noise power within the measurement bandwidth [56].

$$SBR = \frac{P_2(L)}{P_{ASE}} = \frac{\text{¦}\, P_1(0)}{P_{ASE}}, \tag{5.19}$$

Fig. 5.23 shows the SBR of a converted signal at 100 GHz detuning frequency for a range of input pump powers. Interesting to note is that the SBR, unlike the conversion efficiency in Fig. 5.18, does not display a maximum within the range studied. P_{ASE} is inversely dependent on the pump power due to the effects of gain saturation, while the numerator in Eq. (5.19) can be rewritten as,

$$\text{¦}\, P_1(0) = \pm\, \text{¦}\, P_0(0), \tag{5.20}$$

where σ is the ratio of input probe to input pump, which is a constant in these experiments. Therefore the dependencies of both numerator and denominator in Eq. (5.19) on the input pump power indicate that the SBR should increase well beyond the pump power for maximum conversion efficiency [57], which is what is observed. The maximum SBR is found for the standard bias configuration. This result is due to both the high gain at low pump powers and also to the large suppression of the ASE due to increased gain compression at high pump powers, as compared to the two other bias configurations.

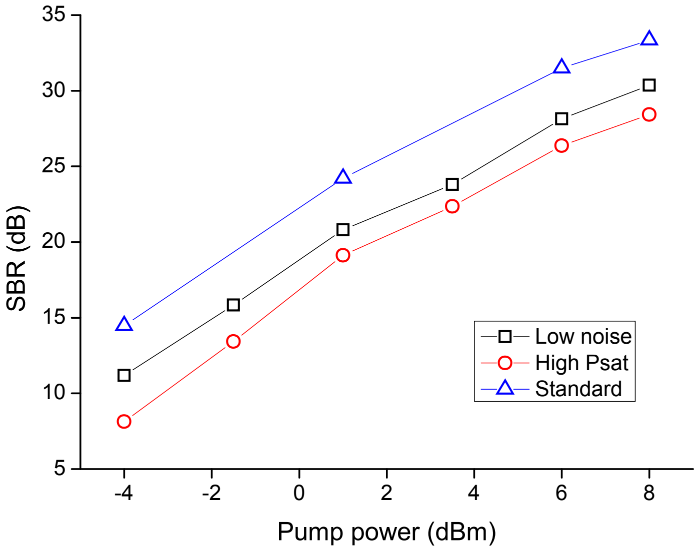

5.23. Signal to ASE background ratio as a function of pump power for frequency detuning of 100 GHz.

The noise figure of the FWM wavelength converter is a way of combining the conversion efficiency and the SBR into a figure of merit for the noise in a practical system. In FWM, the NF is defined as the ratio of the SNR of the input probe signal to the SNR of the converted signal, given by [58],

$$NF = \frac{2\rho_{ASE} + \hbar\omega}{\hbar\omega}, \tag{5.21}$$

where ρ_{ASE} is the ASE power spectral density within the converted signal bandwidth and with the same polarisation as the signal, expressed in *W/Hz*, and ω is the angular frequency of the converted signal. Fig. 5.24 shows the noise figure of the SOA for three bias configurations at a frequency detuning of 100 GHz. The minimum value of NF obtained is 30 dB. As with the SBR trend, the lowest NF is obtained in the standard bias configuration, for the same reasons as before. The NF of the low noise bias configuration is also considerably lower than that of the high P_{sat} configuration, due to the enhanced suppression of ASE noise. A noticeable feature of this plot is that, as opposed to the SBR trend in Fig. 5.23, the NF reaches a minimum value and then begins to increase at a certain input pump power.

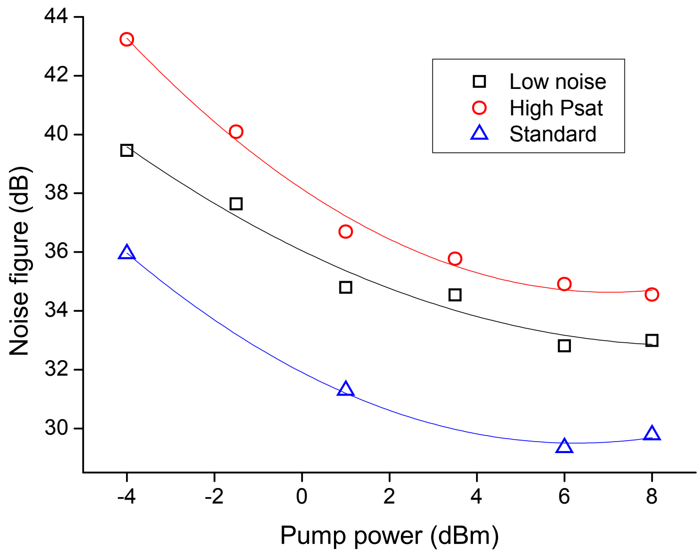

5.24. Noise figure of converted signal as a function of pump power for frequency detuning of 100 GHz.

The reason for this result is that at high enough pump powers, the conversion efficiency drops off, and the contribution to the NF of the decreased conversion efficiency begins to outweigh that of the continually increasing SBR. The large compression of the gain observed in the standard bias configuration at high pump powers is the reason why the NF minimum occurs at a lower pump power relative to the other configurations. The increasing SBR is also the reason why the NF minimum does not generally coincide with the conversion efficiency minimum. A comparison of Fig. 5.18 with Fig. 5.24 shows that the conversion efficiency minimum of the standard bias case is at a pump power of ~ 3 dBm, whereas the NF minimum occurs at ~ 6 dBm.

5.5. Summary

In this chapter, the characteristics of wavelength conversion in a multi-contact SOA were studied, with particular reference to the effect of the injected carrier distribution. The wavelength conversion techniques in question were cross gain modulation (XGM) and four wave mixing (FWM). It was observed that switching between the low noise and high P_{sat} bias configurations has a strong effect on the noise properties and extinction ratio of the XGM wavelength converter. It was also observed that a compromise is necessary between extinction ratio and signal to noise ratio, due to the increasing noise power at high pump signal intensities. The FWM characterisation of the SOA showed that the optical gain is the most important parameter in deciding both the conversion efficiency and the noise performance of the wavelength converter. This observation was inferred from the superior conversion efficiency and noise figure of the standard bias configuration, which displays a higher gain than the other bias configurations. It was also observed that the low noise bias configuration achieved a greater conversion efficiency and lower noise figure than the high P_{sat} configuration, due to the lower saturation power and consequent increased suppression of the ASE noise. The FWM efficiency curves were fitted to a low pass filter function in order to extract the spontaneous and carrier heating lifetimes, as well as the respective linewidth enhancement factors. The results from this fitting indicate that the higher saturation power in the high P_{sat} bias configuration leads to a lower spontaneous emission lifetime. This result indicates that this configuration is well suited to in-line amplification applications, but that switching to the low noise or standard configuration is a better option for wavelength conversion.

References

[1] Agrawal, G.P.; *Fiber-Optic Communication Systems*, John Wiley & Sons, New York (2002)

[2] Saleh, A.A.M.; "Transparent optical networking in backbone networks," *Optical Fiber Communication Conference, 2000*, vol.3, pp.62-64, 2000

[3] Listanti, M.; Eramo, V.; Sabella, R.; "Architectural and technological issues for future optical Internet networks," *Communications Magazine, IEEE* , vol.38, no.9, pp.82-92, Sep 2000

[4] Ramamurthy, B.; Feng, H.; Datta, D.; Heritage, J.P.; Mukherjee, B.; "Transparent vs. opaque vs. translucent wavelength-routed optical networks," *Optical Fiber Communication Conference, 1999, and the International Conference on Integrated Optics and Optical Fiber Communication. OFC/IOOC '99. Technical Digest* , vol.1, no., pp.59-61 vol.1, 1999

[5] Thylen, L.; Karlsson, G.; Nilsson, O.; , "Switching technologies for future guided wave optical networks: potentials and limitations of photonics and electronics," *IEEE Communications Magazine,* vol.34, no.2, pp.106-113, Feb 1996

[6] Yoo, S.J.B.; "Wavelength conversion technologies for WDM network applications," *Journal of Lightwave Technology,* vol.14, no.6, pp.955-966, Jun 1996

[7] Ramamurthy, B.; Mukherjee, B.; "Wavelength conversion in WDM networking," *IEEE Journal on Selected Areas in Communications,* vol.16, no.7, pp.1061-1073, Sep 1998

[8] Held, G.; , "On the road to OC-768 [optical carrier]," *IT Professional* , vol.3, no.2, pp.46-48, Mar/Apr 2001

[9] Brackett, C.A.; , "Dense wavelength division multiplexing networks: principles and applications," *IEEE Journal on Selected Areas in Communications,* vol.8, no.6, pp.948-964, Aug 1990

[10] Kartalopoulos, S.V., “DWDM: Networks, Devices and Technology”, Wiley-Interscience, 2003.

[11] Tyler, E.J.; Kourtessis, P.; Webster, W.; Rochart, E.; Quinlan, T.; Dudley, S.E.M.; Walker, S.D.; Penty, R.V.; White, I.H.; "Toward Terabit-per-Second Capacities Over Multimode Fiber Links Using SCM/WDM Techniques," *Journal of Lightwave Technology*, vol.21, no.12, pp.3237-3243, Dec 2003

[12] Nagarajan, R.; Kato, M.; Pleumeekers, J.; Evans, P.; Lambert, D.; Chen, A.; Dominic, V.; Mathur, A.; Chavarkar, P.; Missey, M.; Dentai, A.; Hurtt, S.; Back, J.; Muthiah, R.; Murthy, S.; Salvatore, R.; Grubb, S.; Joyner, C.; Rossi, J.; Schneider, R.; Ziari, M.; Kish, F.; Welch, D.; , "Single-chip 40-channel InP transmitter photonic integrated circuit capable of aggregate data rate of 1.6 Tbit/s," *Electronics Letters* , vol.42, no.13, pp. 771- 773, 22 June 2006

[13] ITU-T G.694.2, “Spectral grids for WDM applications: CWDM wavelength grid”, Dec. 2003, http://www.itu.int/rec/T-REC-G.694.2-200312-I/en

[14] ITU-T G.694.1, “Spectral grids for WDM applications: DWDM wavelength grid”, Jun. 2002, http://www.itu.int/rec/T-REC-G.694.1-200206-I/en

[15] Kovacevic, M.; Acampora, A.; "Benefits of wavelength translation in all-optical clear-channel networks," *IEEE Journal on Selected Areas in Communications*, vol.14, no.5, pp.868-880, Jun 1996

[16] Teck Yoong Chai; Tee Hiang Cheng; Chao Lu; Gangxiang Shen; Bose, S.K.; "On the analysis of optical cross-connects with limited wavelength conversion capability," *IEEE International Conference on Communications, 2001. ICC 2001*, vol.10, no., pp.3135-3139 vol.10, 2001

[17] Tillerot, F.; Hui Bon Hoa, D.; Auffret, R.; Claveau, G.; "Cascadability of all-optical cross connects based on wavelength conversion," *Optical Fiber Communications, 1996. OFC '96*, pp. 258- 259, 25 Feb.-1 March 1996

[18] Kamatani, O.; Kawanishi, S.; "Add/drop operation for 100 Gbit/s optical signal based on optical wavelength conversion by four-wave mixing," *Electronics Letters* , vol.32, no.10, pp.911-913, 9 May 1996

[19] Tzanakaki, A.; Zacharopoulos, I.; Tomkos, I.; "Optical add/drop multiplexers and optical cross-connects for wavelength routed networks," *Proceedings of 2003 5th International Conference on Transparent Optical Networks, 2003.*, vol.1, no., pp. 41- 46 vol.1, 29 June-3 July 2003

[20] Elmirghani, J.M.H.; Mouftah, H.T.; "All-optical wavelength conversion: technologies and applications in DWDM networks," *IEEE Communications Magazine*, vol.38, no.3, pp.86-92, Mar 2000

[21] Blow, K.J.; Doran, N.J.; Nelson, B.P.; "Demonstration of the nonlinear fibre loop mirror as an ultrafast all-optical demultiplexer," *Electronics Letters* , vol.26, no.14, pp.962-964, 5 July 1990

[22] Jianjun Yu; Xueyan Zheng; Peucheret, C.; Clausen, A.T.; Poulsen, H.N.; Jeppesen, P.; "All-optical wavelength conversion of short pulses and NRZ signals based on a nonlinear optical loop mirror," *Journal of Lightwave Technology,* vol.18, no.7, pp.1007-1017, Jul 2000

[23] Kawaguchi, H.; Magari, K.; Yasaka, H.; Fukuda, M.; Oe, K.; "Tunable optical-wavelength conversion using an optically-triggerable multielectrode distributed feedback laser diode ," *IEEE Journal of Quantum Electronics*, vol.24, no.11, pp.2153-2159, Nov 1988

[24] Nobuhara, H.; Kondo, K.; Yamakoshi, S.; Wakao, K.; "Optical exclusive-OR operation using tunable wavelength conversion laser diode," *Electronics Letters* , vol.25, no.22, pp.1485-1486, 26 Oct. 1989

[25] Stubkjaer, K.E.; "Semiconductor optical amplifier-based all-optical gates for high-speed optical processing," *IEEE Journal of Selected Topics in Quantum Electronics*, vol.6, no.6, pp.1428-1435, Nov/Dec 2000

[26] Asghari, M.; White, I.H.; Penty, R.V.; "Wavelength conversion using semiconductor optical amplifiers," *Journal of Lightwave Technology,* vol.15, no.7, pp.1181-1190, Jul 1997

[27] Nakamura, S.; Ueno, Y.; Tajima, K.; "168-Gb/s all-optical wavelength conversion with a symmetric-Mach-Zehnder-type switch," *IEEE Photonics Technology Letters*, vol.13, no.10, pp.1091-1093, Oct 2001

[28] Xu, C. Q.; Okayama, H.; Kawahara, M.; "1.5 μm band efficient broadband wavelength conversion by difference frequency generation in a periodically domain-inverted $LiNbO_3$ channel waveguide," *Applied Physics Letters*, vol.63, no.26, pp.3559-3561, Dec 1993

[29] Contestabile, G.; Maruta, A.; Sekiguchi, S.; Morito, K.; Sugawara, M.; Kitayama, K.; "160 Gb/s cross gain modulation in quantum Dot SOA at 1550 nm," *35th European Conference on Optical Communication, 2009. ECOC '09.*, vol.2009-Supplement, pp.1-2, 20-24 Sept. 2009

[30] Qasaimeh, O.; , "Characteristics of cross-gain (XG) wavelength conversion in quantum dot semiconductor optical amplifiers," *IEEE Photonics Technology Letters*, vol.16, no.2, pp.542-544, Feb. 2004

[31] Uskov, A.V.; Mørk, J.; Tromborg, B.; Berg, T.W.; Magnusdottir, I.; O'Reilly, E.P.; "On high-speed cross-gain modulation without pattern effects in quantum dot semiconductor optical amplifiers", *Optics Communications*, vol.227, no.4-6, pp.363-369, Nov 15, 2003

[32] Jungho Kim; Laemmlin, M.; Meuer, C.; Bimberg, D.; Eisenstein, G.; "Theoretical and Experimental Study of High-Speed Small-Signal Cross-Gain Modulation of Quantum-Dot Semiconductor Optical Amplifiers," *IEEE Journal of Quantum Electronics*, vol.45, no.3, pp.240-248, March 2009

[33] Leuthold, J.; Marom, D.M.; Cabot, S.; Jaques, J.J.; Ryf, R.; Giles, C.R.; "All-optical wavelength conversion using a pulse reformatting optical filter," *Journal of Lightwave Technology*, vol.22, no.1, pp. 186- 192, Jan. 2004

[34] Nielsen, M.L.; Lavigne, B.; Dagens, B.; "Polarity-preserving SOA-based wavelength conversion at 40 Gbit/s using bandpass filtering," *Electronics Letters*, vol.39, no.18, pp. 1334- 1335, 4 Sept. 2003

[35] Silveira, T.G.; Monteiro, P.M.N.P.; Teixeria, A.L.J.; Tosi Beleffi, G.M.; "Cross-gain modulation bandwidth enhancement in semiconductor optical amplifiers by means of detuned optical filter," *Electronics Letters,* vol.41, no.13, pp. 761- 763, 23 June 2005

[36] Liu, Y.; Tangdiongga, E.; Li, Z.; de Waardt, H.; Koonen, A.M.J.; Khoe, G.D.; Xuewen Shu; Bennion, I.; Dorren, H.J.S.; "Error-Free 320-Gb/s All-Optical Wavelength Conversion Using a Single Semiconductor Optical Amplifier," *Journal of Lightwave Technology*, vol.25, no.1, pp.103-108, Jan. 2007

[37] Manning, R.J.; Yang, X.; Webb, R.P.; Giller, R.; Garcia Gunning, F.C.; Ellis, A.D.; "The turbo-switch - a novel technique to increase the high-speed response of SOAs for wavelength conversion," *Optical Fiber Communication Conference, 2006 and the 2006 National Fiber Optic Engineers Conference. OFC 2006* , 3 pp., 5-10 March 2006

[38] Obermann, K.; Kindt, S.; Breuer, D.; Petermann, K.; , "Performance analysis of wavelength converters based on cross-gain modulation in semiconductor-optical amplifiers," *Journal of Lightwave Technology,* vol.16, no.1, pp.78-85, Jan 1998

[39] Inoue, K.; "Noise transfer characteristics in wavelength conversion based on cross-gain saturation in a semiconductor optical amplifier," *IEEE Photonics Technology Letters*, vol.8, no.7, pp.888-890, July 1996

[40] Pegg, S.I.; Fice, M.J.; Adams, M.J.; Hadjifotiou, A.; "Noise in wavelength conversion by cross-gain modulation in a semiconductor optical amplifier," *IEEE Photonics Technology Letters,* vol.11, no.6, pp.724-726, Jun 1999

[41] de la Corte, M.M.; Elmirghani, J.M.H.; "Accurate noise characterization of wavelength converters based on XGM in SOAs," *Journal of Lightwave Technology,* vol.21, no.1, pp. 182- 197, Jan 2003

[42] Obermann, K.; Kindt, S.; Breuer, D.; Petermann, K.; Schmidt, C.; Diez, S.; Weber, H.G.; "Noise characteristics of semiconductor-optical amplifiers used for wavelength conversion via cross-gain and cross-phase modulation," *IEEE Photonics Technology Letters,* vol.9, no.3, pp.312-314, March 1997

[43] Ghafouri-Shiraz, H.; “The Principles of Semiconductor Laser Diodes and Amplifiers”, Imperial College Press, 2004.

[44] Durhuus, T.; Mikkelsen, B.; Joergensen, C.; Lykke Danielsen, S.; Stubkjaer, K.E.; "All-optical wavelength conversion by semiconductor optical amplifiers," *Journal of Lightwave Technology*, vol.14, no.6, pp.942-954, Jun 1996

[45] Shieh, W.; Willner, A.E.; "Optimal conditions for high-speed all-optical SOA-based wavelength shifting," *IEEE Photonics Technology Letters*, vol.7, no.11, pp.1273-1275, Nov 1995

[46] Wiesenfeld, J.M.; Glance, B.; Perino, J.S.; Gnauck, A.H.; "Wavelength conversion at 10 Gb/s using a semiconductor optical amplifier," *IEEE Photonics Technology Letters,* vol.5, no.11, pp.1300-1303, Nov 1993

[47] Agrawal, G.P.; "Population pulsations and nondegenerate four-wave mixing in semiconductor lasers and amplifiers," *Journal of the Optical Society of America B*, vol.5, no.1, Jan. 1988.

[48] Giller, R.; Manning, R.J.; Cotter, D.; "Gain and phase recovery of optically excited semiconductor optical amplifiers," *IEEE Photonics Technology Letters,* vol.18, no.9, pp.1061-1063, May 1, 2006

[49] Uskov, A.; Mork, J.; Mark, J.; "Wave mixing in semiconductor laser amplifiers due to carrier heating and spectral-hole burning," *IEEE Journal of Quantum Electronics,* vol.30, no.8, pp.1769-1781, Aug 1994

[50] Jianhui Zhou; Namkyoo Park; Dawson, J.W.; Vahala, K.J.; Newkirk, M.A.; Miller, B.I.; "Efficiency of broadband four-wave mixing wavelength conversion using semiconductor traveling-wave amplifiers," *IEEE Photonics Technology Letters,* vol.6, no.1, pp.50-52, Jan 1994

[51] Mecozzi, A.; "Analytical theory of four-wave mixing in semiconductor amplifiers," *Optics Letters*, vol.19, no.12, pp.892-894, 1994

[52] Surre, F.; Kennedy, B.; Landais, P.; Philippe, S.; Bradley, A.L.; "Polarization Resolved Four-Wave-Mixing-Based Measurement in Bulk Material Semiconductor

Optical Amplifier," *2006 International Conference on Transparent Optical Networks*, vol.2, pp.169-172, 18-22 June 2006

[53] Occhi, L.; Ito, Y.; Kawaguchi, H.; Schares, L.; Eckner, J.; Guekos, G.; "Intraband gain dynamics in bulk semiconductor optical amplifiers: measurements and simulations," *IEEE Journal of Quantum Electronics*, vol.38, no.1, pp.54-60, Jan 2002

[54] Agrawal, G.P.; "Intensity dependence of the linewidth enhancement factor and its implications for semiconductor lasers," *IEEE Photonics Technology Letters*, vol.1, no.8, pp.212-214, Aug 1989

[55] Girardin, F.; Eckner, J.; Guekos, G.; Dall'Ara, R.; Mecozzi, A.; D'Ottavi, A; Martelli, F.; Scotti, S.; Spano, P.; "Low-noise and very high-efficiency four-wave mixing in 1.5-mm-long semiconductor optical amplifiers," *IEEE Photonics Technology Letters*, vol.9, no.6, pp.746-748, June 1997

[56] Martelli, F.; Mecozzi, A.; DOttavi, A.; Scotti, S.; Spano, P.; DallAra, R.; Eckner, J.; Guekos, G.; "Noise in wavelength conversion using four-wave mixing in semiconductor optical amplifiers," *Applied Physics Letters*, vol.70, no.3, pp.306-308, Jan 1997

[57] D'Ottavi, A.; Iannone, A.; Mecozzi, A.; Scotti, S.; Spano, P.; Dall'Ara, R.; Eckner, J.; Guekos, G.; "Efficiency and noise performance of wavelength converters based on FWM in semiconductor optical amplifiers," *IEEE Photonics Technology Letters*, vol.7, no.4, pp.357-359, Apr 1995

[58] Summerfield, M.A.; Tucker, R.S.; "Noise figure and conversion efficiency of four-wave mixing in semiconductor optical amplifiers," *Electronics Letters*, vol.31, no.14, pp.1159-1160, 6 Jul 1995

Conclusion and Future Outlook

In this thesis, a thorough characterisation of novel semiconductor optical amplifier designs was presented. The purpose of these designs was to enable control over the limiting factors of an SOA, namely the noise figure and the saturation output power. SOAs have always been deficient in these areas when compared to fibre amplifiers, and much research has focused on alleviating these problems. The basic physics of SOAs and the radiative processes in semiconductor material was first covered as a background for the thesis.

Noise figure and saturation output power control

The origin and description of noise in SOAs was outlined. The relationship between the noise figure and the population inversion factor was established as central to the concept of this thesis. The parameters that affect saturation power in SOAs was also detailed, with the dependence on the spontaneous carrier lifetime, and indirectly the carrier density, established. The concept for controlling the carrier density distribution within the SOA, and thus the noise and saturation behaviour, was outlined. The reduction of noise figure for a chain of amplifiers was illustrated using a deterministic model, and the evolution of the population inversion factor with the carrier density was plotted. The model was also used to show the dependence of the spontaneous carrier lifetime on the carrier density.

Verification of concept

The parameter control concept was tested on two SOA designs, one employing a lateral laser cavity and one employing multiple electrical contacts. Each design aimed to affect the carrier density profile of the SOA in such a way as to alter the device parameters. A simulation was developed to model the SOA and the carrier density control concept. Simulations of the designs showed a clear effect on both the noise figure and saturation power of the SOA. Actual devices incorporating these designs were characterized in the lab. The performance of the lateral cavity SOA was less than expected, with a relatively high noise figure and low gain. The noise figure was found to change when injecting from one side of the device relative to the other, suggesting an effect of the lateral laser. The multi-contact SOA showed more promising results, with an appreciable gain and relatively low noise figure recorded. Again, switching the bias distribution to the opposite side produced a clear difference in noise figure, however the low noise bias distribution did not show an appreciable decrease from that of the control bias configuration. A clear increase in saturation output power was observed, however, when the bias current distribution was shifted towards the end facet. This suggests a potential for high power in-line amplification.

Effects on in-line amplification

The multi-contact SOA was tested in an in-line transmission experiment. The increased noise figure of the high saturation power bias configuration was shown to introduce a power penalty relative to the other bias configuration when amplifying low power signals. There was no improvement in receiver sensitivity found for the low noise configuration compared to the standard configuration. In the high power regime however, the high saturation power configuration showed a clear improvement in error free power range. In this case, the standard bias configuration was found to give the worst performance. This trend was consistent in the characterisation of optical pulses propagating in the SOA. Both the high saturation power and low noise bias configurations exhibited fewer non-linear effects such as pulse broadening and self phase modulation than the standard bias configuration, suggesting that altering the bias current distribution could have a beneficial effect on high power CW and pulsed transmission.

Effects on wavelength conversion

In terms of wavelength conversion, the higher saturation power of the high P_{sat} bias configuration reduces the non-linear effects exhibited by SOAs in the saturation regime, and as such this configuration was found to give the poorest results in cross gain modulation and four wave mixing experiments. The best conversion performance was seen in the standard bias configuration, suggesting that the unsaturated gain is the most important parameter for wavelength conversion efficiency.

Outlook

The characteristics of these devices could be improved in a number of ways. As these are prototype SOAs, their main function is to test the concept of carrier density control. With regards the lateral cavity SOA, it is possible that the etched slots that make up the lateral cavity were too close to the active region, and thus affected the propagating mode. The model of the MC-SOA could potentially be improved by simulating carrier diffusion between the sections, which may help to resolve the issues surrounding the reduction in noise figure. The multi-contact SOA shows promise as a concept and gave impressive results in the high power regime. It is possible that an improvement in the resistance between the slots separating the electrical contacts would lead to an improved noise figure. In this case, the MC-SOA could have potential as a flexible, low cost component for in-line amplification in optical networks.

APPENDIX

A.1. Material gain model

The model for the material gain used in the SOA simulations of both the lateral cavity and multi-contact SOAs is based on the model by Connelly [1]. It describes the gain function for a bulk InGaAsP semiconductor optical amplifier. This is also used as a approximation for the behaviour of the quantum well LC-SOA design, with the purpose of the simulation being to test the concept of the lateral laser. The material gain coefficient is given by,

$$g_m(\nu) = \frac{c^2}{4\sqrt{2}\pi^{3/2} n_r^2 \nu^2 \tau_s}\left[\frac{2m_c m_{hh}}{\hbar(m_c + m_{hh})}\right]^{\frac{3}{2}}\left[f_c(E_a) - f_v(E_b)\right]\sqrt{\nu - \frac{E_g}{h}}\ , \qquad \text{(A.1)}$$

where n_r is the material refractive index, v is the optical frequency, τ_s is the spontaneous carrier lifetime, and m_c and m_{hh} are the effective electron and heavy hole masses, respectively. The occupation probabilities of electrons in the conduction band and holes in the valence band are given as,

$$f_c(E_a) = \frac{1}{1 + \exp\left(\frac{E_a - E_{fc}}{kT}\right)} \qquad \text{(A.2)}$$

$$f_v(E_b) = \frac{1}{1 + \exp\left(\frac{E_b - E_{fv}}{kT}\right)} \qquad \text{(A.3)}$$

where k is the Boltzmann constant and T is the temperature. The conduction and valence band Fermi levels are given by Nilsson approximation [2]. The energies of the conduction band and valence band are given, respectively, by,

$$E_a = (h\nu - E_g)\frac{m_{hh}}{m_c + m_{hh}} \qquad \text{(A.4)}$$

$$E_b = -\left(h\nu - E_g\right)\frac{m_c}{m_c + m_{hh}} \tag{A.5}$$

The bandgap energy with no forward bias applied, i.e. at zero carrier density, is calculated as a quadratic approximation,

$$E_{g0} = e\left(a + by + cy^2\right) \tag{A.6}$$

where e is the electronic charge, y is the molar fraction of Arsenide in the active region and a, b, and c are the bandgap energy quadratic coefficients. The bandgap energy is modified by the injection of carriers by,

$$E_g\left(N\right) = E_{g0} + eK_g N^{1/3} \tag{A.7}$$

where N is the carrier density and K_g is the bandgap shrinkage coefficient.

References

[1] Connolly, M.; "Wideband semiconductor optical amplifier steady-state numerical model", *IEEE Journal of Quantum Electronics*, Vol. 37, No. 3, Mar. 2001.

[2] Nilsson, N.G.; "Empirical approximations for the Fermi energy of a semiconductor with parabolic bands", *Applied Physics Letters*, Vol. 33, No. 7, Oct. 1978.

A.2. Flowchart of simulation

The structure of the SOA model is outlined in the figure below. Starting from initial values of carrier density and SOA parameters, signal and ASE fields are determined and then used in the rate equation. The rate equation is solved to find value of carrier density that yields the minimum value for ΔN, the change in carrier density. This process continues through multiple iterations until a satisfactory convergence is reached. The value of carrier density found as the solution is then used to calculate the gain and consequently the output signal and spontaneous emission power. The noise figure is calculated from the population inversion factor, which is dependent on the determined carrier density.

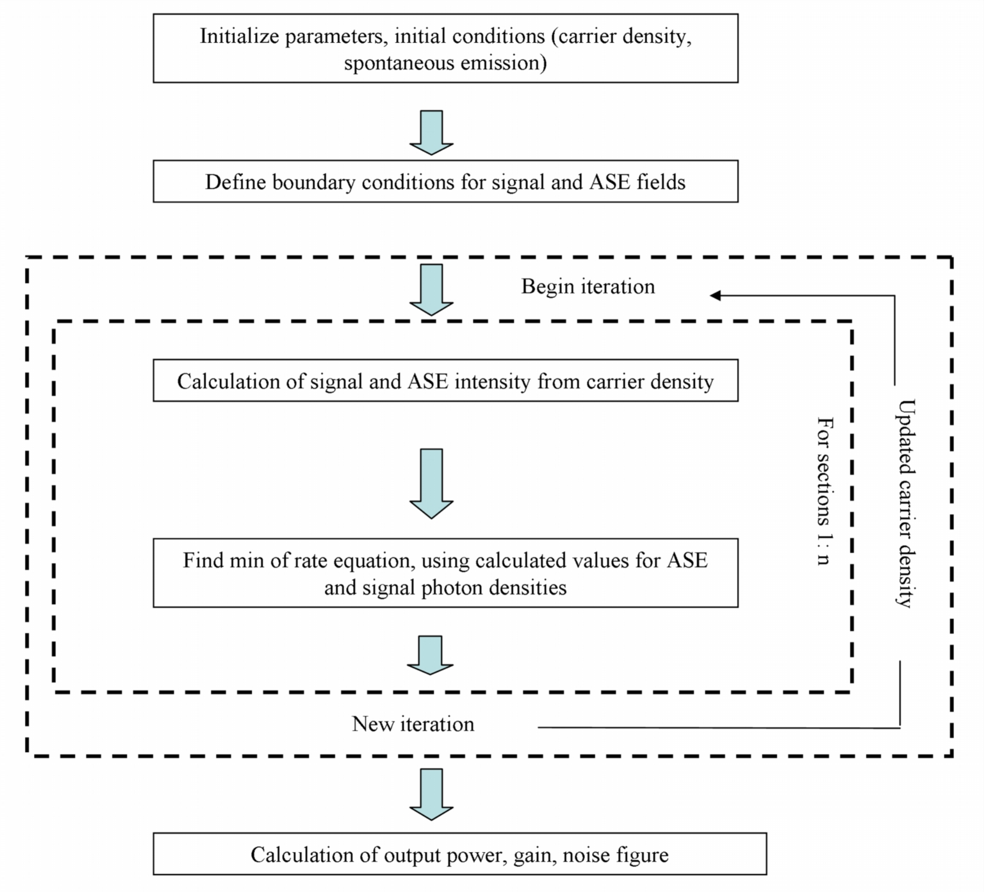

A.1. Flowchart diagram of SOA model

A.3. Parameters of simulation

The parameters of the simulation used in Chapter 3 are presented in Table A.3.1. Most of the values are approximated to common values found in bulk InGaAsP semiconductor materials. The dimensions of the SOA are specific to the SOA being modelled. It should be noted that the confinement factor used for modelling the lateral cavity SOA was the same as that used for the multi-contact SOA. The reason for this was the algorithm's difficulty in converging on a solution for low values of confinement factor.

Parameter	Description	Value
a_1	Differential gain coefficient	1.51×10^{-20} m^{-2}
A	Non-radiative recombination coefficient	1.5×10^{8} s^{-1}
B	Radiative recombination coefficient	2.5×10^{-17} s^{-1}
C	Auger recombination coefficient	3×10^{-41} s^{-1}
d	Active region thickness	0.5 µm
W	Active region width	1.6 µm
L	SOA length	750 µm
n_{e0}	Effective refractive index	3.22
n_{g0}	Group refractive index	3.75
N_0	Carrier density at transparency	1×10^{24} m^{-3}
A	Waveguide losses	3000 m^{-3}
R^2	Reflectivity of facet	5×10^{-5}
dn_e/dN	Refractive index shift coefficient	-1.33×10^{-26} m^{-3}
$d\omega_p/dN$	Gain peak frequency shift coefficient	2.12×10^{-11} m^{3}s^{-1}
Γ	Confinement factor	0.3
ω_{p0}	Gain peak frequency	rads s^{-1}
y	Molar fraction of Arsenide in active region	0.95

A.2. Paramters used for SOA simulation

A.4. List of Acronyms

ASE	Amplified spontaneous emission
BER	Bit error rate
CDP	Carrier density pulsations
CH	Carrier heating
CW	Carrier heating
CWDM	Coarse wavelength division multiplexing
DBR	Distributed Bragg reflector
DWDM	Dense wavelength division multiplexing
EDFA	Erbium doped fibre amplifier
FCA	Free carrier absorption
FPSOA	Fabry-Perot semiconductor optical amplifier
FROG	Frequency Resolved Optical Gating
FWM	Four wave mixing
ISI	Inter-symbol interference
LCSOA	Lateral-cavity semiconductor optical amplifier
LOA	Linear optical amplifier
MCSOA	Multi-contact semiconductor optical amplifier
MOCVD	Metal-organic chemical vapour deposition
MPI	Multi-path interference
NF	Noise figure
NRZ	Non-return to zero
OADM	Optical add-drop multiplexer
ONU	Optical network unit
OLT	Optical line terminal
OSA	Optical spectrum analyzer
OTDM	Optical time domain multiplexing
OXC	Optical cross connect
PON	Passive optical network
PRBS	Pseudo-random binary sequence
QD	Quantum dot
QW	Quantum well
RZ	Return to zero
SBR	Signal to background ratio

SOA	Semiconductor optical amplifier
SHB	Spectral hole burning
SHG	Second harmonic generation
SRS	Stimulated Raman scattering
SNR	Signal to noise ratio
SPM	Self phase modulation
TE	Transverse electric
TM	Transverse magnetic
TMLL	Tuneable mode locked laser
TWSOA	Travelling wave semiconductor optical amplifier
VCSOA	Vertical cavity semiconductor optical amplifier
WDM	Wavelength division multiplexing
XGM	Cross gain modulation
XPM	Cross phase modulation

A.3. List of acronyms used in this thesis.

A.4. List of publications

The following is a list of publications arising from this work.

Refereed journals

K. Carney, R. Lennox, R. Maldonado-Basilio, S. Philippe, A.L. Bradley, P. Landais, "Novel noise controlled semiconductor optical amplifier based on lateral laser cavity", *Electronics Letters*, Vol. 46, No. 18, pp. 1288-1289, September 2, 2010.

R. Lennox, K. Carney, R. Maldonado-Basilio, S. Philippe, A.L. Bradley, P. Landais, "Impact of bias current distribution on the noise figure and power saturation of a multicontact semiconductor optical amplifier", *Optics Letters*, Vol. 36, No. 13, July 1, 2011.

Conference presentations and posters

K. Carney, R. Lennox, R. Maldonado-Basilio, S. Philippe, A.L. Bradley, P. Landais, "Simulation of noise figure and saturation power control technique in multi-section semconductor optical amplifiers", *Photonics Ireland 2011*, September 7 – 9, 2011. (Presentation)

K. Carney, R. Lennox, R. Maldonado-Basilio, S. Philippe, A.L. Bradley, P. Landais, "Multi-electrode SOA for flexible applications in optical networks", *Nanoweek Conference 2011*, January 31 – February 1, 2011. (Poster)

K. Carney, R. Lennox, S. Latkowski, R. Maldonado-Basilio, A.L. Bradley, P. Landais, "*12th International Conference on Transparent Optical Networks, 2010*, pp. 1-4, June 27 – July 1, 2010. (Presentation)

K. Carney, R. Lennox, F. Surre, S. Philippe, A.L. Bradley, P. Landais, "Simulation of a noise controlled semiconductor optical amplifier", *Photonics Ireland 2009*, September 14 – 16, 2009. (Poster)

S. Philippe, F. Surre, K. Carney, R. Lennox, A.L. Bradley, P. Landais, "Novel design for noise controlled semiconductor optical amplifier", *11th International Conference on Transparent Optical Networks, 2009*, pp. 1-4, June 28 – July 2, 2009. (Presentation)

K. Carney, S. Latkowski, R. Maldonado-Basilio, F. Surre, P. Landais, "Measurement of the linewidth enhancement factor using Cassidy's method in a 370 GHz self-pulsating Fabry-Perot laser", *2008 China-Ireland International Conference on Information and Communications Technology*, September 26 – 28, 2008. (Presentation)